

# Novel Micromorph Solar Cell Structures for Efficient Light Trapping and High-Quality Absorber Layers

THÈSE N° 5603 (2012)

PRÉSENTÉE LE 18 DECEMBRE 2012

À LA FACULTÉ DES SCIENCES ET TECHNIQUES DE L'INGÉNIEUR  
LABORATOIRE DE PHOTOVOLTAÏQUE ET COUCHES MINCES ÉLECTRONIQUES  
PROGRAMME DOCTORAL EN SCIENCE ET GÉNIE DES MATÉRIAUX

ÉCOLE POLYTECHNIQUE FÉDÉRALE DE LAUSANNE

POUR L'OBTENTION DU GRADE DE DOCTEUR ÈS SCIENCES

PAR

**Mathieu BOCCARD**

acceptée sur proposition du jury:

Prof. P. Mural, président du jury  
Prof. C. Ballif, Dr M. Despeisse, directeurs de thèse  
Dr F. Finger, rapporteur  
Prof. M. Graetzel, rapporteur  
Prof. M. Topic, rapporteur



ÉCOLE POLYTECHNIQUE  
FÉDÉRALE DE LAUSANNE

Suisse  
2012



# Résumé

Les éléments clés impliqués dans la fabrication des cellules solaires en couches minces de type Micromorphe sont étudiés dans ce manuscrit. Le dispositif Micromorphe est une cellule tandem à deux jonctions comprenant une cellule supérieure en silicium amorphe et une cellule inférieure en silicium microcristallin. En raison de la très petite longueur de diffusion des porteurs photogénérés dans les deux matériaux, les couches photosensibles des deux sous-cellules de dispositifs Micromorphe doivent être maintenues suffisamment minces pour assurer la collecte des porteurs. Pourtant, cette épaisseur limitée ne permet pas d'absorber toute la lumière utilisable (d'énergie plus grande que la bande interdite) après un aller-retour dans le matériau. L'utilisation de stratégies avancées de piégeage de lumière est donc indispensable afin d'atteindre des rendements de conversion élevés. Généralement, des interfaces rugueuses sont utilisées pour induire la diffusion de la lumière dans les couches photosensibles, ce qui améliore leur absorptance.

Une façon simple et analytique de modéliser l'interaction de la lumière avec les différentes couches minces des cellules solaires est notamment présentée. Cette méthode est validée par confrontation avec les mesures expérimentales impliquant différentes interfaces rugueuses. Ensuite, il est montré que la plupart des pertes optiques dans les dispositifs actuels par rapport à ceux idéalisés provient de l'absorption parasite dans les couches périphériques. En effet, les meilleurs régimes de piégeage de lumière actuels s'approchent de la limite classique. En outre, il est démontré que l'absorption parasite est aussi nuisible des deux côtés de la cellule pour la lumière infrarouge.

Pour améliorer le piégeage de lumière de manière significative, des stratégies complémentaires aux interfaces rugueuses doivent donc être appliquées. Pour de telles stratégies, une partie de la lumière s'échappant de la cellule doit être renvoyée à l'intérieur. Ceci peut être obtenu, par exemple, en utilisant un filtre angulaire, qui transmet toute la lumière jusqu'à un certain angle d'incidence, et qui réfléchit toute la lumière ayant un angle d'incidence plus élevé. Un dispositif expérimental optique basé sur un filtrage spatial est développé. Il permet d'empêcher 80 % de la lumière de s'échapper de la cellule, additionnellement aux autres stratégies de piégeage de lumière déjà employées. Une forte amélioration de l'absorption du dispositif complet est démontrée, au prix d'une réduction de l'angle d'acceptance. Cependant, une grande part de la lumière épargnée est absorbée dans les couches non-actives (absorption parasite), indiquant qu'une réduction drastique de l'absorption parasite de ces couches est une condition préalable afin de bénéficier d'un meilleur piégeage de la lumière.

Passant maintenant à l'analyse complète du dispositif, les exigences de l'électrode avant pour

## Résumé

---

les dispositifs Micromorphes à haut rendement sont discutées point par point, en se concentrant à la fois sur les exigences optiques et électriques. La nécessité d'avoir des structures anguleuses et relativement petites pour un couplage efficace de la lumière dans la cellule supérieure est notamment soulignée. La présence de structures de taille suffisante pour diffuser la lumière de grande longueur d'onde (jusqu'à 1100 nm) est ensuite montrée être indispensable pour obtenir un courant élevé dans la cellule inférieure. L'impact négatif des grandes structures anguleuses sur les performances électriques est également soulignée. Cela nous permet d'identifier une morphologie optimale, qui se compose de structures dont la taille est la plus petite permettant de diffuser la lumière jusqu'à 1100 nm, et la forme la plus aigüe ne nuisant pas à la qualité électrique de la cellule inférieure. Ce type de substrat a permis l'obtention d'une cellule Micromorphe affichant une efficacité stable de 11.8% pour moins de 2  $\mu\text{m}$  d'épaisseur totale des couches de silicium.

Pour éviter ce compromis, la combinaison de structures de plusieurs tailles différentes dans une architecture d'électrode multi-échelle est étudiée. Il est montré que, bien qu'aucun gain en termes de diffusion de la lumière ne soit perçu par rapport à une bonne morphologie à échelle unique, une meilleure qualité électrique peut être obtenue, ce qui rend l'approche multi-échelle intéressante. Une efficacité initiale notoire de 14,1% est démontrée avec une telle architecture. Une densité de courant de court circuit de 14 mA/cm<sup>2</sup> est notamment obtenue pour une épaisseur totale des couches de silicium de seulement 3  $\mu\text{m}$ .

Une autre façon d'ajouter un degré de liberté dans la conception d'un dispositif Micromorphe est présenté, consistant en l'insertion d'une couche intermédiaire réfléchissante (IRL) lissante. Plusieurs routes sont explorées, dont le polissage chimio-mécanique et le dépôt par aérosol de ZnO. Des résultats prometteurs ont été obtenus en déposant par spin-coating une laque sur la cellule supérieure puis en la gravant légèrement. Cette étape de gravure dégage les extrémités de la surface de la cellule supérieure, permettant ainsi la conduction électrique, tout en maintenant l'effet lissant. Ce type d'IRL permet un gain de courant considérable dans la cellule supérieure (+2.5 mA/cm<sup>2</sup>), et une amélioration de la tension de circuit ouvert du dispositif (+50 mV), par rapport à un IRL de référence à base d'oxide de silicium.

Les concepts récemment développés permettent une meilleure compréhension des limites et du potentiel actuels des dispositifs Micromorphes. Nous pensons que la mise en œuvre de ces concepts au sein d'une cellule tandem Micromorphe employant les meilleures cellules simples amorphes et microcristallines du moment permettra d'atteindre des rendements stables de 13,5% à 14%. Augmenter l'efficacité des dispositifs Micromorphes au-delà de ces valeurs exigera probablement des améliorations des matériaux photoactifs.

### Mots-clés :

couches minces, silicium, cellules solaires, silicium amorphe, silicium microcristallin, Micromorphe, piégeage de lumière, oxide de zinc, électrodes texturées, morphologie de surface, absorption parasite, réflecteur intermédiaire, haute efficacité, architecture multi-échelle, planarisation.



# Abstract

Key elements involved in the fabrication of Micromorph thin-film silicon solar cells, a tandem device including an amorphous silicon top cell and a microcrystalline silicon bottom cell, are studied in this manuscript. Due to the very short diffusion lengths of photogenerated carriers in both materials, the photoactive layers of both sub-cells of Micromorph devices must be kept thin enough to ensure carrier collection. Due to this limited thickness, not all valuable light (*i.e.* light of higher energy than the band-gap) can be fully absorbed after one pass through the absorber layers. Advanced light-harvesting schemes are thus mandatory to achieve high conversion efficiencies. Random rough interfaces are typically used to induce light scattering in the photoactive layers, thus elongating the light path through these layers, enhancing their absorption.

A simple and analytical way of modeling light harvesting in thin-film solar cells is developed. Its validity is demonstrated by comparing with experimental measurements involving different types of rough interfaces. It is shown that present light-scattering schemes come close to the best theoretically achievable scattering from random rough interfaces. With the morphology of a state-of-the-art rough ZnO layer,  $32 \text{ mA/cm}^2$  can be obtained for a  $1\text{-}\mu\text{m}$ -thick  $\mu\text{c-Si:H}$  layer, compared to  $33.2 \text{ mA/cm}^2$  for the Yablonovitch limit. Most of the gains in terms of light management are therefore to be made by making non-active layers more transparent (since these layers are presently responsible of  $\sim 7 \text{ mA/cm}^2$  of losses for a  $1\text{-}\mu\text{m}$ -thick  $\mu\text{c-Si:H}$  layer). Parasitic absorption in non-active layers is also shown to be equally detrimental on both sides of the cell in the infrared part of the spectrum, corresponding to the wavelength range for which light trapping is most important.

To improve significantly light trapping, complementary strategies to random rough interfaces must therefore be applied. For such a strategy, part of the light has to be prevented to escape from the cell. This can be obtained for example by using an angular filter, transmitting all light up to a certain incidence angle, and reflecting all light of higher incidence angle. An experimental optical setup based on spatial filtering is presented. It is shown to prevent 80% of light from escaping the cell, additionally to other light trapping strategies. A strong absorption enhancement of the complete device is demonstrated, at the cost of a reduction of the acceptance angle. However, most of the spared light is shown to be absorbed in non-active layers. A drastic reduction of parasitic absorption from these layers is therefore identified as a prerequisite to benefit from a better light trapping.

Turning then to complete device analysis, the requirements of the front electrode for high-efficiency Micromorph devices are discussed point-by-point, focusing both on optical and

## Abstract

---

electrical requirements. The need for sharp and relatively small features for an efficient coupling of light in the top cell is notably pointed out, as well as the need for features large enough to scatter light of wavelength up to 1100 nm for a high bottom cell current. The impact of sharp and large features on the electrical performances of the cells is also underlined. An optimal morphology is proposed, exhibiting features that are the smallest enabling scattering of light up to 1100 nm, and the sharpest that do not harm the electrical quality of the bottom cell. A device with a stable efficiency of 11.8% could be obtained on such a substrate.

To avoid this trade-off, the combination of features with different sizes in a multi-scale electrode architecture is studied. It is shown that even though no gain in terms of light scattering is seen compared to a state-of-the-art single-scale morphology, a better electrical quality can be obtained, making the multi-scale approach of interest. A noteworthy 14.1% initial efficiency is demonstrated with such an architecture, with a short-circuit current density of 14 mA/cm<sup>2</sup> for a total thickness of the silicon layers of 3 μm.

Another way to add a degree of freedom in the design of a Micromorph device is also presented, employing a smoothening intermediate layer between both sub-cells. A separate tuning of the morphology inducing light scattering in each sub-cell can be made. Several routes are explored, out of which promising results are obtained by using a spin-coated lacquer on the top cell. A slight etching uncaps the tips of the top cell surface and allow for electrical conduction, whereas the smoothening effect is preserved. A large top cell current boost (up to +2.5 mA/cm<sup>2</sup>) and open-circuit voltage improvement (+50 mV) are obtained, with many adjustable processing parameters to obtain various morphologies.

The newly developed concepts enable a better understanding of the present limitations of Micromorph devices. We believe that, by implementing these concepts in Micromorph tandem devices employing state-of-the-art amorphous and microcrystalline single-junction solar cells, stable 13.5% to 14% efficiency are within reach. Yet, increasing further the efficiency of Micromorph devices will likely require material improvements.

### Key words:

thin-film, silicon, solar cells, amorphous silicon, microcrystalline silicon, Micromorph, light trapping, zinc oxide, textured electrodes, surface morphology, parasitic absorption, intermediate reflector, high efficiency, multi-scale architecture, planarization techniques.

# Contents

<b>Résumé / Abstract</b>	<b>iii</b>
<b>1 Introduction</b>	<b>1</b>
1.1 Solar energy . . . . .	1
1.2 Thin-film silicon technology and the Micromorph concept . . . . .	2
1.3 Status of research on Micromorph technology . . . . .	4
1.4 Structure of this report . . . . .	6
1.5 Contribution of this work to the research field . . . . .	7
<b>2 Details about deposition and characterization</b>	<b>11</b>
2.1 Typical sequence of cell deposition . . . . .	11
2.2 Superstrate properties . . . . .	11
2.2.1 Low-pressure chemical vapor deposited zinc oxide (LPCVD ZnO) . . . . .	11
2.2.2 Replication process . . . . .	12
2.2.3 Hydrogenated indium oxide (IOH) . . . . .	14
2.3 Current-voltage (J(V)) and external quantum efficiency (EQE) measurements . . . . .	15
2.4 Absorptance measurements . . . . .	16
<b>3 Analytical modeling of light trapping</b>	<b>21</b>
3.1 Motivation and mechanism . . . . .	21
3.2 Modeling of light trapping . . . . .	23
3.3 Angular distribution of light entering a cell . . . . .	26
3.3.1 Quantification of the scattering ability . . . . .	26
3.3.2 Typical light-scattering properties of rough electrodes . . . . .	28
3.4 Extension of the model to realistic devices . . . . .	29
3.4.1 Implementation of experimental light-scattering distributions . . . . .	29
3.4.2 Implementation of parasitic absorption and reflection . . . . .	30
3.5 Validation with experimental data . . . . .	32
3.6 Important parameters governing light harvesting . . . . .	35
3.6.1 Effect of changing the light-trapping properties of the front electrode . . . . .	35
3.6.2 About the light path enhancement factor . . . . .	36
3.6.3 Identification of the most limiting parameters . . . . .	37
3.7 Conclusion . . . . .	38

<b>4</b>	<b>The interconnection between parasitic absorption and light trapping</b>	<b>41</b>
4.1	Unlinking absorption and haze in front electrodes . . . . .	42
4.1.1	Experimental details . . . . .	42
4.1.2	Influence of parasitic absorption on the cell current . . . . .	42
4.1.3	Haze influence on the cell current . . . . .	44
4.1.4	Modeling . . . . .	46
4.1.5	Conclusion . . . . .	48
4.2	Effect of parasitic absorption in front and back contacts . . . . .	49
4.2.1	Experimental details . . . . .	49
4.2.2	Experimental results and discussion . . . . .	50
4.2.3	Modeling . . . . .	52
4.2.4	Conclusion . . . . .	53
4.3	Trapping light in the glass to surpass the Yablonovitch limit . . . . .	54
4.3.1	Mechanism and prior art . . . . .	54
4.3.2	Realization and characterization . . . . .	55
4.3.3	Results . . . . .	57
4.3.4	Potential of this approach . . . . .	58
4.3.5	Conclusion . . . . .	62
4.4	Conclusion . . . . .	62
<b>5</b>	<b>Towards optimal textured electrodes for Micromorph devices</b>	<b>65</b>
5.1	Experimental details . . . . .	65
5.2	Influence of the texture feature size . . . . .	66
5.3	Plasma surface-treatment effects . . . . .	68
5.4	Transparency - conduction trade-off for the front electrode . . . . .	70
5.5	Optimal feature size investigation . . . . .	73
5.6	Schematic summary . . . . .	76
5.7	Conclusion . . . . .	77
<b>6</b>	<b>Multi-scale textured substrates</b>	<b>79</b>
6.1	Prior art and motivation . . . . .	79
6.2	All-ZnO-based multitextures: proof of concept . . . . .	80
6.2.1	Experimental details . . . . .	80
6.2.2	Motivation for multi-scale substrates . . . . .	81
6.2.3	Effect of increasing the size of the small features . . . . .	85
6.2.4	Effect of increasing the size of the understructure . . . . .	85
6.2.5	Effect of smoothing the understructure . . . . .	86
6.2.6	Conclusion . . . . .	88
6.3	High-efficiency multitextures: combining nanoimprint lithography, IOH and rough ZnO . . . . .	89
6.3.1	Architecture of the device . . . . .	89
6.3.2	Cell results and discussion . . . . .	91
6.4	Conclusion . . . . .	93

<b>7</b>	<b>Smoothing intermediate reflecting layers</b>	<b>95</b>
7.1	Motivation: mapping of Micromorph properties as a function of the substrate morphology . . . . .	96
7.2	Proof of concept: polishing of SiO <sub>2</sub> -based intermediate reflecting layers . . . . .	98
7.2.1	Experimental details . . . . .	98
7.2.2	Results and discussion . . . . .	98
7.2.3	Conclusion . . . . .	99
7.3	Thick ZnO-based intermediate reflecting layers . . . . .	100
7.4	Spray-coating of ZnO from Zn-acetate . . . . .	102
7.5	Spin-coating of lacquer with selective etching . . . . .	104
7.5.1	Motivation and experimental procedure . . . . .	104
7.5.2	Electrical performance . . . . .	106
7.5.3	Optical effects . . . . .	107
7.5.4	General discussion . . . . .	108
7.6	Potential for high-efficiency Micromorph devices . . . . .	110
7.7	Conclusion . . . . .	111
<b>8</b>	<b>Conclusion and perspectives</b>	<b>113</b>
8.1	General conclusion . . . . .	113
8.2	Perspectives . . . . .	115
<b>A</b>	<b>EQE measurement of multi-junction devices</b>	<b>117</b>
A.1	Bias light . . . . .	117
A.2	Bias voltage . . . . .	117
<b>B</b>	<b>Method for studying the fill factor of Micromorph cells</b>	<b>121</b>
B.1	Problems faced when measuring fill factors in tandem devices . . . . .	121
B.2	Setup presentation . . . . .	122
B.3	Setup calibration . . . . .	123
B.4	Different applications . . . . .	124
<b>C</b>	<b>Other possible uses of lacquer in solar cells</b>	<b>129</b>
C.1	Before silicon deposition . . . . .	129
C.2	After silicon deposition . . . . .	131
<b>D</b>	<b>Micromorph properties as a function of the substrate morphology</b>	<b>133</b>
D.1	Mapping of Micromorph properties . . . . .	133
	<b>Abbreviations and symbols</b>	<b>137</b>
	<b>Bibliography</b>	<b>153</b>
	<b>Acknowledgements</b>	<b>155</b>
	<b>Curriculum Vitae</b>	<b>157</b>



# 1 Introduction

## 1.1 Solar energy

The sun is already the main source of the electricity consumed nowadays. However, most of the present conversion of energy from the sun to electricity uses a long CO<sub>2</sub> cycle: photosynthesis to crack CO<sub>2</sub> and grow plants, sedimentation and maturation for thousands of years to make oil, gas or coal, and a Carnot machine to burn it, give back CO<sub>2</sub> and produce a motion energy, converted to electricity. The efficiency of such a mechanism is quite poor, as the Carnot engine itself saturates at around 35% (for temperatures typically used). Also, the consumption of fossil fuels is much faster than their production, making this electricity production highly unsustainable. By using biomass, the cycle can be shortened to several years only, enabling sustainable production, but with again a very low conversion efficiency from sun energy to electricity. Hydroelectricity can perform a bit better, by using a water cycle of only a few days: sun energy evaporates water, elevates it from sea level to several thousands of meters, and when falling down back to sea level, a tiny fraction of this potential energy is converted to electricity with an alternator. Here again, the conversion efficiency is very low, as even though the alternator is highly efficient, its efficiency applies only to the tiny fraction of potential energy converted with the dam (representing a tiny fraction of the potential energy difference). Wind energy originates also from sun energy that creates wind, again with low global efficiency. Geothermal power exploits natural heat from the Earth's crust. This is not renewable, strictly speaking, as it comes from natural nuclear reactions in the subsoil, but can be sustained for millions of years as long as power consumption is moderate. However, the maximal power output per square meter (around 60 mW/m<sup>2</sup>) is more than three orders of magnitude lower than the average solar irradiance (around 340 W/m<sup>2</sup>). Finally, nuclear energy does not come from the sun, but is absolutely not renewable.

Thus, by converting sunlight to electricity in a very direct way, photovoltaics is a fantastic technology. Moreover, when compared to the above mentioned techniques, present record conversion efficiencies from sunlight to electricity (directly) of above 40% are extremely good (modern nuclear power plants aim at 36% conversion efficiency), and even a common

commercially available solar module with 15% conversion efficiency is not bad at all. The main drawbacks for this technology are that storage is not efficient (as neither sunlight nor electricity can be stored in a cost-effective way, contrary to fossil fuels or water in a dam), and electricity produced from nuclear energy or fossil fuels is nowadays extremely cheap, making photovoltaics non-competitive. However, the price of photovoltaic electricity has shrunk by a factor 20 during the last 30 years, while fossil fuels are getting more and more expensive due to increasing demand and their decreasing availability. Nuclear energy is also increasingly expensive, not only due to the increase in the price of uranium, but also (and mostly) due to increasing security costs. On the other hand, a study of photovoltaics price was shown by Ossenbrink at the 27<sup>th</sup> EU-PVSEC in Frankfurt (September 2012), indicating that modules can be bought for 800 euros per kiloWatt peak (kWp). With a yield of 1300 kWh/kWp/year and a 20-year lifetime, the simplest calculated price of solar electricity is 3 euro-cents per kWh. This price includes only the modules, but extra costs apply for a complete system (mounting, inverter, ...). A more relevant price for grid-connected PV in Europe of 18.5 euro-cents/kWh was derived in the same presentation. It includes the aforementioned extra costs, plus 5% of capital interest rate, 1% of maintenance costs (leading to 2300 euros/kWp), and a yield of 1000 kWh/kWp. With this price, grid parity is already achieved in several sunny European countries including Spain, Portugal and Italy, and in several countries such as Denmark where electricity is expensive.

### 1.2 Thin-film silicon technology and the Micromorph concept

As an in-depth description of thin-film silicon solar cells has recently been published [Shah 10], this section gives only a few insights about the present status and challenges of the field. Thin-film silicon technology consists of growing silicon directly from silane gas ( $\text{SiH}_4$ ), thus bypassing most of the energy-intensive production steps of standard wafer-based silicon technology. The main advantages are lower production cost and lower energy and material use. The disadvantage is that the quality of the photoactive material is lower compared to perfect monocrystalline wafers, making the efficiency (given by the generated watts per unit area divided by the irradiance under standard testing conditions) lower than crystalline technology. This results in a lower yield in terms of kWh/m<sup>2</sup> for most locations. Then, due to fixed costs such as glass support, encapsulation, mounting or transport (that scale with the surface area, and that are very similar for all technologies), the production cost advantage of the module in terms of dollars per kWp is not necessarily maintained for a complete system, as less kWp can be installed per square meter. For this reason, the price of energy in terms of dollars per kWh (which is all that matters at the end) is not favorable to low-cost low-efficiency module concepts. For thin-film silicon technology to survive the present crisis in the very competitive solar energy sector, the current main challenge is to increase the module efficiency. Indeed, despite its current difficulties, thin-film silicon remains a very (if not the most) promising technology for a fast and very large-scale global integration of photovoltaic energy, thanks to its sparse use of abundant and non-toxic material.



## 1.2. Thin-film silicon technology and the Micromorph concept

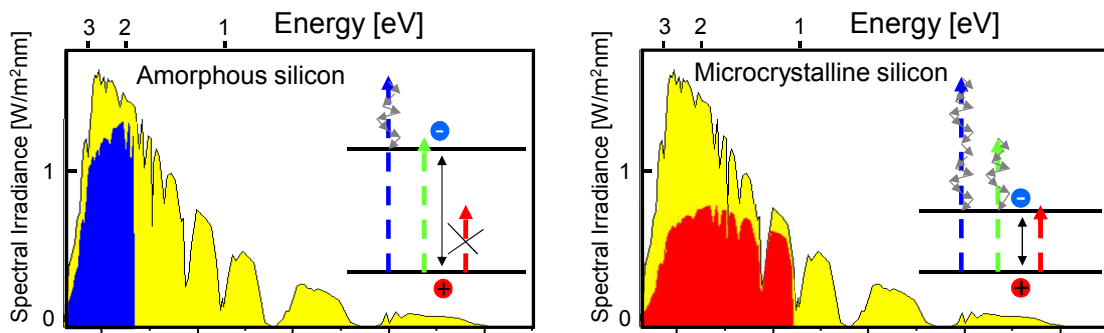


Figure 1.1: Schematic representation of the standard AM1.5G spectrum, with the share of the irradiance that can be converted to electricity with  $a$ -Si:H and  $\mu c$ -Si:H, together with a schematic view of the band-to-band absorption of blue, green and red light in both semiconductor materials.

To boost the efficiency of thin-film silicon technology, tandem or triple junctions are widely developed. One of the most employed structures is the Micromorph cell, introduced in 1994 by IMT in Neuchâtel [Meier 94] and named in 1996 [Meier 96], also called hybrid thin-film silicon solar cell [Yamamoto 03]. It is a tandem device, composed of a hydrogenated amorphous silicon ( $a$ -Si:H) top cell and of a hydrogenated microcrystalline silicon ( $\mu c$ -Si:H) bottom cell. It shows a high-efficiency potential due to its better use of the solar spectrum than single  $a$ -Si:H devices: the lower band-gap of  $\mu c$ -Si:H (1.1 eV compared to typically 1.7 eV for  $a$ -Si:H) permits the absorption of infrared light for which  $a$ -Si:H is transparent, as sketched in Fig. 1.1. Whereas the efficiency of single-junction  $a$ -Si:H modules is  $\sim 7\%$  in mass production, the industrial applicability of Micromorph technology has already been proven with 10%-efficient 1.4 m<sup>2</sup> modules at the production level [Bailat 10, Klein 11]. Yet, the maximum theoretical efficiency of over 30% [Meillaud 06] is still far from being fully explored, and thin-film silicon is still subject to intense research.

In the following, we will consider the superstrate configuration, for which all active layers are deposited on a transparent superstrate (usually glass, but possibly a transparent plastic film) through which light enters the device. The minimal stack consists of (from the superstrate side) a transparent conductive oxide (TCO); p-doped, intrinsic and n-doped  $a$ -Si:H layers; p-doped, intrinsic and n-doped  $\mu c$ -Si:H layers; a back electrode and a back reflector (that can typically be a single metallic layer, or a TCO and a white reflector). In the substrate configuration, typically used when depositing on opaque substrates, the deposition sequence is reversed, and light enters through the last-deposited layer. For both configurations, present devices include many more layers, with typically around six layers for the  $a$ -Si:H top cell (e.g. two  $p$ -,  $i$ - and  $n$ - layers, plus possible buffer layers), also several layers for the bottom cell, an intermediate reflecting layer (IRL), and more sophisticated electrodes. A schematic side view of a baseline Micromorph cell as fabricated in PVlab can be seen in Fig. 1.2.

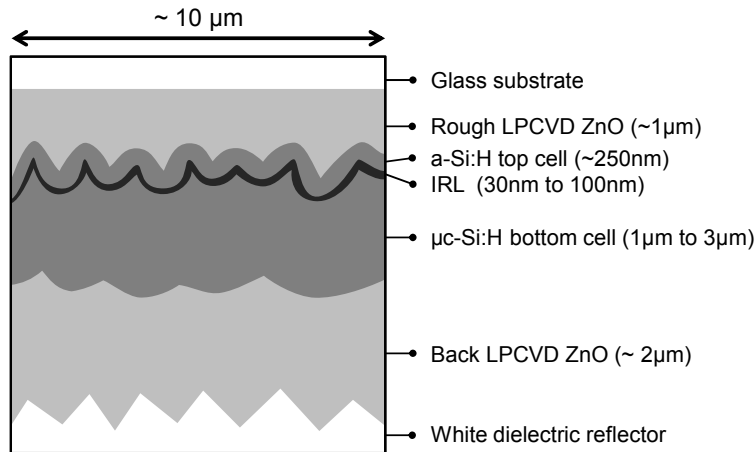


Figure 1.2: Schematic side view of a Micromorph cell. Photons with energies higher than 1.8 eV will be principally absorbed in the top cell. Those with energies between 1.1 eV and 1.8 eV can be absorbed in the bottom one.

### 1.3 Status of research on Micromorph technology

The major limitation to Micromorph efficiency is the need to keep active absorber layers thin enough to mitigate the effects of light-induced degradation in the case of *a*-Si:H [Staebler 77], to keep good diode quality in the case of  $\mu c$ -Si:H [Vetterl 01] and to ensure a higher throughput and industrial competitiveness in both cases. Enhancing the absorption in the thin photoactive layers has thus been one of the main subjects of research for the last decade.

To boost absorption in the *a*-Si:H cell, IRL [Buehlmann 07, Yamamoto 04], inserted between the *a*-Si:H and  $\mu c$ -Si:H cells can be used. The lower refractive index of the IRL ( $n_{IRL} < 2$ ) compared to silicon ( $n_{Si} = 4$ ) results in partial back reflectance in the top cell of light in the 550 nm to 700 nm range that is not fully absorbed in the first pass. The IRL design also ensures a complete transmittance of red and infrared light to the bottom cell. This allows for a controlled split of current between the top and bottom cells, and thus a thickness reduction of the *a*-Si:H absorber layer for a given current density. This is crucial to improve the stabilized efficiencies of Micromorph devices [Söderström 09]. Research on the IRL mostly focuses on lowering its refractive index, from 2 (for zinc oxide, ZnO) or 1.8 (for a typical sub-stoichiometric silicon oxide, SiOx) at present, to values around 1.5 [Feltrin 12]. Implementing photonic crystals [Üpping 11] or metallic nanoparticles [Feltrin 12] has also been attempted, which resulted in a strong improvement of the top cell current, but a detrimental bottom cell current loss.

Another challenge for thin-film silicon solar cells and more particularly Micromorph devices comes from the balance between optimum light management and the material quality of the silicon layers: the morphology of the textured front electrode influences both the scattering of the light in the device [Deckman 83c, Domine 10, Sai 10, Boccard 10b] and the growth of the subsequent silicon layers [Sakai 90, Nasuno 01, Python 08]. Furthermore, the requirements for the morphology of the front electrode for the most efficient light trapping are different

### 1.3. Status of research on Micromorph technology

---

for the top cell and for the bottom cell [Domine 08]. The front TCO electrode is therefore subject to intense research as it should combine not only strong, broad-band light-scattering properties and a surface promoting the growth of silicon layers of excellent material quality but also a high transparency and sufficient electrical conduction. A drastic approach, in the substrate configuration, is the FLiSS [Sai 10], that aims at providing light scattering with a completely flat substrate, by using a rough substrate covered with a “dead” *a*-Si:H layer and subsequently polished. In contrast, trade-offs are sought in the superstrate configuration [Bailat 06, Feltrin 12], as well as alternative light-trapping strategies.

Many recent publication focus on improving light trapping through advanced nanostructures such as nanopillars [Naughton 10], nanodomes [Zhu 10], nanocavities [Battaglia 12b], or metallic nanoparticles inducing plasmonic effects [Moulin 08, Eminian 11, Tan 12]. Even though extremely fashionable and promising according to recent simulations [Vanecek 11, Schiff 11, Yu 10], best thin-film silicon efficiencies are still reported by using traditional self-developed random light-scattering schemes [Benagli 09, Kroll 11, Yan 12]. The use of nanoimprint lithography, widely developed in the last years [Escarré 11, Han 11], might however change this situation, as indicated by the equally good results obtained with a replicated superstrate or a master superstrate [Battaglia 11c]. The versatility of this new tool recently enabled a precise comparison of random and periodic approaches [Battaglia 12b] that indicated that, when proper designs are employed, both approaches can yield equally high efficiencies (10.9% for co-deposited single-junction *a*-Si:H cell) and equally good light management (17.1 mA/cm<sup>2</sup>).

Simulation is also widely used to understand – and determine how to improve – light harvesting in thin-film silicon solar cells. Early modeling works, 30 years ago, are still the reference in terms of fundamental limitations [Deckman 83c, Tiedje 84]. Yet, the mechanism of scattering of light from the electrode to silicon has been widely studied recently with modeling or experimental approaches [Jäger 09, Domine 10, Rockstuhl 10, Schulte 11a, Schulte 11b]. However, up to now, few indications about favorable morphologies could be obtained from simulation that were not already suggested by experimental results. Yet, recent works [Rockstuhl 10, Fahr 11, Battaglia 12a] indicate that improved light harvesting requires enhancing the sharpness of the surface texture, with larger inclinations than used with standard structures. Such sharp structures are, however, undesirable for growing good quality silicon layers. Also, it was shown in [Bittkau 12] that scattering the light reflected at the back of the device, *e.g.* with a rough silver layer, enables higher angles to be reached than by scattering the light transmitted through a rough transparent electrode - silicon interface. Experimentally, Sai *et al.* observed that for light trapping in substrate-type devices, a rough silicon - back electrode interface is more important than a rough front electrode - silicon interface, whereas both are of similar importance for the superstrate configuration [Sai 10].

The need to reduce the parasitic absorption in the electrodes has been shown recently. A large reduction of the absorption in the 600 nm to 1100 nm wavelength range can be obtained by reducing the free-carrier density, leading to significant current increase in  $\mu c$ -Si:H

cells [Berginski 08, Domine 08]. However, doping, thickness, morphology and conductance are strongly interlinked in textured ZnO layers, making separate adjustment of the carrier concentration (varied by doping) very delicate [Berginski 07, Faÿ 06]. Significant improvements in transparency (for a maintained conductance) could still be made by increasing mobility, with new materials like hydrogenated indium oxide ( $\text{In}_2\text{O}_3\text{:H}$ , or IOH) [Koida 10], or post-deposition treatments of ZnO [Ruske 10, Ding 13]. The combination of an insulating rough superstrate with a high-mobility IOH layer already equaled standard TCO, and could enable higher efficiencies with the development of specially designed masters. For back electrodes, the use of photonic crystals as highly reflective layers was also suggested [Krč 09, Isabella 09], but their implementation challenging. Finally, reduction of parasitic absorption in doped layers is also largely studied. The implementation of oxide layers [Sichanugrist 93, Cuony 12, Smirnov 12] or carbide layers [Finger 09, Chen 12] was shown to be promising in improving the current of thin-film silicon solar cells.

### 1.4 Structure of this report

Basic information about experimental details is given in each chapter, in an effort to make it understandable independent of the reading of previous chapters.

In chapter 3, an analytical model of light trapping in solar cells is presented that extends the formalism suggested by Deckman *et al.* [Deckman 83c] based on tracing an average ray of light. Arbitrary light-scattering schemes and parasitic absorption in the cell are implemented, and the approach is validated by comparing with experimental measurements. The intuitive understanding of this extended model is discussed, and it is used to determine the present main limitations of classical light trapping based on random rough substrates. Parasitic absorption is notably shown to be the main cause for current loss in present state-of-the-art devices.

Then, the interconnection between two optical properties of Micromorph devices, light trapping and parasitic absorption, is underlined in chapter 4. The respective influence of haze and free carrier absorption (FCA) of transparent front electrodes on the photogenerated current of Micromorph devices is studied. Parasitic absorption in front and back electrodes is then shown to have an equivalent influence in the long-wavelengths range. The use of microlenses combined with a reflecting silver layer with apertures at the focal points of the microlenses array is also introduced to push further light trapping with an anti-escape system.

In chapter 5, a detailed study of the requirements of a textured electrode for high-efficiency Micromorph devices is given. The respective influences of the typical size and inclination of the features composing the electrode surface are evidenced, leading to a schematic mapping of the electrical properties of Micromorph devices as a function of the typical size and inclination of these features. The conductivity - transparency trade-off is also addressed, leading to the complete description of an optimal single-layer substrate.

## 1.5. Contribution of this work to the research field

---

After seeing that the trade-off between optical and electrical performances limits the light-trapping capacity and the quality of material reachable with standard superstrates, we describe in chapter 6 the development of multi-scale textured superstrates and discuss their potential advantages compared to state-of-the-art single-layer superstrates. In a first part, the conductivity and transparency of the electrodes is not studied: the focus is put on the trade-off between surfaces with good light-scattering capability and surfaces showing favorable morphologies for the growth of high-quality silicon layers. In a second part, high-efficiency devices are targeted by combining the versatility of nanoimprint lithography, the unusually high carrier mobility of IOH (over  $100 \text{ cm}^2/\text{V}\cdot\text{s}$ ), and the unequalled light-scattering properties of self-textured ZnO. This multi-scale electrode architecture is shown to allow efficiencies as high as 14.1% to be reached with a Micromorph device employing only  $3 \mu\text{m}$  of silicon.

Chapter 7 discusses the use and benefits of IRLs that adapt the morphology of the top-cell surface to make it suitable for the growth of the bottom cell. In one approach, small and sharp features only are used for the front electrode (favoring a high top cell current), while large and smooth features are obtained with a  $3\text{-}\mu\text{m}$ -thick ZnO layer used as an IRL. Also, the combination of a single TCO electrode with a smoothening IRL is shown to be more promising to combine high currents and good electrical quality in Micromorph devices. A first approach presented is based on polishing of silicon oxide-based intermediate reflectors (SOIR), whereas a second approach focuses on non-vacuum-deposited layers with planarizing properties. ZnO films sprayed from zinc acetate dissolved in ethanol are shown to lead to good planarization. However, the high deposition temperatures ( $> 250^\circ\text{C}$ ) required for good film properties forbid their use as IRLs. A new technique is then developed employing a partially etched isolating lacquer layer, with promising results.

General conclusions are then drawn, and perspectives for future developments are sketched in chapter 8. Appendix A gives insights about external quantum efficiency (EQE) measurements of Micromorph devices and the potential artifacts to avoid; appendix B introduces a setup used to vary the matching conditions when measuring Micromorph devices; appendix C discusses a few possible uses of lacquer in thin-film silicon solar cells excluding the IRL position; and appendix D finally shows the tables used in chapter 5 to map the Micromorph properties as a function of the typical size and inclination of the features composing the surface of the front electrode.

## 1.5 Contribution of this work to the research field

- A simple analytical way of simulating light management in solar cells is proposed, by including experimental light-scattering properties calculated from the topography of the surface (as proposed by Dominé *et al.*) in the geometrical average-ray tracing introduced by Deckman *et al.* This model enables a fast and intuitive description of light trapping in realistic solar cells [Boccard 12d].
- It is then demonstrated, by combining experimental data and simulations, that current

state-of-the-art light trapping schemes come close to the Lambertian limit. Indeed, parasitic absorption is shown to mostly limit the current outputs of present thin-film silicon solar cells.

- The necessity to reduce parasitic absorption (preferentially simultaneously both in the front and in the back of the cell) in order to fully benefit from better light scattering is also evidenced with the newly developed model.
- The concept of ultra light trapping is validated for thin-film silicon with a microlenses optical system. A large EQE gain (up to +45% in the weak-absorption wavelength range) is obtained when using this system with a  $\mu\text{c-Si:H}$  device employing a state-of-the-art light-trapping scheme.
- The requirements in terms of morphology of the front electrodes for high-efficiency Micromorph devices are experimentally determined. Key parameters to obtain a high top cell current, a high bottom cell current and the growth of homogeneous and high quality silicon layers are identified. An optimal single-scale morphology is depicted, exhibiting the smallest and sharpest features enabling both a haze close to unity up to 1100 nm and the growth of good quality silicon layers [Boccard 12b].
- Two ways of increasing the flexibility in the design of Micromorph cells are experimentally studied, firstly by using multi-scale textured electrodes, secondly by using smoothening IRL. Their main benefit compared to a single-scale texture is shown not to be a gain in light trapping, but the possibility to better address the trade-off between light trapping and good electrical quality of the silicon layers. A Micromorph device with 14.1% efficiency is noteworthy demonstrated with such a multi-scaled textured electrode [Boccard 12a, Boccard 12c].
- A novel technique to fabricate smoothening IRL is introduced. This technique of partial etching enables the use of isolating and low-index ( $n < 1.5$ ) material. The resulting IRL is demonstrated to combine a strong boost of the top cell current with a surface morphology favorable to high-quality  $\mu\text{c-Si:H}$  growth. With simple calculations, this concept is shown to enable a 13.5% stable efficiency Micromorph device employing existing state-of-the-art single-junctions.

The presented work led to several publications as a first author [Boccard 10a, Boccard 10b, Boccard 11, Boccard 12a, Boccard 12b, Boccard 12c, Boccard 12d, Boccard 12e] and as a co-author [Ballif 11, Battaglia 10, Battaglia 11a, Battaglia 11b, Battaglia 11c, Battaglia 12a], [Battaglia 12b, Battaglia 13, Bugnon 11, Cuony 10, Cuony 12, Despeisse 10, Despeisse 11], [Ding 12, Feltrin 09, Hänni 11, Hänni 12, Holovský 12, Meillaud 11, Söderström 10].

All characterization and analysis of the devices presented in this thesis report were carried out by the author, unless stated otherwise. Many TCO and silicon layers were deposited by the author, except for some of the standard top cells, bottom cells or TCO layers that were

## **1.5. Contribution of this work to the research field**

---

deposited in batches in large-area systems. The nanoimprint lithography process to replicate nanostructures in lacquer on glass was performed by Jordi Escarré or Karin Söderström, using the facilities of the EPFL Optics group (EPFL/STI/IMT-NE/OPT).





## 2 Details about deposition and characterization

This chapter gives insights about the main layers and characterization tools used in this document. Standard layers or procedures are not detailed, but more precision is given for the most studied ones. Also, the measurements that are particularly delicate for the precision of the results presented in this document are detailed. In all the following, all cells are deposited in the superstrate configuration, but the terms substrate and superstrate are both used to describe the glass + transparent electrode stack on which the silicon layers are grown.

### 2.1 Typical sequence of cell deposition

The superstrate used for all devices described in this document is a 0.5 mm-thick aluminoborosilicate glass produced by Schott (AF45). Prior to any deposition, it is manually cleaned with a detergent, then in a basic bath, in an acid bath and finally in de-ionized water. Then, the front electrode is deposited on it, followed by the amorphous silicon (*a*-Si:H) top cell, an optional intermediate reflective layer (IRL), the microcrystalline silicon ( $\mu$ c-Si:H) bottom cell, and the back electrode which is always made out of zinc oxide (ZnO) for the presented cells. No back reflector is deposited on the back electrode, but a detached dielectric white reflector of high reflectivity is applied against the back of the cell during optical measurements.

### 2.2 Superstrate properties

#### 2.2.1 Low-pressure chemical vapor deposited zinc oxide (LPCVD ZnO)

LPCVD ZnO obtained from diethyl zinc and water, and doped with diborane, is used extensively in PV-lab for front and back electrodes of thin-film silicon solar cells. In the as-deposited state, it combines a high growth rate (typically 3 nm/s), a large range of doping possibilities (carrier densities from  $1 \cdot 10^{19}$  to  $2 \cdot 10^{20}$  cm<sup>-3</sup>), a high mobility (up to 60 cm<sup>2</sup>/V/s), and a large variety of possible surface textures. All layers used in this document were deposited with temperature, pressure and gas flows adjusted so that pyramidal features form naturally at the

## Chapter 2. Details about deposition and characterization

---

surface of the layer during deposition, which is linked to a preferential orientation of the polycrystals [Nicolay 09]. The typical size of the pyramids scales with the deposition time, for fixed deposition conditions, as can be seen from the scanning electron microscope (SEM) images in Fig. 2.1. Increasing doping leads to a reduction of the size of the features [Fajó 06]. Estimations of the typical sizes of the pyramids were made by taking the square root of the average size of the features. This method allows comparison between samples, but the absolute values are very approximate and user-dependent as no clear definition of the limits of the features exist, and the selection of the representative features is arbitrary.

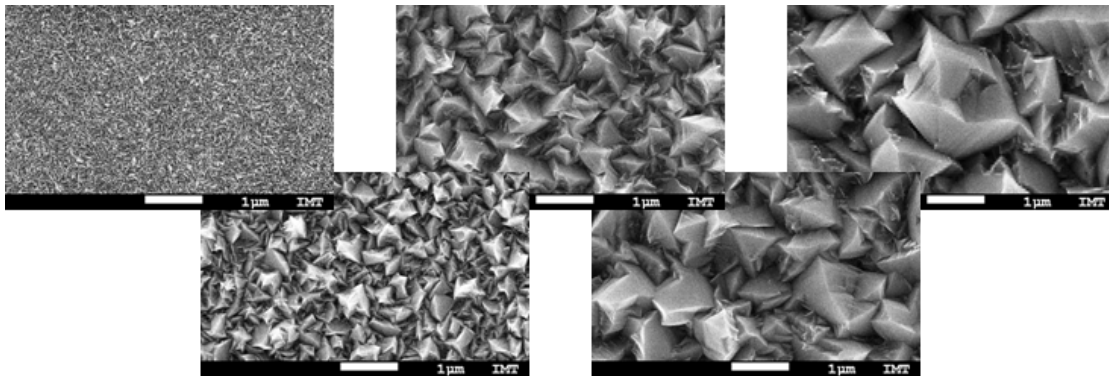


Figure 2.1: SEM images of the surfaces of LPCVD ZnO layers of thicknesses of 0.1  $\mu\text{m}$ , 1  $\mu\text{m}$ , 2  $\mu\text{m}$ , 4  $\mu\text{m}$  and 7  $\mu\text{m}$ .

For the fabrication of multi-scale textured electrodes in chapter 6, ZnO layers of up to 30  $\mu\text{m}$  were deposited and implemented in solar cells. As can be seen in Fig. 2.2, very large features can be obtained with such large thicknesses. For all LPCVD ZnO layers showing the typical pyramidal surface features seen here, a plasma treatment was developed to smoothen the bottom of the valleys surrounding these pyramids [Bailat 06]. This treatment is applied in a reactive ion etching system which applies a negative bias to the substrate holder, using pure argon or a mixture of oxygen and argon, leading to a combination of sputtering and redeposition efficiently rounding the bottom of the ZnO surface features, as seen in Fig 2.2.

The haze spectrum and angle resolved scattering (ARS) function measured at 543 nm for the aforementioned thick ZnO layers are shown in Fig. 2.3. For layers thicker than 15  $\mu\text{m}$ , all transmitted light is scattered, for all wavelengths up to 1500 nm. This scattering (at least for 543 nm light) is moreover very close to Lambertian scattering as seen from Fig. 2.3b. The post-deposition argon plasma treatment allows us to tune the morphology of these layers. Fig. 2.3c shows the effect of varying the duration of the plasma treatment from 0 to 3 hours.

### 2.2.2 Replication process

A high-fidelity replication process for photonic nanostructures was developed in PV-lab independently of this work during the same period [Söderström 11, Escarré 11]. This enables

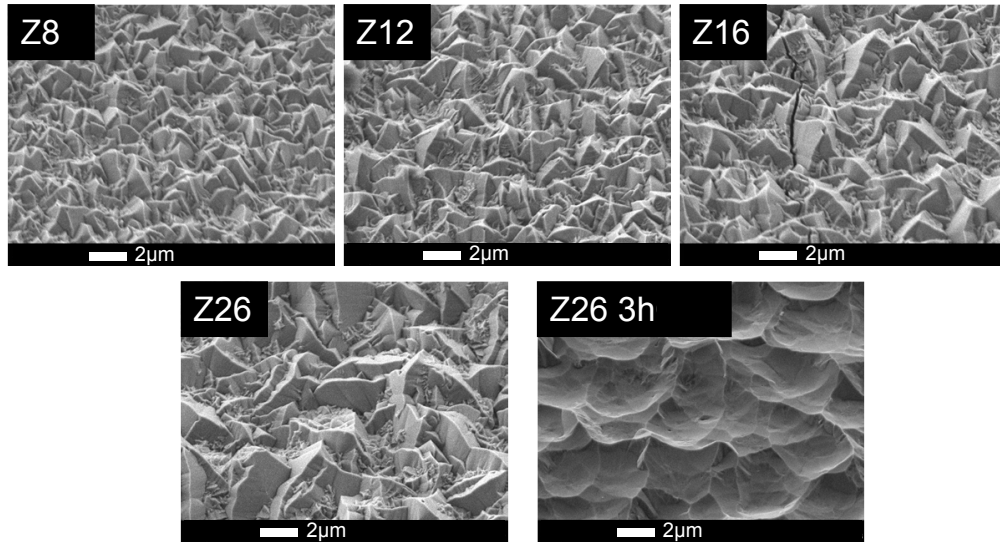


Figure 2.2: SEM images of the surfaces of LPCVD ZnO layers of thicknesses of 8  $\mu\text{m}$ , 12  $\mu\text{m}$ , 16  $\mu\text{m}$ , 26  $\mu\text{m}$  and 26  $\mu\text{m}$  treated for 3 hours in an argon plasma. Note the change of scale compared to Fig. 2.1.

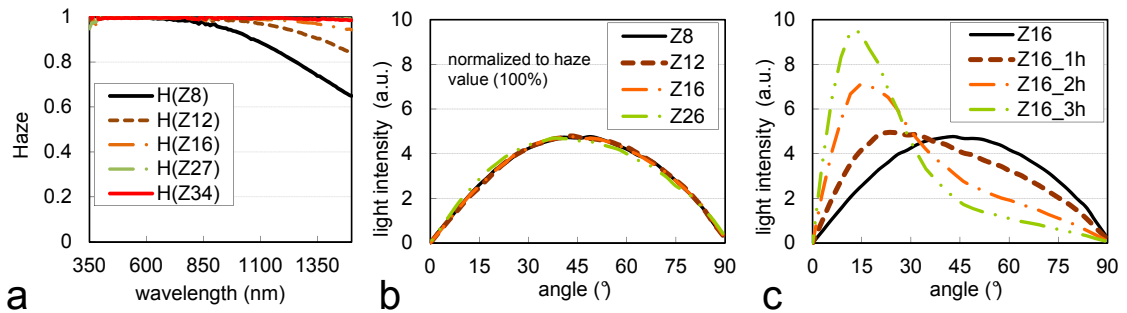


Figure 2.3: a) Haze spectrum and b) ARS function of ZnO layers shown in Fig 2.2. c) ARS of the 16- $\mu\text{m}$ -thick layer after various plasma treatment durations.

a precise reproduction of rough surfaces in a transparent lacquer with electrical and optical properties similar to glass. This process, initially developed for substrate-type solar cells, can be used in the superstrate configuration to provide the textured surface that enables light scattering in the device. This texture has however to be covered by a thin conformal transparent conductive oxide (TCO) layer (such as indium tin oxide (ITO) or hydrogenated indium oxide (IOH)) to ensure carrier extraction. Such architecture was shown in [Battaglia 10] and [Battaglia 11c] to enable at least equally good light trapping compared to standard electrodes. In this document, replication is used for high-efficiency devices in chapter 6 to obtain a micron-scale modulation at the surface of the front electrode in multi-scale textured front electrodes.

A schematic representation of the different steps involved in the fabrication of a replica is given in Fig. 2.4. More details about this process are available in [Söderström 11, Escarré 11].

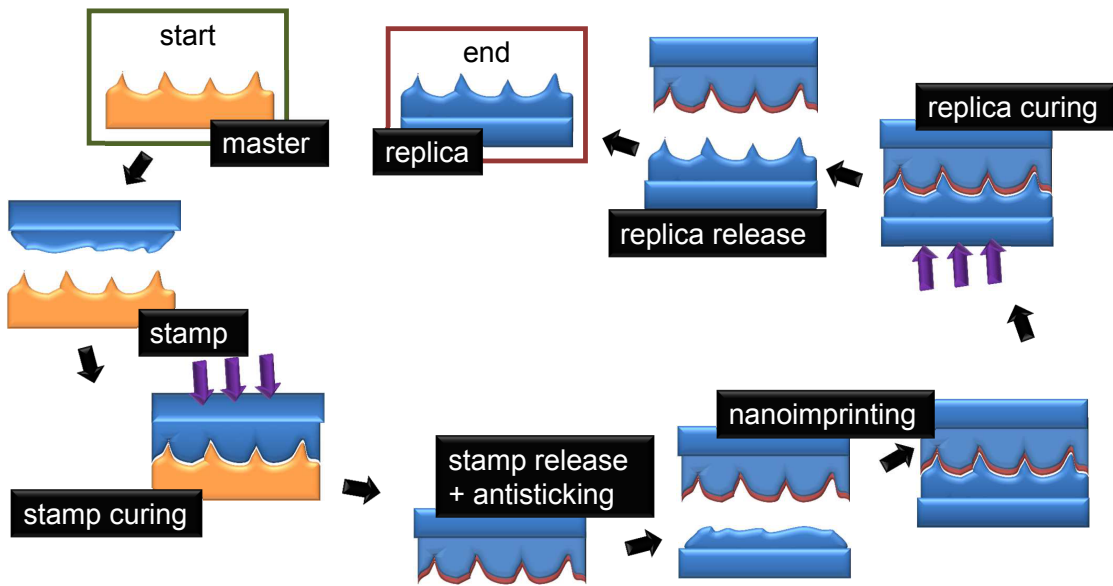


Figure 2.4: Sketch of the different steps involved in the replication process of photonic nanostructures, adapted from the presentation of [Battaglia 12a].

### 2.2.3 Hydrogenated indium oxide (IOH)

Following the recent work from AIST in Japan [Koida 08, Koida 09], IOH was developed independent of this thesis in PV-lab [Battaglia 11b]. This TCO possesses unusually good optical and electrical properties for solar cell electrode application, as detailed in Figs. 2.5 and 2.6. The carrier mobility above  $100 \text{ cm}^2/\text{V/s}$  is a strongly desirable characteristic, as improving the mobility for a given thickness and carrier density enables one to reduce both the sheet resistance and the absorbance due to free carriers. IOH is deposited at room temperature from a pure  $\text{In}_2\text{O}_3$  target by sputtering, at a pressure of 5 mTorr with argon gas. The level of hydrogen doping is adjusted by adding a little flux of water vapor to argon during deposition. This small flux corresponds to a partial pressure in the chamber of  $7.4 \cdot 10^{-6}$  mbar in the absence of argon. Whereas the as-deposited layers are amorphous and show mobility values of around  $50 \text{ cm}^2/\text{V/s}$ , a strong mobility increase together with a reduction by half of the carrier density is observed after the post-deposition annealing process, which is correlated to a crystallization of the film [Koida 10].

Combined with texturing obtained with replication (by nanoimprint lithography), IOH was shown to enable high-efficiency thin-film silicon solar cells [Battaglia 11c, Battaglia 12b]. In the work presented here, IOH is used in chapter 6 to ensure an almost absorption-free electrical conduction in multi-scale textured electrodes. In this configuration, electrical conduction is provided by the stack of an IOH layer and an LPCVD ZnO layer, avoiding thus the resistive losses observed in [Battaglia 11c], in which case IOH is the only conductive layer in the front electrode.

### 2.3. Current-voltage (J(V)) and external quantum efficiency (EQE) measurements

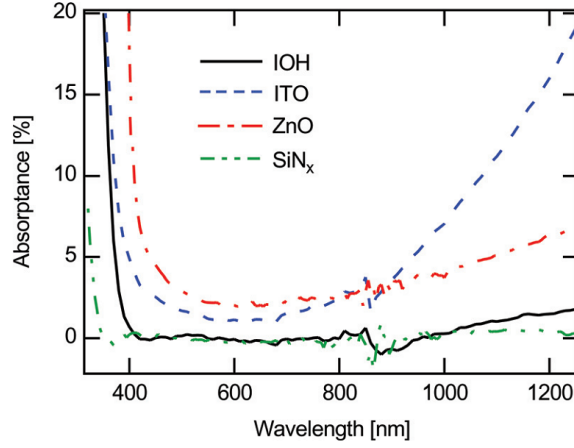


Figure 2.5: Typical absorbance spectra for the TCO used in this document: IOH, ITO and ZnO. The spectrum of a silicon nitride ( $\text{SiN}_x$ ) layer is added as a non-absorbing reference of similar refractive index. From [Battaglia 11b].

TCO	$n$ [ $\text{cm}^{-3}$ ]	$\mu$ [ $\text{cm}^2/\text{V} \cdot \text{s}$ ]	$\rho$ [ $\Omega \cdot \text{cm}$ ]	$t$ [nm]	$R_{\text{sh}}$ [ $\Omega_{\square}$ ]
IOH	$1.1 \times 10^{20}$	104	$5 \times 10^{-4}$	135 (110)	37 (45)
ITO	$7.0 \times 10^{20}$	26	$3 \times 10^{-4}$	135 (110)	26 (32)
ZnO	$4 \times 10^{19}$	37	$4 \times 10^{-3}$	4800	8

Figure 2.6: Typical electrical parameters of standard IOH, ITO and ZnO layers used in this document. From [Battaglia 11b].

### 2.3 Current-voltage (J(V)) and external quantum efficiency (EQE) measurements

To obtain some statistics for all depositions, six individual  $1.04 \text{ cm}^2$  cells are patterned on a  $4 \times 4 \text{ cm}^2$  glass substrate. Their front electrode is continuous over all the substrate but the silicon and back contact is etched away to form the isolated cells.

To avoid collecting light from outside the cell area by trapping in the glass, all J(V) characteristics are measured with a slightly smaller mask ( $1 \text{ cm}^2$ ) under a dual-lamp WACOM sun simulator. A white dielectric back reflector, with two apertures for the contacts for the four-point probe, is pressed against the back electrode. Due to trapping of light in the glass [Springer 03], and the absence of a complete back reflector, the current is underestimated with this configuration. Misalignment between the mask and the cell can also lead to current fluctuations. Thus, whereas the open circuit voltage ( $V_{\text{oc}}$ ) and fill factor ( $FF$ ) values are extracted from this measurement, the short-circuit current density ( $J_{\text{sc}}$ ) values are calculated by integrating the EQE (measured with a setup developed in-house) multiplied with the AM1.5G spectrum between 370 nm and 1100 nm, for better precision. For EQE measurements, the spot of the

probe beam is around  $1 \times 2 \text{ mm}^2$ , which is much smaller than the typical cell size ( $8 \times 13 \text{ mm}^2$ ), making escape of light from the cell through the sides much less detrimental. Also, a dielectric white back reflector can be pressed against most of the cell area, except for a corner where we place the electrical contact.

These differences in the measurement conditions between the  $J(V)$  and EQE setups usually result in an underestimation of the current in the bottom cell by around  $0.5 \text{ mA/cm}^2$  when measured under the sun simulator, compared to the current obtained from the EQE setup. A much lower difference is observed for the top cell current. The efficiency output from the  $J(V)$  measurement is thus an underestimation of the real efficiency of the probed device, as some light is lost through the sides. In addition, the  $FF$  calculated from the  $J(V)$  curve corresponds to a different matching condition than the one obtained from the EQE measurement. As explained in more details in appendix B, since the current in the bottom cell is underestimated, the  $FF$  that would be obtained with the correct current in the bottom cell is overestimated by up to 1% for bottom-limited devices, whereas it is underestimated by up to 0.5% for top-limited devices. The efficiency value obtained by multiplying the  $V_{oc}$  and  $FF$  from the  $J(V)$  measurement with the limiting  $J_{sc}$  obtained from the EQE measurement is therefore systematically wrong with the same trend. A way of correcting this systematic error by modifying the spectrum during  $J(V)$  measurements is given in appendix B.

Details about the issues faced during EQE measurements of multi-junction devices are given in appendix A.

### 2.4 Absorptance measurements

Optical absorption measurements were performed with a dual-beam spectrophotometer equipped with an integrating sphere, as sketched in Fig. 2.7. For transmittance ( $T$ ) measurements, the sample is perpendicular to the optical axis whereas it is slightly tilted for reflectance ( $R$ ) measurements, so that the specularly reflected beam is away from the entrance aperture. This change of angle of incidence between transmission and reflection induces a shift in the interference fringes (especially for thin and flat layers), inducing ripples in raw absorptance ( $A$ ) curves calculated as  $A = 1 - R - T$ . It can be corrected to a first approximation by averaging  $A$  over several points.

To access the single-pass absorptance of a rough TCO sample (typically LPCVD ZnO layers) deposited on glass, a droplet of index-matching liquid (di-iodo-methane,  $\text{CH}_2\text{I}_2$ ) is deposited on the layer and sandwiched by a second glass to reduce light scattering and uncertainty due to trapping of light in the glass and TCO. This makes a significant difference, as can be seen in Figs. 2.8 and 2.9, making the use of index-matching liquid of great importance when measuring the single-pass absorptance. The same procedure was used to measure absorptances of flat samples as well, to keep the same layer structure and also suppress interference fringes thanks to the large thickness of the index-matching liquid layer.

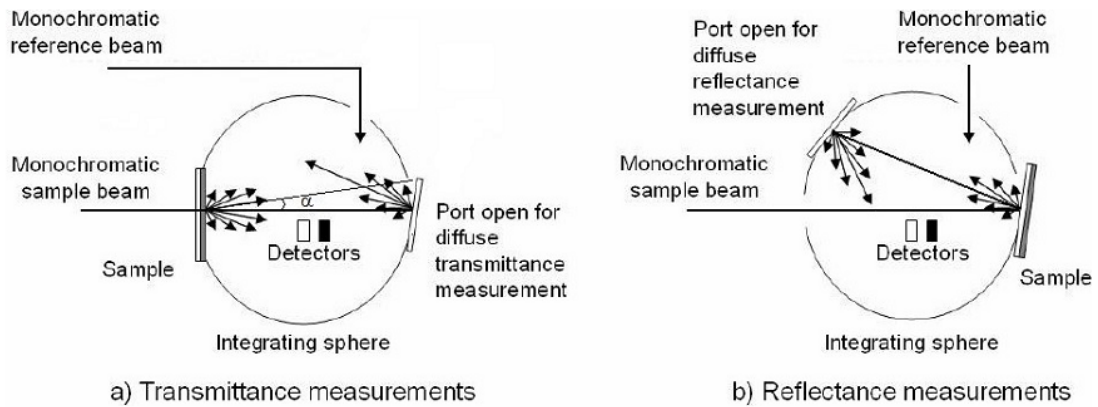


Figure 2.7: Schematic diagram of the configurations used to measure a) transmittance and b) reflectance spectra with an integrating sphere. Adaptation from [Steinhauser 08] taken from [Dominé 09].

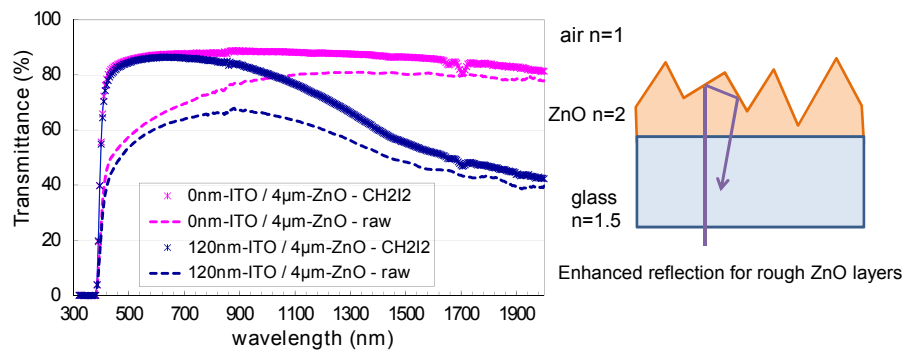


Figure 2.8: a) Transmittance spectra of two rough TCO stacks composed of either a 0 nm- or a 120-nm-thick flat ITO layer followed by a 4-µm-thick ZnO layer, with or without the use of index-matching liquid ( $\text{CH}_2\text{I}_2$ ). The drop in transmission for small wavelengths when  $\text{CH}_2\text{I}_2$  is not used comes with an enhancement of the reflection. This is attributed to a catadioptric effect, as sketched for a two-dimensional case on the right side of the graph.

The total absorptance spectra of complete solar cells (including light trapping in this case) are obtained by measuring the total reflection from the sample and stipulating  $A = 1 - R$  (here,  $T = 0$  as a very thick white dielectric back reflector is used). As the spot of light from the probe beam of the spectrophotometer is of similar size as the cell, measurements of reflection on  $1 \text{ cm}^2$  cells are performed with a mask (made out of highly reflective white dielectric from Gore) slightly smaller than the size of the cell. Unavoidably, due to the finite size of the cell and to the non-negligible thickness of the glass and back reflector, a small part of the light scattered in the device and not absorbed after one round trip can be trapped behind the mask instead of escaping in the integrating sphere, as sketched in Fig. 2.10. This share of light, that should appear in the reflectance spectra, is falsely attributed to parasitic absorption. A more precise characterization of the reflectance spectra can be made with a larger device and a smaller spot size, avoiding the use of a dedicated mask. Yet, the aperture in the integrating

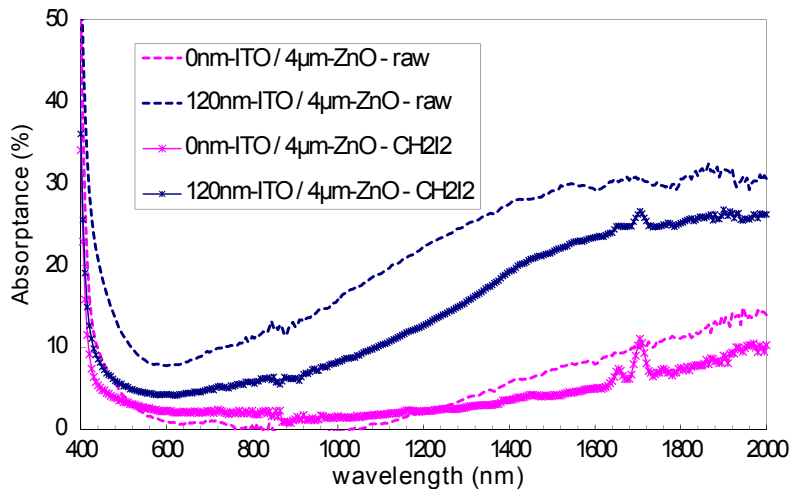


Figure 2.9: Absorbance spectra of two rough TCO stacks composed of either a 0 nm or a 120-nm-thick flat ITO layer followed by a 4- $\mu\text{m}$ -thick ZnO layer, calculated from  $1 - T - R$  with or without the use of index-matching liquid ( $\text{CH}_2\text{I}_2$ ).

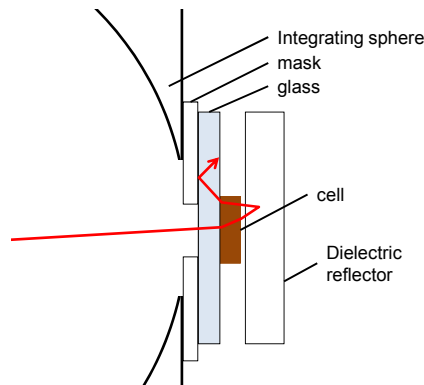


Figure 2.10: Schematic view of light loss during total absorbance measurement on a small cell.

sphere is then a natural mask, and escape through the side is always a possibility, which is especially detrimental for weak absorption of light and good light trapping.

This effect is evidenced in Fig. 2.11, showing absorbance spectra of two different devices of size larger than the aperture in the integrating sphere, and two different spot sizes. The first device ( $\text{SiN}_x$ ) corresponds to a Micromorph solar cell from which all parasitic absorbing layers have been replaced by highly transparent ones: the front electrode is replaced by a replica and a  $\text{SiN}_x$  layer, doped layers are not included, and the back electrode is also replaced by  $\text{SiN}_x$ . The light trapping is thus very similar to the one observed in a real device, but all absorption is coming from the intrinsic silicon layer. This corresponds to an optically idealized cell as shown in [Battaglia 11b]. The second device (ZnO) is identical, but an absorbing back ZnO electrode is included (inducing thus parasitic absorption). Both samples were prepared by Corsin Battaglia. The initial spot size is around  $6 \times 10 \text{ mm}^2$  (graphs labelled large spot), and it



## 2.4. Absorbance measurements

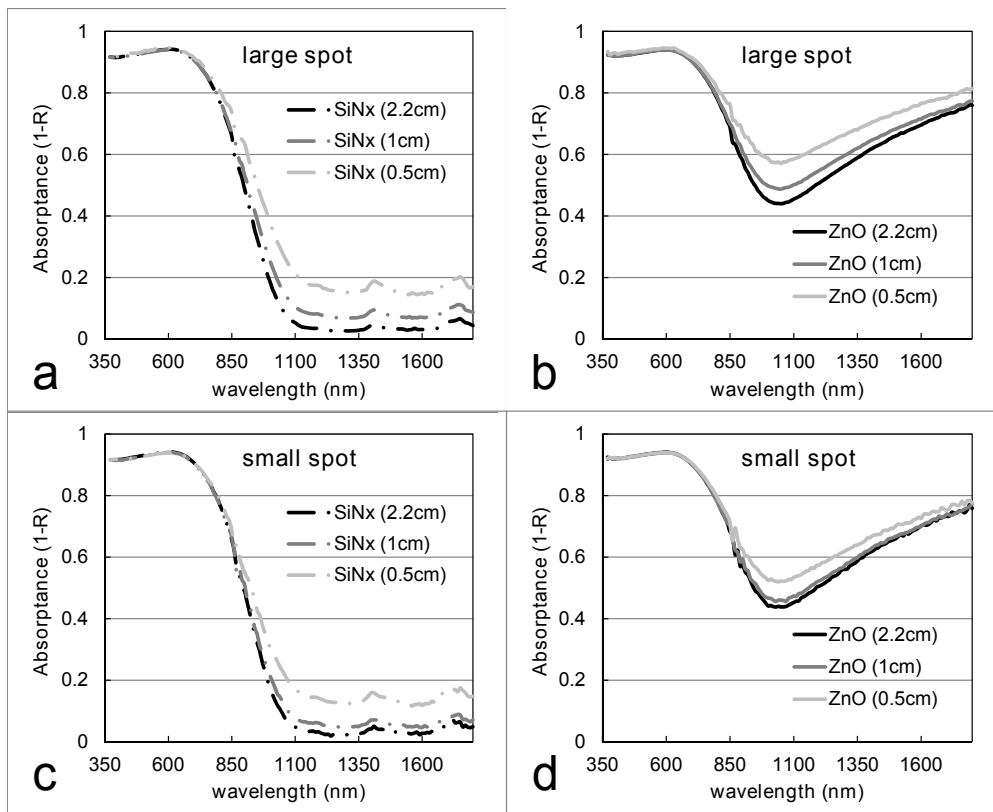


Figure 2.11: Absorbance spectra of two different devices, measured with two different spot sizes, and three different sizes of the aperture in the integrating sphere.

was reduced to  $1 \times 2 \text{ mm}^2$  (graphs labelled small spot) by using lenses. In each graph, three measurements are compared, one with no mask (the aperture in the integrating sphere, of diameter 2.5 cm, being the only limitation), a mask of size  $8 \times 13 \text{ mm}^2$ , and a mask of size  $5 \times 5 \text{ mm}^2$ . The square root of the surface of the aperture is indicated in the legend as a representative parameter for all three cases.

The curves in the graphs do not superimpose, indicating that the measurements are not equivalent. Indeed, by reducing the area of the aperture from which light escaping the cell is collected, the share of light escaping through the side is increased. In a simplistic case of homogeneous lighting of a round aperture, the escaped-light-to-collected-light ratio is proportional to the perimeter of the aperture divided by the surface of the aperture, thus to one over the radius of the aperture. For another extreme case of a point spot in the center of a round aperture, there is an exponential decay of the intensity of light in the device from the center to the periphery that is combined with the geometrical  $1/radius$  decay. This inhomogeneous intensity accelerates the decrease of the fraction of escaping light for increasing aperture surfaces.

An instructive wavelength range is the 1100 nm to 1800 nm range, for which all layers of the SiNx device are transparent. The absorbance should therefore be zero, and all light that is not

## Chapter 2. Details about deposition and characterization

---

reflected into the integrating sphere can therefore be considered as escaped through the sides of the aperture. When reducing the surface of the aperture, more light is indeed lost, as seen in Fig. 2.11a and c. The effect is more pronounced for Fig. 2.11a for which the spot of light is larger, and in the wavelength range for which silicon is absorbing, the difference between the curves shrinks.

For the ZnO device (Fig. 2.11b and d), which is closer to a real solar cell with parasitically absorbing layers, the difference between the curves is smaller. Yet, when the mask with the smallest aperture is used, the absorptance is still significantly stronger than for the other cases, indicating escape of light from the side. On the other hand, from the superimposition of the two other curves in Fig. 2.11d, escape from the side can be neglected when a large mask (or no mask) and a small spot are employed. This is notably due to the small glass thickness (0.5 mm) and the quite strong total absorptance from the silicon layers and the TCO layers.

Absorptance spectra presented in this document are measured with a 1 cm<sup>2</sup> mask and a large spot, corresponding to the dark gray curve in Fig. 2.11b. The gap between this curve and the black one corresponding to no mask indicates that the absorptance spectra are slightly overestimated for values smaller than 60% (a measured absorptance of 50% with this method corresponds to a real absorptance of around 44%, the extra 6% corresponding to light which escaped through the side).

## 3 Analytical modeling of light trapping

This chapter tackles light trapping in solar cells, focusing on thin-film silicon technology, but most of the presented concepts are not limited to this particular case. Most of the developed ideas have been published in [Boccard 12d]. After presenting the motivation for light trapping, we discuss the general mechanism allowing light to be trapped inside a cell by total internal reflection. Then, a simple analytical method of modeling light trapping is presented, which is based on the work presented in [Yablonovitch 82a, Deckman 83c], in which the path of an average ray of light is followed within the cell. This formula is then modified to generalize this approach to an arbitrary light-scattering scheme. This generalization enables an estimation of the current output obtainable with a solar cell for any kind of substrate morphology, using mostly experimental input parameters. The angular distribution of light transmitted through a given transparent electrode is calculated from its topology (obtained from AFM data), characterizing its light-scattering ability. Excellent agreement with experimental data is obtained for four different structures (two cell thicknesses and two electrode morphologies). The limitations of this extended model are discussed, as well as the information it can provide. Our approach suggests that excellent light trapping is currently achieved (*e.g.* LPCVD ZnO has the potential to allow  $J_{sc}$  of over  $32 \text{ mA/cm}^2$  for a  $1\text{-}\mu\text{m}$ -thick  $\mu\text{c-Si:H}$  cell). However, parasitic absorption in the front and back contacts limits strongly the obtained current densities (typically to  $25 \text{ mA/cm}^2$  for the same device). This model gives insights about the limitations of classical light trapping based on random rough substrate surfaces, and the route to overcome them.

### 3.1 Motivation and mechanism

Thin-film silicon is the material of choice to study light trapping. The very short diffusion lengths of the electrical charge carriers in *a-Si:H* and  $\mu\text{c-Si:H}$  makes the use of thin layers (typically  $< 300 \text{ nm}$  and  $< 3 \mu\text{m}$ , respectively) a real necessity (in addition to the industrial incentive to “think thin” or the etymological agreement). Unfortunately, the weak absorption coefficients for wavelengths close to their band gaps (*e.g.*  $2 \cdot 10^5 \text{ m}^{-1}$  for *a-Si:H* at  $700 \text{ nm}$  and  $6 \cdot 10^3 \text{ m}^{-1}$  for  $\mu\text{c-Si:H}$  at  $1000 \text{ nm}$ ) limit strongly the current output obtainable with such thin

### Chapter 3. Analytical modeling of light trapping

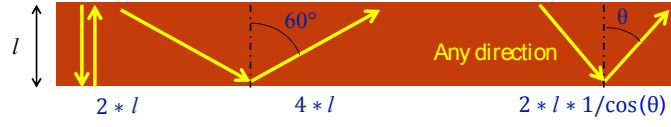


Figure 3.1: Schematic representation of light trapping where a ray of light crosses a thin layer with an angle of incidence with respect to the normal of the surface.

layers.

The maximal current density that could theoretically be delivered by a  $\mu c$ -Si:H layer (*i.e.* the elementary charge times the flux of photons having an energy higher than the band gap of energy of 1.1 eV) from the AM1.5G spectrum is 44 mA/cm<sup>2</sup>. When crossing a 1- $\mu$ m-thick layer once and normally, the fraction of absorbed photons corresponds only to 17 mA/cm<sup>2</sup>. To be able to increase the photon absorption without changing the material, the light path inside the absorber has to be elongated. First, a second pass can be added thanks to a back reflector. Then, light can be forced to travel slanting in the film, increasing the length of one pass by the factor  $a = 1/\cos(\theta)$  with  $\theta$  the angle of the beam with respect to normal, as sketched in Fig. 3.1. Finally, if the angle of the beam is higher than the critical angle for total internal reflection, light will be trapped inside the layer and forced into multiple back- and forward bounces. Indeed, the high index of refraction of silicon (around 3.6) makes the critical angle of total internal reflection as small as

$$\theta_c = \arcsin(1/3.6) = 16^\circ. \quad (3.1)$$

For a slab of material having a much lower thickness than width and length (in most cases a factor of more than 1000 is reached), escape through the border can be neglected and the only way out is the escape cone of aperture  $\theta_c$ . This cone of aperture  $\theta_c$  represents a small part ( $\sigma$ ) of the complete solid angle:

$$\begin{aligned} \sigma &= \frac{\int_0^{2\pi} \int_0^{\theta_c} \sin(\theta) \cdot d\theta \cdot d\phi}{4\pi} \\ &= \frac{1}{2} \left(1 - \cos(\theta_c)\right) = \frac{1}{2} \left(1 - \sqrt{1 - \frac{1}{n^2}}\right) \approx 2\%, \end{aligned} \quad (3.2)$$

with  $\phi$  and  $n$  the azimuthal angle and the refractive index of the considered material. This means that for light (of non-absorbed wavelengths) that would be emitted isotropically in an infinite silicon slab having one side covered by a perfect reflector, only 4% would get out (2% when reaching its surface, and another 2% would escape after specular reflection on the back reflector).

Elongating the light path by scattering light that enters the cell, and exploiting this total internal reflection, is the basis of light trapping as it is currently performed. A theoretical limit – detailed later in this chapter – based on such purely geometrical considerations was suggested

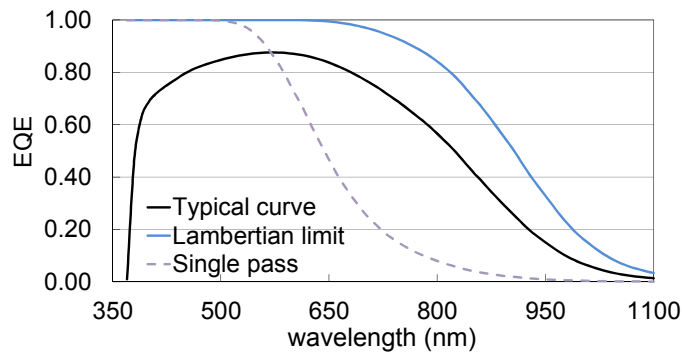


Figure 3.2: EQE of a standard 1  $\mu\text{m}$   $\mu\text{c-Si:H}$  cell, a cell with absolutely no light trapping (single pass) and the theoretically best random light scattering.

in [Deckman 83c], and gives a maximal achievable current of  $33 \text{ mA/cm}^2$  for a 1- $\mu\text{m}$ -thick microcrystalline cell. The corresponding external quantum efficiency (EQE) is presented as the Lambertian limit in Fig. 3.2. Currently, good standard values are around  $24.5 \text{ mA/cm}^2$ , where ultra-violet (UV) parasitic absorption due to the glass and transparent conductive oxide (TCO) ( $1 \text{ mA/cm}^2$ ), primary reflection ( $2 \text{ mA/cm}^2$ ), parasitic absorption ( $4.5 \text{ mA/cm}^2$ ), and sub-optimal light trapping ( $1 \text{ mA/cm}^2$ ) are responsible for the roughly  $8.5 \text{ mA/cm}^2$  of current loss, as estimated from the model developed in this chapter.

Strangely, little interest is currently paid to reducing parasitic absorption, but intensive effort is made to improve light trapping in the field of thin-film silicon solar cells. The historical strategy, and experimentally still the best [Bailat 10, Yamamoto 05], uses the scattering ability of a randomly oriented rough interface between a “low-index” dielectric (typically the TCO,  $n_{\text{TCO}} \approx 2$ ) and the silicon layer [Deckman 83b, Domine 08, Berginski 07]. Recently, photonic and plasmonic concepts have also gained tremendous interest as they are thought to be able to surpass the random approach [Yu 10, Schiff 11], at least for a limited range of wavelengths. These hot topics, which are mentioned in the introduction, are not detailed here. Instead, emphasis is put on light scattering from randomly rough surfaces, as obtained notably with rough ZnO layers deposited by low pressure chemical vapor deposition (LPCVD).

## 3.2 Modeling of light trapping

To simulate light absorption in a solar cell, several approaches are followed, including geometrical ray tracing [Schulte 11b], direct solving of Maxwell’s equations [Naqavi 11], and semi-coherent models such as those used in Sunshine [Krč 03]. For the case of random light scattering, Deckman *et al.* derived a very simple analytical expression, based on “average-ray” tracing [Deckman 83c] and a few assumptions only:

1. Light is randomly scattered when entering the semiconductor film.
2. There is a reflector on one side, and air on the other side.

### Chapter 3. Analytical modeling of light trapping

Then, geometrically following an average ray of light going back and forth in this layer (of thickness, refractive index and absorption coefficient  $l$ ,  $n$  and  $\alpha$ ) enables the calculation of how much light is absorbed in the semiconductor and how much goes out. The resulting formula (explained below) giving the share of effectively absorbed photons per incident photons ( $F^{enh}$ ) is then [Deckman 83c]:

$$F^{enh} = \frac{1 - \eta e^{-2\alpha l} - (1 - \eta) e^{-4\alpha l}}{1 - (1 - \eta) e^{-4\alpha l} + [(1 - \eta)/n^2] e^{-4\alpha l}}. \quad (3.3)$$

Here,  $\eta$  accounts for the fraction of light parasitically absorbed in the material (implemented at the back reflector). This equation results from a geometric summation of absorption for an infinite progression of light going back and forth in the device, as sketched in Fig. 3.3. In the following, the basic principles ruling this equation are detailed. In particular, the physical origin of the factor of two due to the inclination of the ray of light and the  $1/n^2$  escape fraction are discussed.

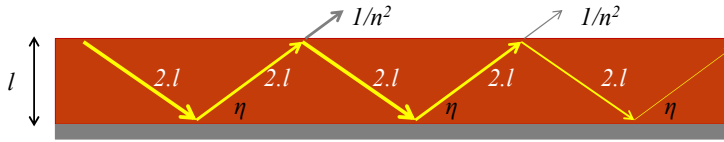


Figure 3.3: Schematic representation of light trapping of an average ray, with parasitic absorption (a fraction  $\eta$  of light is lost each time the ray reaches the back reflector) and losses at the front interface (a fraction of light  $1/n^2$  is lost each time the ray reaches the front interface) in a semiconductor slab.

It is possible to rewrite this equation more explicitly as:

$$F^{enh} = \sum_{k=0}^{\infty} \underbrace{\left[ (1 - e^{-2\alpha l}) + e^{-2\alpha l} (1 - \eta) (1 - e^{-2\alpha l}) \right]}_{A_{\text{double pass}}} \cdot \underbrace{\left[ e^{-4\alpha l} (1 - \eta) (1 - 1/n^2) \right]^k}_{\text{Attenuation}} \quad (3.4)$$

$$= \frac{A_{\text{double pass}}}{1 - \text{Attenuation}}$$

where the first bracket represents the useful absorption (in the photoactive layer) for one passage plus the return ( $A_{\text{double pass}}$ ), and the second bracket includes the attenuation term after traveling back and forth (Attenuation). In this formula, a factor of two doubles the effective thickness of the layer for each pass, and  $1/n^2$  is assumed to escape through the front interface. Both values come from the first of the assumptions of the development, namely that light is randomly scattered when entering the cell. This aspect is discussed in more detail in the following.

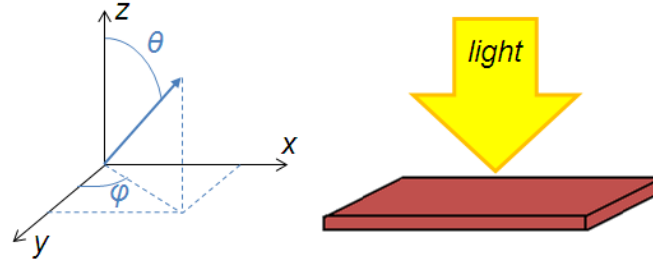


Figure 3.4: Coordinates used in this chapter.

When looking at the cross section of our cell in polar coordinates as in Fig. 3.4, the direction of light is defined by the angles  $\theta$  and  $\phi$ . Randomization of incident light makes the front surface act as a Lambertian diffuser (similar to a white sheet of paper), that is, it emits light equally in all directions, having thus a constant radiance  $L(\theta, \phi) = L$ . Light intensity has therefore no dependence in the  $\phi$  direction, but is dependent on  $\theta$  through the projection factor  $\cos(\theta)$ , *i.e.*  $I(\theta, \phi) = L \cdot \cos(\theta)$ . Normalizing to unity the total intensity of light that entered the cell leads to:

$$\int_0^{2\pi} \int_{\pi/2}^{\pi} I(\theta, \phi) \cdot \sin(\theta) \cdot d\theta \cdot d\phi = \int_0^{2\pi} \int_{\pi/2}^{\pi} L \cdot \cos(\theta) \cdot \sin(\theta) \cdot d\theta \cdot d\phi = 1. \quad (3.5)$$

Thus,  $L = 1/\pi$ . Here,  $\sin(\theta)$  is the Jacobian in spherical coordinates.

Then, the ‘‘average ray tracing’’ approach followed by Deckman leads to searching for the average distance ( $\langle d \rangle$ ) crossed by light during one pass back and forth. Since specular reflection is considered at the back of the cell, the value is the same for both senses (*i.e.*  $I(\theta, \phi) = I(\pi - \theta, \phi)$ ). For light crossing the device with a given angle  $\theta$  with respect to normal, one pass back and forth corresponds to  $d = \frac{l}{\cos(\theta)}$ . Then, the mean value can be calculated by integrating over all directions and weighting with  $I(\theta, \phi) = \frac{1}{\pi} \cos(\theta)$ :

$$\langle d \rangle = a \cdot l = \int_0^{2\pi} \int_{\pi/2}^{\pi} l \cdot I(\theta, \phi) \frac{1}{\cos(\theta)} \cdot \sin(\theta) \cdot d\theta \cdot d\phi = 2 \cdot l. \quad (3.6)$$

The ‘‘average’’ ray travels a distance corresponding to four times the film thickness during one pass back and forth. A factor of two comes from the back reflector, and another factor of two is the mean light path enhancement (referred to as  $a$  in the following) for a Lambertian distribution of light. Now, calculating the fraction of light escaping the device through the front side each time the ‘‘average’’ ray touches it (referred to as  $b$  in the following) requires calculating the fraction of the light intensity that is included in the escape cone of the device after one pass back and forth. This corresponds to light of inclination  $\theta$  included in  $[0; \theta_c]$ . This fraction of lost light is different from the one calculated in equation 3.2 due to the different angular distribution of light (isotropic for equation 3.2 and Lambertian here):

$$\begin{aligned}
 b &= \int_0^{2\pi} \int_0^{\theta_c} I(\theta, \phi) \cdot \sin(\theta) \cdot d\theta \cdot d\phi \\
 &= \int_0^{\theta_c} 2 \cdot \cos(\theta) \cdot \sin(\theta) \cdot d\theta \\
 &= \left[ \sin^2(\theta) \right]_0^{\theta_c} = \frac{1}{n^2}.
 \end{aligned} \tag{3.7}$$

Here, specular reflection is assumed for both interfaces. Also, 100% transmittance is supposed in the case of  $\theta < \theta_c$ , which is not the case for an abrupt silicon - air interface. However, a realistic solar cell includes TCO and glass, with respective indices of 2 and 1.5, that reduce the index step and thus the reflection. In the case of no parasitic absorption, equation 3.3 simplifies to:

$$F^{enh} = (1 - e^{-2a \cdot \alpha l}) \cdot \sum_{k=0}^{\infty} \left[ e^{-4\alpha l} (1 - b) \right]^k \xrightarrow{\alpha l \rightarrow 0} \frac{2a}{b} \cdot \alpha l = 4n^2 \cdot \alpha l, \tag{3.8}$$

where we recognize the famous  $4n^2$  light path enhancement limit [Yablonovitch 82b].

### 3.3 Angular distribution of light entering a cell

All the above discussion treats light trapping using a Lambertian distribution. However, present state-of-the-art devices do not incorporate a Lambertian scatterer as a front contact. In practice, the roughness of the TCO layer that scatters light entering the cell is adjusted to enable both light trapping (requiring sharp morphologies at the TCO - silicon interface) and a high-quality silicon layers growth (requiring a smooth growth surface), as seen in chapter 5. This trade-off can be achieved for example for LPCVD ZnO by applying a plasma treatment to the ZnO surface that smoothens its sharp pyramidal features. An exhaustive analysis of the properties of these typical rough electrodes can be found in [Cuony 11], with their scattering properties for scattering into air. Corresponding calculations for scattering from ZnO into silicon were done in [Dominé 09]. After giving general information about the quantification of the scattering ability of a surface, this section summarizes the insights given in [Battaglia 13] concerning the Lambertian behavior of rough electrodes.

#### 3.3.1 Quantification of the scattering ability

When light enters a cell normally, the angular distribution function (ADF) of its intensity is a probability function, characteristic of the rough interface, that indicates for each wavelength the fraction of light scattered in a given direction. When measuring the angular dependence



### 3.3. Angular distribution of light entering a cell

of light scattering with a goniophotometer, the direct output of the measurement, often called angle resolved scattering (ARS), corresponds to the measurement of the ADF for a given azimuthal angle and a given light intensity ( $I_0$ ):

$$ARS(\theta) = I_0 \cdot ADF(\theta, \phi = \phi_0)|_{\lambda}. \quad (3.9)$$

To express the full characteristic of light scattering by the rough interface at a given wavelength  $\lambda$ , the ARS measurement should be performed for all  $\phi$  angles, giving access to  $ADF(\theta, \phi)$ . For random interfaces, there is no azimuthal dependence, making  $ADF$  independent of  $\phi$ . It is thus possible to express the three-dimensional  $ADF$  function as a function of  $\theta$  only. This is done by integrating over  $\phi$ , so that the value  $ADF(\theta)$  reflects the total fraction of light scattered into an inclination  $\theta$ :

$$ADF(\theta) = \int_0^{2\pi} ADF(\theta, \phi) \cdot \sin(\theta) \cdot d\phi = \frac{1}{I_0} \int_0^{2\pi} ARS(\theta) \cdot \sin(\theta) \cdot d\phi, \quad (3.10)$$

with  $I_0 = \int_0^{\frac{\pi}{2}} ARS(\theta) \cdot \sin(\theta) \cdot d\theta$  (for convenience, the  $ARS$  is expressed in  $[0; \frac{\pi}{2}]$ , equivalently to  $[\frac{\pi}{2}; \pi]$  which better corresponds to light going from the front to back interface).

This value effectively represents the light intensity scattered as a function of inclination (whatever the azimuth), whereas the direct output of a standard ARS measurement,  $ARS(\theta)$ , represents the light intensity scattered as a function of inclination *for a specific azimuth*  $\phi_0$  (that is usually arbitrary and not specified).

The case of specularly transmitted light must be treated with caution. From a strict mathematical view, the light intensity included in a specular beam ( $I_s$ ), having both azimuth and inclination equal to zero, is described by an  $ADF_s(\theta, \phi)$  function including a Dirac function  $ADF_s(\theta, \phi) = I_s \cdot \frac{\delta(\theta, \phi)}{\sin(\theta)}$ . In reality, the output of the measurement does not include a Dirac function due to the non-zero angle of acceptance of the detector, and because the integration is discrete. A pragmatic approach is thus to include in the  $ADF(\theta)$  function a specular contribution ( $ADF(0)$ ) of intensity  $ADF(0) = I_s/I_0$ . Practically, the area under the  $ADF(\theta)$  curve is thus equal to the haze value.

In the case of perfect periodic structures, the result of the ARS measurement will be strongly dependent on the chosen azimuth, and no  $ADF(\theta)$  can be easily derived (as  $ADF$  depends on  $\phi$ ). For periodic structures having many randomly oriented domains, the ARS will be azimuth-independent, as an integration over many randomly oriented domains (equivalently, an integration over many azimuths) is done simply due to the spot size of the incident light. However, the result of such a measurement is an azimuthally *averaged* ARS, and not an integrated one:

$$ARS_A(\theta) = \frac{1}{2\pi} \int_0^{2\pi} ARS(\theta, \phi) \cdot d\phi. \quad (3.11)$$

### Chapter 3. Analytical modeling of light trapping

The corresponding  $ADF(\theta)$  is then  $ADF(\theta) = \int_0^{2\pi} \frac{ARS(\theta)}{I_0} \sin(\theta) \cdot d\phi$ .

#### 3.3.2 Typical light-scattering properties of rough electrodes

Measurements of the angular distribution of scattered light from a TCO into silicon cannot be directly performed, as for scattering into air with a spectrophotometer coupled to a goniophotometer. However, Dominé [Domine 10, Dominé 09] recently suggested a method based on work from Harvey [Harvey 99] to enable calculation of the ADF in any medium from the topology of the rough interface. Such calculations indicate that light is scattered into much lower angles from TCO into silicon than from TCO into air.

Therefore, a TCO exhibiting a textured surface scattering light in a Lambertian way *into air* does not necessarily scatter light in a Lambertian way *into silicon*. This is illustrated in Fig. 3.5. According to this model, light scattering by a rough interface at a wavelength  $\lambda$  is defined by the surface profile of this interface ( $z(x, y)$ ), the wavelength and the refractive indices of the surrounding media ( $n_1$  and  $n_2$ ) through the non-dimensional parameters

$$\frac{n_2 \cdot x}{\lambda}, \quad \frac{n_2 \cdot y}{\lambda}, \quad \text{and} \quad \frac{|n_1 - n_2| \cdot z}{\lambda}. \quad (3.12)$$

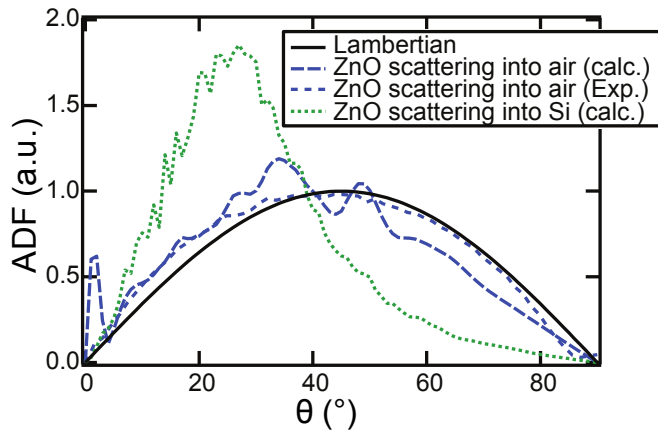


Figure 3.5: From [Battaglia 13]: ADF for an ideal Lambertian scatterer (black curve) and the ZnO morphology for scattering into air (blue curves) and silicon (green curve) at a wavelength of 543 nm. The dashed blue curve was measured experimentally.

To reproduce in silicon the light-scattering properties observed in air, a rough surface would thus need to be shrunk four times in the directions of the plane ( $x$  and  $y$ ) but only twice out of the plane ( $z$ ). This means that rough interfaces would need to have inclinations twice as large compared to as-deposited LPCVD ZnO in order to make light scattering at the TCO - silicon interface Lambertian-like. Interestingly, similar conclusions were drawn from numerical calculations within the much more complicated framework of rigorous coupled wave analysis

(RCWA) [Wiesendanger 11, Fahr 11]. It will be seen in chapter 5 that such a morphology would be extremely detrimental to the electrical quality of the silicon films.

It should thus be kept in mind that light scattering from state-of-the-art textured TCOs into silicon is currently strongly “under-Lambertian”.

## 3.4 Extension of the model to realistic devices

### 3.4.1 Implementation of experimental light-scattering distributions

To implement an arbitrary angular distribution of light in the formalism developed by Deckman *et al.*, one has to replace the factors of 2 and  $1/n^2$  in equation 3.3 by the mean light path enhancement  $a$  and the fraction of light included in the escape cone  $b$  corresponding to this distribution of light. These quantities can be calculated from the  $ARS(\theta, \phi)$  with equations 3.13 and 3.14:

$$a = \int_0^{2\pi} \int_0^{\pi/2} ARS(\theta, \phi) \cdot \frac{1}{\cos(\theta)} \sin(\theta) \cdot d\theta d\phi, \quad (3.13)$$

$$b = \int_0^{2\pi} \int_0^{\theta_c} ARS(\theta, \phi) \cdot \sin(\theta) \cdot d\theta d\phi. \quad (3.14)$$

Even though the  $ARS(\theta, \phi)$  function for light entering the cell is not Lambertian for experimental devices, Yablonovitch [Yablonovitch 82b] already mentioned that “there is a rather overwhelming tendency toward randomization in the angular distribution of light”. This means that the angular distribution of light changes from  $ARS_0(\theta, \phi)$  (where the subscript denotes the first scattering event) towards  $ARS_{Lamb}(\theta, \phi) = \cos(\theta)/\pi$  while light is traveling back and forth through the device and experiencing light scattering at every rough interface. As a first-order approximation, we assume that *only* the first round trip is driven by the scattering properties of the rough interface, and that all light not escaping the device after this first round trip will be scattered in a Lambertian way, as sketched in Fig. 3.6. Mathematically, this is done by treating separately the first term of the summation with  $a$  and  $b$  values corresponding to the experimental distribution of light, whereas the remaining terms will use  $a = 2$  and  $b = 1/n^2$ , corresponding to the Lambertian behavior depicted in equation 3.3:

$$F_{ARS}^{enh} = 1 - e^{-a_0\alpha l} + (1 - \eta)e^{-a_0\alpha l}(1 - e^{-a_1\alpha l}) + e^{-(a_0+a_1)\alpha l}(1 - \eta)(1 - b_1) \cdot F^{enh}. \quad (3.15)$$

Here,  $a_0$  applies to the first pass through the cell, whereas  $a_1$  and  $b_1$  apply to the second pass (*i.e.* the first way back), reflecting the fact that the back reflector is not specular. This distinction is of great importance especially for  $b_1$  which represents the fraction of light included in the escape cone after one round trip, *i.e.* the fraction of light that is lost after only two passes.

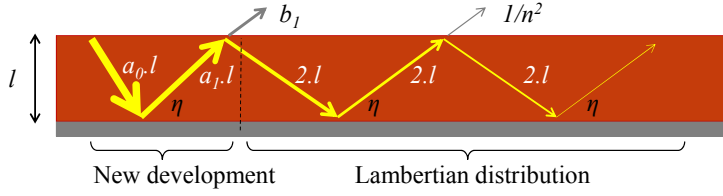


Figure 3.6: Cross section of a semiconductor slab between air and a back reflector, with a schematic representation of light trapping by an average ray for a non-Lambertian distribution of light entering the cell.

Therefore, our first-order approximation requires the calculation of  $ARS_1(\theta, \phi)$ , corresponding to the first way back. This depends strongly on the light-trapping strategy used in the device, and in particular on the back reflector. Metallic reflectors in the close vicinity of silicon and detached back reflectors several microns away from the photoactive layer behave differently [Deckman 83c, Moulin 12]. Note that calculations of  $ARS_1(\theta, \phi)$  were recently presented for metallic back reflectors in [Bittkau 12].

### 3.4.2 Implementation of parasitic absorption and reflection

To complete the modeling of a real device, we further implement primary reflection ( $R_0$ ) and primary parasitic absorption ( $A_{first}$ ), occurring for light entering the device, and treat separately parasitic absorption occurring at the front ( $A_{front}$ ) and at the back ( $A_{back}$ ) of the cell. The resulting extended formula is given by:

$$EQE = (1 - R_0)(1 - A_{front}) \cdot \left[ 1 - e^{-a_0 \alpha l} + (1 - A_{back})e^{-a_0 \alpha l} (1 - e^{-a_1 \alpha l}) \right] + e^{-(a_0 + a_1) \alpha l} (1 - A_{front})(1 - A_{back})(1 - b_1) \cdot F_L^{enh}, \quad (3.16)$$

where  $F_L^{enh}$  corresponds to a Lambertian distribution of light:

$$F_L^{enh} = (1 - R_0)(1 - A_{first}) \cdot \frac{1 - A_{back}e^{-2\alpha l} - (1 - A_{back})e^{-4\alpha l}}{1 - [e^{-4\alpha l}(1 - A_{front})(1 - A_{back})(1 - 1/n^2)]}. \quad (3.17)$$

Similar equations (3.18, 3.19, 3.20) give access to the amount of light that is parasitically absorbed (at the front ( $A_P^{front}$ ) and back ( $A_P^{back}$ ) of the cell), and that is reflected out of the cell ( $R$ ). These three formulas are given here for the Lambertian case only; the contribution of the first pass and attenuation can be obtained similarly to the calculation of EQE in equation 3.16.

$$A_P^{front} = (1 - R_0)A_{first} + (1 - R_0)(1 - A_{first}) \cdot \frac{A_{front}e^{-4\alpha l}(1 - A_{back})(1 - 1/n^2)}{1 - [e^{-4\alpha l}(1 - A_{front})(1 - A_{back})(1 - 1/n^2)]} \quad (3.18)$$

### 3.4. Extension of the model to realistic devices

$$A_p^{back} = (1 - R_0)(1 - A_{first}) \cdot \frac{e^{-2\alpha l} A_{back}}{1 - [e^{-4\alpha l} (1 - A_{front})(1 - A_{back})(1 - 1/n^2)]} \quad (3.19)$$

$$R = R_0 + (1 - R_0)(1 - A_{first}) \cdot \frac{(1 - A_{back})e^{-4\alpha l} 1/n^2}{1 - [e^{-4\alpha l} (1 - A_{front})(1 - A_{back})(1 - 1/n^2)]}. \quad (3.20)$$

$A_{front}$  comprises glass, front TCO and  $p$ -doped layer absorptions, while  $A_{back}$  groups the  $n$ -doped layer, back TCO and back reflector absorptions. Note that  $A_{first}$  differs from  $A_{front}$ . The former describes the first pass where light passes the zone of parasitic absorption only once, doing so without path enhancement. The latter must account for the possibility of two passages including path enhancement (if light is reflected back only at the air-glass interface), or no passages (if light is reflected directly at the silicon - TCO interface). In equations 3.16 to 3.20, parasitic absorption at the front side is treated with a unique term, whereas when rigorously tracing a ray of light through the device, parasitic absorption should occur both before eventual escape from the device and after total internal reflection. Since simplifying this event with one single term modifies slightly the  $R$  term, we made the arbitrary choice to have only one  $A_{front}$  term, which was placed in the equation as happening before the escape event.

Considering this analytical model, several limitations should be kept in mind:

1. No interference effects can be rendered, as coherence is not taken into account.
2.  $A_{front}$  and  $A_{back}$  are supposed to happen at each pass. However, part of the light might be trapped inside the semiconductor only (and thus be prone to front TCO parasitic absorption through evanescent waves only), but part of it might also be trapped between the glass and back reflector, thus crossing it twice at each pass back and forth.  $A_{front}$  and  $A_{back}$  are thus again average values and are not necessarily equal to the absorption values that could be measured by stacking the layers on glass outside the device. For the device architecture treated in this work, we found that an empirically satisfactory way to render parasitic absorption at the front and back of the cell is to set these values to twice the absorptance measured in the absence of light trapping (*e.g.* on glass) (whereas  $A_{first}$  is equal to the absorptance measured for one pass in the absence of light trapping).
3. Scattering of light happens at all rough interfaces. These interfaces cannot be treated as specular with reflection and transmission coefficients and a well-defined escape cone. The calculation of light loss at each pass back and forth in the escape cone is therefore not totally realistic. However, the good agreement with experiment validates its use.
4. As we consider a “mean ray”, which crosses slanting in the layer, the wavelength at which the  $R$  curve deviates from the primary reflection value, which corresponds to the wavelength for which the first photons leave the cell after one pass back and forth

without being absorbed, happens for larger wavelengths for the calculation than for measurements: in reality, part of the photons go straight (crossing thus only twice the cell thickness) whereas in the “mean ray” approach, all photons cross the same amount of material (equal to  $4l$ ).

5. The rough interfaces, which induce light in-coupling and trapping, can also in principle be responsible for light out-coupling from the cell (see *e.g.* [Riedel 10]), diminishing the achievable light trapping.
6. The change of the light distribution in the model between the first event (driven by the rough interface properties) and all the other ones (characterized by Lambertian behavior) is abrupt. This assumption tends to overestimate the EQE in the range where the second pass contributes greatly (typically around 700 nm), especially for the case of weak light scattering. A more realistic behavior would include a progressive change, taking several passes back and forth to be fully achieved.
7. It is difficult to determine  $b_1$  (light having experienced a first TCO - silicon scattering event, a second back reflector scattering event, and a third silicon - front TCO scattering event). Only approximations can be made based on the *ADF* resulting from the initial scattering event and the roughness of the back reflector.

This last point is particularly detrimental to the determination of the maximal light path enhancement (LPE), as the  $4n^2$  limit of LPE in the low-absorption limit becomes with this extension:

$$LPE = a_0 + a_1 + (1 - b_1) \cdot 4n^2. \quad (3.21)$$

This adapted formula points out clearly how detrimental a high  $b_1$  value is, and having an “under-Lambertian” scatterer will thus mainly affect the LPE through the first escape event (characterized by  $b_1$ ).

### 3.5 Validation with experimental data

We validate our model by changing experimentally in a controlled way only one (or a few) input parameters. A first simple example is to take an intrinsic-layer thickness series for  $\mu c$ -Si:H cells, with two different front electrodes. We will see a few other practical examples in the next chapter.

Modeling a thickness series is not completely straightforward, as changing the thickness of the intrinsic layer can lead to collection issues, absorption coefficient variation (through crystallinity changes, for example), boron tailing, and changes in the light-trapping properties (*e.g.* smoothening of the silicon - back ZnO interface). These changes modify collection,  $\alpha$ ,  $A_p$ , and the  $(a_1, b_1)$  couple.

We attempted to simulate all the experimental data by changing in our model only the thickness of the intrinsic layer or the roughness of the electrode. As seen in Fig. 3.7, where two

thicknesses are illustrated, both EQE and  $R$  curves can be nicely reproduced. This is achieved with a single set of parameters for all cases. Only the primary reflection and the  $(a_0, b_0)$  couple are changed to account for differently rough electrodes, and only the thickness of the intrinsic layer is changed in the model between both graphs.

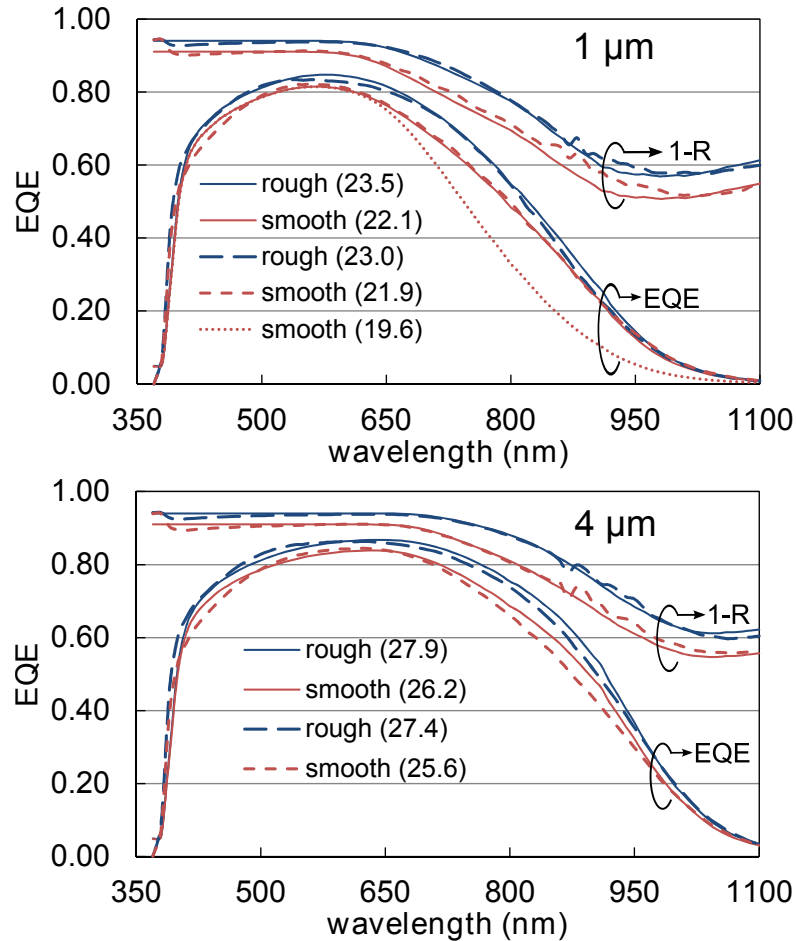


Figure 3.7: Simulated (solid) and experimentally measured (dashed) EQE and  $1 - R$  spectra for  $\mu c$ -Si:H cells on a rough and smooth electrodes, for two different intrinsic layer thicknesses:  $1 \mu\text{m}$  and  $4 \mu\text{m}$ . Numbers in parenthesis are current density values in  $\text{mA}/\text{cm}^2$ . The dotted line is a simulation of the  $1\text{-}\mu\text{m}$ -thick cell on the smooth substrate using the experimental scattering parameters  $(a_0; b_1)$  for all passes.

Table 3.1 shows the parameters used in equations 3.16 and 3.20. The  $p$ -doped layer thickness was determined by fitting one of the EQE curves. The amount of primary reflection was assumed to be constant over all the spectrum, independent of the intrinsic-layer thickness, and set at the value measured at  $500 \text{ nm}$  for the  $4\text{-}\mu\text{m}$ -thick cell. The  $a_0$  and  $b_0$  spectra for the electrodes used for this study are plotted in Fig. 3.9a. The absorptance spectrum of the front and back electrodes (measured on glass in absence of light trapping with an index matching liquid) is given in Fig. 3.8, as well as the absorptance calculated for a single light pass in a  $1\text{-}\mu\text{m}$ -thick slab of the  $\mu c$ -Si:H used for all layers (corresponding to 60% crystallinity. The

### Chapter 3. Analytical modeling of light trapping

Table 3.1: Input parameters used to simulate EQE and  $R$  of all devices.

	Collection efficiency	$R_0$	$a_0$	$b_1$	$p$ -layer thickness ( $\mu\text{m}$ )	$n$ -layer thickness ( $\mu\text{m}$ )
rough	95%	6%	1.20	0.12	0.01	0.03
smooth	95%	9%	1.00	0.20	0.01	0.03

collection efficiency, which was set to 95% for all wavelengths for all devices, is a prefactor to equation 3.16 giving the EQE.

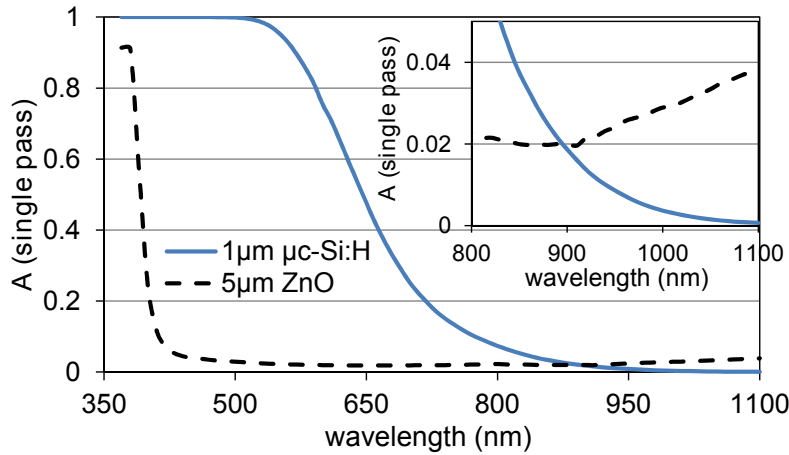


Figure 3.8: Absorptance curve of the 5- $\mu\text{m}$ -thick ZnO layer used as front and back electrodes for all cells of this study (the plasma treatment induces a negligible absorptance variation). Index matching liquid was used to suppress light trapping effects in the absorptance. The absorptance spectra for a single light pass through a 1- $\mu\text{m}$ -thick  $\mu\text{c-Si:H}$  layer is also given for comparison.

The  $J_{\text{sc}}$  values simulated and measured as a function of thickness are plotted in Fig. 3.9b. Considering the precision reachable for characterization and that the aforementioned possible changes when varying the thickness are neglected, a quite good agreement is reached between the measured and simulated current densities. A clear discrepancy appears for large thicknesses (typically after 3  $\mu\text{m}$ ) where collection issues start to become significant, leading to a saturation of the current for increasing thickness [Boccard 11].

Experimentally, a slower current increase is observed when the intrinsic layer is thickened for smooth compared to rough electrodes, which is not observed in simulation. However, it is hard to determine whether this comes from a weakness in the model, or if more parameters should be changed in the model to correctly represent a “simple” thickness change (correct model but wrong hypothesis).

Overall, an accurate reproduction of both the EQE and  $R$  curves could be obtained, which is rarely observed in simulation for such a variety of devices. Some parameters, which are not easily experimentally accessible, were deduced from the measurements (namely the primary



### 3.6. Important parameters governing light harvesting

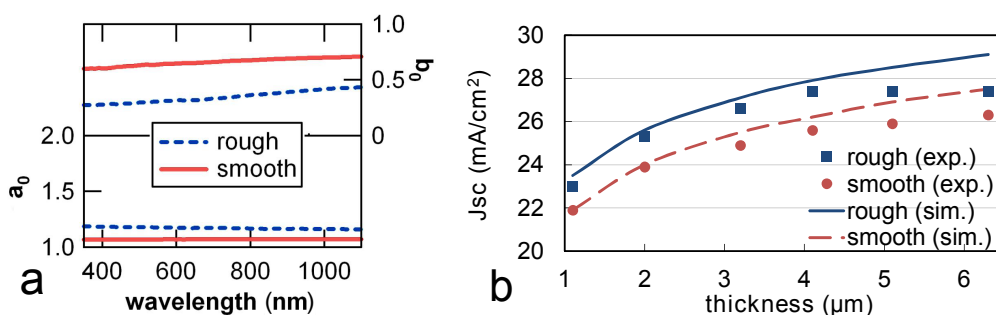


Figure 3.9: a)  $a_0$  and  $b_0$  spectrum calculated for the two electrodes used. b)  $J_{sc}$  as a function of thickness for  $\mu\text{c-Si:H}$  cells on two differently rough electrodes (experiment and simulation).

reflection and the  $p$ -doped layer thickness), but were adjusted once for all simulations. The next chapter contains more comparisons between experiment and simulation, for typical variations in a Micromorph device.

## 3.6 Important parameters governing light harvesting

### 3.6.1 Effect of changing the light-trapping properties of the front electrode

We note that scattering a lot of light towards large angles increases  $a_0$  very strongly (thanks to the  $\frac{1}{\cos(\theta)}$  parameter) whereas avoiding small angle light scattering maintains  $b_0$  at small values. A precise calculation of the intensity of scattered light for both high angles and low angles is therefore needed, which is not easy to achieve. The method that we used here for calculating the  $ADF$  tends for example to underestimate scattering at large angles [Haug 11].

To improve standard random light trapping, it should be tried to improve the first light-scattering event by scattering light mostly at large angles. This would help maintain the EQE at high values for a larger wavelength range, but it is unlikely that the weak absorption region will be strongly changed. Indeed, a study of the influence of the first light-scattering event was recently reported in [Böttler 12], in the  $n-i-p$  configuration. A current gain could be demonstrated when increasing the angle of maximal light scattering, but it only originates from EQE gain in the 500 – 900 nm range, whereas the 900 – 1100 nm range is kept unchanged. It was also reported in chapter 8 of [Dominé 09] that, in the weak absorption region, the EQE is insensitive to the roughness of the front electrode. Corrected EQE ( $\text{EQE}_c$ ) spectra, for which the contribution of parasitic absorption is removed, were shown to superimpose after 950 nm for various substrates.

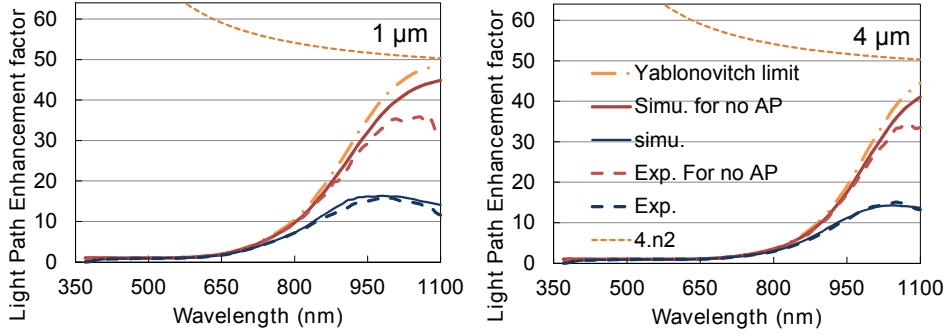


Figure 3.10: Experimental and simulated LPE as a function of wavelength for 1- $\mu\text{m}$ -thick and 4- $\mu\text{m}$ -thick  $\mu\text{c-Si:H}$  cells, the same without parasitic absorption, together with the “Yablonovitch limit” of equation. 3.22 for the same device thickness. The dotted line denotes the  $4n^2$  value, using the refractive index of  $\mu\text{c-Si:H}$ .

### 3.6.2 About the light path enhancement factor

The maximal achievable light path enhancement (LPE) is often said to be  $4n_{\text{Si}}^2$ , which is achieved for a Lambertian distribution of light in the cell. This value is indeed an approximation of the LPE in the limit of weak absorption, and should not be applied outside of this region (*i.e.* for  $\alpha \cdot l > 0.001$ ), since an absorption of  $1 - \exp(-4n_{\text{Si}}^2 \alpha l)$  is not theoretically achievable on the whole spectrum for Lambertian light scattering. Outside the weak absorption region, the LPE does not give rise to a simple formula, but the absorption enhancement can be calculated by dividing the EQE by the single-pass absorption, as described in [Deckman 83c]:

$$LPE(\alpha, \eta) = F^{enh}(\alpha, \eta) / (1 - e^{-\alpha l}). \quad (3.22)$$

The calculated LPE of the 1- $\mu\text{m}$ -thick and 4- $\mu\text{m}$ -thick  $\mu\text{c-Si:H}$  cells on the rough electrode are plotted in Fig. 3.10, as well as the same calculation in the absence of parasitic absorption, the corresponding simulated curves, and the “Yablonovitch limit” (corresponding to no  $A_p$  and Lambertian scattering). These curves are compared to  $4n^2$ . It can be seen that parasitic absorption drastically lowers the achievable enhancement. Even without parasitic absorption and for Lambertian light trapping (Yablonovitch limit), the  $4n^2$  value is not reached even at 1100 nm, especially for the thick cell. This indicates that the absorption is still too large at 1100 nm for the weak absorption approximation to be valid.

The deviation of the simulated and experimental curves comes most probably from the increase of the measurement uncertainties, as the absorption becomes extremely low (especially for the single pass case). The decrease observed for the largest wavelengths, both in the experiment and the simulation, comes from the increasingly detrimental parasitic absorption. Moreover, since the absorption coefficients of most known TCO are much larger than

### 3.6. Important parameters governing light harvesting

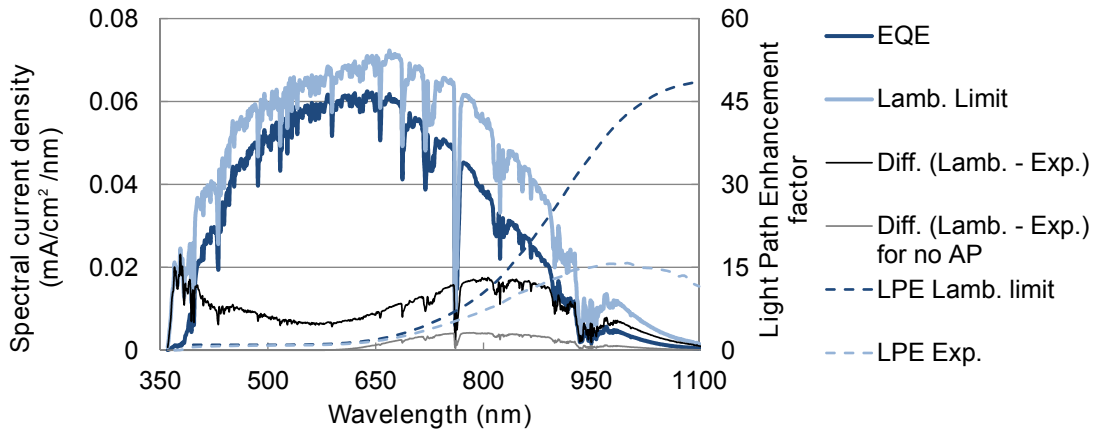


Figure 3.11: Spectral current density (SCD) for the 1- $\mu\text{m}$ -thick  $\mu\text{c}$ -Si:H cell grown on the rough substrate, as well as the SCD for Lambertian scattering and no parasitic absorption (corresponding to the Yablonovitch limit) and the difference in SCD between both. The gain in SCD between the estimated EQE in the absence of parasitic absorption ( $\text{EQE}_c$ ) and the Yablonovitch limit is indicated as a gray line. The LPE is indicated on the right scale with dashed thinner lines.

that of  $\mu\text{c}$ -Si:H starting from wavelengths around 1000 nm (Fig. 3.8), large EQE values in this wavelength range with thin layers can only be obtained by using more transparent TCOs.

Even though the LPE is an indicative value which can be useful to quantify light trapping, the spectral range of greatest interest for current generation (and thus for light trapping improvement) is not the one where the maximal absorption enhancement occurs. As can be seen from the light gray curve in Fig. 3.11, the wavelength range with the most current losses is in the near infrared region (700 – 900 nm). In this wavelength range, the reachable LPE for a Lambertian distribution is below 30, still far from the  $4n^2$  value. Also, comparing the light gray and the dark gray curves in the same graph indicates that most of the potential improvements rely on parasitic absorption reduction (throughout the spectrum).

#### 3.6.3 Identification of the most limiting parameters

It should be noted that a precise prediction of the potential of a structure was not the main objective of our approach; it was rather an intuitive description of the key parameters governing light harvesting in solar cells, their interdependence, and the gain to expect when improving each one of these parameters. These parameters are mainly the absorption in the photoactive layer ( $\alpha \cdot l$ ), light scattering ( $a_0$ ,  $a_1$  and  $b_1$ ), and the parasitic absorption terms. To illustrate this point, we reproduce in Fig. 3.12 the EQE curves that are potentially obtainable when improving the absorption coefficient (going to 100% crystallinity), light trapping (going to a fully Lambertian distribution), and parasitic absorption (suppressing it) for our 1- $\mu\text{m}$ -thick cell on the rough substrate. We compare this to the maximal achievable curve (Yablonovitch

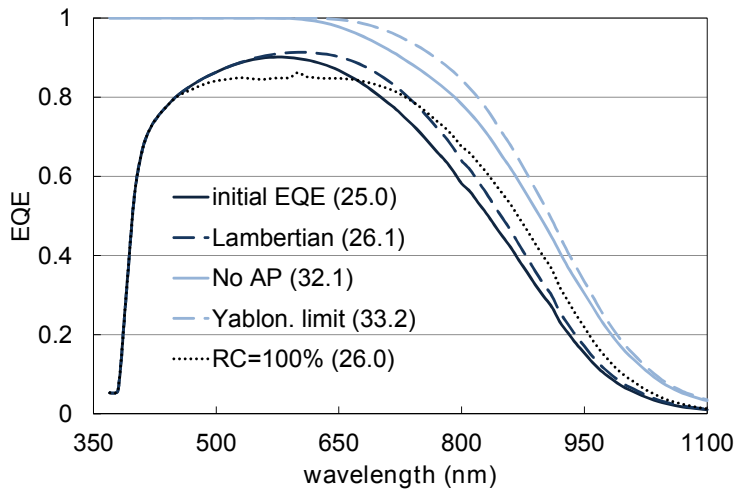


Figure 3.12: Simulated EQE curves of a 1- $\mu\text{m}$ -thick  $\mu\text{c-Si:H}$  cell on a rough electrode (initial EQE), and EQE to expect when going to Lambertian light scattering (Lambertian), suppressing all parasitic absorption (No AP), or using an absorber layer of 100% crystallinity (instead of 60% in other cases). The Yablonovitch limit is also indicated. The numbers in parenthesis are current densities in  $\text{mA}/\text{cm}^2$ .  $R_0$  was set to zero for all simulated curves.

limit, obtained by setting  $\eta = 0$  in equation 3.3), obtained for no parasitic absorption and immediate Lambertian light scattering. As can be seen, most of the potential gain ( $7 \text{ mA}/\text{cm}^2$ ) comes from the reduction of parasitic absorption ( $6 \text{ mA}/\text{cm}^2$ ) and not from light trapping improvement (only  $1 \text{ mA}/\text{cm}^2$ ).

Since the  $4n^2$  limit is a strong consequence of the Lambertian distribution of light, and as such a distribution unavoidably comes after several light-scattering events from any scattering interface [Yablonovitch 82b, Deckman 83a], it is unlikely to be strongly surpassed by standard light-trapping schemes that can mostly act on the first scattering events. Periodic gratings might have a chance to improve further the first few passes, but the question remains: how to prevent an interface that can couple light into guided modes in a high-index medium from also out-coupling it? Finding ways to reduce this out-coupling will be the key to improving light trapping.

### 3.7 Conclusion

We generalized the formula proposed by Deckman *et al.* to obtain a correct representation of light management in real solar cells. We suggested an extension of the formula to experimental distributions of scattered light for light entering the cell by modifying only the first two passes and treating light that does not escape the cell in a Lambertian way. Further implementing primary reflection and parasitic absorption at the front interface of the cell gave rise to a correct reproduction of EQE and  $R$  curves for various  $\mu\text{c-Si:H}$  solar cells. This simple model enables an intuitive representation of light scattering in solar cells, and a fast way of determining

the predominant parameters limiting the  $J_{sc}$ . We could in particular show that the most limiting parameter of our devices is currently parasitic absorption rather than sub-optimal light trapping, and we could also highlight the particularly important role of scattering light into large angles for the first scattering events to elongate as much as possible the effective light path before the first escape event occurs. The link with the classical  $4n^2$  limit was outlined, and this limit was discussed for our devices.

It would be of interest to compare the presented average ray tracing approach with conventional ray tracing and other simulation methods, and also to apply this model to other device geometries (such as  $n-i-p$ , or with metallic back reflectors). In the following chapter, other comparisons between experimental EQE curves and calculated ones are presented. The typical parameters studied include parasitic absorption of both electrodes and light-trapping capacity.



## 4 The interconnection between parasitic absorption and light trapping

In this chapter, we study systematically the interdependence between light scattering and parasitic absorption in Micromorph devices with three approaches.

We first unlink their respective influence by developing bilayer front electrodes: a flat ITO layer ensures conduction and allows us to tune parasitic absorption, while the haze is adjusted by varying the thickness of a highly transparent rough ZnO layer. We show how a minimum amount of parasitic absorption leads only to a few percents of absorptance for a single light pass but to a strong reduction of the cell current in the infrared part of the spectrum. Conversely, a current enhancement is shown with increasing front electrode haze up to a saturation of the current gain. This saturation correlates remarkably well with the calculated haze of the front electrode into silicon, validating this approach.

Then, we show that parasitic absorption in the front and back electrodes is equally important at large wavelengths, and that they are strongly interlinked: when reducing one electrode absorptance, the largest EQE gain is obtained when parasitic absorption in the other electrode is the lowest. This effect highlights the importance of reducing parasitic absorption simultaneously in both electrodes. This can be achieved, for a given sheet resistance, by lowering the free-carrier density (doping) and compensating with the thickness.

Finally, we suggest an anti-escape system based on a microlenses array that enables to reach extremely efficient light trapping, even further than the Yablonovitch limit. Based on geometric optics, a reduction by a factor of five of the share of light escaping the device can be achieved, at the cost of a reduction by the same factor of the solid angle of acceptance. With an imperfect optical setup including 20% of extra losses, we experimentally observe a strong improvement of the EQE in the wavelength range of weak absorption for  $\mu\text{c-Si:H}$ , by up to 45% for wavelengths above 1000 nm. We use this system as a tool to probe the influence of parasitic absorption for very good light-trapping conditions, highlighting the need for very low parasitic absorption to take advantage of an excellent light trapping and convert it into a high current density.

These three experimental sets of data are also used to validate the model presented in the

previous chapter. Very good agreement is observed for all three case studies, except when light scattering is very weak.

### 4.1 Unlinking absorption and haze in thin-film silicon solar cell front electrodes

The experimental results presented in this section have been published in [Boccard 10b] but not the modeling part. We study here the respective influence of haze, the ratio of scattered transmitted light to total transmitted light, and free-carrier absorption (FCA) of transparent front electrodes on the photogenerated current of Micromorph thin-film silicon solar cells.

#### 4.1.1 Experimental details

In the superstrate configuration, LPCVD-ZnO-based front electrodes are ideally suited for high-efficiency thin-film silicon solar cells thanks to a high transparency, good electrical properties, a naturally rough surface with excellent light-scattering properties and a deposition rate of over 3 nm/s [Faÿ 06, Domine 08]. However, the surface morphology and FCA of a LPCVD ZnO film depend both on its thickness and doping [Faÿ 06]. The respective influences on the cell current of FCA and light-scattering characteristics – that both act in the infrared region of the spectrum – are therefore difficult to separate.

We present here bilayer TCO front electrodes which permit us to decouple haze from FCA. Micromorph tandem cells with SOIR [Buehlmann 07] are made on glass by plasma-enhanced chemical vapor deposition. Bilayer front electrodes are made of flat sputtered ITO followed by rough non-intentionally-doped (n-i-d) LPCVD ZnO. ITO's high free-carrier density of around  $7 \cdot 10^{20} \text{ cm}^{-3}$  leads to strong absorption, while a 30 times smaller carrier density makes rough n-i-d ZnO highly transparent [Steinhauser 07]. The back contact is made of 6- $\mu\text{m}$ -thick n-i-d ZnO.

#### 4.1.2 Influence of parasitic absorption on the cell current

To study the FCA influence on the cell current, we deposit various thicknesses of ITO on glass: 0 nm, 60 nm, 120 nm and 180 nm. We subsequently deposit a 4- $\mu\text{m}$ -thick n-i-d LPCVD ZnO on top of each ITO layer (Fig. 4.1a) to ensure identical light-scattering properties for all four bilayer front electrodes. A systematic increase in the NIR absorptance is observed for increasing ITO thickness (Fig. 4.1b) while the ZnO layer shows a remarkably low absorptance below 2% up to 1100 nm for a sheet resistance as low as  $23 \Omega/\square$ .

Fig. 4.1c shows that an increase of the front electrode absorptance lowers the EQE of the  $\mu\text{c}$ -Si:H bottom cell and the reflectance ( $R$ ) of the stack ( $1 - R$  increases) in the infrared. Tab. 4.1 summarizes for all front electrodes the currents as well as the current losses compared to the



## 4.1. Unlinking absorption and haze in front electrodes

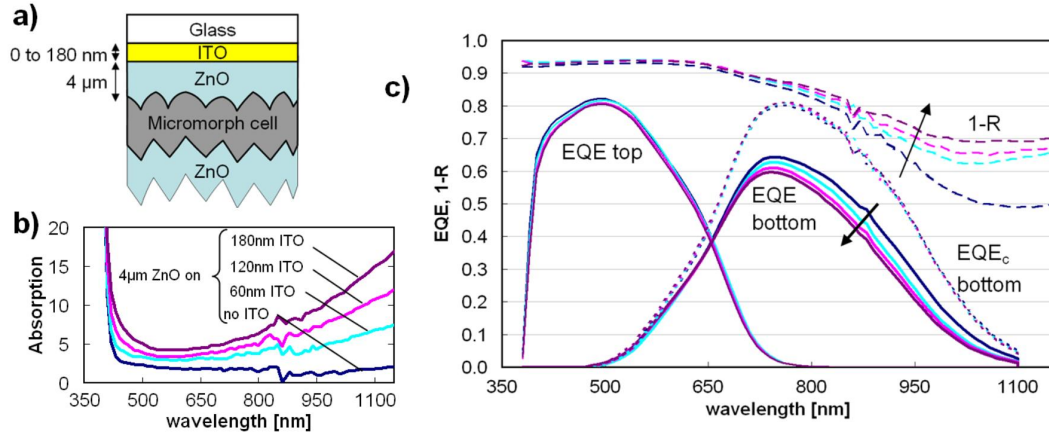


Figure 4.1: a) Schematic cross-section of the studied device. ZnO is undoped and highly transparent. b) Absorbance of front electrodes made of 0 to 180 nm ITO under 4  $\mu\text{m}$  ZnO. c) EQE and  $1 - R$  of Micromorph cells grown on the same front electrodes. Arrows show the effect of thickening the ITO from 0 to 180 nm. Dotted lines are  $\text{EQE}_c$  of bottom cells, simulating no parasitic absorption.

cell with no ITO.  $0.8 \text{ mA}\cdot\text{cm}^{-2}$  (corresponding to 6% relative) is lost when introducing 60 nm ITO to the ZnO-only front electrode. Introducing twice (three times) as much ITO lowers the current by  $1.1 \text{ mA}/\text{cm}^2$  ( $1.4 \text{ mA}/\text{cm}^2$ ).

Table 4.1: Top and bottom cell currents for Micromorph cells grown on various bilayer front electrodes of which single pass absorbance at 900 nm is indicated. The bottom cell current shift compared to the first cell of each series is also indicated.

ITO (nm)	ZnO ( $\mu\text{m}$ )	A(900) (%)	$J_{\text{sc,top}}$ ( $\text{mA}/\text{cm}^2$ )	$J_{\text{sc,bot}}$ ( $\text{mA}/\text{cm}^2$ )	$J_{\text{sc,bot}}$ shift ( $\text{mA}/\text{cm}^2$ )
0	4	0.9	12.4	12.6	0.0
60	4	3.7	12.3	11.8	-0.8
120	4	6.1	12.1	11.5	-1.1
180	4	8.2	11.9	11.2	-1.4
60	0.1	2.5	8.4	8.4	0.0
60	1	3.1	12.4	11.0	+2.6
60	2	4.1	12.7	11.8	+3.4
60	4	3.7	12.2	12.0	+3.6
60	7	4.3	12.3	12.7	+4.3

Between 700 nm and 850 nm, linear bottom-cell EQE loss and  $1 - R$  increase are observed with increasing ITO thickness. Above 850 nm, a deviation from linearity is due to the lower refractive index of ITO ( $\approx 1.6$  at 1100 nm) compared to ZnO ( $\approx 2.0$ ) because of its high doping, modifying the total internal reflection in the cell. In the cell, the significant current loss due to ITO in the NIR comes from efficient light trapping inducing multiple light passes not only in the photoactive layers but also in the TCO. Its absorbance is then stronger than the one measured outside the cell (Fig. 4.1b). High current gains are thus expected in cells by reducing

## Chapter 4. The interconnection between parasitic absorption and light trapping

the front electrode FCA, even for little-absorbing TCOs.

A way to compare the light-scattering properties of different front electrodes is to calculate corrected EQE ( $EQE_c$ ) and R ( $R_c$ ) assuming no parasitic absorption ( $A_p$ ) in our device (mainly from TCO and doped layers). For good carrier collection, we have  $EQE + A_p + R = 1$  so  $EQE + R = 1 - A_p$ . Without parasitic absorption,  $EQE_c + R_c = 1$ . This normalization is obtained by defining  $EQE_c = EQE / (1 - A_p)$  and  $R_c = R / (1 - A_p)$ , which means splitting equitably  $A_p$  between current conversion and reflectance. Finally,  $EQE_c = EQE / (EQE + R)$ . The  $EQE_c$  of the aforementioned bottom cells are plotted as dotted curves in Fig. 4.1c. Their excellent superposition confirms that light scattering is identical for all the front electrodes and that the EQE reduction can be attributed exclusively to FCA.

### 4.1.3 Haze influence on the cell current

Micromorph cells are deposited on ITO-ZnO bilayer front electrodes (Fig. 4.2a). A 60-nm-thick ITO layer ensures conduction and an almost identical FCA up to 1100 nm for all cases (e.g. at 900 nm, Tab. 4.1). ZnO thickness is varied from 0.1 to 7  $\mu\text{m}$  to improve light scattering (Fig. 4.2b) thanks to increased pyramidal feature size ( $\approx 0.4 \mu\text{m}$  for 2- $\mu\text{m}$ -thick films) [Faÿ 06]. SEM images of the surface of these layers are given in Fig. 2.1. The angular dependence of light scattering (Fig. 4.2c) is identical for all cases.

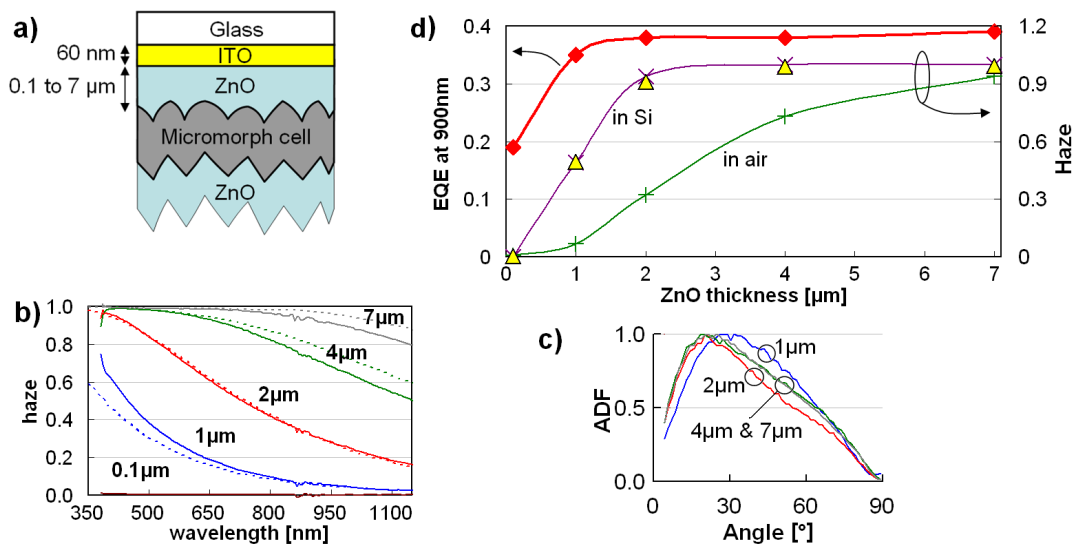


Figure 4.2: a) Schematic cross-section of the studied device. b) Haze measured (and calculated, dotted lines) in air for 0.1- $\mu\text{m}$ - to 7- $\mu\text{m}$ -thick ZnO layers on 60-nm-thick ITO layer. c) ADF of the front electrodes, with their maximum normalized to 1. d) Haze at 900 nm measured in air or calculated in silicon of the same TCO stacks (right axis) and EQE value at 900 nm for cells grown on these substrates (left axis). Triangles are haze values measured in air at 450 nm.

Improving the front electrode haze enhances the bottom cell current (Tab. 4.1). Part of this gain comes from the 500 nm to 700 nm range of the EQE and is accompanied by a top cell

## 4.1. Unlinking absorption and haze in front electrodes

current loss coming from the same range as seen in Fig. 4.3 (especially for ZnO layers thicker than 2  $\mu\text{m}$  as shown in Tab. 4.1). This can be due to the increased typical size of the features of the front electrodes [Dominé 06] and can be linked to a worsening of the light coupling in the top cell, as discussed in chapter 5. The EQE gain in the bottom cell between 700 nm and 900 nm is ascribed to a decrease of the reflection of the SOIR (which was optimized for a thickness of 4  $\mu\text{m}$ ) due again to the increased roughness.

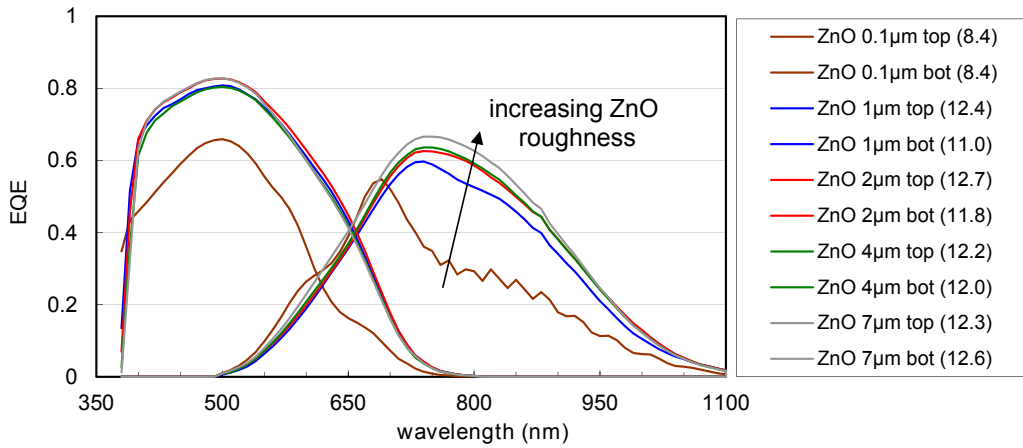


Figure 4.3: EQE of Micromorph devices deposited on 0.1- $\mu\text{m}$ - to 7- $\mu\text{m}$ -thick ZnO layers on 60-nm-thick ITO layers.

EQE values at 900 nm (Fig. 4.2c) are then used to quantify the impact of our front electrodes' scattering characteristics, to minimize the above-mentioned effects while maintaining large enough values.

The cell response at 900 nm increases for increasing ZnO thickness in the front electrode, up to saturation for 2- $\mu\text{m}$ -thick films (Fig. 4.2d). No EQE enhancement is seen from 2- $\mu\text{m}$ - to 7- $\mu\text{m}$ -thick films despite the continuous haze increase measured in air (Fig. 4.2d). A similar observation was made in [Krč 04]. Indeed, light scattering due to a rough interface into silicon (as in a cell) is different from that into air because of the different refractive indices of air and silicon. The haze of a front electrode into silicon cannot be directly measured, but it can be calculated for any ambient medium from AFM data with a recently developed Fourier method [Domine 10]. The results of such haze calculations for our front electrodes into air are shown in Fig. 4.2b. The excellent agreement with measurements validates the method which we now use to determine the haze of our front electrodes for scattering into silicon. These calculated haze values into silicon at 900 nm are plotted in Fig. 4.2d and correlate well with the EQE enhancement at the same wavelength.

In the model presented in [Domine 10], as well as in scalar scattering theory (see *e.g.* in [Domine 08]), the haze created at an interface depends mostly on a phase shift  $\delta$  of the incoming light induced by its roughness. This phase shift is proportional to  $2\pi|n_1 - n_2|\zeta/\lambda$ ,  $\zeta$  being a length characterizing the roughness of the surface,  $n_1$  and  $n_2$  the refractive indices of the surrounding media and  $\lambda$  the wavelength of the incident light. For TCO ( $n_1 = 2$ ) into air

Table 4.2: Input parameters of the model for the different front electrodes.

ITO (nm)	ZnO ( $\mu\text{m}$ )	$R_0$	Haze	$a_0$	$b_1$	$A_{first}(800 \text{ nm})$
0	4	0.08	1	1.2	0.15	0.046
60	4	0.08	1	1.2	0.15	0.070
120	4	0.08	1	1.2	0.15	0.082
180	4	0.08	1	1.2	0.15	0.095
60	0.1	0.18	0	1	0	0.070
60	1	0.09	0.5	1.1	0.36	0.070
60	2	0.08	0.9	1.18	0.16	0.070
60	7	0.08	1	1.2	0.15	0.070

( $n_2 = 1$ ), we have  $\delta \propto 2\pi \cdot \zeta / \lambda$  and for TCO into silicon ( $n_2 = 4$ ), as in the cell,  $\delta \propto 2\pi \cdot 2\zeta / \lambda$ . So the phase shift, and thus the haze, due to the rough surface of a TCO layer into silicon for a wavelength  $\lambda$  is equal to its haze into air but at the wavelength  $\lambda/2$ . The haze measured in air at 450 nm for the same series of front electrodes is plotted as triangles in Fig. 4.2c. It matches very well the calculated value into silicon at 900 nm.

Thus, as a rule of thumb, haze values of TCO-based front electrodes measured in air at a given wavelength can be correlated to the EQE enhancement of the thin-film silicon solar cell *but at twice the wavelength*. Consequently, measuring haze values of TCO-based front electrodes in air at wavelengths over 550 nm do not give direct information about their light-scattering potential for silicon solar cell applications.

#### 4.1.4 Modeling

We simulate the series in absorption or haze of the front electrode with the model presented in chapter 3. Main results are shown in Figs. 4.4 and 4.5. One set of input parameters is used for modeling all cells, with only the necessary changes to reproduce the physical differences. Within the ITO thickness series, only  $A_{front}$  and  $A_{first}$  are varied, and their values are obtained experimentally by measuring the absorptance of the front electrode stack on glass (with  $A_{front}$  arbitrarily set to  $2 \cdot A_{first}$  as discussed in chapter 3). For the ZnO thickness series, only primary reflection and haze (resulting in different  $a_0$  and  $b_1$ ) are modified. The haze values were calculated from AFM data. Input parameters are given in Tab. 4.2. All parameters, except for the absorption coefficient of  $\mu\text{c-Si:H}$  and the parasitic absorptances, are set to be constant for all wavelengths, based on their very small variations observed in the wavelength range of interest here (800 nm to 1100 nm).

In order to reproduce the absorption of the top cell, a contribution from a 1- $\mu\text{m}$ -thick  $a\text{-Si:H}$  layer was added to the parasitic absorption in front of the  $\mu\text{c-Si:H}$  cell. Such a large value (compared to the real top cell thickness of 300 nm) was needed to reproduce approximately the shape of the EQE of the bottom cell in the 500 nm to 700 nm range, as light of these wavelengths is trapped in the top cell due to the SOIR. This adaptation fails to reproduce precisely the

#### 4.1. Unlinking absorption and haze in front electrodes

shape of the curve, which depends strongly on the near-field interaction of light with the  $\alpha$ -Si:H cell and the intermediate reflector. Yet, a correct modeling of this wavelength range in Micromorph devices is out of the scope of our approach, and we will focus on wavelength values above 800 nm.

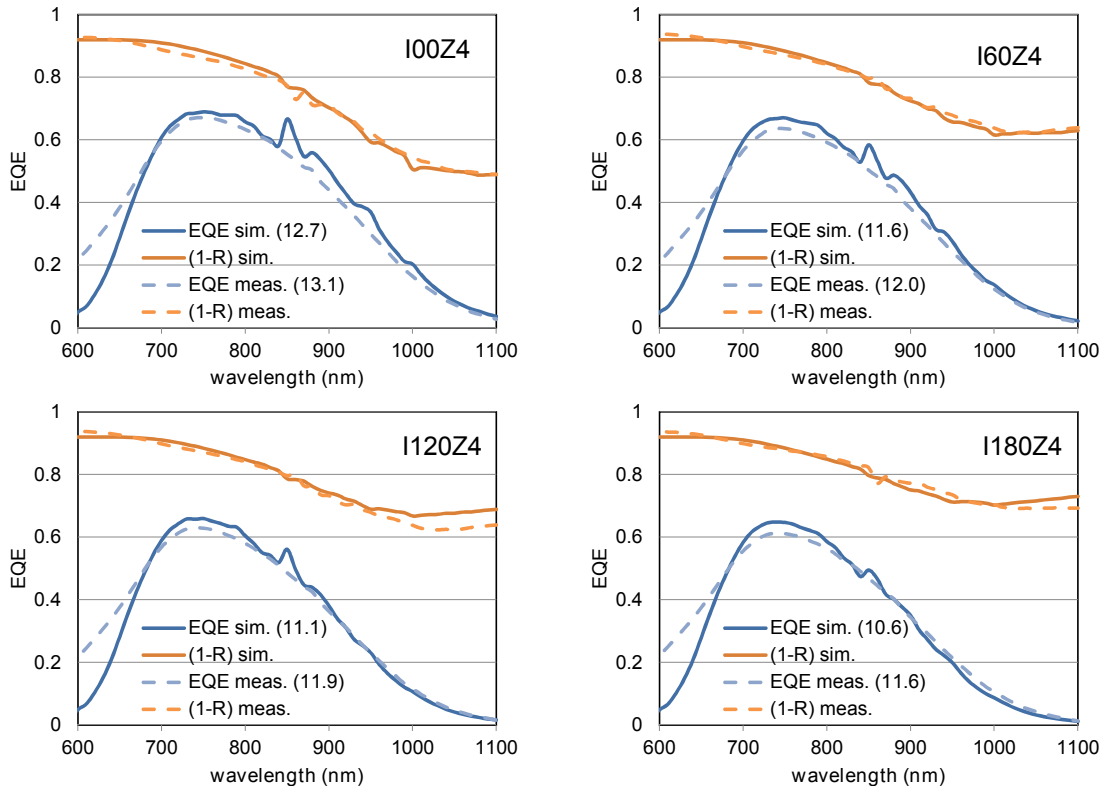


Figure 4.4: Measured and simulated EQE and (1-R) curves for the bottom cells of the Micromorph devices presented in Fig. 4.1. The labels  $I_xZ_y$  account for the bilayer substrate composed of a  $x$ -nm-thick ITO layer followed by a  $y$ - $\mu\text{m}$ -thick ZnO layer.

A good agreement is found in the case of the ITO thickness series, with the strongest current gain observed between no ITO and 60 nm of ITO. Concerning the ZnO thickness series, the model fails to reproduce the EQE on the flat substrate (I60Ze). Indeed, our approach is not suited for such flat cases, especially when (as is the case here) the main scattering interface is not the front electrode surface (in this case the back of the ZnO back contact and the white reflector are diffusive). Yet, the correct trend is observed for other substrates, except for the interferences in the 1-R curve for the 1- $\mu\text{m}$ -thick ZnO layer.

Globally, the analytical model presented in chapter 3 reproduced well the trend experimentally observed when varying the parasitic absorption and the light scattering of the front electrode. The precision improves when light trapping is improved, as could be expected from the large importance of the parameter  $b_1$  which is harder to determine for weak light trapping, and the assumption that the distribution of light not escaping the device after one round trip will

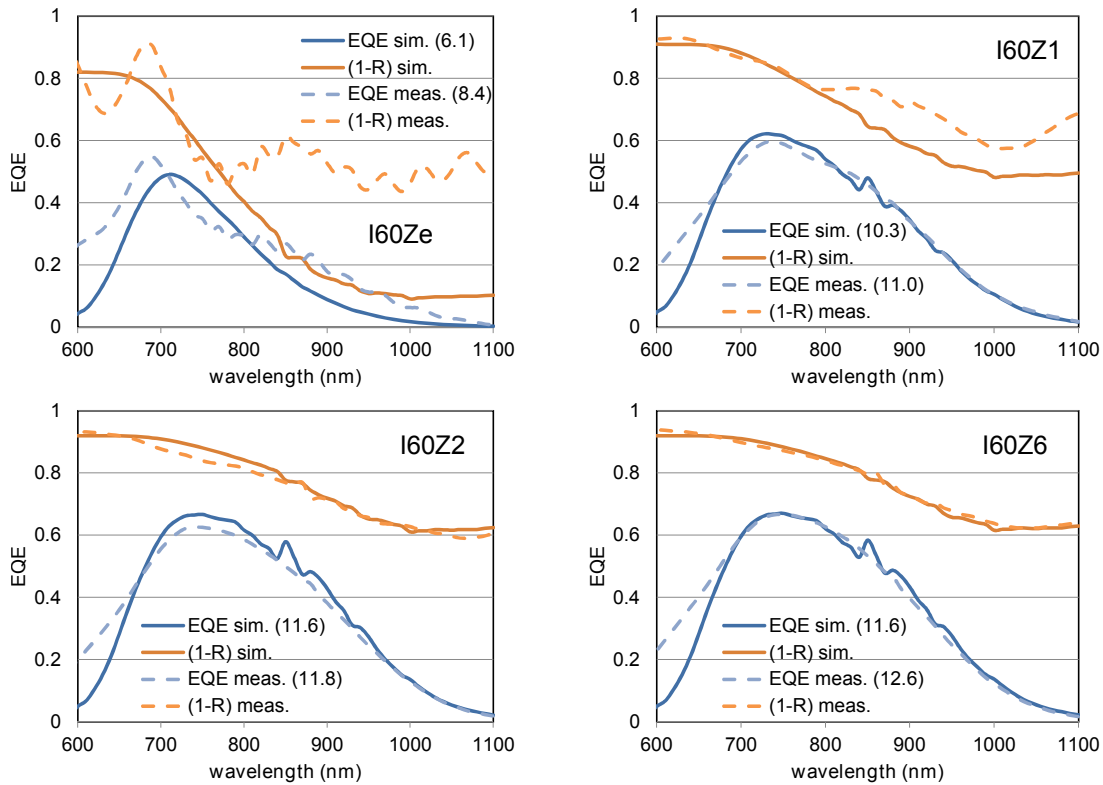


Figure 4.5: Measured and simulated EQE and (1-R) curves for the bottom cells of the Micro-morph devices presented in Fig. 4.2.

directly become Lambertian for the subsequent passes.

#### 4.1.5 Conclusion

We were able to separate the relative influence of front electrode haze and FCA by using LPCVD ZnO and ITO bilayer electrodes. An EQE decrease and a reduction of  $R$  from the cell is observed when increasing FCA for a unique morphology. The current loss is shown to be quite dramatic even for a few percents of absorptance in the TCO, therefore demonstrating the need to develop TCOs with very low absorptances (typically  $< 2\%$  between 400 nm and 1100 nm). On the other hand, enhancing the haze for a given FCA improves the bottom cell current. The EQE gain at large wavelengths is well correlated to the haze value of the front electrode calculated into silicon but not to its value into air. A convenient scaling law is proposed to approximate haze into silicon at a wavelength  $\lambda$  by its measurement into air at  $\lambda/2$ . Bilayer front electrodes combining a flat, conducting and highly transparent TCO (e.g. IOH [Koida 09]) with 2- $\mu\text{m}$ -thick n-i-d LPCVD ZnO featuring small pyramids with sufficient haze would thus be excellent to reach high top and bottom cell currents in Micro-morph solar cells. This will be demonstrated in detail in chapter 5, in which a detailed optimization of the substrate morphology for high-efficiency Micro-morph devices (requiring also electrical considerations)

is presented.

### 4.2 Effect of parasitic absorption in front and back contacts

When it comes to parasitic absorption in thin-film silicon solar cells, most studies focus on one electrode only, most of the time the substrate (in  $n-i-p$  configuration) or superstrate (in  $p-i-n$  configuration). We will investigate here the influence of the absorption in both front and back electrodes on the EQE in  $p-i-n$  configuration, and their interconnection. We will compare four possible combinations of front and back electrodes with two different doping levels, but identical sheet resistance and identical light-scattering properties.

#### 4.2.1 Experimental details

The devices studied here are Micromorph cells deposited in a small-area research-scale reactor by PECVD. An in-situ 70-nm-thick SOIR is inserted between the 240-nm-thick  $a$ -Si:H top cell and the 2.8- $\mu\text{m}$ -thick  $\mu\text{c}$ -Si:H bottom cell. Front and back electrodes are made of LPCVD ZnO.

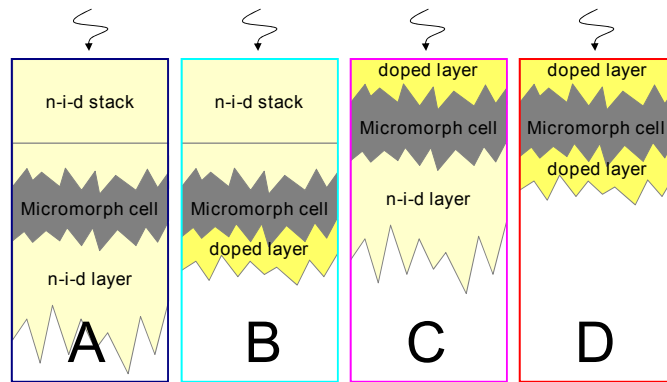


Figure 4.6: Schematic view of the stacks composing the A, B, C and D Micromorph devices. Only the front and back electrodes are changed. Light enters the devices from the top.

Fig. 4.6 schematically presents the four Micromorph devices compared in this section. Their front and back electrodes are the only changing parameters and two options are compared: thick,  $n-i-d$  LPCVD ZnO or thin, doped LPCVD ZnO. The free-carrier density in the  $n-i-d$  ZnO is around  $1.2 \cdot 10^{19} \text{ cm}^{-3}$  and it is  $1.0 \cdot 10^{20} \text{ cm}^{-3}$  in the doped one. The sheet resistance is kept similar for all electrodes (between  $7$  and  $12 \Omega/\square$ ) thanks to the much larger thickness in the  $n-i-d$  case. In order to keep the same morphology for both types of front electrodes, a stack of two layers is used in the  $n-i-d$  case. A  $7\text{-}\mu\text{m}$ -thick layer is first deposited on glass and chemo-mechanically polished to erase the very large pyramidal features that naturally form on its surface during layer growth [Faÿ 06]. To inhibit epitaxial growth on this polished surface, an ultra-thin ( $< 5 \text{ nm}$ )  $n$ -doped  $\mu\text{c}$ -Si:H layer is subsequently deposited; a  $n-i-d$  ZnO film is then deposited on top, with thickness adjusted to match the surface morphology of the  $2\text{-}\mu\text{m}$ -thick doped layer. Due to a reduction of grain growth rate when doping LPCVD ZnO

[Faÿ 06], this rough n-i-d layer is only 1.6  $\mu\text{m}$  thick.

#### 4.2.2 Experimental results and discussion

Fig. 4.7a compares absorptance measurements of the 8- $\mu\text{m}$ -thick n-i-d ZnO stack and the 2- $\mu\text{m}$ -thick doped ZnO layer. For wavelengths up to 550 nm the doped layer absorbs less than the n-i-d stack. This is due first to the Burstein-Moss effect, widening the band-gap in the case of the doped ZnO [Steinhauser 08], but also to enhanced sub-gap absorption in the n-i-d stack because of the larger thickness. However, above 550 nm, the higher FCA in the doped single layer makes the n-i-d stack more transparent despite its larger thickness.

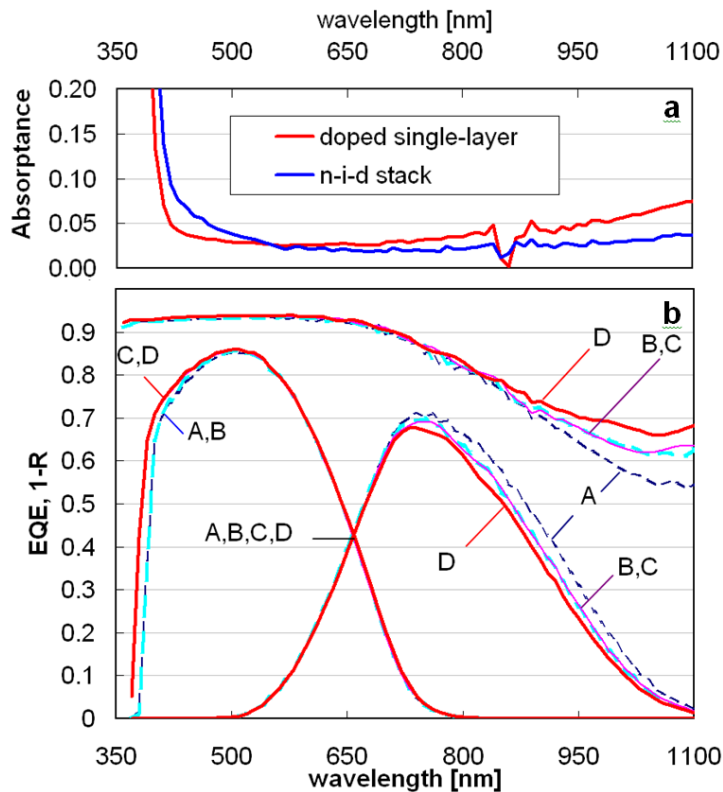


Figure 4.7: a) Absorptance of ZnO front electrodes used in this study as sketched in Fig. 4.6. These measurements were made in air with an index-matching liquid. b) EQE and 1-Reflection (1-R) of the four Micromorph devices sketched in Fig. 4.6 having only their ZnO electrodes changed.

Fig. 4.7b shows the EQE of top and bottom cells for the four possible Micromorph configurations employing these electrodes in front and back. The similarity of the morphology of all front electrodes is assessed by the perfect matching of the crossing of the top and bottom EQE curves for all substrates at the same wavelength (650 nm), as will be seen in chapter 5 and [Boccard 12b]. The top cell current is only affected for such a thick cell by the front electrode (A, B and C, D are superimposed), and the thin doped layer enables a  $0.2\text{mA}/\text{cm}^2$  current



## 4.2. Effect of parasitic absorption in front and back contacts

gain. Then, the bottom cell is sensitive to the transparency of both electrodes, and in a very similar way, as deduced from the striking superimposition of the B and C curves and the identical currents (Tab. 4.3). Also, Fig. 4.8a indicates the relative parasitic absorption for all cases compared to case A, evidencing the identical effect of FCA in the back or front electrode.

Table 4.3: Top cell, bottom cell and summed currents for Micromorph cells using various front and back electrodes as sketched in Fig. 4.6.

	A	B	C	D
Top	13.3	13.3	13.5	13.5
Bottom	13.4	12.7	12.7	12.2
Sum	26.7	26.0	26.1	25.8

As shown in Tab. 4.3, the current gain obtained in the bottom cell by improving the transparency of the back electrode (B to A or D to C) depends on the front electrode properties ( $0.7 \text{ mA/cm}^2$  for B to A or  $0.5 \text{ mA/cm}^2$  for D to C). The same applies when improving the transparency of the front electrode:  $0.7 \text{ mA/cm}^2$  are gained in the bottom cell for C to A, but only  $0.5 \text{ mA/cm}^2$  for D to B. Fig. 4.8b emphasizes the influence of the absorption of the front electrode on the current gained when making the back electrode more transparent by comparing the gain of spectral current densities between configuration B and A, or D and C.

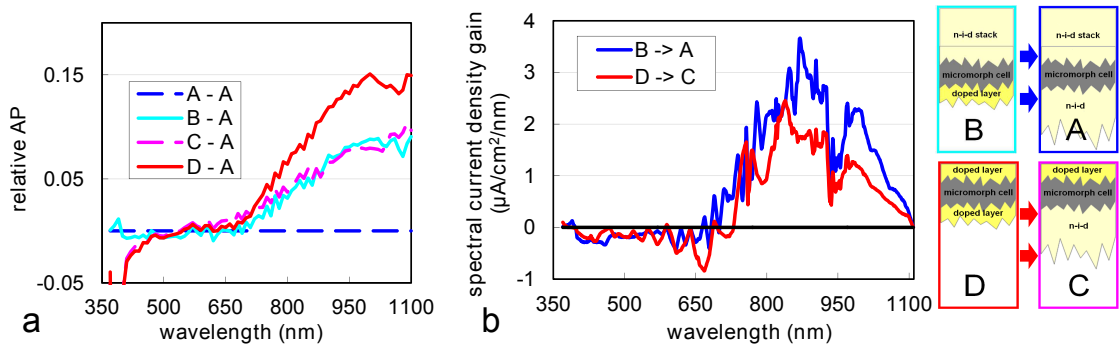


Figure 4.8: a) Relative parasitic absorption in the four Micromorph devices sketched in Fig. 4.6 compared to case A where both electrodes are lightly doped, and thus very transparent. b) Spectral current density gain between configurations B and A, or D and C. In both cases, the same modification is made at the back electrode.

This difference comes from the fact that the light saved from parasitic absorption in the front (resp. back) electrode by making it more transparent will be distributed between valuable absorption (EQE), escape from the cell ( $R$ ) and parasitic absorption in the remaining parasitically absorbing layers ( $A_P$ ). The probability of the latter increases with the parasitic absorption of the back (or front) electrode.

### 4.2.3 Modeling

This effect can efficiently be modeled with the model presented in the chapter 3 (Fig. 4.9). We first use the  $EQE_c$  to adapt the unknown parameters ( $a_0$  and  $b_0$ ,  $R_0$ , and the  $p$ -layer thickness) once for all cells. Then, implementing in  $A_{front}$  and  $A_{back}$  the measured absorptances of the two different types of layers leads to a correct reproduction of the experimental data. The notable discrepancy of the simulation compared to the measurement likely comes from the many additional interlayers present in the real Micromorph device, such as intermediate reflector and  $a$ -Si:H doped layers, inducing extra parasitic absorption and reflection. Also, possible collection issues (modeled as 2% in the whole spectrum) are assimilated to  $A_p$  in the measurements. It is seen that parasitic absorption in the front (resp. back) layers of the cell changes as the back (resp. front) layers' transparency is modified.

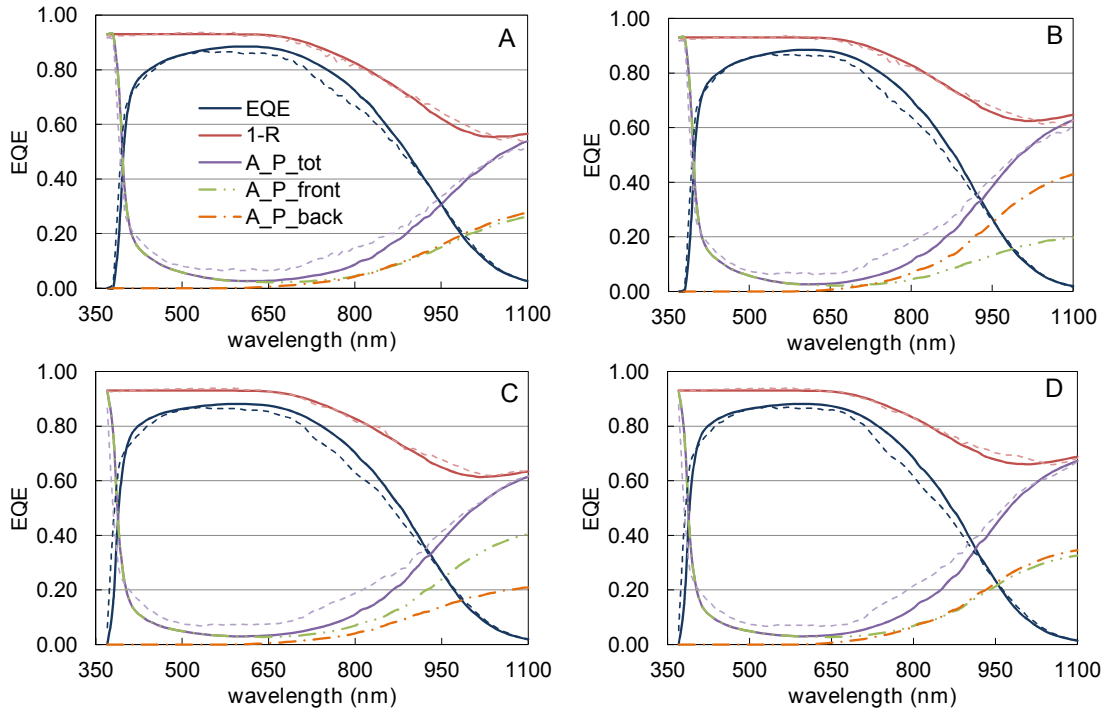


Figure 4.9: Simulated (solid) and measured (dashed) EQE, total absorptance ( $1 - R$ ) and front, back and total  $A_p$  curves simulated from experimental absorption data for the Micromorph devices presented in Fig. 4.6.

Reducing  $A_{front}$  without changing the back electrode leads to an increase in the parasitic absorption in the back electrode, as seen when comparing C to A, and D to B. The same applies when reducing  $A_{back}$  ( $A_p^{front}$  is higher in A than in B, and in C than in D). Also, very similar  $A_p^{front}$  and  $A_p^{back}$  are observed in symmetrical devices (A and D), which is in agreement with their similar importance experimentally observed. To see the effect of modifying the front and/or back electrode absorptance, Fig. 4.10 gives the  $J_{sc}$  as a function of the attenuation of the parasitic absorptance of the front and back electrodes. The reference is taken for the case D, with doped front and back electrodes, and the value gives the multiplying factor applied

## 4.2. Effect of parasitic absorption in front and back contacts

to the absorptance for each wavelength. It can be seen with this graph that strong current gain is possible only by reducing  $A_P$  in both electrodes: removing completely  $A_P$  from the front (resp. back) electrode makes the current increase from  $26.8 \text{ mA/cm}^2$  to  $29.0 \text{ mA/cm}^2$  (resp.  $28.1 \text{ mA/cm}^2$ ), but  $29.9 \text{ mA/cm}^2$  can be obtained when removing 80% of  $A_P$  from both contacts, and  $31.1 \text{ mA/cm}^2$  when removing all  $A_P$ . The asymmetry in favor of reduction of  $A_P$  in the front electrode is due to the first pass.

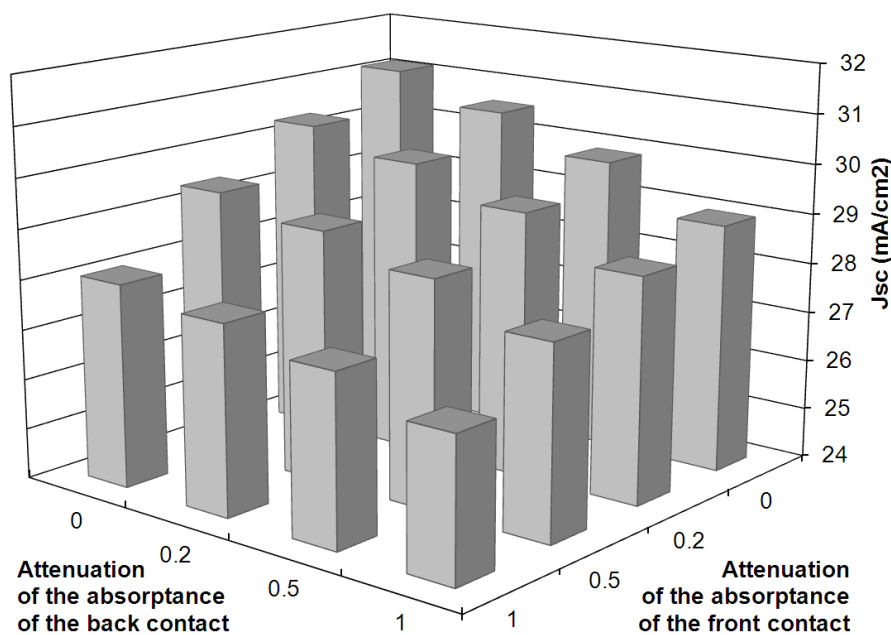


Figure 4.10: Calculated  $J_{sc}$  obtained when attenuating the absorptance of the front or back electrode (e.g. by multiplying the absorptance by 0.5 for the 0.5 line).

### 4.2.4 Conclusion

We showed in this section that parasitic absorption in a solar cell is self-influenced. We validated our model for light management in  $\mu\text{c-Si:H}$  cells for parasitic absorption modification, as, even if the simulated curves did not exactly match the experimental ones, the same trends and conclusions were obtained by simulations and experiments. We also emphasized that a larger gain can be obtained when reducing parasitic absorption in a device showing little remaining  $A_P$ : light saved will be shared between the remaining  $A_P$ ,  $R$  (escape from the cell) and the EQE. However, as evidenced by Battaglia *et al.* [Battaglia 11b], doped layers also contribute to parasitic absorption: thus, their contribution to parasitic absorption might at some point become larger than the contribution of the electrode, making further improving the electrode of little effect.

### 4.3 Trapping light in the glass to surpass the Yablonovitch limit

The possibility of going beyond the Yablonovitch limit of  $4n_{Si}^2$  has recently been subject to intense discussion. Some argue that periodic structures can grant better light trapping than random structures [Yu 10]; others argue that light trapping inside the TCO lowers this theoretical value to  $4(n_{Si}^2 - n_{TCO}^2)$  [Haug 11]. All these discussions focus on trapping light between an air-glass (or air-TCO) interface and the back reflector. Applying, in addition to state-of-the-art light management schemes, an anti-escape strategy at the front air-glass interface of the device is a very promising way of improving significantly light trapping in our devices. A similar concept was thought up for crystalline silicon devices in [Green 95], and referred to as “ultra light trapping” in [Ulbrich 08, Zhang 12].

#### 4.3.1 Mechanism and prior art

One way of preventing light from escaping at the glass front surface is to split this surface between a perfectly reflecting part (like flat silver, reflecting light that is in the optical system back to the silicon layers) and a transparent (unmodified) part where all incoming light will be guided, for example with lenses or microlenses as sketched in Fig. 4.11. With standard microengineering, a hexagonal array of microlenses can be obtained. If the light distribution in the device is still homogeneous (*i.e.* light is equally present in the semiconductor behind the silver-coated parts and behind the openings), the escape probability from the semiconductor is drastically reduced. This comes from a spatial filtering of the transmission through the glass - air interface, as light can escape only at the position of the openings.

This requires that light is spread again after being forced into the transparent openings, which can be done for example by placing the silicon layer far enough from the air - glass interface, as sketched in Fig. 4.11. As incoming light has to be focused through openings, this system has an acceptance angle that gets smaller when the size of the apertures is reduced. Tracking of the sun could be achieved by placing the opening-containing silver layer on the glass of the cell, and moving the lenses relative to it. Another approach is to use a cylindrical design for the lens array (and bands of silver as the reflecting part) with an angle of acceptance of  $50^\circ$ , allowing (for our latitudes) direct light to be accepted all day all year long (if properly oriented).

A similar concept was introduced in [Green 95], without any experimental validation. This type of device was also used for thin-film organic photovoltaic cells in [Tvingstedt 08], in which such a microlens array is suggested as a replacement of standard light-trapping approaches based on a rough or structured active layer. The authors obtained a 25% gain in current density compared to a flat reference with a hexagonal array of microlenses combined with a silver reflecting layer. We will demonstrate here that this concept can not only be used to replace conventional light-trapping approaches, but that it can also be used together with state-of-the-art light-trapping approaches, enabling us to enhance the light path in a solar cell way above the standard  $4n^2$  limit.

### 4.3. Trapping light in the glass to surpass the Yablonovitch limit

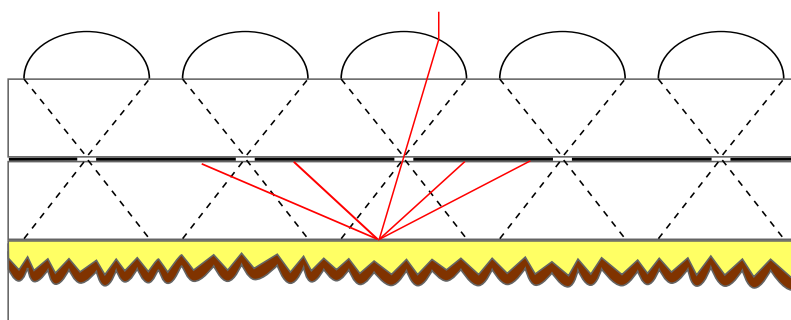


Figure 4.11: Sketch of the microlenses and solar cells.

Indeed, by placing such a microlens/silver optical system in front of the glass substrate of the cell with an air gap, light trapped in the cell has first to escape the cell's glass substrate before reaching the silver layer with openings. This means that only light in the escape cone has a chance to go through the openings in the silver, keeping the light-trapping capability of the initial device. On the other hand, if an index-matching liquid were used between both glasses, all light reaching the openings in the silver would escape through it (whatever their angle compared to the surface, as there is no more optical interface). There would therefore be no more angular filtering of escaping light through the glass-air interface (reducing the  $4n^2$  limit to  $4n^2/n_{\text{glass}}^2$  corresponding to light trapping between glass and silicon). On the contrary, by maintaining an air gap, a combination of angular and spatial filtering of escaping light is obtained.

An alternative approach to this spatial anti-escape was presented in chapter 7 of [Ulbrich 11] as “ultra light trapping”. It is based on angular filtering, preventing transmission of light of certain inclinations through the glass-air interface. We refer to this approach again at the end of subsection 4.3.4.

#### 4.3.2 Realization and characterization

The realization of the lenses was done by Toralf Scharf and Irène Philipoussis from the Applied Optics Laboratory (EPFL STI IMT-NE OPT). We designed a hexagonally packed array of 50- $\mu\text{m}$ -thick cylinders of diameter 242  $\mu\text{m}$  for a 250  $\mu\text{m}$  pitch by photo-lithography. After reflow at 80°, microlenses are formed. A stamp is prepared to replicate them in optical glue on 300- $\mu\text{m}$ -thick glass wafers. A 120-nm-thick silver layer is deposited on the other side of the glass with 100- $\mu\text{m}$ -diameter openings (obtained by lift-off after a photo-lithography step) at the focal point of the lenses. Pictures taken through an optical microscope are given in Fig. 4.12.

The resulting coverage fraction of 1) lenses on the front glass is 85%, and 2) silver on the back is 85%. This is a coincidence, as both are not interlinked. Transmittance and reflectance measurements, performed with an integrating sphere for both light directions, are given in

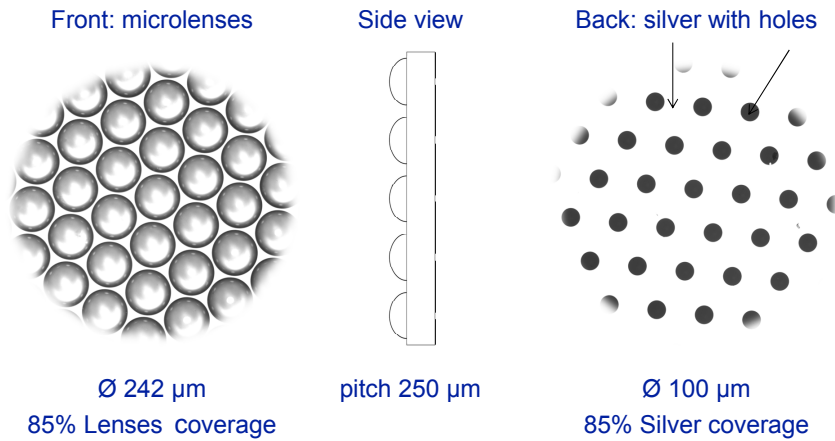


Figure 4.12: Pictures of both sides of the substrate with the microlenses optical system, with a schematic side view (not scaled).

Fig. 4.13. A reference glass substrate with only microlenses (and no silver layer) was measured also in transmission and reflection. A correction was applied to all measured values so that the corrected sum  $T + R$  without silver equals 100% (as the measured  $T + R$  was around 105% due to the strong scattering of light, the calibration made for a straight beam and the imperfection of the integrating sphere). A quite good agreement with calculation is obtained, with 79% of transmittance of light entering from the lenses side (in average between 400 nm and 1100 nm). As light crossing the system through the lenses and openings see an air-glass and glass-air interface, expected first order approximated transmittance is  $(100\% - 4\%) \cdot 85\% \cdot (100\% - 4\%) = 78\%$ , relatively close to the experiment. As the measurement is as high as the theoretical calculation, we conclude that there is no mis-alignment and that all light incident on the lenses effectively passes through the openings. Possible reasons for the higher experimental value are a slight transmittance of the silver layer (due to a too small thickness), but a possible artifact from the integrating sphere should not be excluded.

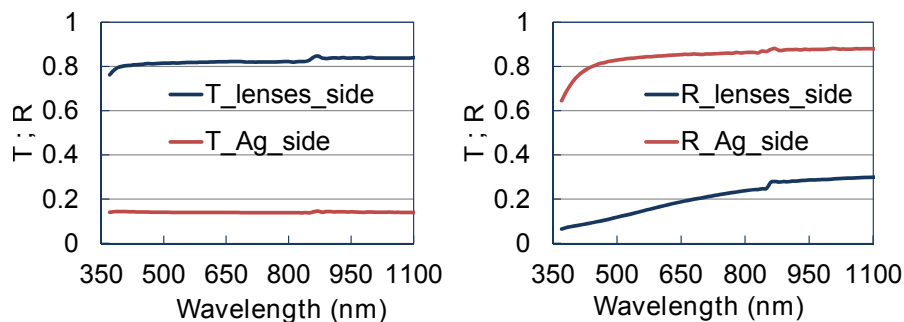


Figure 4.13: Transmittance and reflectance spectra of the microlens system for light entering the system from the lens side and from the silver side.

#### 4.3.3 Results

When placing this optical system simply in front of a solar cell, an air gap is kept between the partly silver-coated surface and the air-glass interface of the cell. We expect therefore the same transmittance as when measured with the spectrometer, leading to a reduction of the EQE on all the spectrum of about 21% according to spectrometer transmittance value. We expect however a great increase in the IR region as light hitting the silver-coated surface is reflected with more than 80% probability in the [550 nm; 1100 nm] wavelength range, reflecting more than 80% of non-absorbed light back to the cell. Fig. 4.14a presents the measured EQE of a 0.8- $\mu\text{m}$ -thick  $\mu\text{c}$ -Si:H cell deposited on a 2.5- $\mu\text{m}$ -thick lowly doped LPCVD ZnO layer (Z2.5) treated for four minutes in an argon plasma to smoothen its surface [Bailat 06], with a Z2.5 back contact, with and without the microlens/silver optical system in front. This cell incorporates an  $a$ -Si:H  $n$ -doped layer responsible for the dip around 600 nm. The estimated EQE (including the corresponding  $J_{\text{sc}}$ ) in absence of additional reflection losses due to the microlens/silver system are plotted Fig. 4.14b. This curve was obtained by stretching the measured curve by a factor  $\frac{1}{0.79}$ .

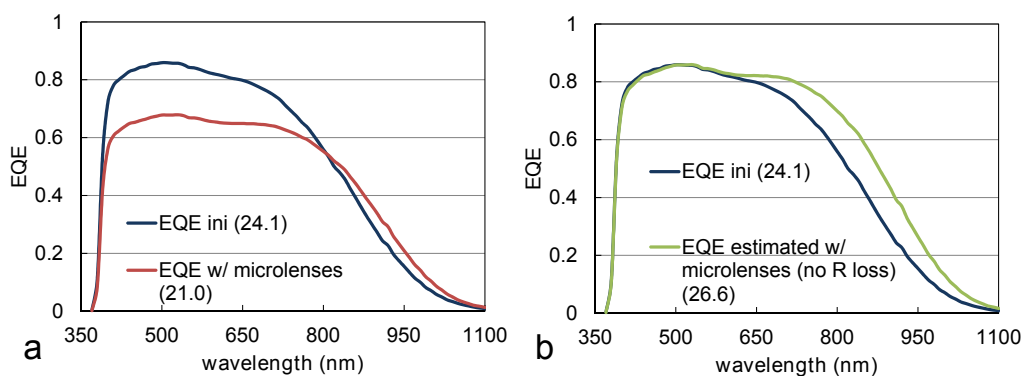


Figure 4.14: a) EQE measured for a typical 0.8- $\mu\text{m}$ -thick  $\mu\text{c}$ -Si:H cell using 2.5- $\mu\text{m}$ -thick lowly doped ZnO electrodes without (blue) or with (red) the microlens/silver system in front. b) Estimation of the same EQE curves in absence of additional reflection losses due to the microlens/silver system.

The experimental EQE with the microlens/silver system corresponds very well to the expected behavior. Note that the increased primary reflection is overcompensated by the anti-escape effect for wavelengths above 800 nm. Also, the stretched curve of Fig. 4.14b is very close to the initial EQE curve in the blue part, where no light escapes the cell, validating the absence of additional losses. In Fig. 4.15a, we reproduce the initial EQE, reflectance and  $\text{EQE}_c$  curves of the  $\mu\text{c}$ -Si:H cells with the model presented in chapter. 3. On the right, the only changes in the model parameters are an increase of primary reflection of 21% and an 81% reduction of the escaping fraction for all escaping events, which is efficient to well reproduce the measured EQE curve with microlenses.

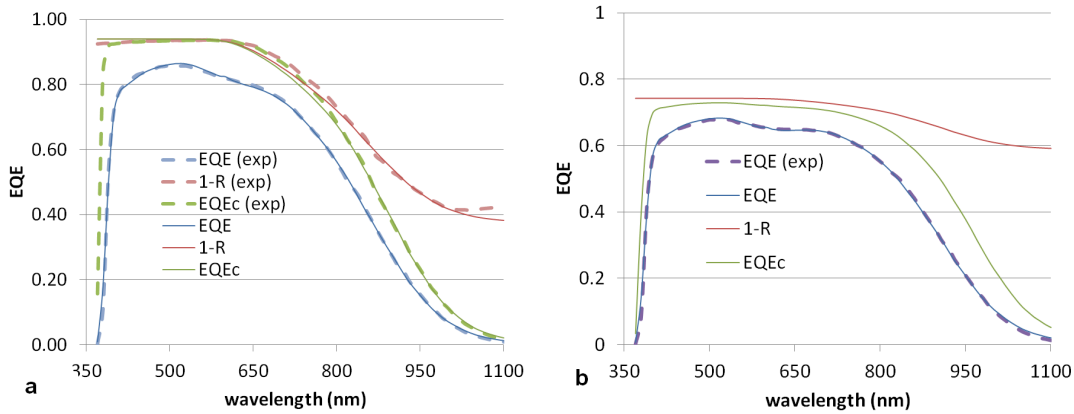


Figure 4.15: a) EQE (blue), EQE<sub>c</sub> (green) and total absorption (1 – R) (red) curves measured (dashes) or simulated (straight line) for a typical thin  $\mu c$ -Si:H cell using 2.5- $\mu\text{m}$ -thick low doped ZnO electrodes ( $J_{\text{sc}} = 24.1 \text{ mA/cm}^2$ ). b) Same for the case with microlenses in front ( $J_{\text{sc}} = 26.6 \text{ mA/cm}^2$ )

#### 4.3.4 Potential of this approach

In this part, we assume that the microlens/silver system can be made without reflection losses. This would be the case by making larger microlenses (to cover all the front surface) and by applying an anti-reflection coating on both sides.

#### Importance of parasitic absorption

We plot in Fig. 4.16a the experimental and simulated EQE, total absorption (1 – R) and EQE<sub>c</sub> of a 0.8- $\mu\text{m}$ -thick  $\mu c$ -Si:H cell deposited on a Z2.5 treated four minutes, with a Z2.5 back contact. The experimental curves are plotted in dashed lines. The EQE of the same cell with a microlens optical system in front is simulated in Fig. 4.16b (the covering fraction is set to 81%). As can be seen, most of the reflection in the infrared is suppressed and most of the light is absorbed in the cell stack. However, most of the additionally absorbed light is parasitically absorbed and only  $3 \text{ mA/cm}^2$  are gained (which is already considerable as no loss is expected in other parameters).

The same optical systems are simulated with the assumption that parasitic absorption is strongly reduced from 3% to 1% in both front and back contacts. The corresponding plots are given in Fig. 4.17a for the case without microlenses, and in Fig. 4.17b for the case with microlenses. It can be seen that reducing strongly  $A_p$  leads to a  $J_{\text{sc}}$  increase of  $1.5 \text{ mA/cm}^2$  for the simple cell, but when microlenses are implemented in front, the gain is almost doubled, emphasizing the paramount importance that  $A_p$  reduction takes when light trapping is improved.

To illustrate the impact of  $A_p$ , Fig. 4.18 presents the evolution of  $J_{\text{sc}}$  as the reflecting area



### 4.3. Trapping light in the glass to surpass the Yablonovitch limit

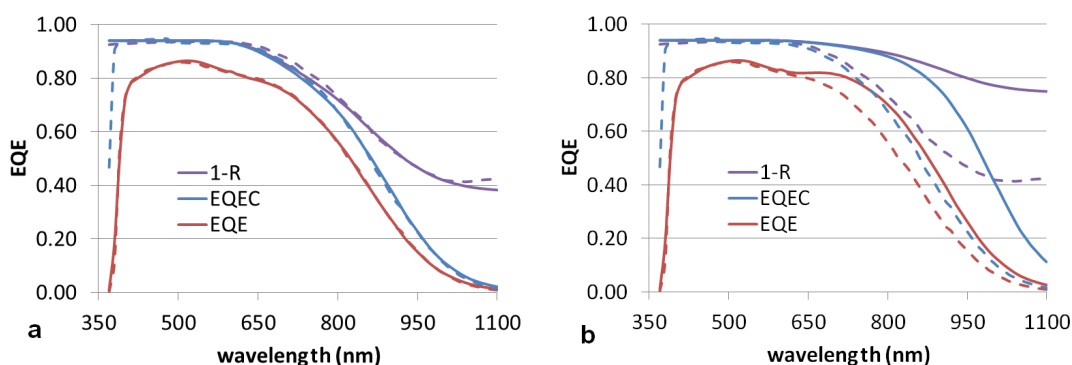


Figure 4.16: a) EQE (red),  $EQE_c$  (blue) and total absorption ( $1 - R$ ) (purple) curves measured (dashes) or simulated (straight line) for a typical thin  $\mu c$ -Si:H cell using 2.5- $\mu$ m-thick low doped ZnO electrodes ( $J_{sc} = 24.1 \text{ mA/cm}^2$ ). b) Same for the case with microlenses in front ( $J_{sc} = 26.6 \text{ mA/cm}^2$ )

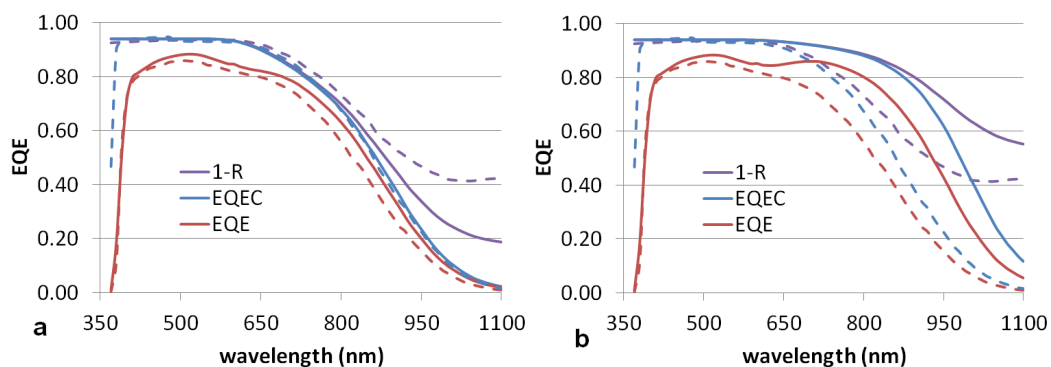


Figure 4.17: a) EQE (red),  $EQE_c$  (blue) and total absorption ( $1 - R$ ) (purple) curves of the same cell with only 1% of  $A_p$  in front and back contacts ( $J_{sc} = 25.6 \text{ mA/cm}^2$ ). b) Same for the case with microlenses in front ( $J_{sc} = 29.5 \text{ mA/cm}^2$ ).

fraction increases for various parasitic absorption values in front and back contacts ( $A_f$  and  $A_b$ ). In Fig. 4.18a, a constant spectrum (AM1.5G) is considered for all cases, so that the current variation reflects only the change in the EQE. As seen from this graph, the current increases exponentially for weakly absorbing electrodes whereas it saturates fast for strongly absorbing ones, little light being retrievable from reflection in this case as most of the lost light is parasitically absorbed.

To take into account the reduction of the acceptance angle when reducing the size of the openings (*i.e.* increasing the reflecting area fraction), Fig. 4.18b shows the same evolution of  $J_{sc}$  but with an adjusted spectrum (lying between AM1.5G and AM1.5D depending on the size of the openings, as described in the following paragraph). It can be seen from this graph that the weak EQE gain achieved when parasitic absorption is strong cannot compensate for the

## Chapter 4. The interconnection between parasitic absorption and light trapping

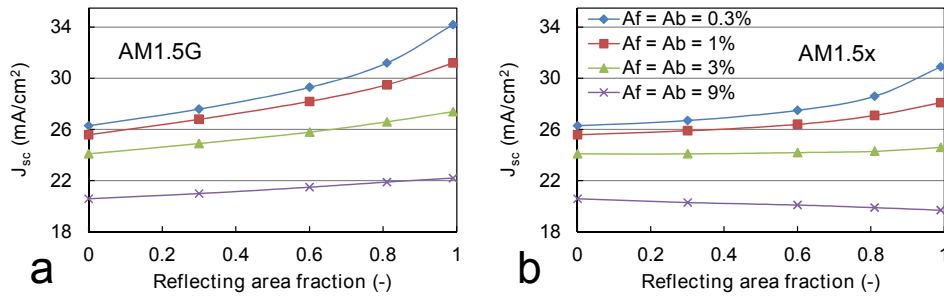


Figure 4.18: Evolution of  $J_{sc}$  as the reflecting area fraction increases for various parasitic absorption values in front and back contacts ( $A_f$  and  $A_b$ ), when using AM1.5G spectrum for all cases, or an intermediate spectrum (AM1.5x) between AM1.5G and AM1.5D adjusted to correspond to the acceptance angle.

decrease in irradiance when reducing the size of the openings. For standard electrodes ( $A_f = A_b = 3\%$ ), both effects compensate whereas a significant 17%  $J_{sc}$  gain is achievable for very transparent electrodes ( $A_f = A_b = 0.3\%$ ).

Very transparent electrodes are therefore mandatory to convert an improvement of light trapping into a gain in current density. In real devices,  $A_p$  can be greatly reduced by replacing standard TCOs, designed to provide enough conduction by themselves, by a very transparent TCO (such as < 100-nm-thick  $\text{In}_2\text{O}_3\text{:H}$ ) seconded by a metallic grid (reflecting some light thus inducing shadowing losses). Since most of the light that entered the cell's glass substrate cannot escape the optical system, the shadowing losses should not be detrimental.

### Geometrical aspects

To allow an anti-escape effect, *i.e.* a selection of the rays of light escaping the device, a selection of the rays of light incoming the device had to be made as well (as, in equilibrium in a thermal bath, as many photons have to enter and to escape). This selection is made amongst the inclination of the incoming light, through the size of the apertures in the focal plane of the lenses.

The spectrum of incident light is therefore modified from AM1.5G, for an infinite size of the apertures (*i.e.* no reflecting layer and no anti-escape effect) to AM1.5D, for the minimal size of the apertures corresponding to a cone of acceptance equal to the cone of vision of the whole sun, of angular diameter 9.6 mrad. A theoretical limit of anti-escape effect can be derived identically to the limit of maximum concentration, the maximal anti-escape effect being thus a reduction by a factor  $1/46200$  [Würfel 00]. For a more realistic limit, the surface of the openings for an angular diameter of acceptance of 9.6 mrad must be  $\pi \cdot (f \times \sin(9.6 \cdot 10^{-3})/2)^2 = 8 \cdot 10^{-5} \cdot f^2$ , with  $f$  the focal distance of the lenses. Assuming a focal distance equal to the pitch of the array (similar to the diameter of the lenses), the covering fraction ( $A$ ) of the apertures, for a

### 4.3. Trapping light in the glass to surpass the Yablonovitch limit

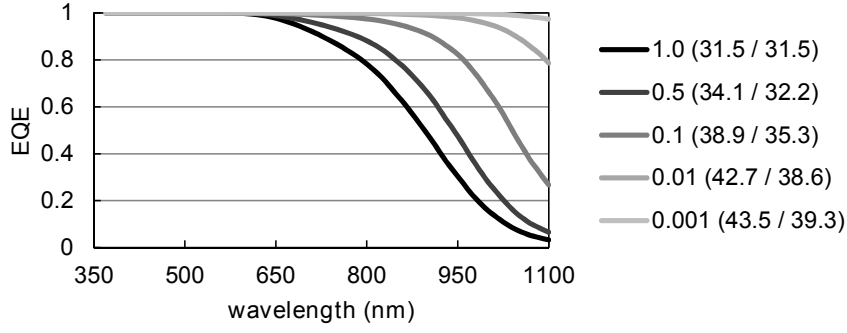


Figure 4.19: Simulation of the evolution of the EQE of a  $\mu c$ -Si:H cell including standard light trapping but with no parasitic absorption or reflection losses when changing the covering fraction of the apertures from 1 to 0.001. The numbers in parenthesis are the  $J_{sc}$  values in  $\text{mA}/\text{cm}^2$  corresponding to the EQE spectra, for the AM1.5G spectrum, or an intermediate spectrum (AM1.5x) between AM1.5G and AM1.5D adjusted to correspond to the acceptance angle.

hexagonal array, is then equal to :

$$A = \frac{8 \cdot 10^{-5} \cdot f^2}{\sin(\pi/3) \cdot f^2} \approx 1 \cdot 10^{-4}. \quad (4.1)$$

In addition to the technological challenge to reach the required precision, the diameter of the openings would be  $5 \mu\text{m}$  for a  $250 \mu\text{m}$  pitch, for which geometric optics might no longer be enough to analyze this system. This calculation shows however that escape from the cell can technologically be reduced by a factor of 1000, which would enable the  $4n^2$  limit in the weak absorption region to be changed to  $1000 \cdot 4n^2$ . For a  $1\text{-}\mu\text{m}$ -thick  $\mu c$ -Si:H cell, in the absence of parasitic absorption and primary reflection, the change in the EQE curve obtained when reducing the covering fraction of the apertures from 1 (no anti-escape) to 0.001 (99.9% of light is reflected back) is shown in Fig. 4.19. The evolution of the current density can be seen in the legend of Fig. 4.19. Whereas the first number takes only the EQE change into account (the spectrum is kept unchanged, being AM1.5G for all cases), the progressive reduction of acceptance angle is taken into account for the second number. A progressive change from AM1.5G to AM1.5D is made, assuming that the diffuse radiation is homogeneously distributed. The spectrum corresponding to a reduction of escaping light by a factor  $x$  is therefore approximated by  $1/x \cdot \text{AM1.5G} + (1 - 1/x) \cdot \text{AM1.5D}$ , being very close to AM1.5D for large anti-escape factors, but equal to AM1.5G for no anti-escape.

Note that a similar study was performed in chapter 7 of [Ulbrich 11], with an angular filter to prevent light of higher inclination than a threshold value from crossing the air-glass interface (in both senses). She further suggests to apply a selection amongst energy of light, to apply this angular filtering only to light of lower energy than a threshold value ( $E_{th}$ ). No anti-escape is therefore applied on light of energy higher than  $E_{th}$ , but no restriction of the acceptance

## Chapter 4. The interconnection between parasitic absorption and light trapping

---

angle apply for this part of light.

With perfect tracking, Ulbrich mentions that an increase of the annual energy yield can be obtained for all cell thicknesses (when considering idealized crystalline silicon device having a perfectly reflecting back reflector), with up to 32.5% of gain with 1- $\mu\text{m}$ -thick cells. However, in the absence of tracking, the loss in the acceptance angle cannot be compensated by the improved light trapping, and no annual energy yield is observed (except for a 1% improvement in a narrow range of  $E < E_{th}$  and  $\theta_{th}$  for 1  $\mu\text{m}$ -thick cells).

An interesting combination of both approaches for non-tracked systems would be to combine cylindrical microlenses with an energy-selective reflecting layer (instead of the silver layer). If both are well designed, all direct light can be accepted all day long and all year long, and most of the diffuse light is accepted for all angles.

### 4.3.5 Conclusion

We used in this section a microlens array combined to a silver layer with apertures to provide geometrical light trapping that can be combined with standard approaches based on a rough interface between the electrode and the photoactive layer. We used this tool to emphasize the enhanced importance of reducing parasitic absorption when light trapping is improved. This strategy applies only for direct light, making this approach hardly industrial for thin-film silicon. Nevertheless, an interesting point for light trapping is that it can lead to two types of improvement: for thin films, mostly a gain in terms of current is observed, but, for wafer-based technology, light trapping mostly makes possible the use of thinner wafers without current loss. This translates into  $V_{oc}$  increase thanks to the higher injection level [Tiedje 84], shifting the maximal efficiency *c*-Si:H cell to thinner wafers. Thus, microlenses might efficiently be used in heterojunction solar cells, where excellent passivation can be exploited and thickness reduced to around ten microns, leading to  $> 800$  mV  $V_{oc}$ , for cells maintaining a  $J_{sc}$  of over  $40 \text{ mA/cm}^2$ . This corresponds to an efficiency boost similar to the one obtained with concentration, but without changing the power density that typically requires advanced heat management.

## 4.4 Conclusion

We demonstrated in this section the strong interdependence of parameters involved in light management in thin-film silicon solar cells. In particular, significant improvement in terms of light trapping can be obtained only if both light trapping and parasitic absorption are improved. Also, parasitic absorption in both contacts is equally detrimental for the EQE in the infrared. Parasitic absorption could be identified as the biggest limitation currently faced, since, in the region where silicon is weakly absorbing, standard TCOs have a higher absorptance than the photoactive layer. Also, a microlens array combined with a reflecting layer with an array of apertures was shown to efficiently prevent light from escaping the cell, but enable direct light to enter the cell. With this optical tool, we demonstrated a significant

potential gain in EQE, both in the weak absorption region and in the intermediate absorption region (700 nm to 900 nm range) which is of greater interest as seen in chapter 3. Modeling was performed for all experimental data, and a correct reproduction of all trends was observed. It could finally be shown by simulation that the gains obtained by further improving light trapping for existing state-of-the-art devices depends strongly on parasitic absorption. In order to benefit from advanced light-trapping schemes in terms of EQE, and not only in terms of total absorption, parasitic absorption must be drastically lowered (at least by one order of magnitude), or light must be trapped in silicon only, to avoid parasitic absorption from the electrodes for each round trip. This might be possible with a device architecture with a low roughness to enable waveguides and a back reflector structure enabling scattering of all light at large angles (above the critical angle for total internal reflection between the front electrode and silicon, typically  $\theta_c = \arcsin(2/4) = 30^\circ$ ). Yet, parasitic absorption in doped layers might at some point become limiting, as FCA was also shown to be significant in doped layers [Battaglia 11b], requiring the use of alloys such as silicon oxide or silicon carbide from the point of view of optics.



## 5 Towards optimal textured electrodes for Micromorph devices

In this chapter, the requirements of textured electrodes for high-efficiency Micromorph devices are detailed, main results being published in [Boccard 12b]. It is shown that high currents and high efficiencies can be achieved in Micromorph devices with thin cells by combining both a robust cell design and efficient light management schemes. In this chapter, three key requirements for the TCO electrodes are identified. Firstly, strong light scattering into large angles is needed within the entire useful wavelength range: a front electrode texture with large enough features is shown to grant a high total current (typically  $> 26 \text{ mA/cm}^2$  with a  $2.4\text{-}\mu\text{m}$ -thick absorber material) while sharp features are reported to allow for high top cell current ( $> 13 \text{ mA/cm}^2$ ) and reduced reflection at the ZnO-silicon interface. Secondly, sufficiently smooth substrate features are needed to guarantee a high quality of the silicon active material, ensuring good and stable electrical properties (typically  $V_{oc}$  around  $1.4 \text{ V}$ ). Thirdly, conduction and transparency of electrodes must be cleverly balanced, requiring high TCO mobility ( $> 50 \text{ cm}^2/\text{V/s}$ ) to maintain the sheet resistance below  $30 \Omega/\square$  while keeping absorption as low as possible.

### 5.1 Experimental details

ZnO front electrodes are grown on glass by LPCVD from diethyl zinc and water vapor precursors. Diborane can be added in order to adjust the  $n$ -type doping. Non-intentionally doped (n-i-d) material (*i.e.* with no boron adjunction) still exhibits a strong  $n$ -type doping with carrier density values above  $10^{19} \text{ cm}^{-3}$ . When growing under particular conditions, small polycrystalline grains form and enlarge as growth is continued. This results in pyramidal surface features with typical sizes scaling with the layer thickness (Fig. 5.1) [Nicolay 09, Faÿ 06, Steinhauser 07].

A plasma surface treatment of argon can be applied before deposition of the silicon layers. A short treatment (typically one minute) only cleans the surface whereas longer treatments smoothen its morphology: sharp V-shaped valleys surrounding ZnO pyramids are changed into U-shaped valleys [Bailat 06]. As will be seen in the following, this treatment influences

both optical and electrical properties of the device, since the morphology of the textured front electrode influences both the scattering of the light [Domine 10, Sai 10, Calnan 08, Poruba 00] and the growth of the subsequent silicon layers [Sakai 90, Python 09, Nasuno 01, Li 09].

The Micromorph cells are deposited by PECVD from a  $\text{SiH}_4/\text{H}_2$  gas mixture for intrinsic layers. *p*- and *n*- type doping are respectively achieved by adding  $\text{B}(\text{CH}_3)_3$  and  $\text{PH}_3$ . A small area research reactor as well as small and medium size versions of industrial KAI reactors were employed in this study. An in-situ grown SOIR [Buehlmann 07] is used, as well as other  $\text{SiO}_x$ -doped layers [Despeisse 11, Cuony 10], produced by adding  $\text{CO}_2$  to the gas mixture. The back contact is made of lightly doped LPCVD ZnO with carrier density around  $4 \cdot 10^{19} \text{ cm}^{-3}$ , and a white dielectric is used as the back reflector. Standard  $J(V)$  measurements are performed using a dual-lamp solar simulator. Top and bottom cell currents are calculated from external quantum efficiency (EQE) measurements. Reflection, total transmission and diffuse transmission measurements are performed with a spectrophotometer comprising an integrating sphere.

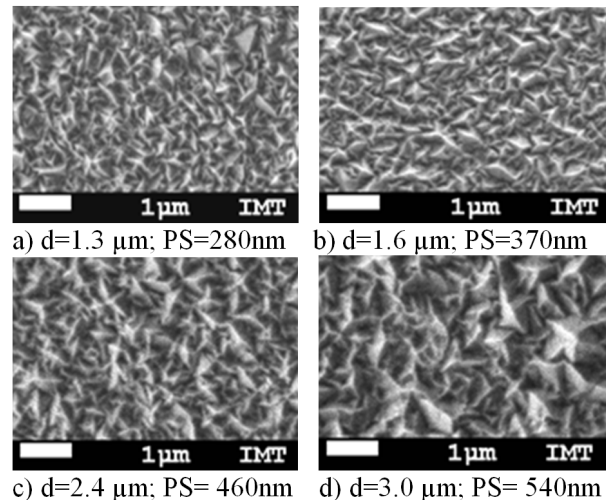


Figure 5.1: SEM top view of four LPCVD ZnO layers with different thicknesses ( $d$ ) and estimated characteristic pyramid sizes ( $\text{PS}$ ).

### 5.2 Influence of the texture feature size

Commonly, the ratio of diffused to total transmitted light (haze) is used to quantify the light-scattering capability of a rough electrode [Calnan 08, Krč 10, Zeman 08]. Based on a theoretical model [Domine 10], we showed in chapter 4 that the light-scattering capability in silicon of a rough surface at a given wavelength can be well correlated with the haze value measured for scattering in air, but at half the wavelength. Thus, the haze value measured in air at 540 nm is chosen as a quantitative measure for light scattering into silicon at long wavelengths (roughly 1080 nm), similarly to [Krč 03]. It should be noted that the size of the surface features obtained for a given thickness depends strongly on the deposition conditions and in particular on



## 5.2. Influence of the texture feature size

Table 5.1: Micromorph cell parameters for four different front ZnO electrode thicknesses. Typical characteristics of the surface of the TCO layers are indicated in the last three rows (taken from chapter 3 of [Cuony 11]).

	Z1 (1.3 $\mu\text{m}$ )	Z2 (2 $\mu\text{m}$ )	Z3 (3 $\mu\text{m}$ )	Z5 (5 $\mu\text{m}$ )
Haze at 540nm	0.15	0.40	0.93	0.98
$J_{sc}$ ( $\lambda > 800$ nm) ( $\text{mA}/\text{cm}^2$ )	2.67	2.88	3.53	3.24
$J_{sc,c.}$ ( $\lambda > 800$ nm) (no $A_P$ )	(4.22)	(5.03)	(5.46)	(5.46)
$J_{sc}^{top}$ ( $\text{mA}/\text{cm}^2$ )	10.7	11.1	10.8	10.2
$J_{sc,c.}^{top}$ (no $A_P$ )	(12.1)	(12.6)	(12.1)	(11.6)
$V_{oc}$ (V)	1.37	1.34	1.26	1.24
$V_{oc}$ (V) without SiO	1.32	1.24	1.21	1.20
RMS roughness (nm)	40	100	140	200
peak-to-peak height (nm)	300	700	1000	1400
Median inclination ( $^\circ$ )	30	40	43	45

doping [Fay 06]. The thickness of the layer is thus only a relative probe of the features size and thus of light-scattering potential.

Tab. 5.1 shows a series of Micromorph cells grown on 1.3- $\mu\text{m}$ - to 5- $\mu\text{m}$ -thick LPCVD ZnO front electrodes (referred to as Z1 to Z5). The light-scattering capability of these TCO layers is enhanced for thicker electrodes, as assessed by the haze value at 540 nm shown in the first row. The light-trapping performance for long wavelengths is evaluated by calculating from the spectral response the short-circuit current densities created by the photons with a wavelength larger than 800 nm (Tab. 5.1, second row). For all cells, not only current density values are indicated in Tab. 5.1, but also corrected current densities that would be obtained in the case of no parasitic absorption ( $A_P$ ) in the device. These values are deduced from corrected EQE ( $\text{EQE}_c$ ) curves calculated from the cell EQE and reflection measurements ( $\text{EQE}_c = \text{EQE}/(\text{EQE}+R)$ ), as detailed in chapter 4 and in [Dominé 09]. The  $\text{EQE}_c$  allows for a more precise quantitative comparison of light-trapping efficiency between the morphologies, as the varying front electrode absorptions do not contribute to  $\text{EQE}_c$ . A current gain in the long wavelengths range is observed when thicker ZnO layers are used (see Tab. 5.1); but no significant current gain is observable between 3  $\mu\text{m}$  and 5- $\mu\text{m}$ -thick films, in agreement with the almost identical haze value at 540 nm recorded for both layers.

The short-circuit current density values indicated are calculated from EQE measurements, and the current densities evaluated in an idealized case with all parasitic absorption suppressed are indicated in the same cells but in brackets. The last two rows indicate open circuit voltages of two sets of cells with different doped layers, one employing SiOx-doped layers and the other standard doped layers (without SiO). The low top cell currents are due to the small thickness of the intrinsic  $a$ -Si:H layer (180 nm).

The top cell current (Tab. 5.1, row 4) exhibits a maximum for a 2- $\mu\text{m}$ -thick front ZnO, then decreases for thicker films. The gain between 1- $\mu\text{m}$ - and 2- $\mu\text{m}$ -thick ZnO layers comes from a

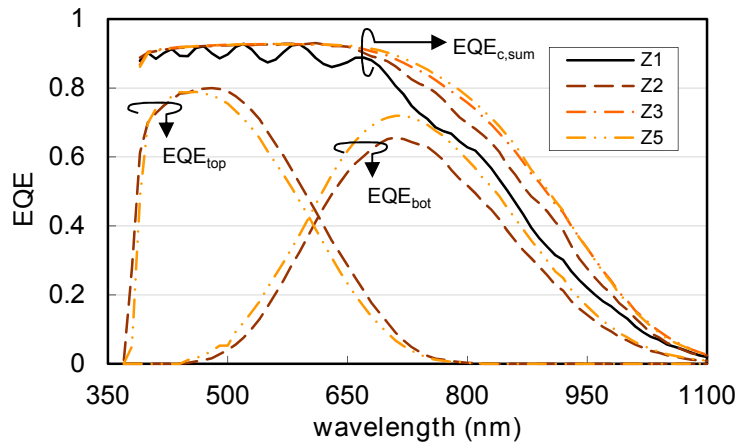


Figure 5.2: EQE curves of the top and bottom cells of Micromorph cells deposited on Z2 and Z5, and corrected summed EQE (simulating no parasitic absorption) of Micromorph cells deposited on 1.3- $\mu\text{m}$ - to 5- $\mu\text{m}$ -thick ZnO electrodes (Z1 to Z5).

reduced reflection at the ZnO-silicon interface and achievement of sufficient light scattering for the whole wavelength range of absorption of  $a\text{-Si:H}$ : this is indicated by the disappearing of ripples in  $\text{EQE}_{c,\text{sum}}$ , as shown in Fig. 5.2. The subsequent loss for electrodes thicker than 2  $\mu\text{m}$  can be attributed to a reduced efficiency of the IRL because of the large roughness [Dominé 06]. It is also possible that the very large features of ZnO layers thicker than 3  $\mu\text{m}$  are intrinsically less efficient for light in-coupling in the thin  $a\text{-Si:H}$  top cell. In conclusion, an optimal ZnO front electrode should have a high haze value at 540 nm for a large summed current, while small feature sizes are shown to provide large top cell current through efficient light in-coupling and interplay with the IRL. Tab. 5.1 also shows the open circuit voltages ( $V_{\text{oc}}$ ) of the same cells, both for cells implementing SiOx-doped layers and for cells implementing standard  $\mu\text{c-Si:H}$ -doped layers. The use of SiOx-doped layers improves  $V_{\text{oc}}$  values on all substrates; but a dramatic  $V_{\text{oc}}$  loss occurs in both cases when the roughness of the ZnO layer is increased. Yet, silicon oxide doped layers allow a significant reduction of the  $V_{\text{oc}}$  gap between 1.3- $\mu\text{m}$ - and 2- $\mu\text{m}$ -thick ZnO substrates with only 30 mV difference, therefore allowing for a better resilience of the cell design to the substrate texture [Despeisse 11, Cuony 10]. Still, in the case of large and inclined pyramidal features (such as Z3 or Z5), the low  $V_{\text{oc}}$  compared to the small features shows that cell design alone is not sufficient to ensure good electrical quality for Micromorph devices. As-grown rough LPCVD ZnO layers with large features enabling a haze in air at 540 nm close to one are thus less suitable for targeting Micromorph devices with high electrical quality than layers with smaller features.

### 5.3 Plasma surface-treatment effects

A plasma surface treatment was introduced to smoothen the large and sharp features of as-grown LPCVD ZnO, allowing for the growth of high-quality  $\mu\text{c-Si:H}$  single-junction cells [Bailat 06]. In this case,  $V_{\text{oc}}$  and  $FF$  were greatly improved by applying a long plasma treatment

Table 5.2: Micromorph cell parameters for various ZnO substrates plasma post-treatments (PT)

	1.5 $\mu\text{m}$ no PT	3 $\mu\text{m}$ 5 min PT	3 $\mu\text{m}$ 10 min PT	3 $\mu\text{m}$ 20 min PT
Haze at 540 nm	0.32	0.83	0.70	0.62
$V_{oc}$ (V)	1.33	1.28	1.30	1.33
$FF$ (%)	70	68	69	70
$J_{sc,top}$ (mA/cm <sup>2</sup> )	13.0	12.7	12.2	11.9
$J_{sc,bot}$ (mA/cm <sup>2</sup> )	11.6	12.5	12.6	12.9
$J_{sc,sum}$ (mA/cm <sup>2</sup> )	24.6	25.2	24.8	24.8

of typically one hour at the cost of a moderate  $J_{sc}$  loss. The improved cell quality was correlated with a reduction of the density of porous defective areas induced by non-adapted growth surface acting as low-quality diodes (high  $J_0$ ) in the intrinsic  $\mu c$ -Si:H film [Sakai 90, Python 09]. Tab. 5.2 compares Micromorph cells grown on a 1.5- $\mu\text{m}$ -thick ZnO layer (reference sample) with cells grown on a 3- $\mu\text{m}$ -thick ZnO layer on which plasma treatments of different durations were applied. The haze at 540 nm in air is again indicated in the first row. The second row shows the  $V_{oc}$  gain due to increasing plasma treatment duration. The changes in  $FF$  for these cells are affected by the changing current matching conditions and will not be discussed here. Interestingly, a sufficiently long plasma treatment (here 20 minutes) allows full recovery of the  $V_{oc}$  to the value obtained on the thin substrate.

However, the fourth row shows that this plasma treatment also lowers the top cell current density. This loss is partly compensated by an increase in bottom cell current density as shown in the last row. The corresponding EQE for top and bottom cells are plotted in Fig. 5.3 as well as one minus the reflectance (1-R) of the cells, which represents the light that is absorbed. The top cell current loss can be separated in two spectral parts. A first absolute loss principally originating from the short wavelengths range (up to 600 nm). As reflection is very little modified, it is attributed to a stronger absorption in the  $p$ -layer of the top cell or possibly in the TCO in the case light is diffusively reflected at the TCO-silicon interface, and trapped in the TCO. This comes from the smoothening of the substrate by the plasma treatment. A second loss is due to a modification of the share between top and bottom cell EQE (650 nm - 750 nm) and is compensated by an equivalent bottom cell EQE gain. This weakening of the light coupling in the top cell by the IRL is attributed to the rounding of the valleys between ZnO pyramids. This smoothening of the surface morphology is well correlated with the narrowing of the ARS of light by the rough ZnO surface as measured in air with a green laser (insert in Fig. 5.3). This is in agreement with [Domine 08, Dominé 09] in which it was suggested that a broad ARS (although it is a far-field measurement in air several centimeters from the optical interface) is a good indicator of a strong light-coupling in the top cell by the IRL (even though such effects take place in the first hundreds of nanometers after the interface).

The plasma treatment is thus shown to be efficient to improve the electrical quality of Micro-

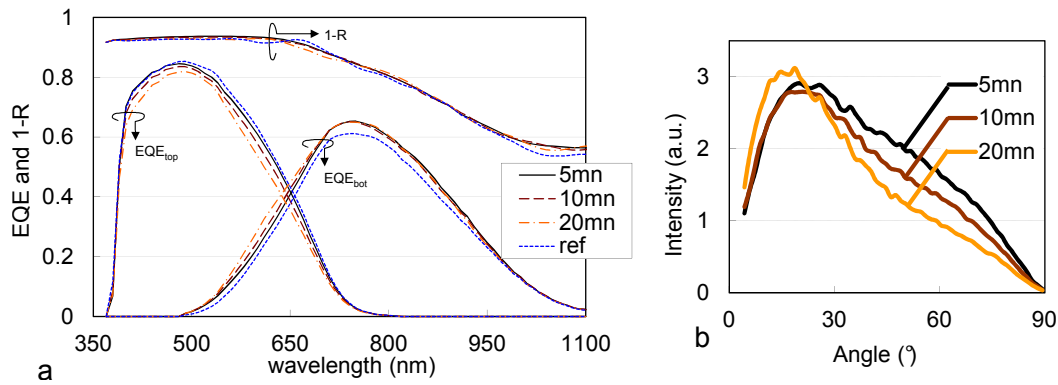


Figure 5.3: a) EQE curves of the top and bottom cells of Micromorph devices grown on 3- $\mu\text{m}$ -thick ZnO substrates on which a 5-minute to 20-minute plasma treatment was applied. Total absorbance (1-R) is also plotted. Blue dotted curve shows the same curves for the reference device deposited on a 1.5- $\mu\text{m}$ -thick substrate. b) ARS of the substrates used in a), showing the effect of the treatment time.

morph cells but decreases the top cell current, so that its implementation requires the use of a thicker IRL or *a*-Si:H absorber layer to maintain similar current levels.

#### 5.4 Transparency - conduction trade-off for the front electrode

The optimal TCO sheet resistance ( $R_{sq}$ ) value for use as front electrode is still controversial; low resistance typically degrades the transparency, because of enhanced FCA [Boccard 10b, Berginski 07], but simultaneously reduces resistive losses in the cell ( $FF$  improvement) [Battaglia 11c]. The optimization of this trade-off in a tandem junction is particularly delicate as FCA impacts mostly the infrared spectral range. The bottom cell current is therefore mainly affected, resulting in a change of spectral matching of the device, in turn modifying the  $FF$  [Nakajima 04, Ulbrich 11]. This effect is illustrated in Fig. 5.4 by measuring a Micromorph device under tuned blue-rich to red-rich spectra, obtained by slightly modifying the AM1.5G spectrum of the solar simulator. The total current of top and bottom cell is kept constant along the spectral shift by simultaneously attenuating blue light and increasing red light. A strong bottom current limitation is generally favorable to the  $FF$ , as can be seen in Fig. 5.4.

Decreasing the  $R_{sq}$  of a TCO can thus improve the  $FF$  via series resistance reduction but also through enhanced bottom cell current limitation. To separate these effects, Fig. 5.5 compares three Micromorph cells having only their front electrode sheet resistance varied. The morphology of all three substrates is kept identical. The first one, having the lowest sheet resistance of  $6\Omega/\square$  is a 2- $\mu\text{m}$ -thick doped layer and the last one with  $31\Omega/\square$  is a 1.6- $\mu\text{m}$ -thick n-i-d layer. The intermediate one uses a 2- $\mu\text{m}$ -thick n-i-d LPCVD ZnO layer that is chemo-mechanically polished as bulk. After the deposition of an ultra-thin silicon-based inter-layer to interrupt ZnO epitaxial growth, the polished bulk is topped with a 1.6- $\mu\text{m}$ -thick n-i-d LPCVD ZnO layer, as shown in Fig. 5.6. Such a thick stack is an efficient way to lower the

## 5.4. Transparency - conduction trade-off for the front electrode

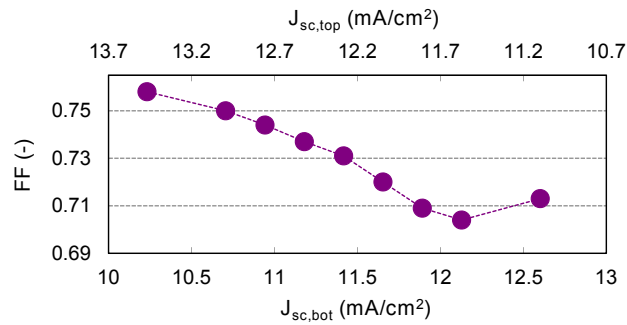


Figure 5.4: Fill factor of a typical bottom-limited Micromorph cell as a function of the illumination spectrum when altering the AM1.5G spectrum from blue-rich to red-rich. An average 1.7% of  $FF$  gain for 1 mA/cm<sup>2</sup> of mismatch is observed.

sheet resistance instead of doping, while keeping a similar morphology, resulting in a very moderate FCA increase. This is assessed in Fig. 5.5 by the strong bottom cell current gain between 6  $\Omega/\square$  and 20  $\Omega/\square$  and the very small one between 20  $\Omega/\square$  and 31  $\Omega/\square$ .

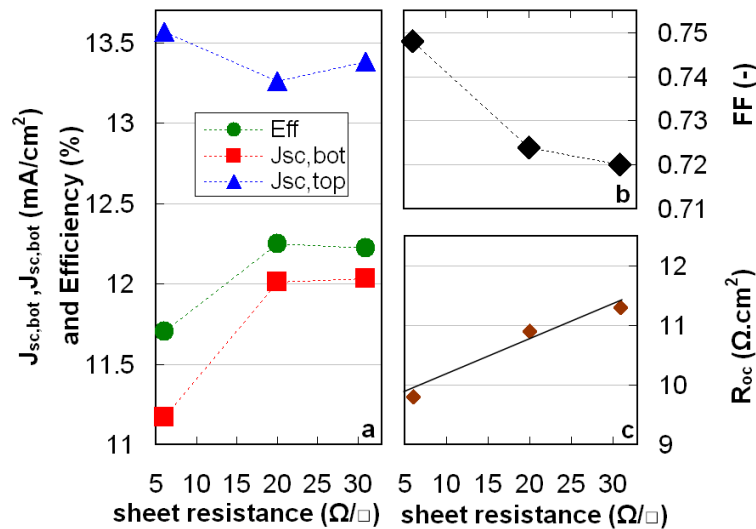


Figure 5.5: a)  $J_{sc,top}$ ,  $J_{sc,bottom}$  and efficiency for three 1 cm<sup>2</sup> Micromorph cells as a function of their front electrode  $R_{sq}$ . b)  $FF$  drop for the same cells when increasing the front electrode  $R_{sq}$ . This  $FF$  loss comes from series resistance increase but also to a great extent from current matching improvement (illustrated in a). c) Open-circuit resistance of these cells as a function of the front electrode  $R_{sq}$ . The line is a linear fit.

In Fig. 5.5b, a much stronger  $FF$  decrease is observable between the two first points than between the two last ones. As the sheet resistance gap is comparable in both cases, such a drop is unlikely to come only from series resistance increase. The open-circuit resistance ( $R_{oc}$ ) of these Micromorph cells is plotted in Fig. 5.5c, and can be linearly fitted to  $R_{sq}$  for our cell

geometry (Equation 5.1):

$$R_{oc} = 9.8 + 0.059 \cdot R_{sq}. \quad (5.1)$$

The relatively high offset value of  $9.8 \Omega \cdot \text{cm}^2$  indicates the presence of undesired resistive losses coming from silicon layers or back contact (having a  $R_{sq}$  of  $15 \Omega/\square$ ) in addition to the recombination losses. The impedance of our cell at the maximum power point being around  $100 \Omega \cdot \text{cm}^2$  (corresponding to  $1100 \text{ mV}/11.0 \text{ mA}/\text{cm}^2$ ),  $1 \Omega \cdot \text{cm}^2$  of  $R_{oc}$  increase represents 1% of relative power loss. The  $1.1 \Omega \cdot \text{cm}^2$  rise between the first two points corresponds thus to around 1.1% relative power loss. By considering that only the  $FF$  is affected, this corresponds thus to less than 0.9% absolute  $FF$  loss. This indicates that within the 2.5%  $FF$  loss, 1.6% is most probably due to current matching modification. The mismatch being reduced by  $1.1 \text{ mA}/\text{cm}^2$ , Fig. 5.4 roughly suggests a  $FF$  loss of 1.9%, validating the previous calculation. Similar calculations made for the substrates having  $20 \Omega/\square$  and  $31 \Omega/\square$  give also a consistent result with around 0.1%  $FF$  increase due to matching modification overcompensated by 0.3% loss coming from series resistance.

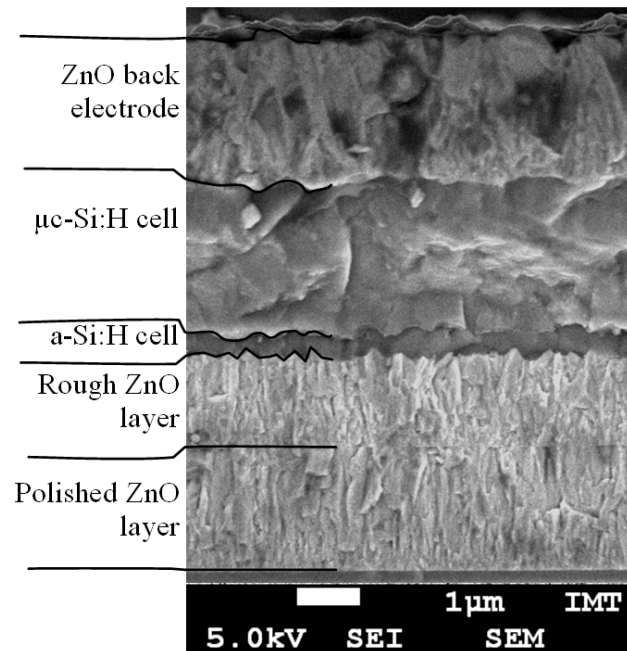


Figure 5.6: SEM cross section of a Micromorph cell where the LPCVD ZnO front electrode is made of a polished 2- $\mu\text{m}$ -thick layer covered by a 1.6- $\mu\text{m}$ -thick one.

Note that it is also possible to calculate the relative power losses due to series resistance using equation 5.2 suggested in [Hanak 79], from cell width ( $w$ ), maximum power point current

density ( $J_{MPP}$ ) and voltage ( $V_{MPP}$ ):

$$\frac{\Delta P}{P} = \frac{w \cdot J_{MPP} \cdot R_{sq}}{3 \cdot V_{MPP}}. \quad (5.2)$$

As one contact is taken in the middle of the back contact, and the other one on each side of our  $1 \text{ cm}^2$  cell ( $8 \text{ mm} \times 12.5 \text{ mm}$ ), our cell geometry corresponds to a 4.5 mm segment width in a module configuration. Maximum power point voltage and current are around 1100 mV and  $11.0 \text{ mA/cm}^2$ , so that a  $14 \Omega/\square$  sheet resistance increase results in a 0.95% relative power loss in good agreement with the previous calculations. Finally, this experiment validates the use of front electrodes having sheet resistance values up to  $30 \Omega/\square$  for Micromorph cells with a segment width of 4.5 mm. Also, the losses in the bottom cell current due to the use of a homogeneously doped electrode are clearly seen, and its replacement by n-i-d ZnO results in a significant efficiency gain.

### 5.5 Optimal feature size investigation

Fig. 5.7 compares the performances of Micromorph cells (top and bottom cells thicknesses are respectively 250 nm and  $2.4 \mu\text{m}$ , and a 70 nm-thick SOIR is used) combining all the aspects previously studied. They are grown on n-i-d ZnO electrodes with enlarging surface features as shown in Fig. 5.1, resulting in increasing haze values (Fig. 5.7a). The total ZnO thickness is kept constant at  $3 \mu\text{m}$  for all by stacking a naturally rough layer on top of a polished bulk as illustrated in Fig. 5.6. Similar sheet resistance values (around  $20 \Omega/\square$ ) are obtained for all for a moderate absorptance. The thicknesses of the top covering rough layers are  $1.3 \mu\text{m}$ ,  $1.6 \mu\text{m}$ ,  $2.4 \mu\text{m}$  and  $3.0 \mu\text{m}$  and a plasma surface treatment is applied on their surface. Its duration is adapted to the surface feature size of the layers (1 min, 2 min, 4 min, and 7 min respectively) to keep good-quality cell growth on all the substrates without degrading excessively the top cell current. This results in a high and similar  $V_{oc}$  above 1.4 V (Fig. 5.7b) for all cells and high  $J_{sc,top}$  above  $13 \text{ mA/cm}^2$  for all substrates, with only a very slight loss for the thickest layers ( $0.3 \text{ mA/cm}^2$ ) attributed to a narrowing of the ARS for short wavelengths (Fig. 5.8a).

Yet, for larger wavelengths, even though the angle of maximum scattering decreases slightly when enlarging the features (dashed arrow in Fig. 5.8b), the intensity of light scattered at large angles (*e.g.*  $> 45^\circ$ ) still increases. This improved light management directly results in a  $J_{sc,bottom}$  increase (Fig. 5.7c) accompanied by a strong efficiency gain. The latter is moderated by a significant *FF* loss from 73% to 70%, mostly due to improved current matching: with  $1.7 \text{ mA/cm}^2$  mismatch reduction, the expected *FF* loss is around 2.9% as deduced from Fig. 5.4. The highest efficiency of the series of 13.0% is finally obtained on the substrate having the largest features, providing a strong bottom cell current. This could be achieved thanks to an adapted treatment time allowing excellent quality cell growth and still a high top cell current.

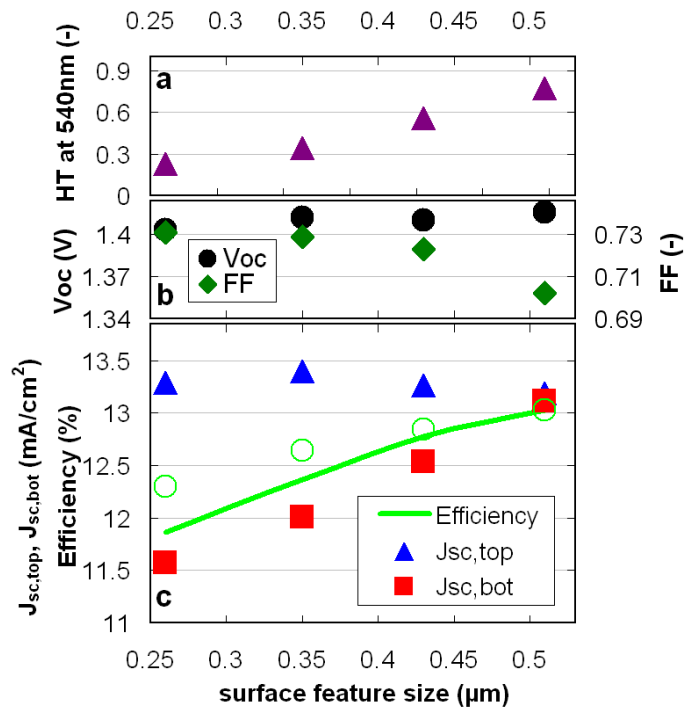


Figure 5.7: a) Haze in transmission of ZnO substrates measured in air at 540 nm as a function of their typical surface feature size. b) Open circuit voltage and fill factor of Micromorph cells grown on n-i-d ZnO of increasing surface feature size. c) Top and bottom cell current densities as well as the efficiency of the aforementioned cells. The estimated efficiency obtained for a perfectly matched case is also indicated as open circles.

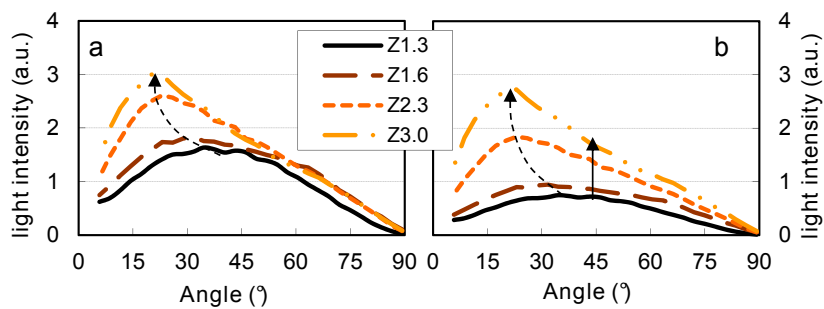


Figure 5.8: ARS of transmitted light for 1.3  $\mu\text{m}$  to 3- $\mu\text{m}$ -thick rough ZnO layers measured in air with a green laser (541nm) normalized with the haze value measured in air at a) 380 nm, and b) 540 nm. In both cases, the angle of maximum light scattering decreases for enlarging features (dashed arrow) but in b), the intensity of light scattered at large angles is still increased (solid arrow).



## 5.5. Optimal feature size investigation

To assess the potential of this new ZnO electrode approach, a broad-band antireflection coating was used on the light-incoming side of the glass and a 2.4- $\mu\text{m}$ -thick n-i-d ZnO electrode was deposited on the opposite side. A 4-minute plasma surface treatment was applied on its surface. A mobility value over  $50 \text{ cm}^2/\text{V/s}$  was obtained and a haze value of 70% at 540 nm. SiO<sub>x</sub>-doped layers (both *p*- and *n*-type) were used in both sub-cells to improve their electrical characteristics. With this configuration, a 13.5% initial efficiency Micromorph device could be obtained with a 280-nm- and a 2.8- $\mu\text{m}$ -thick top and bottom cells showing a  $V_{\text{oc}}$  of 1.39 V and a *FF* of 70.0%. The EQE of this device is shown in Fig.5.9 with high matched current of  $13.8 \text{ mA}/\text{cm}^2$ .

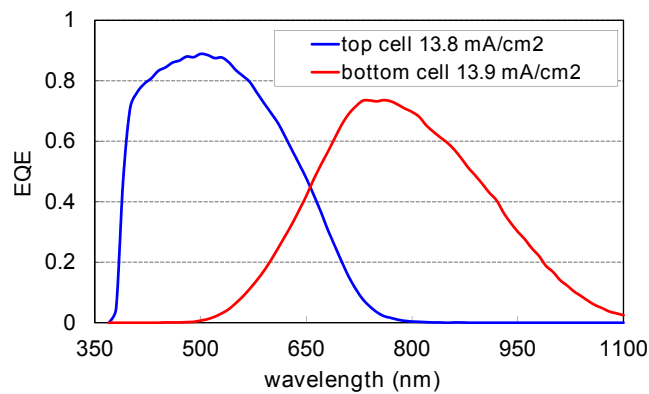


Figure 5.9: EQE curve of an optimized Micromorph device deposited on a 2.4- $\mu\text{m}$ -thick n-i-d LPCVD ZnO electrode treated for 4 minutes.

This top limited device, particularly sensitive to light-induced degradation, stabilized after 1000 hours of standard light soaking procedure without encapsulation at 11.5% efficiency ( $1.35 \text{ V}$ ,  $63.8\%$  and  $13.5 \text{ mA}/\text{cm}^2$ ) thanks to reasonable top cell thickness. Further developments conducted simultaneously in our group including optimization of the *p-i* interface of the top cell, improvements of the process of the bottom cell [Bugnon 12], and implementation of SiO<sub>x</sub> doped layers [Cuony 12], have permitted improving the stable efficiency of devices using the ZnO substrate developed in this study to 11.7% and 11.8% for intrinsic  $\mu\text{c-Si:H}$  layer thicknesses of  $1.1 \mu\text{m}$  and  $1.3 \mu\text{m}$  respectively. These efficiencies, amongst the highest reported values, validate the excellent light-harvesting properties of our newly developed single-layer substrate which we expect to permit over 12% stable efficiency.

As n-i-d ZnO layers are very sensitive to post-deposition oxidation, and as this can be significantly quenched by a little doping in the layer (leading to carrier densities around  $2 \cdot 10^{19} \text{ cm}^{-3}$ ) [Steinhauser 07], without significantly impacting the transparency of the layer, a 2- $\mu\text{m}$ - to 2.4- $\mu\text{m}$ -thick lowly doped ZnO layer, plasma treated for four minutes, has become at the time of writing the standard reference substrate that is used for Micromorph depositions in PV-lab, and that will be designed as “ref” or “std” layer in the following.

## 5.6 Schematic summary

A schematic view summarizing the morphological aspects discussed here can be seen in Fig. 5.10. This figure is a graphical representation of Micromorph device properties as a function of the two main morphological characteristics of the substrate: the typical size of the features composing its surface, and their typical inclination angle (characterizing the sharpness of the features). Three commonly used rough TCO-based substrates are represented: textured tin oxide (Asahi), sputter-etched zinc oxide (Jülich) and the reference 2.4  $\mu\text{m}$  LPCVD ZnO layer, treated for 4 minutes, optimized for Micromorph devices as seen in this chapter. The typical size of the surface features was taken as the square root of the typical area of the features estimated from SEM pictures. Typical inclination angles were estimated based on previous characterizations [Cuony 11].

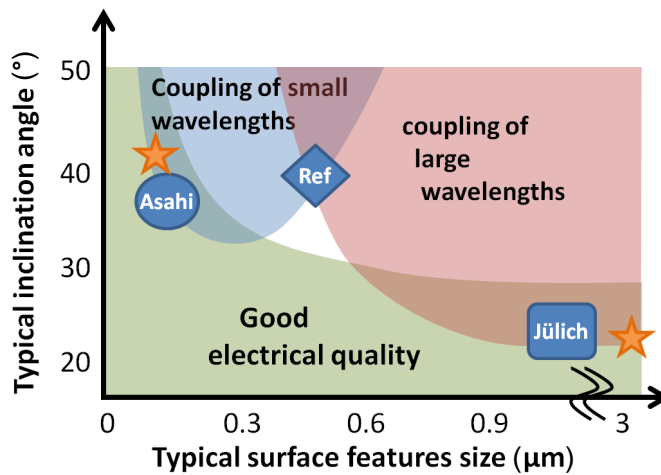


Figure 5.10: Schematic distribution of Micromorph device characteristics as a function of two main morphological properties of the substrate: the typical size of the features composing its surface and their typical inclination angle. Three state-of-the-art TCO substrates are represented: Tin oxide (Asahi), sputtered-etched ZnO (Jülich) and in-house LPCVD ZnO (Ref). The stars correspond to the multi-scale textured substrate presented in chapter 6.

Three main areas are sketched, corresponding to substrate morphologies favoring coupling of small wavelengths (requiring small and sharp features), scattering of large wavelengths (requiring large features) and good electrical quality (requiring small or smooth features). These areas are derived from experiments presented in this chapter and in appendix D. It is also in agreement with recent simulation work [Ding 11]. It is possible to combine two out of the three qualities in a single substrate, but no substrate has all three qualities. This is what we seek with the multi-scale morphology presented in the next chapter, combining textures corresponding to the orange stars in Fig 5.10, which exhibits small and sharp features on top of large and smooth ones.

## 5.7 Conclusion

We described the development of record Micromorph devices on LPCVD ZnO substrates. In particular, the ideal front electrode morphology to target is precisely depicted. First, a haze factor at 540 nm in air close to unity is shown to be needed for high total currents, requiring large enough features. However, large features are reported to be detrimental to good material quality. A plasma surface treatment, smoothening the surface, allows one to maintain good electrical performances on substrates with large haze values but this surface treatment causes a significant top cell current loss. Thus, small and sharp features should be preserved to enhance the top cell current. Overall, the optimal morphology is demonstrated to exhibit the smallest features fulfilling the requirement of haze at 540 nm in air close to unit, and the shortest treatment time to recover good electrical properties. Then, the need to avoid TCO doping for large total currents is emphasized, while  $FF$  losses observed when the sheet resistance of the substrate is increased are clarified. In particular, means of separating the shares of the resistive losses and of the modified matching is suggested. Also, the use of thick n-i-d LPCVD ZnO is presented as a favorable alternative to doping in adapting the sheet resistance of a substrate. Fine optimization of the front electrode leads to a 13.5% initial efficiency (11.5% after light soaking) Micromorph device with a 2.8- $\mu\text{m}$ -thick bottom cell on a 2.4- $\mu\text{m}$ -thick n-i-d LPCVD ZnO layer which was treated for only four minutes. This approach remains valid for thinner cells, as can be seen in [Despeisse 11] with an 11.3% stable Micromorph cell using a 1.1- $\mu\text{m}$ -thick bottom cell. These guidelines lead to the use of a new standard ZnO front layer in PV-lab for Micromorph development, characterized by a low doping and a thickness between 2  $\mu\text{m}$  and 2.5  $\mu\text{m}$ , on which stable Micromorph efficiencies of 11.8% were obtained. Finally, it should be mentioned that all the presented results concerning the influence of the front electrode on the silicon layer quality are based on the standard cells used in PV-lab at the moment of the experiments. Developing a deposition process which would be less favorable to “cracks” formation, or layers that mitigate their effects would lead to a different optimum. However, we believe that the trend would be similar, with a shift towards more rugged morphologies.



## 6 Multi-scale textured substrates

This chapter details the fabrication of multi-scale textured front electrodes, first using self-textured ZnO only, and second combining nanoimprint lithography with ZnO. Most of the presented results were published in [Boccard 12a] and [Boccard 12c]. The potential of multi-scale textured substrates when implemented in Micromorph devices is discussed. Such substrates allow separate optimization of light trapping in the top and bottom cells, and efficient decoupling of transparency and conduction. In particular, a sharp, nano-scale texturing for anti-reflection and light trapping in the top cell is shown to enable  $J_{sc}$  values over  $14\text{ mA/cm}^2$  with  $< 300\text{ nm}$  thickness. A  $\sim 1\text{-}\mu\text{m}$ -thick LPCVD ZnO layer is shown to be well suited for this task. It is also evidenced that smooth, micron-scale texturing can improve large-wavelength light management with limited impact on the quality of the silicon material subsequently grown on this texture. By combining the appropriate morphologies, it is demonstrated that similar currents can be reached with a multi-scale texture as with an optimal single texture, both in the top and bottom cells. Moreover, when a smooth enough large-scale texture (with typical inclinations under  $25^\circ$ ) is employed, the electrical quality of the silicon layers can be better preserved than for an optimal single scale-texture, with around  $20\text{ mV}$  of  $V_{oc}$  enhancement. Finally, in section 6.3, the concept of multi-scale architecture is validated with a  $14.1\%$  efficient Micromorph device combining nanoimprint lithography for the large-scale texture and a thin ZnO layer for the small-scale texture. To ensure a sheet resistance of  $25\ \Omega/\square$  while maintaining a high transparency, n-i-d ZnO is used in this electrode, seconded by a  $100\text{-nm}$ -thick hydrogenated indium oxide layer exhibiting mobility values of  $100\text{ cm}^2/\text{V/s}$ . The improved transparency obtained with this advanced electrode is shown to be a significant element permitting the reported high efficiency to be attained.

### 6.1 Prior art and motivation

Historically, multi-scale textures based on  $\text{SnO}_2$  were already reported by Asahi Glass Co. [Kambe 07]. A strong improvement of the haze measured in air, especially in the infrared part of the spectrum, was reported, but no significant cell results. This concept was pioneered simultaneously with ZnO in PV-lab by Didier Dominé [Dominé 09], to provide a strong light

trapping for both sub-cells of Micromorph devices. The few attempts made at this time did not give rise to promising result.

However, in 2010, the combination of textured glass with LPCVD ZnO was shown by Oerlikon and Corning to result in a record independently certified stabilized efficiency for a Micromorph cell of 11.9% [Bailat 10] (and later on a 12.3% efficiency device, non independently certified [Kroll 11]). A strong current increase in the infrared part of the spectrum was achieved with the multi-texture, compared to devices using only the texture of ZnO.

The similar concept of modulated surface textures was introduced in parallel to these results in [Isabella 10b] for single-junction *a*-Si:H cells. The combination of periodic (resp. random) structures, in lacquer (resp. glass), covered by a rough ZnO layer was presented. Compared to cells employing only the rough ZnO layer, a moderate current gain was observed. The contribution of the reduction of the reflection losses at the glass - ZnO interface and of the shift of the interference fringes of the EQE curve could not be precisely determined. A theoretical explanation of the scattering mechanism of modulated surface textures was then offered [Isabella 10a].

Full-ZnO-based modulated surface textures were demonstrated in [Owen 10] by applying to a sputtered ZnO layer a two-step etching process, combining the different etching characteristics of hydrochloric acid (leading to large features) and fluoridric acid (leading to smaller features) [Hüpkes 12].

Within these achievements, the focus is put on an improvement of light scattering, and the multi-scale texture is compared to one or the other texture used alone. In this chapter an experimental study of multi-scale textured substrates for Micromorph applications is presented, not only in terms of light management, but also in terms of electrical performances. To fairly determine the potential of such advanced superstrates for high-efficiency Micromorph devices, both textures are optimized, to compare the optimal combination of textures to state-of-the-art single-scale front electrodes, of which the morphology is detailed in chapter 5.

## 6.2 All-ZnO-based multitextures: proof of concept

### 6.2.1 Experimental details

ZnO front electrodes are deposited on glass by LPCVD. When using electrodes consisting of a stack of two ZnO layers, a thin (< 5 nm), *n*-doped  $\mu$ c-Si:H layer is inserted to prevent epitaxial growth of the second layer. As detailed in chapter 2, a large variety of morphologies can be obtained: for given deposition conditions, the typical size of the pyramids scales with the thickness of the film, reaching several  $\mu\text{m}^2$  for layers thicker than 10  $\mu\text{m}$  (Fig. 6.1).

The sharp, pyramidal features that naturally form can progressively be changed into smooth, crater-like features by applying a plasma treatment of adjusted duration. This well-known

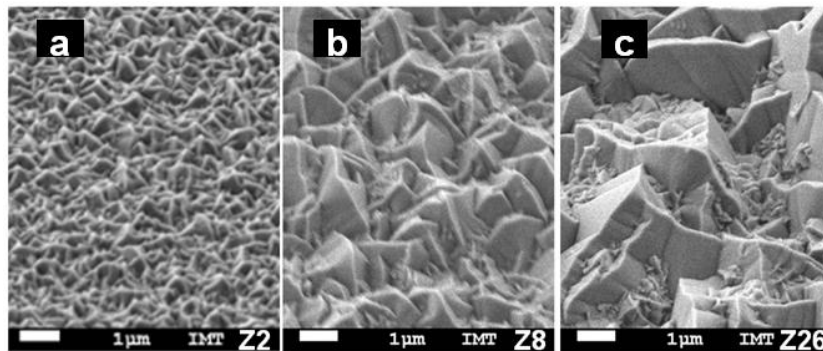


Figure 6.1: SEM images of the surface of three as-grown LPCVD ZnO layers of different thicknesses: a) 2.4 μm, b) 8 μm, and c) 26 μm.

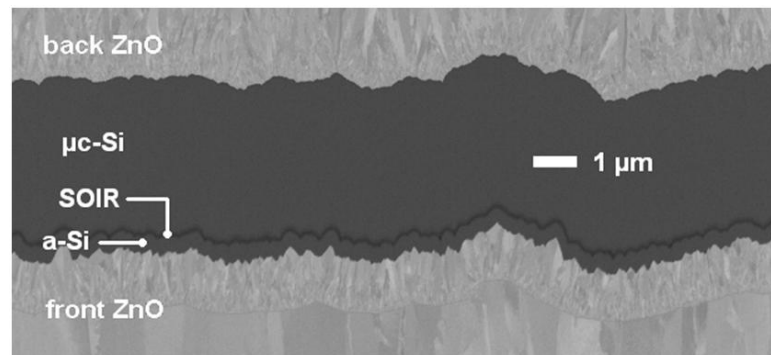


Figure 6.2: SEM cross section of a focused ion beam cut of a Micromorph cell grown on multi-scale textured electrode made out of two LPCVD ZnO layers: a 1.2-μm-thick layer on top of a 12-μm-thick layer that was plasma-treated for 4 hours.

treatment for standard layers (up to 5 μm thick) was thus extended to much larger feature sizes. Fig. 6.3b shows the surface of a 26-μm-thick layer smoothed by 3 hours of plasma treatment. Micromorph cells are then deposited by PECVD in a small area research-scale reactor or KAI industrial reactors of small and medium sizes. A silicon-oxide-based intermediate reflector (SOIR) is used in all devices. The back contact is a 2.4-μm-thick lightly doped LPCVD ZnO layer (carrier density of around  $4 \cdot 10^{19} \text{ cm}^{-3}$ ), and a white dielectric is used as the back reflector during measurements. An SEM cross section of a Micromorph cell can be seen in Fig. 6.2.

### 6.2.2 Motivation for multi-scale substrates

Multi-scale textured front electrodes aim at providing an adequate morphology to both cells, both for light management and to promote the growth of good-quality silicon material. The front electrode must ensure 1) a large current in the top cell, 2) a large summed current in the device, and 3) compatibility with high quality  $\mu\text{c-Si:H}$  junction growth. These requirements, taken individually, recommend the following front electrode surface morphologies, as seen in the previous chapter:

1. Small and sharp features, ensuring a strong light incoupling in the top cell and an efficient interplay with the IRL.
2. Large features, scattering all the transmitted light in silicon for wavelengths up to 1100 nm (*i.e.* a haze measured in air close to 100% up to 550 nm). These features also allow for a rough interface between the silicon and the back electrode, enabling diffuse reflection at this interface, that plays a significant role in light trapping as pointed out in [Sai 10].
3. Smooth or small features, preventing the formation of “cracks” during  $\mu c$ -Si:H growth that result in bad-quality diode areas.

Fig. 6.3 shows SEM images of the surface of four LPCVD ZnO layers (referred to as samples A, B, C, and D) and Fig. 6.4 presents the characteristics of Micromorph cells grown on these substrates. Sample A is an as-grown 0.5- $\mu\text{m}$ -thick ZnO layer. Its sharp, small features are favorable for high top cell current (Fig. 6.4d), but are too small to provide light scattering of large wavelengths, resulting in low bottom-cell current ( $< 10 \text{ mA/cm}^2$ ). Its features are also small enough to prevent the formation of cracks in the top and bottom junctions, as demonstrated by a reasonably good open-circuit voltage ( $V_{oc}$ ) of 1.4 V (Fig. 6.4b). Sample B is a substrate favorable to high-efficiency  $\mu c$ -Si:H cells: it exhibits strong light scattering in silicon (haze of 100%) for all wavelengths up to 1100 nm due to the very large features formed during the growth of this 26- $\mu\text{m}$ -thick layer. A three-hour plasma treatment was applied to smoothen the surface morphology. The resulting morphology is very similar to the morphology of sputtered ZnO films after etching in hydrochloric acid [Berginski 07], which are known for their suitability for high-quality  $\mu c$ -Si:H material growth [van den Donker 07]. Consequently, the Micromorph cell grown on this substrate shows an excellent  $V_{oc}$  of around 1.43 V. In spite of strong bottom-cell current, the lack of sharp, small features is detrimental to top-cell current (Fig. 6.4d). It should be noted that the 26- $\mu\text{m}$ -thick ZnO substrate (sample B) induces an additional parasitic absorption ( $A_p$ ) in the cell, making direct current density comparisons between the morphologies biased. The current density values that would be obtained if the  $A_p$  were similar to standard values are indicated with open symbols in Fig. 6.4. They are derived from a “comparable” EQE ( $EQE_{comp}$ ) obtained from equation 6.1, which was derived from [Dominé 09], that gives the EQE values that would be obtained if the  $A_p$  were the same as for a reference sample. (Sample C is taken as the reference sample.)

$$EQE_{comp} = \frac{EQE}{EQE + R} \cdot (EQE + R)_{ref} \quad (6.1)$$

Sample C is the reference single-scale texture morphology optimized for Micromorph cells, as detailed in chapter 5. It is a 2.4- $\mu\text{m}$ -thick layer that has been smoothened slightly by a 4-minute plasma treatment. This short treatment allows the deposition of good-quality material as judged from the good  $V_{oc}$  value (Fig. 6.4b), while maintaining sharp features resulting in a strong top-cell current (Fig. 6.4d). The bottom-cell current is also boosted by a haze close to



## 6.2. All-ZnO-based multitextures: proof of concept

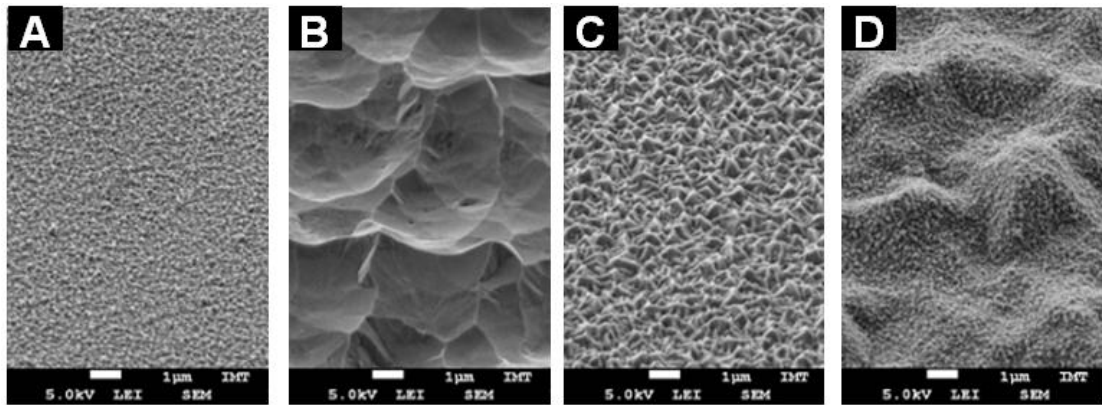


Figure 6.3: SEM images of a) a 0.5- $\mu\text{m}$ -thick ZnO layer, b) a 26- $\mu\text{m}$ -thick ZnO layer with 3 hours of plasma treatment, c) a 2.4- $\mu\text{m}$ -thick, optimal, single-texture substrate with four minutes of plasma treatment, and d) a double-texture substrate consisting of a stack of the first two layers.

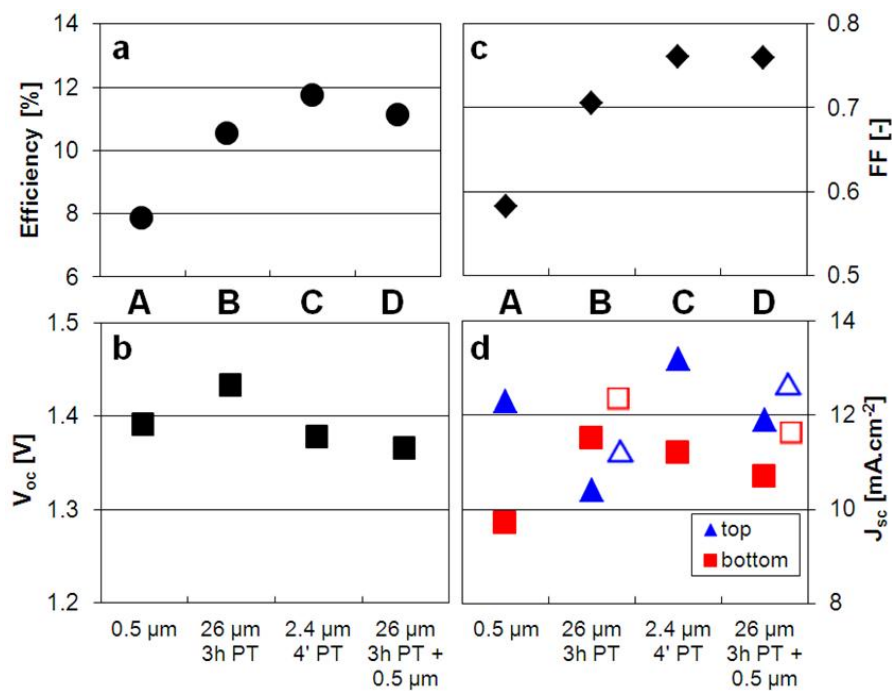


Figure 6.4: Performance of Micromorph cells grown on the substrates presented in Fig. 6.3: a) efficiency, b)  $V_{oc}$ , c)  $FF$ , and d)  $J_{sc}$  of the top and bottom cells. The open symbols in d) represent simulated current density values for Micromorph cells on substrates B and D in the case where the absorption in the front TCO is the same as in C.

unity even for large wavelengths.

Sample D shows a multi-scale textured substrate composed of a stack of the first two layers (0.5- $\mu\text{m}$ -thick as-grown ZnO on a three-hour plasma-treated 26- $\mu\text{m}$ -thick ZnO layer). Compared to sample B, the addition of the sharp, small features generates a strong  $V_{oc}$  loss of 80 mV, but induces an impressive  $1.5\text{ mA/cm}^2$  gain in the top-cell current density at the cost of a smaller loss in the bottom-cell. This comes from two different effects as can be seen from the EQE curve and the total absorption curve (plotted as one minus reflection,  $1 - R$ ) in Fig. 6.5. The first effect is a reduction of primary reflection at the ZnO-silicon interface thanks to the roughness: a 2% reduction of  $R$  up to 500 nm and suppression of the ripples between 500 nm and 870 nm. The second effect is an increase in the effect of the IRL, with a boost of the top-cell EQE in the 500 nm - 750 nm range thanks to the sharp, small features.  $V_{oc}$  and  $FF$  for sample D are only slightly lower than on the reference sample (sample C) and light incoupling in the top cell is not as good. This can be improved by tuning the properties of both morphologies as discussed in the next section. A thin as-grown LPCVD ZnO layer is thus an efficient layer to achieve high top-cell current densities, even when put on top of larger features that scatter large wavelengths. These large features are here obtained by LPCVD ZnO, but textured glass or sputtered-etched ZnO could for example be substituted.

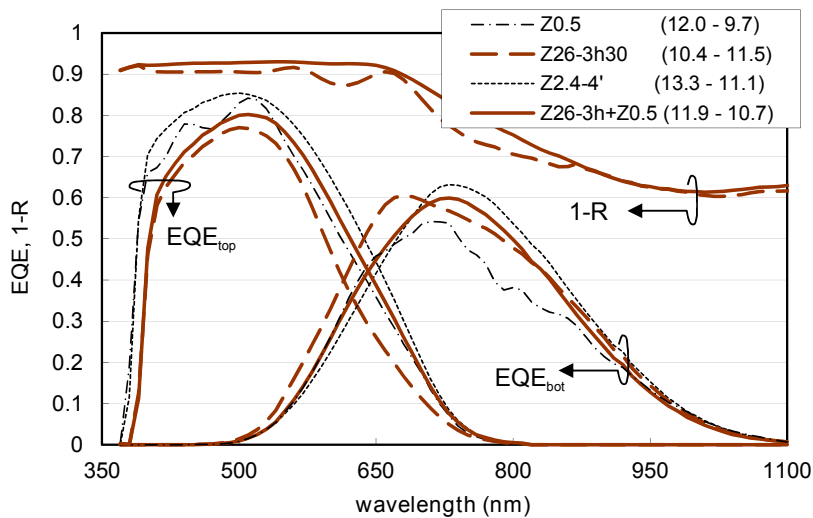


Figure 6.5: EQE of Micromorph cells grown on the substrates presented in Fig. 6.3. In the legend, the numbers in parentheses are top- and bottom-cell currents in  $\text{mA/cm}^2$ . The addition of small pyramids on top of Z26-3h results in a reduction of reflection for wavelengths  $< 870$  nm and a strong increase of the top-cell EQE compared to Z26-3h. Parasitic absorption in the 26- $\mu\text{m}$ -thick ZnO layer reduces the top-cell EQE. The 0.5- $\mu\text{m}$ -thick substrate is not rough enough to remove interference fringes in both top- and bottom-cell EQE curves.

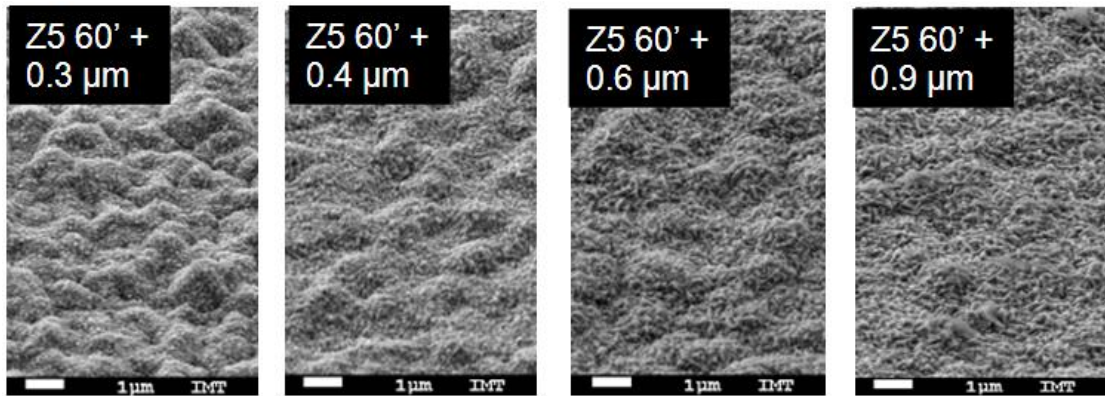


Figure 6.6: Influence of the thickness of the second ZnO layer: smoothing of the large features accompanied by an increase in the size of the small features.

### 6.2.3 Effect of increasing the size of the small features

We showed in the previous section that adding small, sharp features on top of large, smooth features improves light incoupling in the top cell. We observe here the influence of the size of these small features by depositing a 300-nm- to 900-nm-thick ZnO layer on top of a 5- $\mu\text{m}$ -thick ZnO layer smoothed by one hour of plasma treatment (Fig. 6.6). The two effects observed in Fig. 6.5 can also be seen in Fig. 6.7a: the top-cell current is increased due to the thin LPCVD ZnO layer, and reflection losses are reduced. We can further see that the top-cell current boost scales with the thickness of the second ZnO film with up to a  $0.7 \text{ mA/cm}^2$  gain for the 900-nm-thick layer. Also, ripples are progressively suppressed in the  $1 - R$  curves in the 530 nm to 630 nm and 640 nm to 840 nm wavelength ranges (only the thickest ZnO layer is efficient for the latter). This is explained by improvement of light scattering thanks to the small pyramids alone. Fig. 6.7b shows that the haze calculated for scattering in silicon from AFM data is increased due to the enlarged features. It reaches high values in the whole range of interest for the *a*-Si:H cell (*e.g.* 0.7 at 700 nm) for only the thickest, 900-nm-thick layer. Finally, even though significant gains are observed in top-cell and summed currents ( $+0.7 \text{ mA/cm}^2$  and  $+0.4 \text{ mA/cm}^2$ , respectively, between 300 nm and 900 nm), a  $V_{\text{oc}}$  loss can be seen, especially for the thickest layer (Fig. 6.7c). This can be attributed to the appearance of “cracks” in the silicon due to features greater than a critical size, or to a reduction of the thickness of the top-cell doped layers because of the larger ironed surface.

### 6.2.4 Effect of increasing the size of the understructure

In this section we vary the thickness of the first ZnO layer to change the size of its surface features. By adjusting the duration of the plasma treatment, the morphology can be further tuned as assessed by the changes in ARS shown in Fig. 6.8a. Also, it is possible to reproduce the same surface morphology for different feature sizes with a plasma treatment of duration proportional to the features. This can be assessed through ARS measurements (Fig. 6.8b).

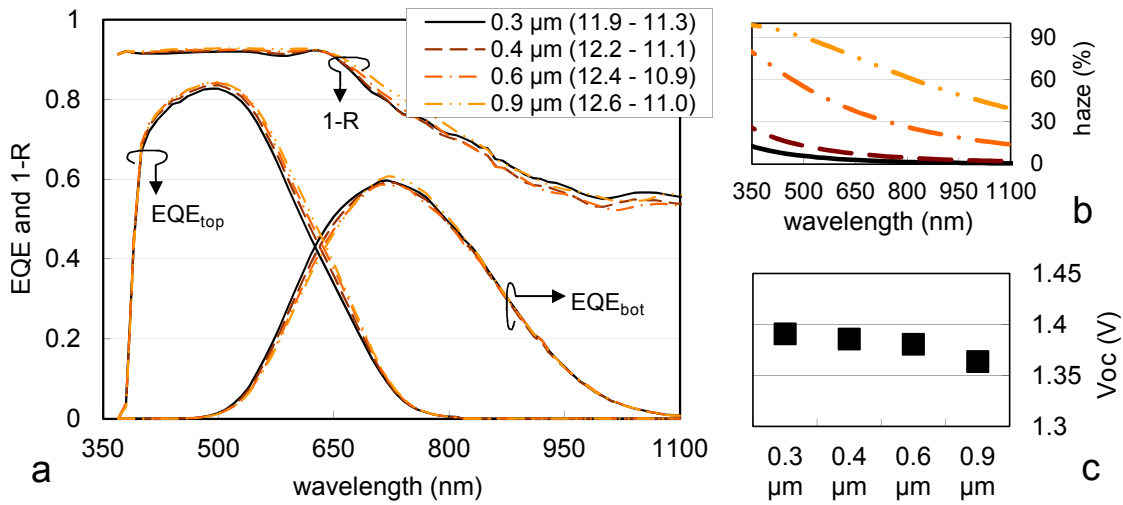


Figure 6.7: a) EQE of Micromorph cells grown on the substrates presented in Fig. 6.6. In the legend, the numbers in brackets are top- and bottom-cell currents in mA/cm<sup>2</sup>. b) Haze calculated for scattering in silicon for 300-nm- to 900-nm-thick ZnO layers. c)  $V_{oc}$  of the same devices. A gain in top-cell EQE is evident while a  $V_{oc}$  loss occurs for increasing thickness of the covering ZnO layer.

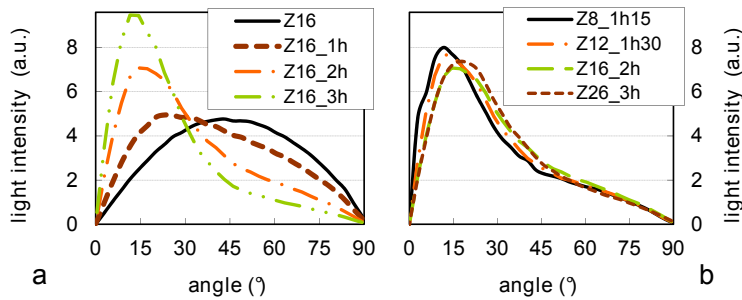


Figure 6.8: a) ARS of a 16- $\mu\text{m}$ -thick ZnO layer, as deposited or plasma treated for one, two, or three hours. b) ARS of 8- $\mu\text{m}$ - to 26- $\mu\text{m}$ -thick layers treated proportionally to the size of their surface features in order to get similar morphologies (probed via ARS measurements).

When depositing a thin ZnO layer on top of the first layer, different morphologies are obtained, with an improvement of the conformality and a reduction of “pinching” for the largest understructure features (Fig. 6.9). However, very little effect is seen on cell performance (Fig. 6.10): the  $V_{oc}$  remains stable whereas the  $FF$  fluctuates slightly without any trend. The efficiency drops only because of the lower transparency of the thickest layers (top- and bottom-cell currents decrease).

### 6.2.5 Effect of smoothening the understructure

Large-scale morphologies can be smoothened with a long plasma treatment. Micromorph cells were made on bi-morphology substrates of 12- $\mu\text{m}$ -thick ZnO layers with various treatment

## 6.2. All-ZnO-based multitextures: proof of concept

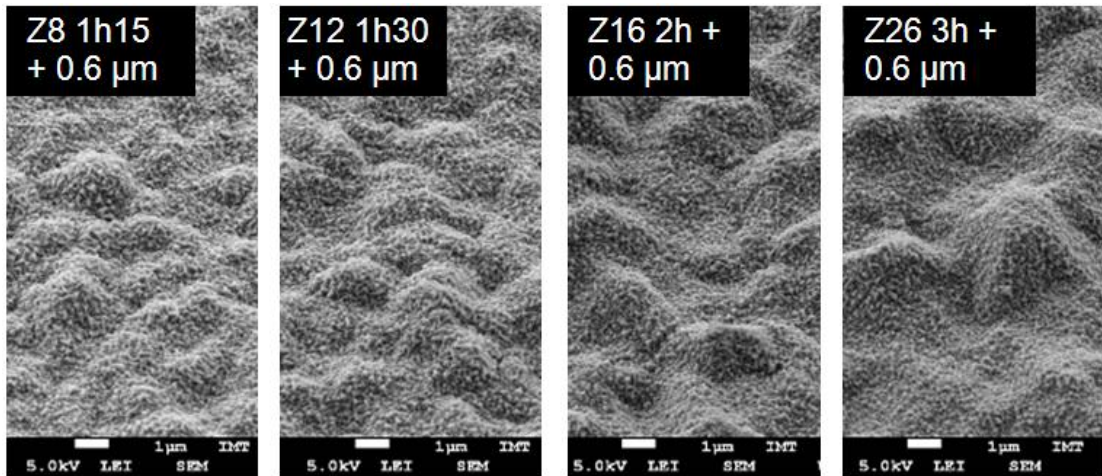


Figure 6.9: Influence of the scale of the large features for similar morphologies and thin covering layer thickness. “Pinching” is reduced when going to huge textures.

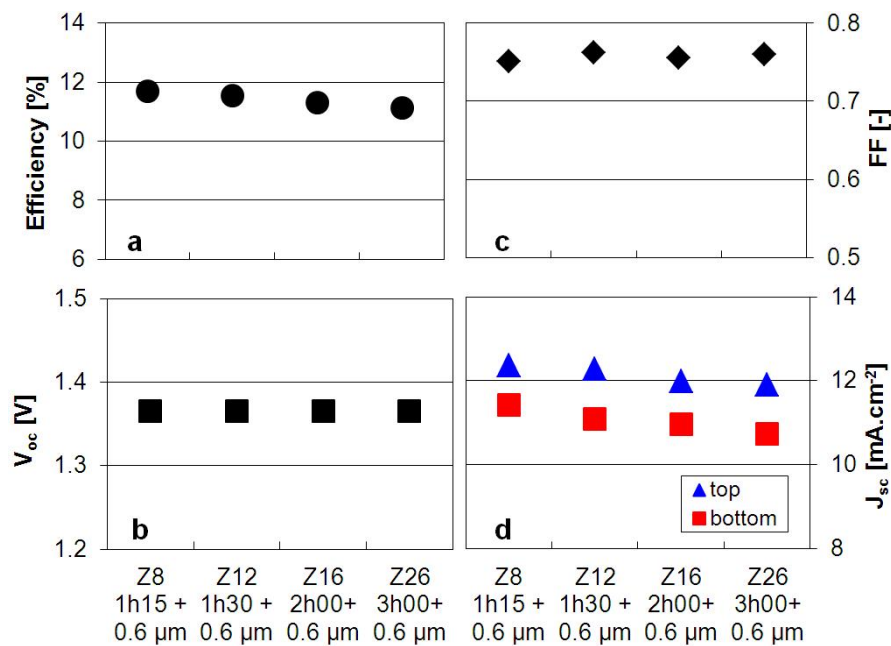


Figure 6.10: Performance of Micromorph cells grown on the substrates presented in Fig. 6.9: a) efficiency, b)  $V_{oc}$ , c)  $FF$ , and d)  $J_{sc}$  of the top and bottom cells.



durations (1 hour to 4 hours) topped by a 0.9- $\mu\text{m}$ -thick ZnO layer. Again, a single-layer reference substrate (2.4- $\mu\text{m}$ -thick with 4 minutes of plasma treatment) is used as a comparison. Fig. 6.11 shows that smoothing of large-scale features is efficient in attaining  $V_{oc}$  and  $FF$  values even higher than for the reference substrate. Interestingly, this improvement is not achieved at the cost of a large top-cell current loss as is the case in single-layers thanks to the additional sharp, small features. Finally, the efficiency is the same as on the reference substrate, which is very promising considering the stronger absorption of the thick, double-scale ZnO layer. Such morphologies, in which large, very smooth features lie under sharp, small features are thus very promising for high-efficiency Micromorph cells. By replacing the thick, heavily treated ZnO layer with its lacquer replica covered by IOH [Koida 08], we will see in the next section that absorption can be greatly reduced while conduction is maintained through IOH.

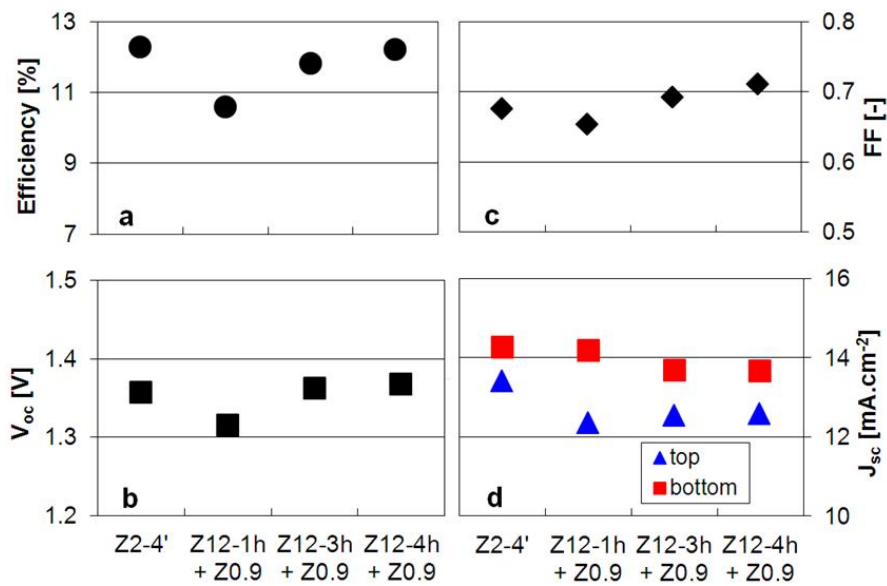


Figure 6.11: Performance of Micromorph cells grown on multi-scale substrates with increasing treatment of the large structures: a) efficiency, b)  $V_{oc}$ , c)  $FF$ , and d)  $J_{sc}$  of the top and bottom cells.

### 6.2.6 Conclusion

Multi-scale textured substrates were developed and implemented in Micromorph devices. Such substrates allow a two-step tuning of the morphology that can be beneficial for each sub-cell. It is demonstrated that when using a substrate with large, smooth features, the addition of small features provided by thin as-grown LPCVD ZnO layers can efficiently improve top-cell current while still allowing for high-quality silicon layer growth. The surface features of thin LPCVD ZnO layers are therefore shown to be an efficient final texture to be applied onto the substrate immediately before silicon deposition. Large features, which provide light scattering for large wavelengths, are still necessary, and we saw that a broad range of typical sizes can be used. However, it is shown that their shape must be smooth enough to maintain good

### 6.3. High-efficiency multitextures: combining nanoimprint lithography, IOH and rough ZnO

electrical quality in the device. Similar to previous chapter, these conclusion are thought to be precise only for the cell deposition processes used at the moment of the experiment in PV-lab, but the trends remain valid for most processes. For example, using processes more prone to the formation of porous areas of low electrical quality in the silicon (such as high-rate deposition of  $\mu c$ -Si:H) would probably enhance the electrical gain when using multi-scale textures.

## 6.3 High-efficiency multitextures: combining nanoimprint lithography, IOH and rough ZnO

### 6.3.1 Architecture of the device

The multi-scale concept is here extended by introducing a third functional layer to the front electrode, to improve its transparency without compromising its conductance. Based on the results of previous section, the multi-scale morphology studied further in this section corresponds to the orange stars in the schematic view of Fig. 5.10. An SEM top view is given in Fig. 6.12a. The two distinct textures are designed to achieve excellent light management for both sub-cells, and to enable the growth of high-quality silicon material.

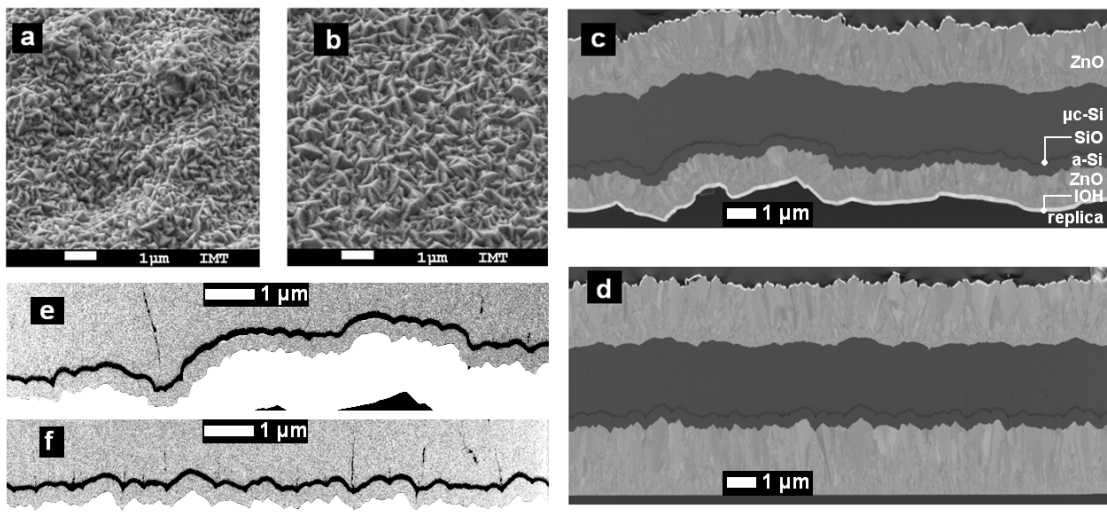


Figure 6.12: a, b) SEM images of the surfaces of a) the multi-scale textured electrode and b) the reference ZnO electrode. c, d) SEM images of a FIB cut across a Micromorph cell deposited on c) a multi-scale textured substrate and d) on a reference ZnO layer. e, f) high-contrast zoom image of c) and d) emphasizing bad areas (dark vertical lines) formed at the beginning of  $\mu c$ -Si:H growth when pinches are present at the SOIR surface due to the roughness of the front electrode.

Fig. 6.12c presents an SEM image of a cross section milled with a focused ion beam (FIB) through a Micromorph cell deposited on this multi-scale textured substrate, and Fig. 6.13 shows a schematic representation of this cross section. A smooth, micron-scale texture is first

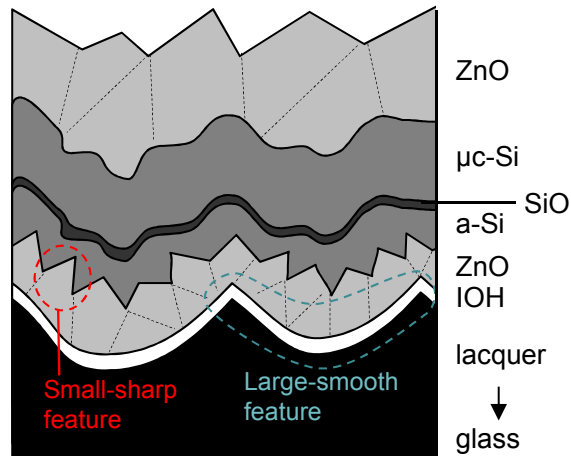


Figure 6.13: Schematic drawing of a cross section of a Micromorph cell deposited on a multi-scale textured substrate evidencing the small-sharp and large-smooth features.

obtained on flat glass by replication via a high-fidelity UV nanoimprint lithography technique [Escarré 11]. The master used here is a 16- $\mu\text{m}$ -thick LPCVD ZnO layer smoothed by a 3-hour plasma treatment. Its surface corresponds to the right side orange star in Fig. 5.10. Next, a 120-nm-thick IOH layer is deposited on top by sputtering [Battaglia 11c]. Its high mobility and low carrier density ( $\mu > 100 \text{ cm}^2/\text{V/s}$  and  $N = 1 \cdot 10^{20} \text{ cm}^{-3}$ ) make it highly transparent for the whole wavelength range of interest for silicon solar cells for a sheet resistance ( $R_{sq}$ ) below  $50 \Omega$ . Finally, a 1- $\mu\text{m}$ -thick n-i-d LPCVD ZnO layer is deposited on top. Its  $R_{sq}$  of approximately  $50 \Omega$  makes the front electrode stack  $R_{sq}$  approximately  $25 \Omega$  while its low carrier density keeps the electrode absorption low.

Micromorph cells are then grown by PECVD in a dual-chamber research-scale system. The thicknesses of the intrinsic layers of the top and bottom cells are 290 nm and 2.6  $\mu\text{m}$ . A 60-nm-thick SOIR is used. Doped silicon-rich silicon oxide layers are also implemented in the bottom cell to limit the influence of inhomogeneous and low-quality silicon regions on cell performance.

For comparison, the same Micromorph structure is also deposited on a reference flat substrate (sample A, flat glass / IOH and a thin protective ZnO layer), a state-of-the-art single-layer LPCVD ZnO electrode of which the surface is shown in Fig. 6.12b (sample B, flat glass / 2.4- $\mu\text{m}$ -thick ZnO), and an electrode stack with only the small-scale morphology (sample D, flat glass / IOH / 1- $\mu\text{m}$ -thick ZnO stack). A 1-minute plasma surface treatment is performed on all substrates before silicon deposition. A 4-minute treatment is also applied to the state-of-the-art ZnO layer to reduce the typical inclination of the surface and make it more suitable for high-quality silicon deposition. For all samples, the back contact is a lightly doped 2.4- $\mu\text{m}$ -thick LPCVD ZnO layer, and a white dielectric reflector is applied against the back of each cell during measurements.



### 6.3. High-eff. multitextures combining NIL, IOH and rough ZnO

Table 6.1: Characteristics of 1 cm<sup>2</sup> Micromorph cells grown on various substrates.

	$V_{oc}$ (V)	$FF$ (%)	$J_{sc,top}$ (mA/cm <sup>2</sup> )	$J_{sc,bottom}$ (mA/cm <sup>2</sup> )	$J_{sc,sum}$ (mA/cm <sup>2</sup> )	Eff. (%)
A) Flat IOH	1.432	71.8	12.6	11.0	23.6	11.3
B) Ref LPCVD ZnO	1.395	72.4	14.8	13.1	27.9	13.2
C) Multi-scale texture	1.411	71.5	14.3	14.0	28.3	14.1
D) IOH + thin LPCVD ZnO	1.420	75.0	14.5	12.6	27.1	13.4

#### 6.3.2 Cell results and discussion

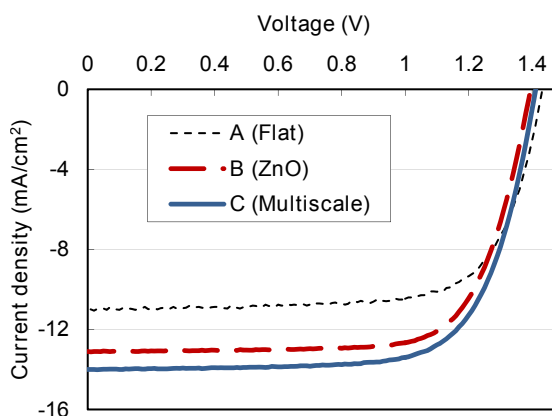


Figure 6.14:  $J(V)$  curves of Micromorph cells deposited on a flat substrate (A), on a reference ZnO electrode (B) and on a multi-scale textured substrate (C).

Fig. 6.14 presents current density-voltage ( $J(V)$ ) characteristics of the cells deposited on substrates A, B and C, measured with a dual-lamp sun simulator in standard test conditions. Tab. 6.1 summarizes their  $V_{oc}$ ,  $FF$ ,  $J_{sc,top}$ ,  $J_{sc,bottom}$ ,  $J_{sc,sum}$  and efficiencies. The highest initial efficiency of 14.1% is obtained on the multi-scale substrate, which is a 2.8% absolute gain compared to the flat substrate and a 0.9% gain compared to the single-layer reference ZnO substrate. As can be seen in Fig. 6.14, the efficiency gain is obtained through both  $J_{sc}$  and  $V_{oc}$  increases. This suggests that our approach allows for both better material quality and efficient light management.

Concerning the  $J_{sc}$  values, it can be seen that high top cell currents ( $> 14 \text{ mA/cm}^2$ ) can be obtained on all rough substrates, due to the particularly suitable morphology of LPCVD ZnO. However, a high bottom cell current is achieved only on the multi-scale textured substrate. This can clearly be attributed to better light trapping than in devices A and D, where no large-scale texture is present to provide light scattering of large wavelengths. The comparison to the reference ZnO substrate is less straightforward, as discussed in the following. Fig. 6.15 presents the EQE of the top and bottom sub-cells of devices A, B and C as well as total device absorption (represented as one minus the reflection from the device (1-R)) for devices B and C. One can first notice that part of the current gain in the bottom cell for device C compared to device B is obtained in the 550 nm to 750 nm range. This is accompanied by a loss in the top

cell, and thus does not represent improved light trapping. Another striking point is that more light is actually coming out of the device on the multi-scale textured electrode than on the reference ZnO substrate. As the EQE curve is higher for the multi-scale textured electrode, this indicates a reduction in parasitic absorption ( $A_P$ ). As seen previously,  $A_P$  comes mostly from the doped layers, the electrodes and the back reflector in our devices. As the doped layers, the back electrode, and the back reflector are the same in all cases, this difference can be attributed to better transparency of our multi-scale textured electrode. Thus, our multi-scale texture enables a higher summed current than our optimal single-scale texture not due to a better light trapping ability, but because it has a better transparency for as good light trapping.

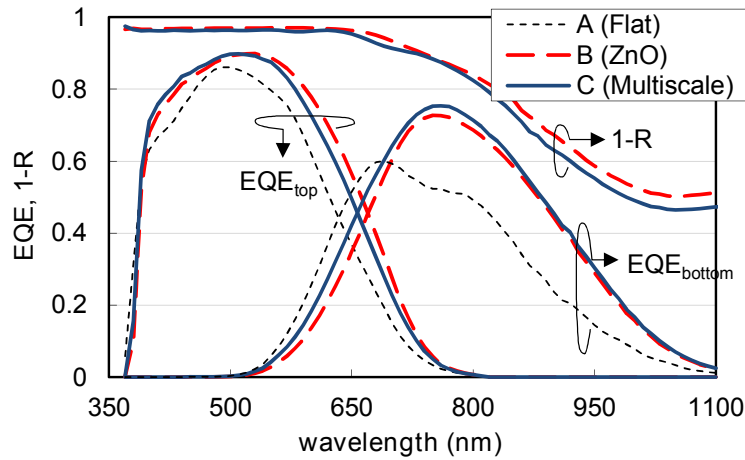


Figure 6.15: EQE curves of top and bottom sub-cells of Micromorph cells deposited on a flat substrate (A), a reference ZnO substrate (B) and a multi-scale textured substrate (C). Total device absorption (corresponding to 1-R) is also plotted for B and C (1-R is omitted for A for a better clarity).

Turning now to the  $V_{oc}$ , which is sensitive to the electrical quality of the junctions, the highest value is achieved on the flat substrate (A), as expected from Fig. 5.10. For the reference ZnO substrate, the roughness drastically reduces the  $V_{oc}$  with a 37 mV loss caused by creation of defective areas. With the multi-scale texture, the loss is reduced to only 21 mV, indicating a more homogeneous material. This correlates well with the reduced number of cracks in the  $\mu c$ -Si:H layer (appearing as dark lines in the cross sections in Fig. 6.12e and 6.12f). From the  $V_{oc}$  value observed on device D, we can deduce that around 10 mV are still to be recovered by improving the small features, and the same by improving the large features.

Finally, as mentioned in chapter 5, the  $FF$  of tandem devices is strongly influenced by the difference between the  $J_{sc}$  of the top and bottom sub-cells, also called mismatch. The lowest  $FF$  of the series is obtained for device C, which also has the closest sub-cells currents. Indeed,  $FF$  gains of up to 2% per  $\text{mA}/\text{cm}^2$  of mismatch were observed in the previous chapter for similar cells. This explains a large part of the 3.5%  $FF$  drop between device D and device C, where the introduction of large-scale features generates a  $1.6 \text{ mA}/\text{cm}^2$  mismatch reduction. The  $FF$  loss

between the reference ZnO and the multi-scale textured electrode can also be attributed to mismatch reduction. Indeed, observing only 1% of  $FF$  loss for  $1.4 \text{ mA/cm}^2$  mismatch reduction suggests that better-quality material is grown on the multi-scale substrate. This correlates well with the  $V_{oc}$  trend and the crack densities observed in the SEM cross sections in Figs. 6.12c and 6.12d.

Overall, a better initial efficiency with a multi-scale textured substrate compared to a state-of-the-art substrate could be shown. The gain lies in the electrical quality of the silicon layers (thanks to a reduction of the “cracks” in the silicon layers) and in the better transparency (for identical sheet resistance) of the stack lacquer - IOH - thin ZnO compared to a standard  $2.4\text{-}\mu\text{m}$ -thick ZnO layer. Due to the large thickness of the top cell [Benagli 09], and the presence of a thick SOIR [Cuony 11], all cells from this series degraded heavily after 1000 hours of light soaking under standard conditions. Stabilized efficiencies of 9.6% and 9.8% were obtained for the reference ZnO substrate (−27%) and the multi-scale substrate (−30%). The stronger degradation of the cell employing a multi-scale textured substrate is ascribed to the less-favorable matching, leading to a top-limited device in the degraded state. Yet, these devices were designed for a high initial efficiency, and a higher stable efficiency should be achievable with thinner intrinsic layers and a thinner IRL.

## 6.4 Conclusion

The potential of multi-scale textured electrodes was reviewed in this chapter. It was shown that the numerous conflicting tasks that the front electrode has to perform can be split by using several dedicated layers. A smooth and large-scale texture, that can be replicated in lacquer by nanoimprint lithography for a perfect transparency, can ensure scattering of infrared light for the bottom cell while preserving a morphology suitable for high-quality silicon growth. A subsequent  $1\text{-}\mu\text{m}$ -thick, highly transparent LPCVD ZnO layer can provide small and sharp features, necessary to a good coupling of UV and visible light into the top cell, again with minimal impact on silicon growth and with low absorption. Finally, a thin, high-mobility hydrogenated indium oxide layer completes the conductance of the stack for electrical carrier extraction without compromising transparency. Compared to state-of-the-art substrates, this new approach demonstrated similar light-scattering properties together with higher transparency and better suitability for high-quality silicon growth. A noteworthy 14.1% initial efficiency was achieved. This approach opens new roads for light harvesting in solar cells, by validating the possibility to split the spectrally wide requirements into several different dedicated photonic structures. While we restricted our study to the morphologies accessible with LPCVD ZnO, many other photonic structure combinations are possible and easily accessible thanks to the versatility of nanoimprint lithography.



## 7 Smoothing intermediate reflecting layers

In this chapter, the concept of smoothing intermediate reflecting layers (IRLs) is introduced. The aim of such structures is to provide a well suited surface morphology on which to grow good electrical quality  $\mu c$ -Si:H, especially in Micromorph devices including a rough front electrode enabling good light scattering. This concept is first validated by showing a 50 mV  $V_{oc}$  enhancement when employing a polished SiO<sub>x</sub>-based IRL (using chemo-mechanical polishing, CMP) [Boccard 12e]. Shunting of the top cell due to the irregular surface of the random rough electrode and additional reflection losses ( $-0.7 \text{ mA/cm}^2$  in the bottom cell) due to the resulting flat interfaces show the limitations of this technique, highlighting the need to smoothen without completely flattening. An alternative approach, for which the front electrode is designed for the  $a$ -Si:H cell only, and the IRL is designed for the  $\mu c$ -Si:H cell, is briefly presented. The validity of the concept could be demonstrated with a 3- $\mu\text{m}$ -thick ZnO IRL (10% bottom cell current gain compared to a flat IRL) but no electrical and optical gain is simultaneously obtained.

Liquid-based deposition of IRLs is studied in the last sections. Good smoothing is achieved with spray coating of ZnO from Zn-acetate, but this method is abandoned because the deposition temperature ( $> 250^\circ\text{C}$ ) required is too high. A new technique is then developed to enable the use of highly transparent – but isolating – UV-curable lacquer thanks to selective etching: since the lacquer preferentially settles in the bottoms of the structure rather than at the tips, a short dry-etching can unveil the tips of the surface, enabling electrical conduction. Planarization of the surface of the top cell is demonstrated, with a  $V_{oc}$  boost of up to 50 mV compared to a standard IRL. A strong top cell current boost is also shown, of up to  $2.3 \text{ mA/cm}^2$  (20% relative), compared to  $1.8 \text{ mA/cm}^2$  with a standard IRL. Adjusting the volume of lacquer composing this advanced interlayer enables a fine tuning of its opto-electrical properties.

By combining this technique with state-of-the-art electrodes and sub-cells, we believe that over 13.5% stable devices are within reach (with *e.g.* 1.4 V,  $14 \text{ mA/cm}^2$ , and 70% of  $V_{oc}$ ,  $J_{sc}$  and  $FF$ ).

## 7.1 Motivation: mapping of Micromorph properties as a function of the substrate morphology

In chapter 6, we presented a multi-scale texturing architecture for the front electrode to provide light trapping to both sub-cells and a suitable surface for the growth of high-quality silicon layers. Another route to combine good electrical performance in thin-film silicon solar cells employing advanced light-trapping schemes is here suggested, by smoothing the surface on which the  $\mu\text{c-Si:H}$  solar cell is grown. This is achieved by introducing a smoothing layer between the  $a\text{-Si:H}$  top cell and the  $\mu\text{c-Si:H}$  bottom cell. This smoothing interlayer can also play the role of an IRL, typically made of  $\text{SiO}_x$  (SOIR) or  $\text{ZnO}$  (as detailed in previous thesis works [Dominé 09, Cuony 11]), and used in state-of-the-art devices.

We suggested in chapter 5 a schematic representation of Micromorph device properties as a function of two front electrode parameters that are the typical size and typical inclination of the features composing its textured surface. We reproduce it in Fig. 7.1a, to restate the current impossibility to fulfill with a single texture all the requirements of a high-efficiency Micromorph cell, that are 1) efficient coupling and scattering of light in the top cell, 2) efficient coupling and scattering of light in the bottom cell and 3) a morphology suitable for the growth of silicon layers with good electrical quality. A multi-scale texture adds a degree of freedom as the different requirements can be fulfilled by the addition of two different textures (represented by orange stars in Fig. 7.1a). Alternatively, introducing a smoothing IRL unlinks the morphology seen by the top and bottom sub-cells, as sketched in Fig. 7.2b-d: the sharpness needed for high top cell current is no longer detrimental to a good bottom cell electrical quality, extending the “good electrical quality” area towards sharper morphologies (Fig. 7.1b).

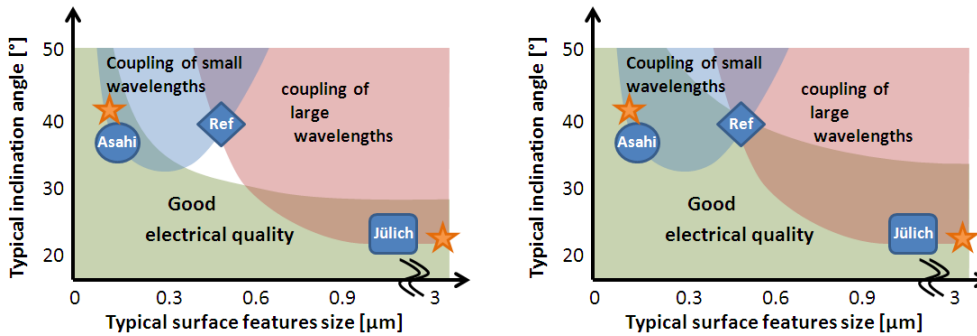


Figure 7.1: a) (as in chapter 5) Schematic distribution of Micromorph device characteristics as a function of two main morphological properties of the substrate: the typical size of the features composing its surface and their typical inclination angle. Three state-of-the-art TCO substrates are represented: Tin oxide (Asahi), sputtered-etched  $\text{ZnO}$  (Jülich) and in-house LPCVD  $\text{ZnO}$  (Ref). The stars correspond to the multi-scale textured substrate. b) Schematic representation of the effect of the smoothing IRL: the “good electrical quality” area is extended towards sharper substrate morphologies, now including the Ref substrate morphology.

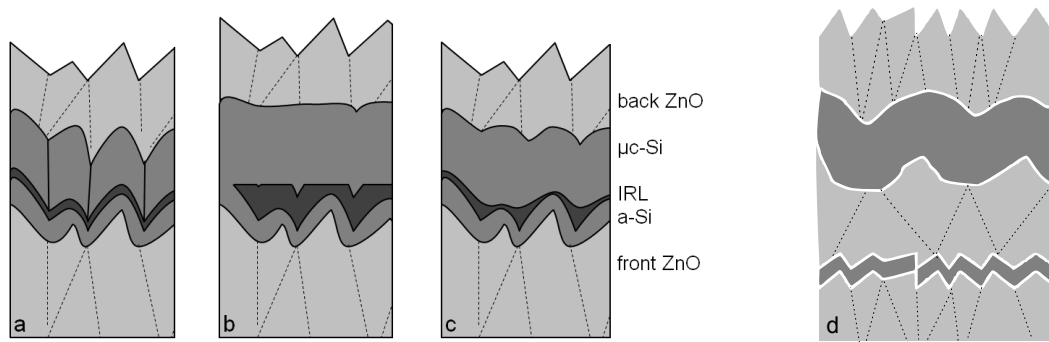


Figure 7.2: a) Schematic side view of a Micromorph tandem cell with (from bottom to top) polycrystalline LPCVD ZnO front contact, *a*-Si:H top cell, IRL, *μc*-Si:H bottom cell and LPCVD ZnO back contact. Cracks in the *μc*-Si:H layer are represented by black lines. b to d) Same with b) a thick polished, c) a naturally smooth, or d) a thick and smoothed IRL, preventing the formation of cracks.

Planarization is a standard process for microelectronics, but it usually includes high temperature steps (over 300°C), and uses isolating material. On the other hand, to be used as IRL in thin-film silicon solar cells, a planarizing layer should:

1. Be not completely isolating: for a 100-nm-thick layer, a conductivity of  $10^{-5}$  S/cm induces  $1 \Omega \cdot \text{cm}^2$  of series resistance, representing 1% of the impedance of a Micromorph device.
2. Be transparent: light trapped in the cell will cross this layer too, so its absorption should be small (typically  $< 10 \text{ cm}^{-1}$ ).
3. Be resistant to a high vacuum and to 200°C processes without damaging or outgasing.
4. Involve only low-temperature processes during fabrication ( $< 200^\circ\text{C}$ ).

Amongst the available techniques, polishing of a standard IRL, plasma treatment of a thick ZnO-based IRL, spray coating of ZnO and spin coating of a UV-curable lacquer (which resists our standard PECVD process) were tested. For the first technique, the challenge is to prevent shunting and specular reflection at the IRL - silicon interface; for the second one the challenge comes from shunt interconnection due to the large lateral conductivity, and the limitation is caused by the parasitic absorption of a thick ZnO layer; for the third one, complete decomposition of the precursor into ZnO must be achieved at a low temperature; whereas for the fourth one, electrical transport through the IRL is the main issue.

## 7.2 Proof of concept: polishing of SiO-based intermediate reflecting layers

### 7.2.1 Experimental details

Results presented in this section were published in [Boccard 12e]. Micromorph cells were deposited on glass in the superstrate configuration. First, a 2.5- $\mu\text{m}$ -thick lowly doped ZnO layer was deposited by LPCVD. A 4-minute plasma treatment was applied on its surface to slightly soften its morphology. Such a front electrode offers good characteristics for high-efficiency Micromorph devices, as detailed in chapter 5. Then, a *p-i-n a*-Si:H top cell was deposited by PECVD. A silicon-oxide-based IRL (SOIR) [Buehlmann 07] was deposited on top. The device was then submerged in an aqueous colloidal silica suspension (OP-S from Struers GmbH), and polishing was performed by scanning a rotating head made out of fabric on the surface of the IRL. The intensity of the mechanical polishing was adjusted by varying the dilution of the solution in de-ionized water. Ratios of 1/8 and 1/24 were used here. Then, the  $\mu\text{c}$ -Si:H bottom cell was deposited, followed by a lowly doped LPCVD ZnO back contact and a white dielectric back reflector. J(V), EQE and R measurements were performed with a dual-lamp WACOM sun simulator, an in-house optical setup and a dual-beam spectrophotometer respectively.

### 7.2.2 Results and discussion

Tab. 7.1 presents the evolution of the parameters of Micromorph devices including SiO-based IRLs of two different thicknesses (150 nm and 300 nm) with various degrees of polishing. They were obtained through dilution of the colloidal silica suspension solution in deionized water (ratios 1/8 to 1/64). A device with no IRL is included, as well as a device including a non-polished IRL. A clear  $V_{\text{oc}}$  gain is observed on all samples when polishing is performed, validating the positive effect of a smoothing IRL. This is accompanied by a FF increase, that is however mainly due to the very strong mismatch change when a polished IRL is used, as the bottom cell current drops. This bottom cell current loss is caused by additional reflection losses from the flat IRL -  $\mu\text{c}$ -Si:H cell interface, as demonstrated by the EQE and reflection measurements (Fig. 7.3). It should be noted that shunted top cell currents (indicated by \*) are artificially low due to measurement issues, notably when polishing is too strong (the low 0.4%-illumination  $V_{\text{oc}}$  value confirms the shunting of the top cell). By proper choice of SiO thickness and of polishing force, shunting can be avoided (*e.g.* with a 300-nm-thick SiO layer and 1/24 polishing intensity). However, the most important limitation of the technique originates from the strong additional reflection losses generated by the actual flattening. These losses are thought to come mostly from the suppression of the natural texture that develops at the back of the  $\mu\text{c}$ -Si:H cell when a polished IRL is used (Fig. 7.4). The importance of having a texture at the back of the silicon layers, even for the superstrate configuration, was unambiguously shown in [Sai 10].



## 7.2. Proof of concept: polishing of SiO-based IRLs

Table 7.1: Micromorph device parameters for different IRLs. Top cell currents with \* indicate underestimated values due to measurement problems caused by shunting of the top cell (as assessed by the low 0.4%-illumination  $V_{oc}$  value).

	$V_{oc}$ (V)	$FF$ (%)	$V_{oc}$ 0.4% <i>ill</i> (V)	$J_{sc,top}$ (mA/cm <sup>2</sup> )	$J_{sc,bottom}$ (mA/cm <sup>2</sup> )	Eff. (%)
No IRL	1.359	70.0	0.881	11.96	13.05	11.4
SiO 150nm	1.338	74.1	0.858	13.89	11.32	11.2
SiO 150nm pol. 1/24 dil.	1.371	75.0	0.499	12.99*	10.63	10.9
SiO 300nm pol. 1/24 dil.	1.385	77.8	0.847	14.05	9.03	9.7
SiO 300nm pol. 1/8 dil.	1.385	77.8	0.338	13.35*	9.3	10.0

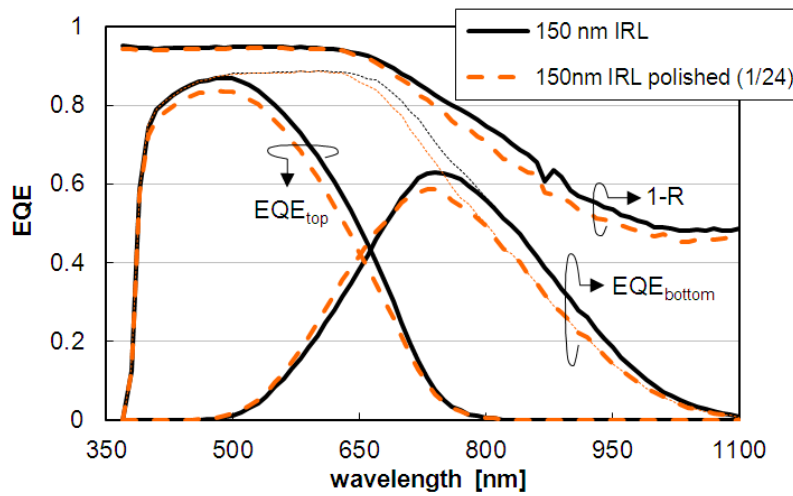


Figure 7.3: EQE and  $1 - R$  of Micromorph cells with a 150-nm-thick SiO-based IRL polished or not. Dotted lines correspond to the summed EQE curves ( $EQE_{top} + EQE_{bottom}$ ).

### 7.2.3 Conclusion

We introduced the concept of a smoothening IRL in Micromorph devices, in order to prevent the inhomogeneous growth of  $\mu c$ -Si:H that typically occurs when challenging substrates are used. We validated the gain in terms of material quality by showing an increase in  $V_{oc}$  when polished SiO-based IRLs are used (around +30 mV), confirming that smoothening the morphology before adding the  $\mu c$ -Si:H bottom cell increases the device electrical performance. However, shunting of the top cell and additional reflection were identified as the two main reasons for discarding the use of this technique. The additional reflection, ascribed to the flattening of the silicon - back ZnO interface, indicates that a complete flattening is undesirable, and that the ideal surface morphology for the IRL is smooth but not flat. Other methods to obtain smoothening IRL are currently under investigation, including post-deposition plasma treatment of standard IRLs, as well as new alternatives to directly obtain a smooth morphology, notably with liquid-phase deposition techniques exploiting the wettability of the surface. Such techniques are very promising to reproduce the gains observed with polished SiO-based IRLs

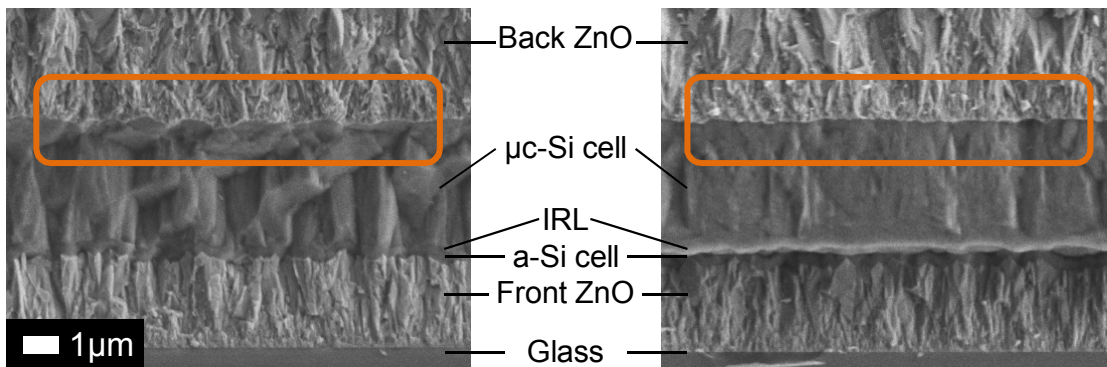


Figure 7.4: Cross section SEM view of Micromorph devices including (left) a standard IRL or (right) a polished one. The highlighted area shows the absence of the natural texture at the back of the  $\mu\text{c-Si:H}$  cell when a polished IRL is employed.

without shunting or drastic losses in reflection and are further described in sections 7.4 and 7.5.

### 7.3 Thick ZnO-based intermediate reflecting layers

Another route consists of inserting a textured IRL, with a morphology dedicated to the bottom cell, enabling the front electrode morphology to be optimized only for the top cell. This concept has been suggested in [Obermeyer 08] based on simulations, and was successfully implemented for  $n-i-p$  cells in [Söderström 09], for which a textured ZnO IRL was shown to enable a top cell current boost compared to a flat IRL. This approach is not strictly speaking a smoothing of the IRL surface, but rather a multi-scale texturing, for which the morphology required for a high-efficiency bottom cell is adjusted with the IRL. Fig. 7.5 shows EQE of Micromorph cells where a textured LPCVD ZnO IRL enhances the bottom cell current and efficiency. Increasing the thickness of the LPCVD ZnO IRL increases the size of the features composing its surface, enhancing the scattering of large wavelength light, as described in chapter 5.

This result validates the concept of introducing a dedicated light-scattering strategy for each sub-cell. However, the four devices compared in Fig. 7.5 include a thin and doped front electrode, which is not suitable for high-efficiency Micromorph cells. To verify the advantage of this approach compared to a single light-scattering strategy given by the rough electrode only, a second set of experimental data is presented in Tab. 7.2. In this study, a Micromorph device with a rough 3- $\mu\text{m}$ -thick ZnO (Z3) front electrode and a SOIR is compared to devices with a 1- $\mu\text{m}$ -thick ZnO (Z1) front electrode and a SOIR, a rough Z3 IRL or a smooth Z3 IRL. All ZnO layers are non-intentionally-doped ( $n-i-d$ ), and a 120-nm-thick IOH layer is deposited before the Z1 to ensure sufficient conduction. The smoothness of the Z3 layer was set by adjusting the duration of an argon plasma post-deposition treatment [Bailat 06] between 7 minutes (rough) and 21 minutes (smooth). The effect of the plasma treatment is discussed in

### 7.3. Thick ZnO-based intermediate reflecting layers

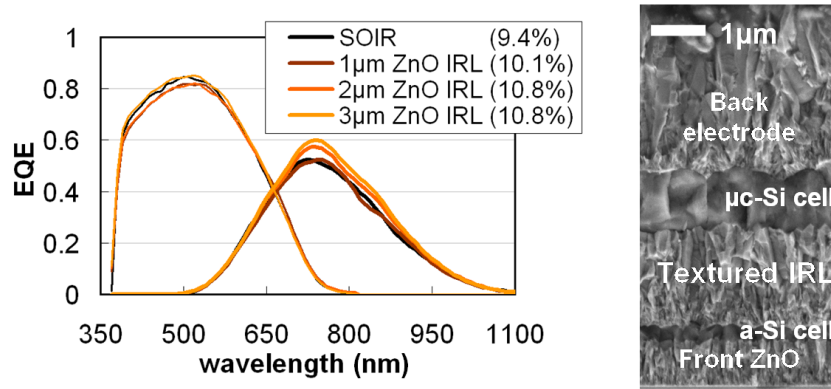


Figure 7.5: EQE of thin Micromorph cells (bottom cell of 1.2  $\mu\text{m}$ ) grown on a thin (1.1  $\mu\text{m}$ ) LPCVD ZnO front electrode using different intermediate reflectors: a 100-nm-thick SOIR, or a 1- $\mu\text{m}$ -, 2- $\mu\text{m}$ - or 3- $\mu\text{m}$ -thick ZnO IRL (corresponding SEM graph on the right). The two latter enhance the bottom cell current (and the efficiency indicated in brackets) thanks to improved light scattering at large wavelengths.

Table 7.2: Micromorph devices parameters for different ZnO front electrode thicknesses and IRL types. Top cell currents with \* indicate underestimated values due to measurement problems caused by shunting of the top cell (as assessed by the low 0.4%-illumination  $V_{oc}$  value). The top cell current for these devices is estimated to be above  $12\text{ mA/cm}^2$ , making them bottom limited.

	$V_{oc}$ (V)	$FF$ (%)	$V_{oc}$ 0.4% <i>ill</i> (V)	$J_{sc, top}$ ( $\text{mA/cm}^2$ )	$J_{sc, bottom}$ ( $\text{mA/cm}^2$ )	Eff. (%)
rough-Z3 w/ SOIR	1.37	68.8	0.89	12.3	11.0	10.4
Z1 w/ SOIR	1.41	72.9	0.96	12.1	10.1	10.4
Z1 w/ rough-Z3-IRL	1.35	71.9	0.31	9.4*	11.3	11.0
Z1 w/ smooth-Z3-IRL	1.36	74.7	0.31	11.2*	10.6	10.8

chapter 5.

As seen in the  $V_{oc}$  values shown in Tab. 7.2, using a Z3 in any place in the device induces 40 mV to 60 mV of losses compared to the use of a Z1 only. The presence of a ZnO-based IRL is also shown to favor shunting of the top cell, probably by interconnection of the shunts in the top cell through the conductive ZnO-based IRL. This makes a top-cell current discussion difficult, but Fig. 7.5 suggests that the top cell current is not drastically changed when replacing a SOIR by a thick ZnO-based IRL. Also, the bottom cell currents obtained with a Z1 electrode combined with a Z3 IRL are not much larger than with a Z3 electrode combined with a SOIR. Therefore, no significant improvement of the trade-off between light-harvesting and the quality of the silicon layers could be shown by using a thick ZnO-based IRL. The higher efficiency that is yet observed compared to the devices using a SOIR originates principally from a  $FF$  gain compared to devices using a SOIR, partly due to a too resistive SOIR layer inducing an extra open-circuit resistance of  $3\Omega\cdot\text{cm}^2$ , corresponding to around 2% of  $FF$  change as discussed in

chapter 5.

No strong benefit of using this architecture could finally be shown. This is mostly due to the high sensitivity towards shunting of Micromorph devices implementing a very conductive IRL. Also, as parasitic absorption is a strong limitation in terms of light harvesting (chapter 3), the use of a 3- $\mu\text{m}$ -thick ZnO-based IRL does not appear to be a very attractive approach. In the following more transparent and resistive IRLs are studied.

### 7.4 Spray-coating of ZnO from Zn-acetate

All experimental work presented in this section was performed by Hamed Achour during his Master's thesis work [Achour 12]. The aim here was to deposit a non-conformal ZnO layer that would be thicker in the bottom of the features than at the tips. This is expected with liquid-based deposition on a surface with a favorable wettability, contrary to CVD deposition, which favors pinching. A picture of the setup is shown in Fig. 7.6a, and a sketch of the process is given in Fig. 7.6b. The setup consisted of a hot plate on which the substrate was heated to the desired temperature, a manual nozzle, a pressured nitrogen gas input and a container for the solution of the Zn precursor. Thermally assisted oxidation uses ambient air as an oxygen source.

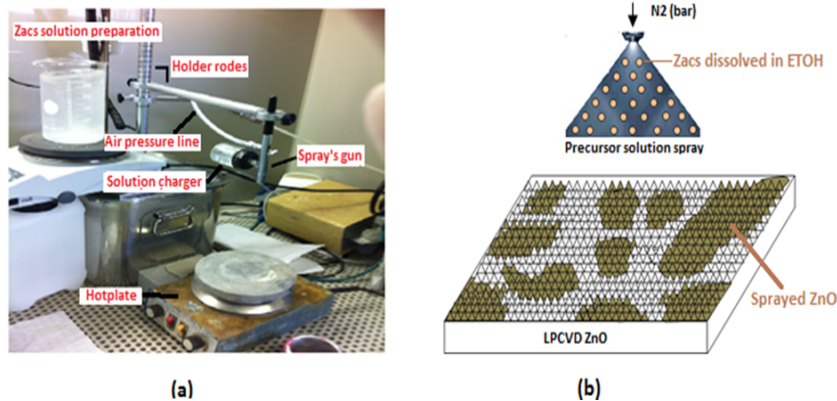


Figure 7.6: a) The setup mounted for ZnO spraycoating. b) Sketch of the deposition process. [Achour 12]

Zinc acetate di-hydrate (Zn-Ac) was chosen as a precursor, and ethanol as a solvent, as this combination is widely used for ZnO spraycoating [Aranovich 79]. Ethanol was also preferred to water as the latter does not wet the rough surface of the *a*-Si:H cell. Zn-Ac requires high temperatures to fully decompose into ZnO (typically above 300 °C), which were experimentally shown to be detrimental to the *a*-Si:H top cell, even for a short time of a few minutes. Nevertheless, partial oxidation was observed for temperatures as low as 180 °C, as observed from Fourier transform infra-red spectroscopy measurements of films deposited at various temperatures. This partial oxidation allowed the coplanar resistivity of 400-nm-thick layers

#### 7.4. Spray-coating of ZnO from Zn-acetate

deposited at 180 °C and annealed at 180 °C for one hour to be around  $2 \cdot 10^6 \Omega \cdot \text{cm}$ , whereas 100 nm thick layers deposited at 350 °C exhibited three orders of magnitude lower values. For a 100-nm-thick IRL to be implemented without significant resistive losses in a Micromorph device, a maximal resistivity of  $1 \cdot 10^5 \Omega \cdot \text{cm}$  can typically be tolerated [Cuony 11], making the layers deposited at 180 °C apparently too resistive. Also, contrary to SOIR layers, no strong difference between transverse and coplanar resistivity values were seen. To improve the conductivity of sprayed ZnO films, a higher deposition temperature can be used.

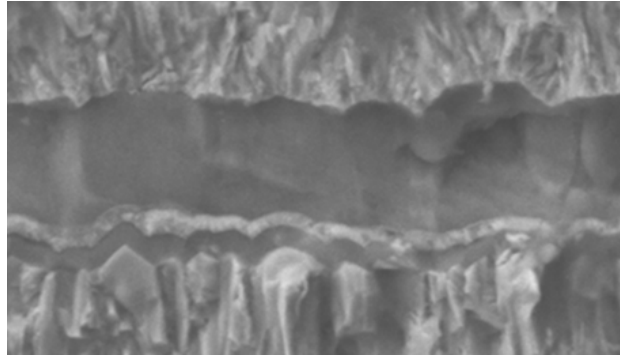


Figure 7.7: SEM cross section of a Micromorph device including a sprayed ZnO IRL obtained by cutting the device. [Achour 12]

First implementations of sprayed ZnO IRL in Micromorph devices were made, with a 250-nm-thick layer deposited at 250 °C, in spite of a known degradation of the *a*-Si:H top cell for this temperature. This led to promising results in terms of morphology as seen in Fig. 7.7. Concerning the electrical parameters, a large gain in terms of *FF* was observed, as seen in Fig. 7.8, mostly due to the shunt-quenching effect of the sprayed ZnO IRL, compared to a standard deposited ZnO, due to the low lateral resistivity. No noticeable series resistance increase was observed, indicating that layers deposited at 250 °C are conductive enough.

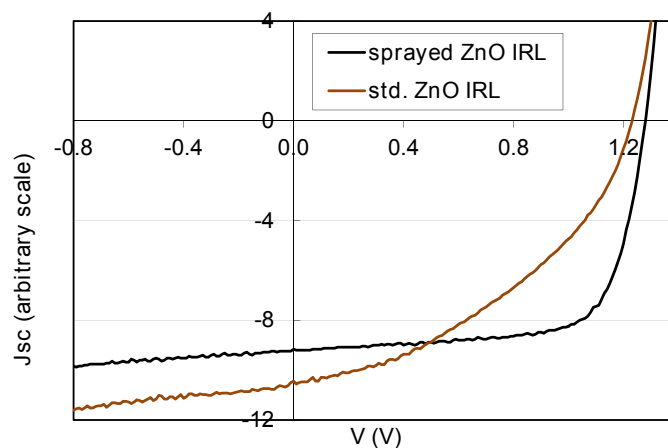


Figure 7.8: *J*(*V*) characteristics of Micromorph devices with a standard vacuum-deposited ZnO IRL or a sprayed ZnO IRL. [Achour 12]

Nevertheless, no high-efficiency device including a sprayed ZnO-based IRL could be obtained, and no clear  $V_{oc}$  gain was observed (as was expected from the planarizing effect, possibly due to a  $V_{oc}$  degradation of the top cell during the ZnO-based IRL deposition). Also, no potential gain could be evidenced when comparing with a SOIR. Overall, this approach remains of interest, considering the many positive properties of sprayed ZnO: planarizing effect; low lateral conductivity for a sufficient transverse conductivity; possible porosity, leading to a low refractive index; and easy process with low deposition costs. On the other hand, the following limitations apply: thermal damage of the top cell or resistive losses depending on the deposition temperature; enhanced reflection losses / parasitic absorption when employing sufficiently thick films for planarization; and challenging film uniformity and homogeneity with low-cost equipment. Spray-coating of ZnO IRL remains thus an attractive approach which still requires further development to be applicable.

## 7.5 Spin-coating of lacquer with selective etching

### 7.5.1 Motivation and experimental procedure

The approach studied in the following, sketched in Fig. 7.9, is to spin-coat a lacquer on top of the *a*-Si:H cell to act as a planarizing IRL by exploiting the natural propensity of the lacquer to fill the sharp valleys of the structure. The lacquer used here is an insulating glass-like material that ensures a maximal transparency and a low refractive index (around 1.5). First attempts showed that a layer of spin-coated lacquer prevents the correct flow of carriers through the device: S-shape curves were obtained, even for diluted lacquer (leading to thin layers). A slight polishing was shown to circumvent these losses, but similar reflection losses and shunting issues occurred as for polished SiO-based IRLs. Including nanoparticles or nanowires of conductive material in the lacquer matrix was attempted, so far without success. The two main limitations of this approach are that transparency is reduced when including conductive material, and that a high density of particles is needed to ensure percolation. This track was abandoned to focus on partial etching of the lacquer IRL.

The lacquer used was Ormocer from Microresist technology GmbH, which is organic and inorganic and possesses the quality of being UV-curable (thus requires no high temperature step to cure it), resistant to high vacuum and high temperature processes (up to 250 °C) and highly transparent. It can be etched with a fluor- and oxygen-containing plasma, *e.g.* SF<sub>6</sub> mixed with O<sub>2</sub>. This plasma composition corresponds to the composition used to etch silicon. Protection of the *a*-Si:H cell before lacquer deposition and etching is thus imperative. A thin (10 nm) sputtered ZnO layer was used to fulfill this etch-stop role.

The fabrication sequence of a Micromorph cell with such an IRL is sketched in Fig. 7.9, and two cross section views (at different locations) of this type of device are shown in Fig. 7.10. As the surface of the *a*-Si:H top cell is rough, lacquer preferentially fills the pinches, and is thinner on top of the tips (Fig. 7.9, 3). By tuning the roughly non-selective plasma etching time,



## 7.5. Spin-coating of lacquer with selective etching

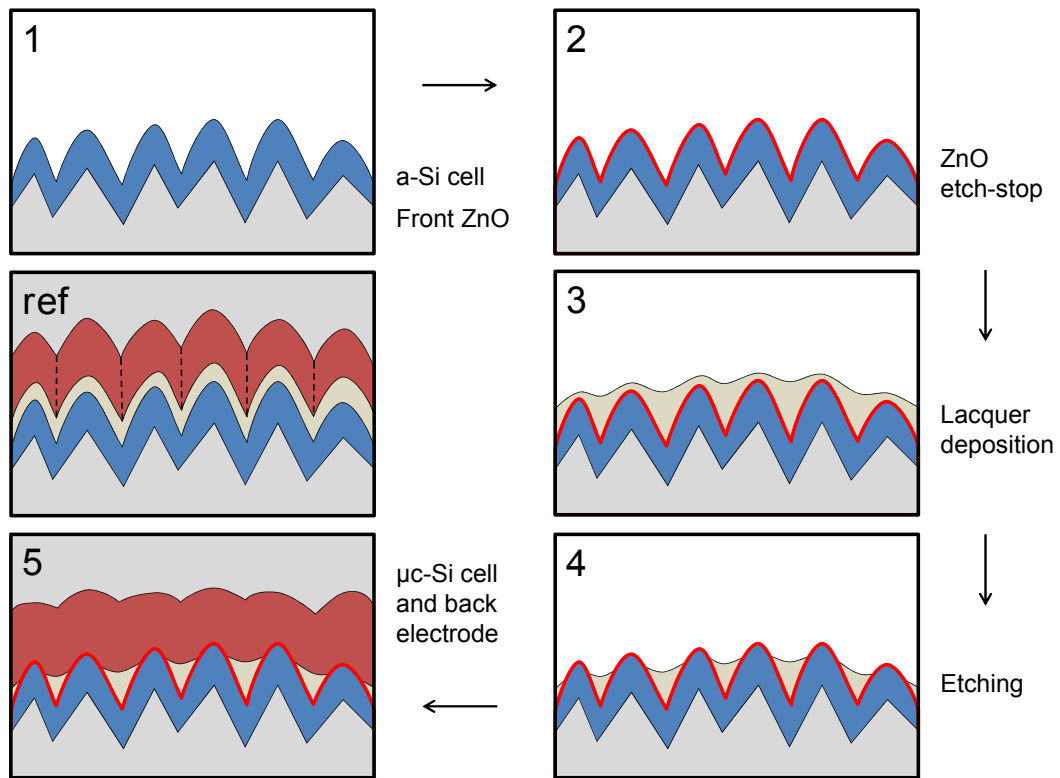


Figure 7.9: Schematic view of the processes leading to a Micromorph cell with a smoothing IRL (1 to 5). A schematic view of a reference Micromorph including a standard IRL is also indicated.

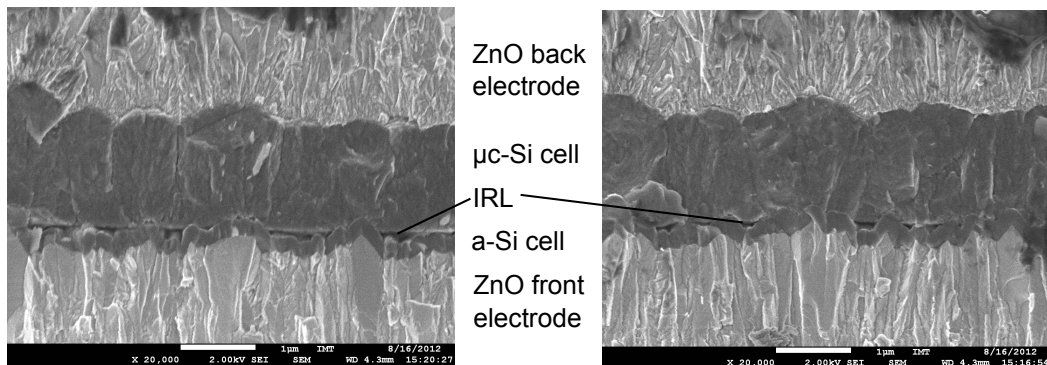


Figure 7.10: SEM side-view of a Micromorph device including an IRL made of partially etched lacquer. The front electrode is a 2.5- $\mu\text{m}$ -thick ZnO layer, lacquer dilution is 1/16 and etching time was three minutes. Note that the interface between the silicon and the ZnO back electrode layers still exhibits a significant micron-scale modulation.

it is possible to free the tips while keeping lacquer in the pinches (Fig. 7.9, 4). This allows the electrical series connection between the top and bottom cells. The lacquer can also be diluted in a specific solvent to thin the resulting layer. The solution is spin coated, then solvent is

evaporated by placing the samples on a hot plate (90° for 15 min), and the samples are placed under UV light to cure the lacquer for 1 h.

Overall, adjustable parameters are the lacquer dilution (to thin the lacquer layer) and the etching time (to partially remove lacquer). In a complete device, a smoothing IRL should enable the use of rougher electrodes or more sensitive  $\mu c$ -Si:H material (such as high-rate deposited or more crystalline), compared to a conformal IRL, making complete device optimization required to fully benefit from this advanced layer.

### 7.5.2 Electrical performance

The electrical parameters of Micromorph devices deposited on reference substrates (2.5- $\mu\text{m}$ -thick lowly doped ZnO layer smoothed by an argon plasma for four minutes) including a spin-coated IRL are shown in Fig. 7.11. Note that no optimization was made (the matching was not adapted), so that a simple comparison of the efficiencies is not representative of the potential of each structure.  $V_{oc}$  improvements were observed when using a spin-coated IRL compared to no IRL or a standard SOIR, with values up to 1.39 V compared to 1.34 V and 1.36 V for the references, validating the smoothing effect. The  $FF$  was not affected by the presence of the isolating lacquer, indicating that the partial etching provides a sufficient conduction path. Also, high top cell currents (similar to or higher than the one obtained with a SOIR) are obtained, making this smoothing layer an efficient IRL. However, a good tuning of the etching time of the spin-coated IRL is necessary to find a good trade-off between optical and electrical performance: a too long etching time (removing most of the lacquer, also from the pinches) lowers the  $V_{oc}$  gain, but a too short etching time induces losses in the bottom cell current (as seen for only 2 minutes of etching in Fig. 7.11). This optical effect and its dependence over the roughness of the front electrode will be discussed in section 7.5.3.

Fig. 7.12 shows the electrical parameters of Micromorph devices deposited on a 5- $\mu\text{m}$ -thick lowly doped ZnO layer smoothed by an argon plasma for 10 minutes. The large and sharp features composing the surface of this substrate (peak-to-peak height of 1.3  $\mu\text{m}$  and median inclination of 40°) lead to the formation of pinches after the deposition of the top cell (and possibly SOIR), resulting in an inhomogeneous deposition of  $\mu c$ -Si:H, with low-density areas that are growing above the pinches (as sketched by dashed lines in Fig. 7.9, and detailed in chapter 3 of [Cuony 11]). This explains the 10 mV lower  $V_{oc}$  value obtained for the device using a SOIR compared to the corresponding devices on the reference substrate.  $V_{oc}$  values of reference  $a$ -Si:H single-junction devices on both substrates were 0.90 V, indicating that both substrates yield good-quality  $a$ -Si:H cells. Yet, when using a spin-coated IRL etched for 2 minutes,  $V_{oc}$  values of 1.39 V can be obtained on both substrates, indicating that the morphology of the IRL surface is efficiently smoothed.

For all  $a$ -Si:H top cells, a triple-thickness ( $\sim 90$  nm) SiO  $n$ -doped layer was included, in order to prevent possible partial etching of the  $n$ -doped layer of the top cell during selective etching of the lacquer (due to the very thin ZnO etch-stop layer employed). Fig. 7.12 shows that



## 7.5. Spin-coating of lacquer with selective etching

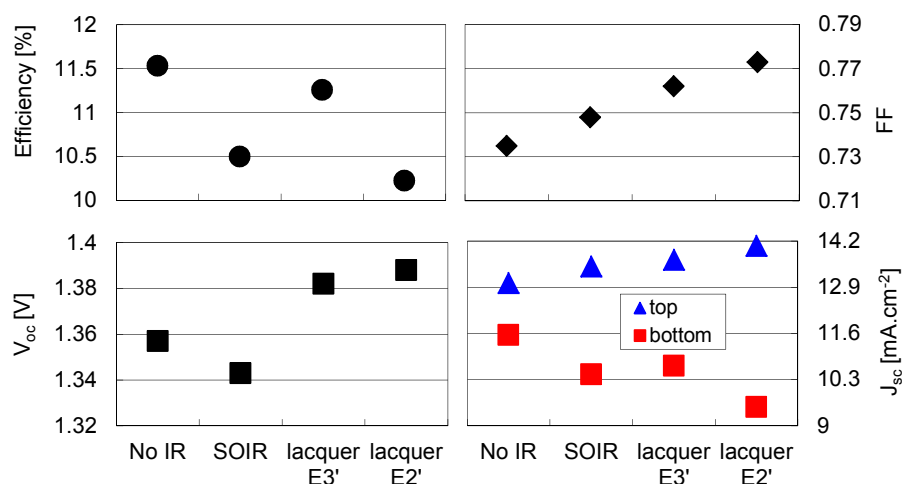


Figure 7.11:  $V_{oc}$ ,  $FF$ ,  $J_{sc}$  and efficiency values of Micromorph cells deposited on a 2.5- $\mu\text{m}$ -thick ZnO front electrode etched for 4 minutes, with no IRL, a SOIR, or an IRL made by spin-coating a lacquer diluted at 1/16, or subsequently etching it for 3 minutes or 2 minutes. In all cases, the top cell includes a triple-thickness ( $\sim 60$  nm) SiO  $n$  layer in addition to a single-thickness  $\mu\text{c-Si:H}$   $n$ -doped layer (for IRL effect and shunt quenching).

similar electrical performances can be obtained with a single-thickness  $\mu\text{c-Si:H}$   $n$ -doped layer, infirming this hypothesis.

### 7.5.3 Optical effects

Figs. 7.13 and 7.14 show the influence of the front electrode roughness and of the etching time on the optical effects of the smoothing IRL. The reduction in the bottom cell EQE is due to reflection losses (as verified by spectrometer measurements on another series). From these graphs, it can be seen that increasing the etching time reduces the reflection losses, and that these losses are reduced faster when the substrate roughness is higher. This can be intuitively understood by considering that a roughly constant volume of diluted lacquer is spin-coated for all substrates, making the final lacquer volume remaining after evaporation of the solvent constant. When the roughness is increased, the volume needed to fill the valleys increases as well, and the thickness of the lacquer on top of the tips is reduced, hastening their unveiling by plasma etching.

A large current increase is observed in the top cell with the spin coated IRL, even larger than the one with a standard SOIR with two minutes of etching. This is ascribed to the lower refractive index of the lacquer ( $< 1.5$ ) compared to the SOIR (typically 1.8). This could be due also to a larger thickness, but as the SOIR is conformal but the spin-coated IRL not, any thickness comparison is not straightforward. In the case of the lacquer etched for three minutes, the currents in the top cells are similar to the ones obtained with the SOIR, with however a lower total current. Overall, optical performances are balanced, with a possible larger current gain than the SOIR in the top cell, but at the cost of larger losses in the bottom cell current. Tuning

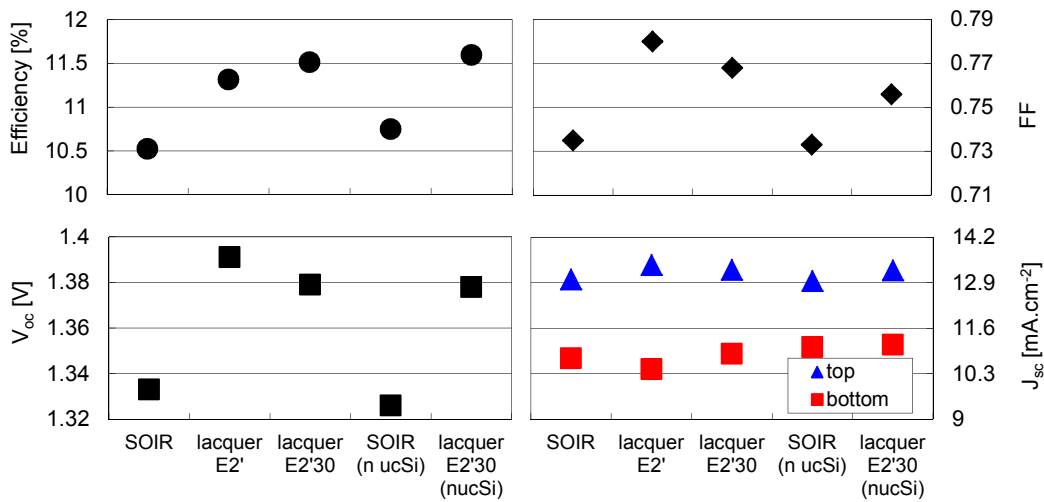


Figure 7.12:  $V_{oc}$ ,  $FF$ ,  $J_{sc}$  and efficiency values of Micromorph cells deposited on a 5- $\mu\text{m}$ -thick ZnO front electrode etched for 10 minutes, with a SOIR, or an IRL made by spinn-coating a lacquer diluted at 1/16, and subsequently etching it for 2.5 minutes. The top cell includes a double-thickness SiO  $n$ -doped layer in addition to a single-thickness  $\mu\text{c}$ -Si:H  $n$ -doped layer for the first three points, and only a single-thickness  $\mu\text{c}$ -Si:H  $n$ -doped layer for the last two points.

of the etching time could lead to a good compromise.

#### 7.5.4 General discussion

Overall, in addition to efficiently smoothing the top-cell surface (as assessed by a 50 mV  $V_{oc}$  gain compared to a standard IRL), this new layer fulfills all the requirements for an IRL described in section 7.1:

1. The transverse conduction is ensured through the uncovered tips of the features (assessed by no additional series resistance and excellent  $FF$ ),
2. The transparency is excellent and is accompanied by a very low refractive index of  $\sim 1.5$  (assessed by the high top-cell and total currents measured),
3. No thermal damage for the  $a$ -Si:H cell, as the solvent evaporates at 90 °C and the lacquer is then cured under UV light (no deterioration of the electrical performance of the top cell), and
4. The Resilience to the bottom cell deposition conditions, especially heating up to 200 °C under high vacuum (excellent properties of the bottom cell, with no collection issue indicating that no contamination occurred).

This newly developed technique that allows an efficient planarization with partial covering could be of interest for other photovoltaics technologies or at other places in thin-film silicon cells, as illustrated in appendix C. Finally, the use of spin-coated IRLs brings a new way of

## 7.5. Spin-coating of lacquer with selective etching

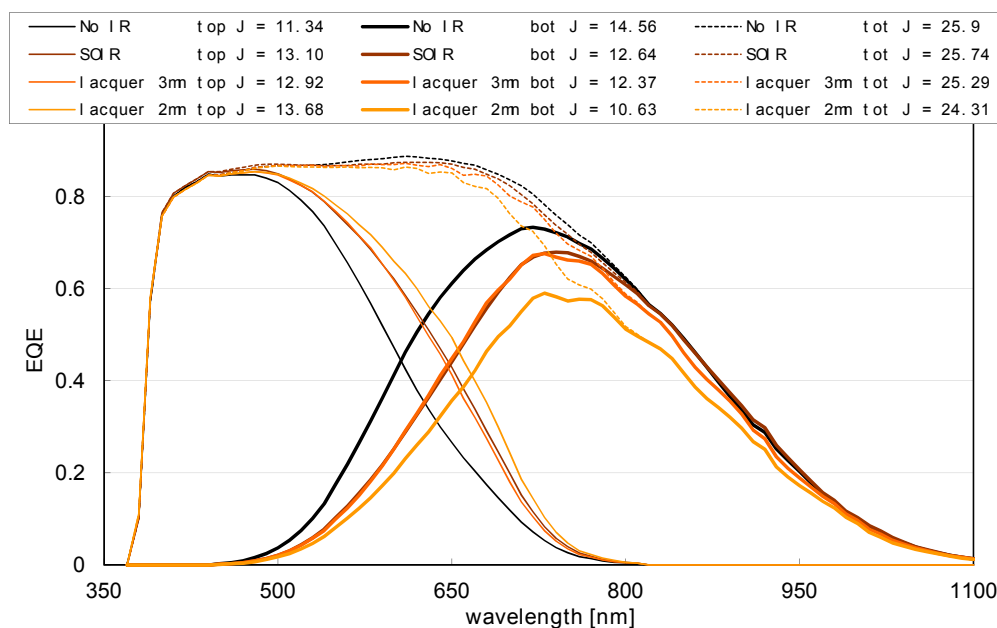


Figure 7.13: EQE of Micromorph cells deposited on a 2.5- $\mu\text{m}$ -thick ZnO front electrode, with no IRL, a SOIR, or an IRL made by spin coating a lacquer diluted at 1/16, and subsequently etching it for 3 minutes or 2 minutes.

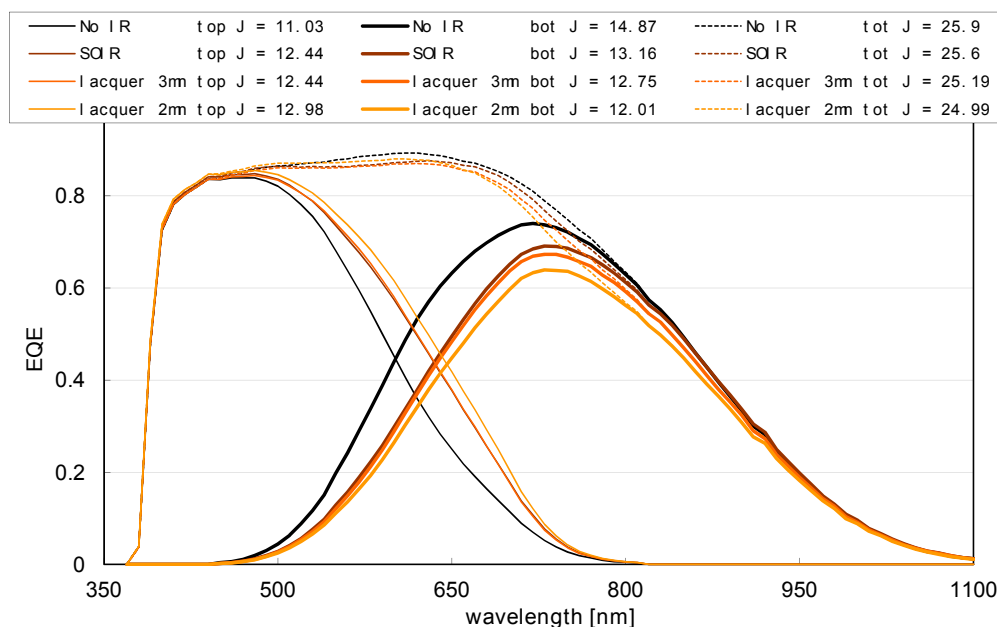


Figure 7.14: EQE of Micromorph cells deposited on a 5- $\mu\text{m}$ -thick ZnO front electrode, with no IRL, a SOIR, or an IRL made by spin coating a lacquer diluted at 1/16, and subsequently etching it for 3 minutes or 2 minutes.

unlinking light trapping in the top cell, light trapping in the bottom cell and the morphology of the surface on which the  $\mu c$ -Si:H sub-cell is grown. With this additional tool, a new optimum single-scale substrate morphology could potentially be found towards sharper and larger features, as suggested in Fig. 7.1.

### 7.6 Potential for high-efficiency Micromorph devices

All along the previous chapters, an analysis of the requirements, in terms of device architecture, for high-efficiency Micromorph cells has been presented. Based on recent developments, it is thought that the detrimental influence of the rugged morphology on the electrical performances is mostly due to the presence of nanoporous 2D regions that typically form during  $\mu c$ -Si:H growth above the bottoms of the substrate features [Bugnon 12]. In the case of Micromorph tandem devices, even when a smooth substrate is employed, the deposition of the  $a$ -Si:H layers usually worsen the sharpness of these bottoms (commonly referred to as “pinching”). This effect is described in [Cuony 10, Python 10] and can be seen in Fig.6.12.

The formation of this defective localized nanoporous region can be limited by the use of adapted plasma conditions when growing the  $\mu c$ -Si:H layers; or their effect can be reduced by employing resistive layers in the architecture of the devices. Both approach are however limited, and the best efficiencies for single-junction  $\mu c$ -Si:H cells grown on LPCVD ZnO are still reported on a substrate that was smoothed in an argon plasma [Hänni 12, Bugnon 12]. A drastic efficiency improvement is therefore expected by applying a smoothing treatment before growing the  $\mu c$ -Si:H cell in the case of Micromorph tandem devices.

As seen in this chapter, such morphology adaptation is challenging but some of the presented concepts are promising. In the case an excellent morphology could be obtained, similar to the one used in [Hänni 12] and [Bugnon 12], a high quality bottom cell enabling for a  $J_{sc, sum}$  of  $27.4 \text{ mA/cm}^2$  could be obtained. Together with a high-quality top cell, as recently presented in [Matsui 12], a 13.5% stable efficiency Micromorph device is within reach, as detailed in Tab. 7.3 in which both sub-cells are simulated with a two-diodes model including a recombination term [Python 08].

No extra loss or extra gain was included in the calculation. This simple calculation gives yet an immediate potential of 13.5% for Micromorph devices including existing single-junctions. The two challenges to realize this device are the reaching of  $14 \text{ mA/cm}^2$  in the top cell (requiring an efficient IRL) and the deposition of a  $\mu c$ -Si:H cell of quality similar to the one obtained in single-junction. Both of them require the use of an advanced smoothing IRL, making the development of such a layer of great potential. We believe that with fine-tuning and advanced light management, efficiencies of up to 14.5% can still be reached, with the paramters given for the Micromorph<sup>++</sup>. The improvement of  $V_{oc}$  would here reflect the possibility to use a thinner bottom cell for similar  $J_{sc, sum}$ . Indeed, to benefit in terms of  $J_{sc}$  from a better light trapping (mostly improving the weak absorption region of the complete device, thus mostly the bottom cell), the top cell current should be improved as well. Doing so would allow for

Table 7.3: First two columns: electrical parameters of state-of-the-art single-junction  $a$ -Si:H and  $\mu c$ -Si:H solar cells. Next two columns: calculated individual parameters of these single-junction devices when implemented in a Micromorph tandem (modification of the photogenerated current). Fifth column: calculated electrical performance of the resulting Micromorph device. Last column: calculated electrical performance for a more optimistic device.

	$a$ -Si:H	$\mu c$ -Si:H	$a$ -Si:H	$\mu c$ -Si:H	Micromorph	Micromorph <sup>++</sup>
$V_{oc}$ (V)	0.882	0.535	0.878	0.513	1.391	1.45
$FF$ (%)	69.0	74.3	69.2	73.2	73.6	74.0
$J_{sc}$ (mA/cm <sup>2</sup> )	15.8	27.4	14.2	13.1	13.2	13.5
Eff. (%)	9.6	10.9	8.6	4.9	13.5	14.5

Micromorph devices to attain 15% efficiency, which is also possible by improving the materials or interfaces of the single-junction devices. It should be kept in mind that the theoretical limit of the Micromorph concept lies above 30% efficiency [Meillaud 06], and that an efficiency over 16% in the middle term is not unrealistic with slightly improved materials (*e.g.* with  $V_{oc}$ ,  $FF$  and  $J_{sc}$  values of 1.5 V, 74% and 14.5 mA/cm<sup>2</sup>, which were all independently achieved already). The recent achievement in PVlab of  $\mu c$ -Si:H cells with a  $V_{oc}$  of up to 609 mV is to this respect a promising step.

## 7.7 Conclusion

Smoothing the IRL surface was shown to have a high potential to bypass the present efficiency limitation in Micromorph devices. With finely tuned layers, an improvement of the electrical performance can be obtained without optical losses, which is usually not the case as seen in previous chapters (*e.g.* when varying the substrate roughness or conductivity). Polishing of standard IRLs was shown to enable  $V_{oc}$  increase at one sun illumination, but to lead to shunting issues and reflection losses. Thick ZnO IRLs, which enable dedicated features for the top cell and dedicated features for the bottom cell, were also studied. Even though the concept is of interest, the lateral conductivity of such IRLs induces shunting issues. The possibility of using spray-coated ZnO IRLs was also probed. The main issue that arose was to combine sufficient conductivity with a low deposition temperature. Finally, a new interlayer was developed, using an isolating lacquer, deposited by spin-coating, and selectively plasma-dry-etched to open a path for carrier conduction. This new type of IRL was shown to combine excellent transparency with a low refractive index, sufficient transverse conduction and tunable smoothing. With this type of smoothing IRL, varying the lacquer dilution and the etching time allows a smooth but not flat IRL - bottom cell interface to be obtained. Significant improvements in terms of efficiency are expected by combining this new type of IRL with adapted device architectures (typically using rougher electrodes and more crystalline  $\mu c$ -Si:H bottom cells than present high-efficiency devices). Lacquer can also be used at the front or back of the cell, to adapt the morphology of the electrode or the cell, and to attenuate

## **Chapter 7. Smoothing intermediate reflecting layers**

---

the effect of the local porous areas, as briefly described in appendix C. By combining an advanced device architecture with current state-of-the-art single junction devices, it has been shown that a 13.5% efficiency Micromorph is within reach.

# 8 Conclusion and perspectives

## 8.1 General conclusion

We combined in chapter 3 the recent developments of Dominé allowing an easy calculation of the light-scattering properties of any rough substrate with the 30-year-old formalism introduced by Deckman *et al.* to calculate light absorption in solar cells incorporating light-trapping strategies. A fair agreement with experiment was demonstrated, along with an intuitive understanding of the interdependence of the main parameters. We showed that present state-of-the-art light-trapping strategies (*e.g.* with as-deposited 2- $\mu\text{m}$ -thick LPCVD ZnO) come close to the Lambertian limit introduced by Yablonovitch; most of the losses come currently from parasitic absorption. Our model suggests that this limit could be overpassed by scattering light at a large angle for the first scattering events, thus elongating greatly the light path before the first escape possibility can occur (*i.e.* before light reaches the front interface again).

Chapter 4 was dedicated to the optical properties of Micromorph devices. The link between haze calculated for scattering from a TCO to silicon and the current output was experimentally assessed, confirming the validity of the theoretical developments. Also, as a first approximation, it was suggested to use the haze measured for scattering from a TCO to air, but at a wavelength  $\lambda/2$  as an estimate for the light haze value for scattering in silicon at a wavelength  $\lambda$ . The impact of parasitic absorption, and in particular free-carrier absorption (FCA) was evidenced. An experimental validation of the “corrected EQE” introduced by Dominé could also be obtained. The similar influence of FCA in the front and back electrodes was then experimentally assessed. Their interdependence was also shown, and the importance of working in reducing parasitic absorption for both electrodes was evidenced. In a final section an advanced concept enabling excellent light trapping was suggested, based on a microlens array. Such a geometrical optical system enables all light (of normal incidence) to enter the cell through apertures in a perfectly reflecting layer, but prevents escape for 80% of the light. In spite of around 20% of recoverable losses, we showed a current gain in the weak absorption region of the spectrum. For such excellent light trapping, enabling light to experience additional

## Chapter 8. Conclusion and perspectives

---

passes back and forth between the front and back interfaces, parasitic absorption is even more critical and limits massively the reachable current. Most of the absorption enhancement in the experimental device could indeed be attributed to parasitic absorption. Improving parasitic absorption was thus shown to be mandatory to benefit from improved light-trapping schemes.

In chapter 5, a thorough investigation of the superstrate requirements for high-efficiency Micromorph devices was made. The double trade-off between, on the one hand, conduction and transparency and, on the other hand, light scattering and electrical quality is addressed. The different morphology requirements when aiming at a high current in the top cell or in the bottom cell were also shown. A comprehensive graphical mapping of the properties of Micromorph cells as a function of the typical size and inclination of the features composing the surface of the superstrate was made. Even though it depends on the device architecture (in particular the resilience to high aspect ratio structures and local low-quality material), this graphical representation points out the need for more degrees of freedom in a tandem device. Concerning conduction and transparency, the use of thick and lowly doped TCO is shown to better address the trade-off than thin and doped material. A maximum sheet resistance value was determined for the cell geometry used in this document, and the link to series resistance losses was clearly shown. The influence of the matching conditions between both sub-cells ( $J_{sc, top} - J_{sc, bottom}$ ) on the  $FF$  of the device was quantified, with notably up to 2% of  $FF$  increase per  $\text{mA}/\text{cm}^2$  of bottom limitation.

Chapter 6 introduced superstrates exhibiting multi-scale textures for Micromorph devices. In the first part, the possibility of better addressing the morphological trade-off between electrical quality and a high current in both sub-cells was verified. It was thus shown that a thin (1- $\mu\text{m}$ -thick) LPCVD ZnO layer provides small and sharp features that are efficient to suppress reflection losses at the TCO - silicon interface, and to enable a good light trapping in the top cell. Implementing a larger-scale texture underneath was shown to enable a bottom cell current increase up to values similar to the values obtained with state-of-the-art single-scale textures. Also, when the large-scale texture was chosen smooth enough, the resulting multi-scale morphology resulted in an improvement of the electrical quality of the Micromorph device. In the second part of the chapter, the large-scale morphology was imprinted in lacquer, and conduction was ensured with a thin, high-mobility hydrogenated indium oxide layer, in addition to a 1- $\mu\text{m}$ -thick n-i-d LPCVD ZnO layer. With this three-layer architecture, a 14.1% efficiency device with a  $14 \text{ mA}/\text{cm}^2$  short-circuit current density was obtained.

Another approach to add a degree of freedom to the morphological optimization was suggested in chapter 7, by adapting the surface on which the  $\mu\text{c-Si:H}$  cell grows. This is achieved by developing smoothening intermediate reflecting layers (IRL). Polishing a thick IRL deposited from standard vacuum techniques was shown to lead to  $V_{oc}$  improvements but also to shunting issues and reflection losses, making this solution unfavorable. Then, the use of sprayed ZnO as a smooth IRL was shown to lead to promising morphologies, but the high temperatures needed to completely oxidize the zinc acetate precursor degrade the  $a\text{-Si:H}$  top cell. Finally,



an innovative way of obtaining a smooth IRL was developed by using a partially etched spin-coated lacquer. By adapting the dilution of the lacquer, the initial thickness of the lacquer layer could be tuned, to enable filling of the pinches that develop during the *a*-Si:H cell deposition. A short plasma dry-etching can then completely remove lacquer from the tips, while leaving lacquer in the pinches. To prevent damage to the *a*-Si:H cell, a 15-nm-thick ZnO etch-stop layer was deposited on the *a*-Si:H cell before lacquer coating. Significant  $V_{oc}$  gains, with a large IRL effect were obtained, making this layer very promising.

Globally, a promising state-of-the-art architecture that is derived from the studies presented in this document is given in Fig. 8.1. Combined with state-of-the-art single junction devices, a Micromorph device with a stabilized efficiency of 13.5% is within immediate reach (with *e.g.* 1.39 V, 73.6% and 13.2 mA/cm<sup>2</sup> of  $V_{oc}$ ,  $FF$  and  $J_{sc}$ ).

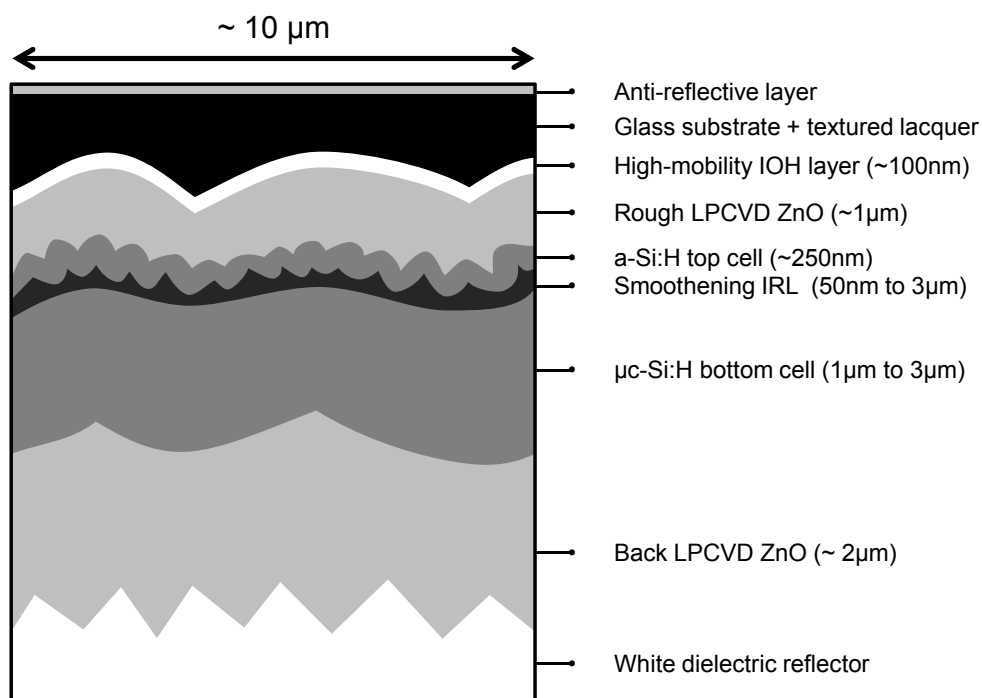


Figure 8.1: Schematic of a Micromorph device including the developments presented here.

## 8.2 Perspectives

A comparison of the simple modeling approach presented in chapter 3 with other (more rigorous) simulation techniques would be of interest to clarify the range of validity of this approach, as well as modeling other device configurations (such as substrate type). This model points out the importance of the first way back of light in the light harvesting, which should be verified experimentally by developing light-harvesting schemes that better scatter light hitting the back of the silicon layer at a large-angle. To achieve this, metallic reflectors in the close vicinity of the silicon layers (such as a thin ZnO / silver back reflector stack) may be helpful.

In the quest for high-efficiency devices, most of the gains in current have been obtained by reducing parasitic absorption in the device, through more transparent electrodes, or more transparent doped layers. Significant gains are still expected by continuing to identify the sources of parasitic absorption. A precise quantification of the share of the electrodes, doped layers, and back reflector could be done experimentally by selectively omitting each layers in the cell stack, measuring total absorptance and comparing the results with simulation. For such a study, escape from the side of the cell — experimentally attributed to parasitic absorption — should be precisely quantified.

Concerning the morphology of the electrode, ways of improving the resilience of the cell to rugged morphologies should be looked for. A promising approach by using lacquer, which should be further validated, is depicted in appendix C. Also, the benefit of a smoothening IRL made of lacquer should be studied for various front electrode roughnesses, and bottom cell qualities, by going notably to more crystalline  $\mu c$ -Si:H intrinsic layers. Also, the combination of multi-scale architectures and smoothening IRLs may be a promising approach towards better efficiencies. Importantly, more extreme morphologies with high aspect ratios ( $> 1$ ) were not studied in this work, but remain extremely promising for significant light-harvesting improvements. Among them, nanopillars are the most popular, but their implementation requires a high resilience to sharp features, and this concept has not been fully validated yet. Another possible route would be to use multi-scale structures combining a thin LPCVD ZnO layer with features of several tens of microns of typical size (such as craters). Such structures may exhibit very tall walls while keeping a rounded bottom. It is anticipated that such very large structures would not be detrimental to electrical quality of the silicon layers.

Finally, large room for improvement remains for thin-film silicon technology on the silicon material side, by understanding the physical processes limiting the  $V_{oc}$  of  $a$ -Si:H and  $\mu c$ -Si:H cells to values much lower than can be expected from the band gap, and finding ways to counteract these processes. A strong emphasis was recently put on the evaluation of the drastic influence of the nanoporous 2D region of low-quality materials (“cracks”) which develop in  $\mu c$ -Si:H layers grown on rough substrates. Since methods preventing their formation or limiting their impact have been developed (morphology adaptation, plasma-conditions adaptation, shunt-quenching resistive layers), the limiting parameter for the  $V_{oc}$  in “cracks-free” devices should be evidenced. The respective influences of the bulk material, of the interfaces and of the doped layers is still to be clarified. In the short term, light harvesting progress and device architecture can enable module efficiencies to be increased from present 10% to around 12.5%. Reaching over 14% stable efficiency remains realistic, but it needs the materials or interfaces of the sub-cells to be improved, requiring the scientific effort to be maintained in the very fashionable — in an ephemeral way — thin-film silicon photovoltaic field. In spite of the present crisis, thin-film silicon technology has unique qualities to be part of a wide photovoltaic electricity deployment, and we hope that this contribution will help to maintain the global effort aimed at making photovoltaics a source of abundant, daily renewed and equally distributed electricity.

# A EQE measurement of multi-junction devices

## A.1 Bias light

To correctly measure EQE spectra, one should ideally use a sun simulator to provide an AM1.5G light background; then a very weak chopped probe beam would be used for characterization; and the saturation of the sub-cell which is not measured would be achieved with a selective light of which the intensity would be set to the minimal value avoiding this cell to be current limiting. Practically, this is impossible to achieve, notably due to limitations of lock-in amplifiers. The choice is thus made to have a medium-intensity white light background illumination, a strong bias light and a weak probe beam.

In the setup used in PV-lab, a halogen lamp with a blue / infrared filter is used for biasing the bottom / top cell; and the probe beam intensity is relatively high, especially for the positions of the peak intensity of the xenon lamp used to provide the monochromatic probe beam (together with a monochromator). This results into “spikes” in the EQE curve (seen for the bottom cell in Fig. A.1) when the bias light is not strong enough (*e.g.* for a bad focus of the bias light on the measured cell, or a bad selectivity of the bias light, possibly due to a too thin or too thick top cell). Then, white LEDs bring a background light of which the importance can be seen in Fig. A.2, showing the same Micromorph device measured with and without this white light background, after 1000 h of light soaking. No difference is observed for the  $\mu c$ -Si:H bottom cell, but a higher EQE is observed for the *a*-Si:H top cell when a light background is present, due to a better collection.

## A.2 Bias voltage

An additional issue comes from the bias voltage of the probed junction, which is depending on the bias light intensity and on the probe light intensity, as seen in Fig. A.3. A bias voltage must therefore be applied to measure a sub-cell in short-circuit conditions *for this subcell*. Importantly, for short-circuit conditions of the Micromorph device, the voltage applied to each sub-cell depends on the current matching conditions: only in case of perfect matching

## Appendix A. EQE measurement of multi-junction devices

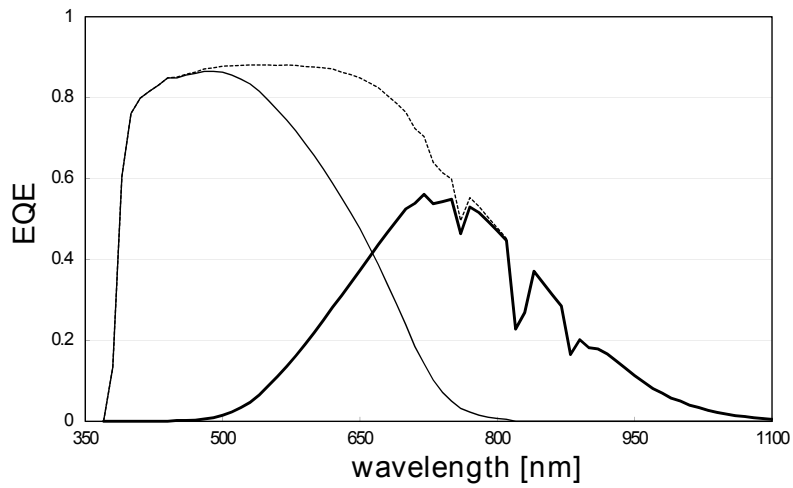


Figure A.1: EQE of a Micromorph device in the case the intensity of the light biasing the top cell is too weak compared to the probe beam for the wavelengths corresponding to the high intensity peaks of the xenon lamp.

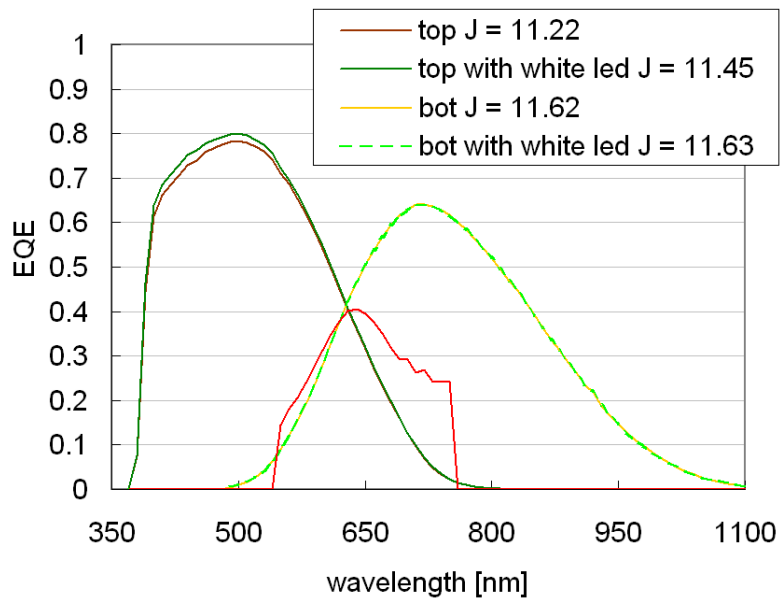


Figure A.2: EQE of a Micromorph device, after 1000 h light soaking, in dark or with white bias light.

both sub-cells are at short-circuit conditions. Otherwise, the limiting sub-cell is negatively biased, while the other is forward biased, as seen in Fig. B.1. To precisely measure the  $J_{sc}$  of a Micromorph devices with an EQE setup is therefore impossible. However, for good devices having reasonably good collection, the impact of bias voltage is not extremely strong, making measurement of the limiting sub-cell at  $0\text{ V}$  and  $-V_b\text{ V}$ , with  $V_b$  the  $V_{oc}$  of the biased sub-cell for its bias light very close. As  $J_{sc}$  lies between these two values, the error in the measurement is usually reasonable.

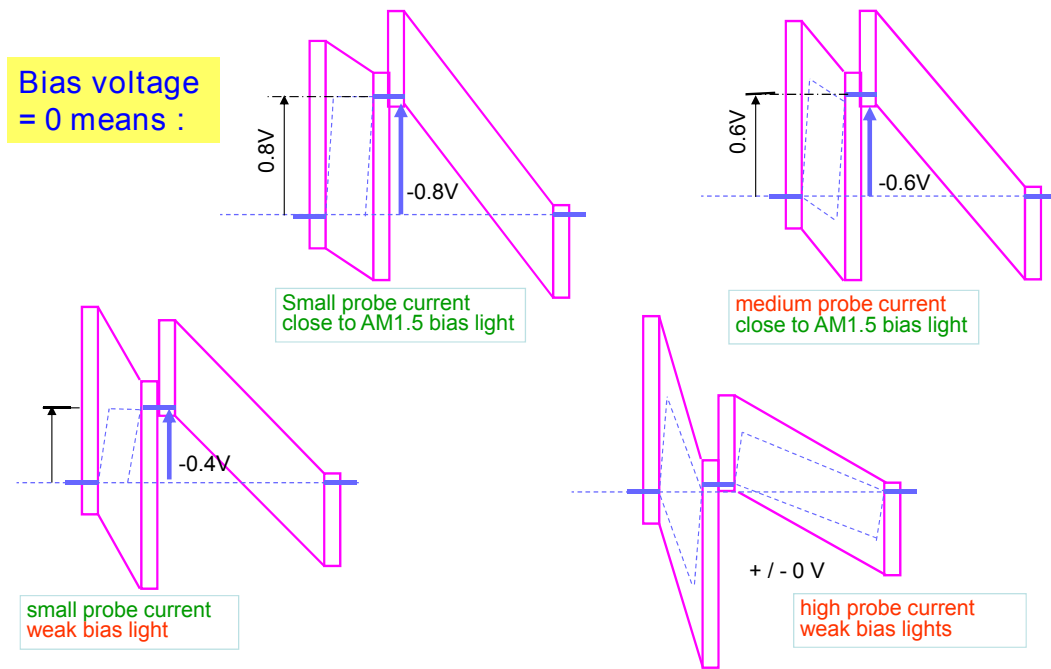


Figure A.3: Schematic band diagram of a tandem device (Micromorph for the values) during the EQE measurement. Bias light is supposed to be perfectly selective for the bottom cell only, and the top cell is probed. In the last case, the top cell is not clearly limiting and thus the measurement output has no physical meaning.

Overall, there is no perfect way of measuring EQE curves and the aforementioned aspects should be kept in mind when measuring, and when analyzing the results.



# B Method for studying the fill factor of Micromorph cells

## B.1 Problems faced when measuring fill factors in tandem devices

In tandem devices, the general parameters ( $V_{oc}$ ,  $J_{sc}$  and  $FF$ ) of the  $J(V)$  curve have very different dependences over their equivalent in subcells. The  $V_{oc}$  is in theory the simplest parameter as it is the sum of the  $V_{oc}$ 's of the subcells (under their relative illumination). These can be measured by exciting as much carriers in each subcell as in standard operation but by using only selective light, so that it becomes possible to see only one  $V_{oc}$  at a time. In practical, this experimental separation is extremely delicate (if not impossible), since a very low light intensity is enough to induce a substantial  $V_{oc}$  in the non-probed sub-cell, making an extremely good selectivity of the bias light mandatory. The short circuit current density is already more tricky to analyse, and depends on the short circuit resistance of the different sub-cells, but can be well approximated (yet always underestimated) in “standard devices” by the limiting current between the  $J_{sc}$  of the two sub-cells. “Standard devices” stands here for tandem junctions with reasonable mismatch (typically less than 20%) and with reasonable short-circuit resistances (typically over  $1000\Omega.cm^2$ , corresponding to cells which are not severely shunted and have not severe collection issues). Both subcells currents can be measured with a spectral response setup (giving the spectral external quantum efficiency, EQE). Yet, there is no straightforward way of calculating the resulting  $FF$  of the tandem connection of two given subcells, nor to get back to the  $FF$  of the two subcells by knowing the one of an existing tandem device. Moreover, in addition to the subcells quality and the electrodes characteristics, the  $FF$  of a tandem device strongly depends on the matching conditions between the two subcells. It will thus be greatly influenced by a small spectrum modification (such as, in outside normal use, between the red-rich sunrise solar spectrum and the blue rich noon one) or a slight modification of the subcells thicknesses. The  $J_{sc}$  will as well be affected, but in an easily predictable way. Fig. B.1 shows examples of electrical simulations of Micromorph devices (using two two-diodes models in series) illustrating the previous statements.

This  $FF$  volatility becomes a real issue when trying to optimize the trade-off between conduction and transparency in electrodes of Micromorph devices. Indeed, decreasing the free

## Appendix B. Method for studying the fill factor of Micromorph cells

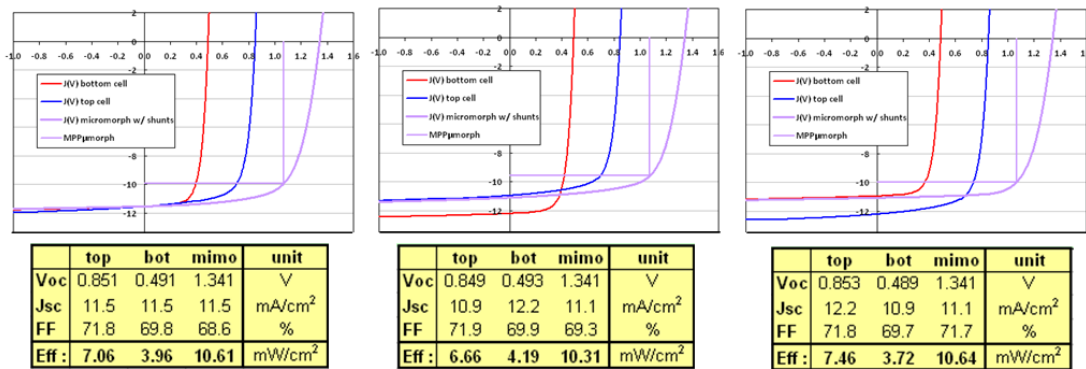


Figure B.1: Simulated  $J(V)$  curves and summary of the main parameter for Micromorph tandem devices and for the corresponding sub-cells. The summed current is the same for all 3 examples ( $23 \text{ mA/cm}^2$ ) but the repartition is changed: equal split for the first case, while 10% is exchanged between top and bottom cells in the two other graphs. One can see the changes in the tandem device characteristics in terms of  $V_{oc}$  (no change),  $J_{sc}$  (the limiting on is a close underestimation of the tandem one),  $FF$  (no clear trend) and efficiency ( $J_{sc}$  loss partly compensated in some cases by  $FF$  gain so unpredictable change).

carriers density makes the electrode more transparent but usually also less conductive. The series resistance of the devices thus increases, degrading the  $FF$ . But at the same time, the modified transparency of the new electrode changes the matching condition: the bottom cell current will increase thanks to reduced FCA, while the top cell current might increase or decrease (e.g. because of the Burstein-Moss effect). This matching effect might induce stronger  $FF$  alteration than the added series resistance, making a direct comparison of two different electrodes impossible. One would thus have to optimize the devices on both substrates to fairly compare their potential.

The current matching machine developed at PVlab allows to make fair comparisons between different electrodes within a cell co-deposited by altering the spectrum of the solar irradiation. The goal here is not to adapt the spectrum of the sun to get the maximum efficiency for each device, but to reproduce the same matching conditions for all. This gives then precious indications about the potential of each substrate and the modifications in the silicon deposition sequence to make in order to get the best out of a given electrode.

## B.2 Setup presentation

A LED based setup was developed in-house to be able to finely tune the matching between top and bottom cells currents in the vicinity of standard test conditions. The typical standard process is as follows: a first step is to attenuate slightly the solar simulator light. For example, 15% of the light can be removed by inserting two glass slides with a small angle relative to horizontal between the sample and the light source. Then, this photogenerated current loss is carefully compensated by adding some extra light of selected wavelength to the solar simulator.



This is done via two selective LEDs sets: the first one with a peak intensity centered at 470 nm generates current mainly in the top cell, while the other one with a peak intensity centered at 870 nm generates current mainly in the bottom cell. By calibrating their photon flux density, and by knowing the EQE of our cell at the corresponding wavelengths, it is possible to obtain the same subcell currents as in standard test conditions (without glass slide nor LED). A scheme is shown in Fig. B.2. Then, the strong dependence of the light intensity of the LEDs with the current applied to their terminals allows us to easily individually tune the subcells photocurrents. In particular, it is possible to keep the summed current unchanged while varying the share between both subcells. This would have the same effect than modifying the top cell thickness or changing the power of the intermediate reflector. A similar setup was simultaneously developed at Forschungszentrum Jülich and described in [Ulbrich 11].

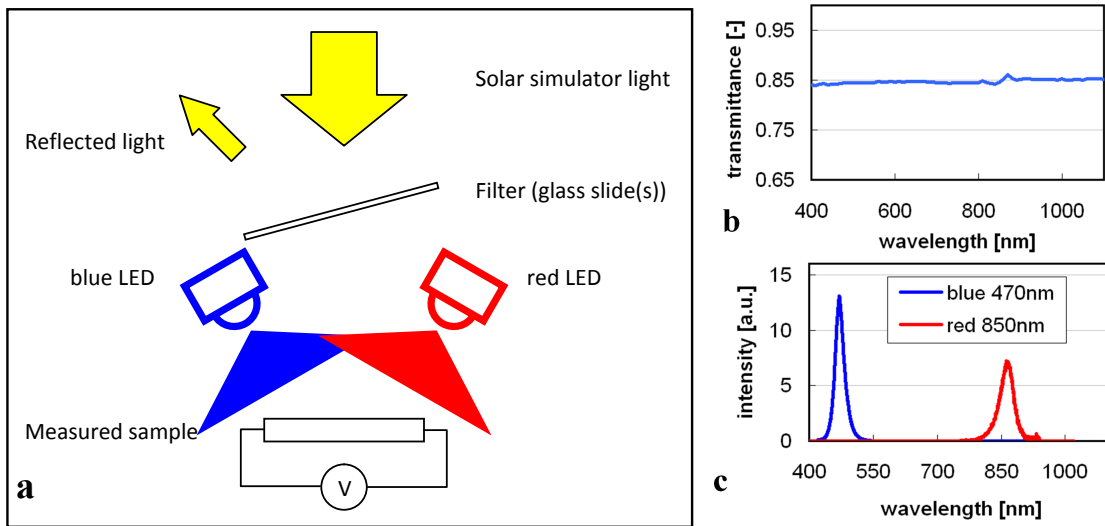


Figure B.2: Schematic view of the current matching machine. Part of the solar simulator light is removed by a filter (consisting of two tilted glass slides reflecting 15% of the light as plotted in b). This light is compensated by some blue and red light from two LEDs sets (470 nm peak intensity for the blue, 870 nm for the red as plotted in c). This is then possible to modify the matching conditions by playing with the LED light intensity.

### B.3 Setup calibration

To calculate the photon flux density on the substrates surface, we use a reference microcrystalline cell of which the EQE is known. If the spectrum of emission of the LED ( $I_{LED}(\lambda)$ ) is known, we obtain the current to input the LED to generate a certain  $J_{sc}$  in the tested cell ( $J_{LED}(J_{sc})$ ) by inverting equation B.1. This allows thus to add any desired photocurrent in the cell.

For a given current in the blue LEDs, we measure experimentally  $J_{sc,ref}$  and equation B.1 gives

## Appendix B. Method for studying the fill factor of Micromorph cells

the corresponding  $J_{sc,top}$  addition.

$$J_{sc}(J_{LED}) = \int_{spectrum} \frac{EQE(\lambda)}{EQE_{ref}(\lambda)} \cdot I_{LED}(\lambda) \cdot d\lambda \cdot J_{sc,ref}(J_{LED}) = a \cdot J_{sc,ref}(J_{LED}) \quad (B.1)$$

There is thus a simple correction factor between  $J_{sc}(J_{LED})$  and  $J_{sc,ref}(J_{LED})$ , assuming that the LED spectrum does not vary with intensity. Both curves are plotted in Fig. 3 b). The same applies to red LEDs, as plotted in Fig. B.3c).

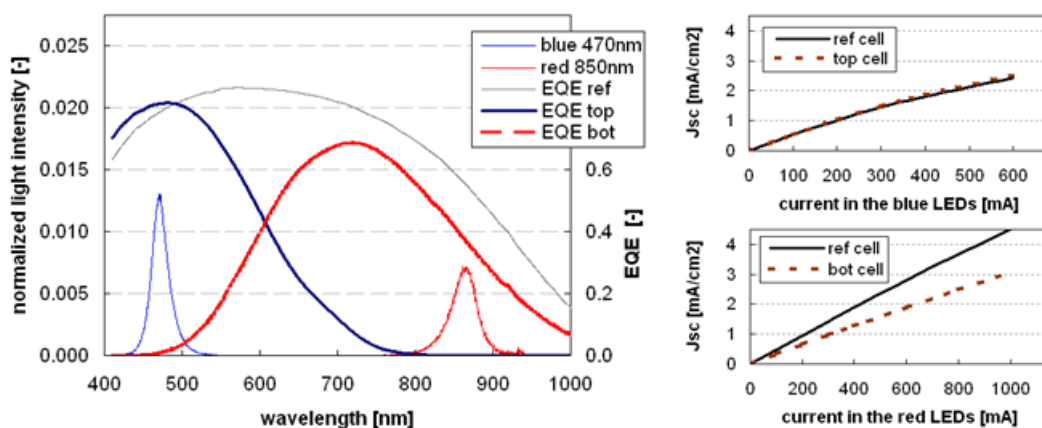


Figure B.3: a) EQE of the reference cell and of both subcells of the studied device. Both LEDs spectra are plotted as well. b)  $J_{sc}$  added in the reference cell as well as in the top cell per current flowing through the blue LEDs. c) Same as b) but with the bottom cell and red LEDs.

## B.4 Different applications

### Reproduction of any spectrum

It is possible to simulate any kind of spectrum, for example the daily variations (red-rich - blue-rich - red-rich). To simulate a red rich spectrum, close to AM1.5G, one just needs to calculate from this spectrum and the top and bottom cells EQEs of the studied tandem device the top and bottom cells current densities. Then, the required light intensity in the blue and red LEDs to meet the aforementioned current densities can be calculated. To keep a close to AM1.5G spectrum, 85% of this current can be provided by the solar simulator attenuated by two glass slides reflecting 15% of the light.

### Estimation of the potential of any substrate

When depositing a tandem junction on an unknown substrate, or with a new recipe, it is hard to obtain the ideal device at first glance. Instead of making several depositions to know whether

Table B.1: Micromorph devices parameters for different matching condition as obtained with the matching machine. The discrepancy between the current measured at IV and the one from EQE is due to light which is lost by trapping in the glass or scattering at the back reflector when measuring currents with the IV setup.

	$V_{oc}$ (V)	$FF$ (%)	$Eff$ (%)	$J_{sc,mimo}$ (J(V)) (mA/cm <sup>2</sup> )	$J_{sc,top}$ (EQE) (mA/cm <sup>2</sup> )	$J_{sc,bot}$ (EQE) (mA/cm <sup>2</sup> )
initial	1.415	72.7	10.9	10.7	10.8	13.3
artificially matched	1.414	71.4	11.6	11.5	11.9	11.9

the recipe is good or bad it is possible to tune the spectrum to correct an eventual mismatch, giving thus an indication about the efficiency potential of an equivalent but adapted device. An example is added here, with a top limited device, having 10.9% efficiency, that would have in a matched case (e.g. with a thicker intermediate reflector) 11.6% efficiency, as seen in Tab. B.1.

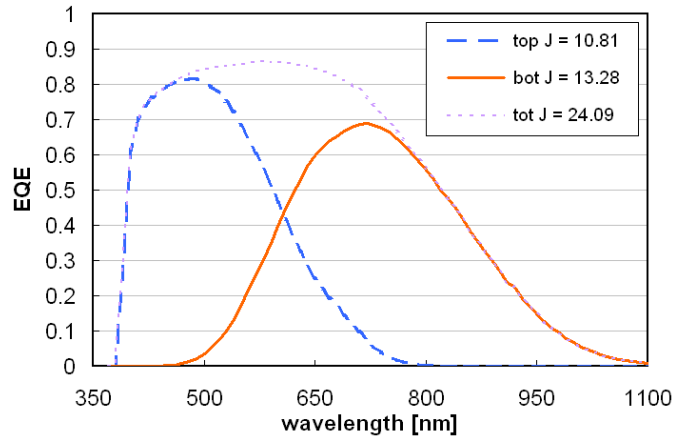


Figure B.4: EQE of a very top limited micromorph cell. The IV characteristics of this cell are reported in the table B.1 (first row). The second row gives the IV characteristics after using the current matching machine to get to a matched case, including 0.3 mA/cm<sup>2</sup> of extra losses. This simulates a thicker intermediate reflector use.

### Comparison of different substrates

The matching conditions of a tandem device strongly depend on the front substrate choice. Some substrates will scatter little light in the infra-red and absorb a lot of it while some others can have the opposite behavior. If the same tandem cell is deposited on two substrates like these ones, then their matching will be very different. One will thus automatically be favored even if the silicon layers are identical. Different depositions, optimized for each substrates, have thus to be done to be able to know which substrate is the best one. This can be time-consuming, and implies to compare cells that were not deposited in the same conditions which can be problematic in case of sensitive processes.

## Appendix B. Method for studying the fill factor of Micromorph cells

---

With the matching machine, it is possible to find identical matching conditions for all substrates without modifying the summed current of any of them. This avoids to make one deposition with adapted top cell thickness or intermediate reflector thickness for each substrate. In addition to saving time, this avoids the issues linked to poor reproducibility of the cells depositions. The maximal short circuit current point (matched point) can for example be chosen, or the maximal efficiency point. One has nevertheless to keep in mind that this manipulation replaces a physical change in the cell deposition. Increasing exorbitantly the top cell current density might be hard to reproduce without losses due to the intermediate reflector or the increased thickness.

### Precise measurement of the efficiency of isolated cells

When measuring an isolated cell employing elements that scatter light (in most cases the rough electrode and thick white dielectric), a direct and precise measurement of the cell efficiency is impossible. If no mask is used, and the white reflector extends outside of the cell, current will be overestimated as light hitting aside the cell can be scattered and enter the cell after traveling laterally in the glass. If all light hitting aside the cell is absorbed (*e.g.* with a mask or black paint), then current will be underestimated as some of the light not fully absorbed after one round-trip will escape around the cell through the glass or white back reflector. In a complete module, the same amount of light would be gained in the same way. With a black mask much smaller than the cell centered on the cell, and if the cell is large enough so that escape by the side of light hitting the center can be neglected, then the current can be well estimated. However, as part of the cell is in dark conditions, the  $V_{oc}$  will be underestimated. Acceptable compromises can be found for single-junction solar cells, notably by using the current value derived from the EQE measurement.

Yet, the case of multi-junction devices is much more delicate as all the previous effects are wavelength-dependent. In the case of Micromorph devices, when a mask corresponding roughly to the size of the cell is used (standard measurement), we observe a systematic underestimation of the current of bottom limited devices by  $0.5 \text{ mA/cm}^2$  compared to the value calculated from EQE measurement. A good agreement is however found for (more than  $0.5 \text{ mA/cm}^2$ ) top limited devices. This current loss in the bottom cell influences the  $FF$  of the device, and taking the current value derived from the EQE and the  $V_{oc}$  and  $FF$  values obtained from  $J(V)$  measurement leads to an overestimation of the efficiency, while efficiency directly obtained from  $J(V)$  is an underestimation of the real value.

The approach that that was developed during this work for a precise determination of the efficiency of a Micromorph device is to measure the cell with a mask and adjust the spectrum to reproduce the matching observed from EQE measurement. Practically, it is achieved by adding some infra-red light to the light coming from the sun simulator, to compensate for the losses by the side. A scan of the matching can also be performed by removing 15% of the sun simulator light and compensating with the blue and/or infra-red LEDs to measure the  $J(V)$

curve at the matching point corresponding to the one from EQE.

### **Record cells fine tuning**

It is very hard to know by advance the ideal matching to aim to get the best efficiency for a device. To avoid many missed depositions, it is possible to see after one deposition by modifying the spectrum slightly whether a thinner or a thicker IRL would be better. Then, the perfect deposition can be done right after. And it is possible to check that the target was not missed !



# C Other possible uses of lacquer in solar cells

## C.1 Before silicon deposition

Lacquer can be used to smoothen the sharp features of a rough substrate, similarly to the argon plasma treatment of LPCVD ZnO. To allow conduction, a conductive layer should be added on top of the lacquer, or for a conductive substrate, etching the lacquer to selectively unveil the tips of the substrates could be enough. If the doped layers are not conductive enough to allow for lateral carriers extraction from the bottom of the valleys to the unveiled tips of the substrate, a thin conductive layer can be inserted. In the particular case of  $\mu c$ -Si:H, the conductivity of this layer should be finely tuned to enable current extraction while preventing local porous areas to drain the carriers through the bad quality diodes (*i.e.* to ensure a shunt-quenching effect similarly to SiO doped layers [Despeisse 10].)

First promising attempts towards this use were performed in the superstrate configuration for a  $\mu c$ -Si:H cell (Fig. C.1. A significant  $V_{oc}$  gain was obtained, but collection issues remained (no conductive channel was inserted) and reflection losses were observed due to the high refractive index step between smooth lacquer and silicon (as seen in Fig. C.2).

The observed reflection losses tend to indicate that this method is more compatible with substrate-type devices, for which an increased reflection directly on the back reflector is an advantage. the collection issues indicate that a conducting channel for this type of use is needed (for the series of devices presented here, only a thin P-SiO layer was used, not providing a sufficient lateral conduction). A structure consisting of a flat silver substrate partially covered with rough lacquer embedded in thin TCO layers, as sketched in Fig. C.3 would be a very promising substrate to enable for large angle light scattering without sharp valleys nor plasmonic parasitic absorption and with minimal free carriers absorption in the TCO. Such a substrate would be compatible with flexible substrates, which is usually not the case for thick LPCVD ZnO.

### Appendix C. Possible uses of lacquer in solar cells

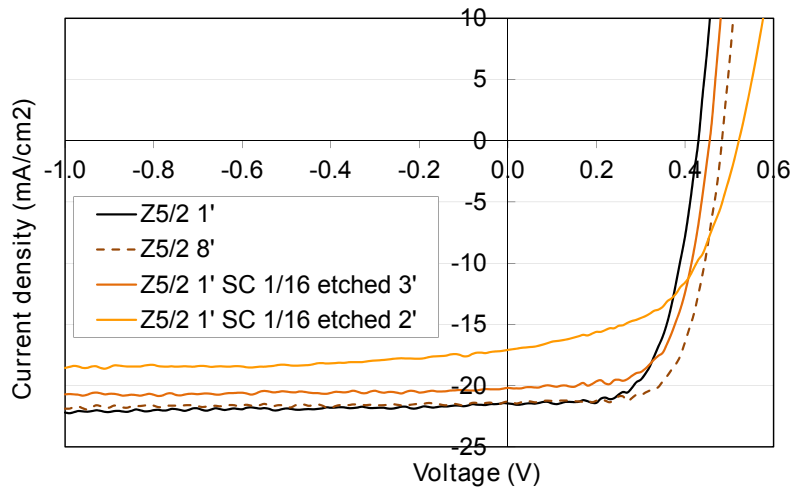


Figure C.1: J(V) curve of  $\mu c$ -Si:H cells deposited on a 2.5  $\mu\text{m}$  thick ZnO superstrate treated for one or eight minutes, or treated for one minute and with a 1/16 diluted lacquer spin coated on top and etched for two or three minutes.

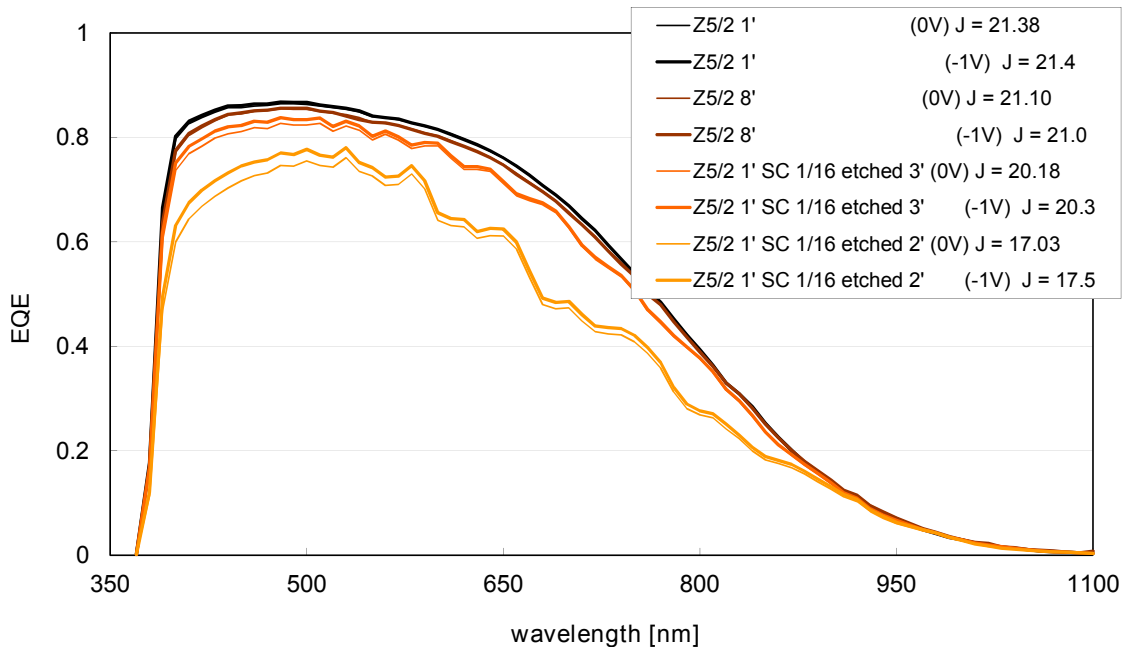


Figure C.2: EQE curve of  $\mu c$ -Si:H cells deposited on a 2.5- $\mu\text{m}$ -thick ZnO superstrate treated for one or eight minutes, or treated for one minute and with a 1/16 diluted lacquer spin coated on top and etched for two or three minutes.



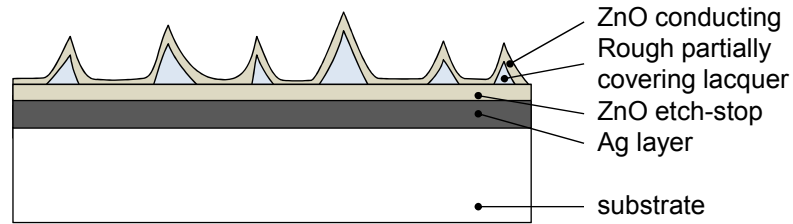


Figure C.3: Sketched of a substrate enabling light scattering and carrier extraction together with minimal parasitic absorption.

## C.2 After silicon deposition

Instead of preventing the formation of cracks, it is possible to quench them as seen with SiO doped layers [Despeisse 11]. When applied on the silicon layers, lacquer can fulfill the same role, as it will preferentially stay in the pinches after etching, isolating thus the cracks (that end at the bottom of pinches) from the electrode. Inserting a finely tuned conductive channel should in principle enable the efficient extraction of photogenerated carriers while preventing them to recombine or be drained in the cracks. For this architecture, the superstrate configuration is favorable as reflection at the silicon - lacquer interface will improve the back reflector.

Fig. C.4 shows  $J(V)$  curves of  $\mu c$ -Si:H cells on two different electrodes, with or without a stack of 30-nm-thick ZnO / 1/16 diluted lacquer etched for three minutes, before the LPCVD ZnO back contact. A  $V_{oc}$  gain is observed for both substrates, more pronounced for the roughest one (Z5), confirming a quenching of the bad quality diodes. A current increase is also observed, attributed to the enhanced reflection at the interface silicon - lacquer (compared to silicon - TCO). The maximum power point is however not much affected for both substrates, due to increased series resistance and collection issues for the Z5 45, as determined from the shape of the  $J(V)$  curve, and mostly due to collection issues for the Z5. Both issues can be due to the damaging of the n-doped layer during the sputtering of the thin protecting ZnO layer, or during the partial etching of the lacquer, or to a lack of lateral conduction at the silicon - lacquer interface. Both issues should be solved by using a thicker n-doped layer or a thicker ZnO layer. The drawback would probably be the loss of the  $V_{oc}$  gain, but there might be a compromise to find to obtain a gain in the maximal power point efficiency (which is all that matters in the end).

In summary, the two different roads to obtain a gain in efficiency are:

1. Quenching cracks ( $V_{MPP}$  gain): lacquer should be here etched a lot (leaving some only in the deep pinches), and the conductive channel should be kept resistive enough.
2. Reducing absorption losses in the back electrode stack, either originating from FCA in the TCO, or from plasmonic losses in the metallic back reflector ( $J_{MPP}$  gain): a maximal amount of lacquer should here be maintained and the conductive channel should be optimized for negligible resistive loss and minimal FCA. This applies especially

## Appendix C. Possible uses of lacquer in solar cells

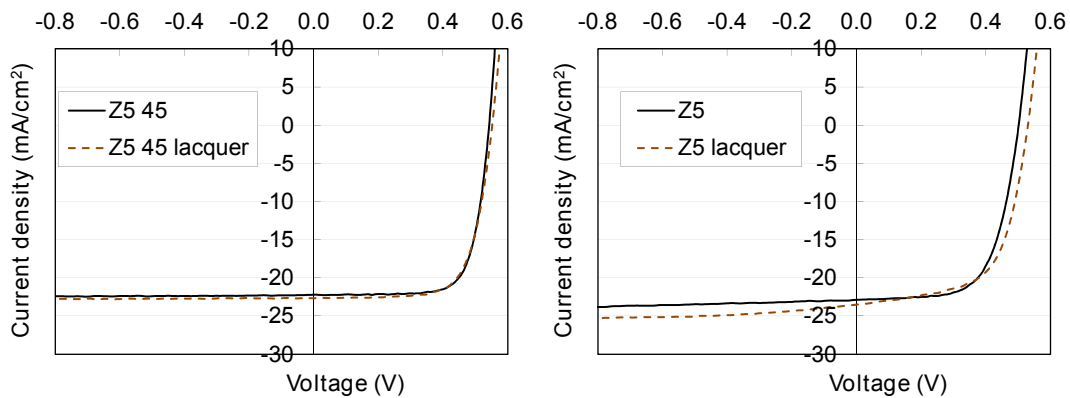


Figure C.4: J(V) curves of  $\mu c$ -Si:H cells deposited on a 5- $\mu\text{m}$ -thick ZnO superstrate (Z5), untreated or treated for 45 minutes, with or without lacquer between silicon and the back TCO.

to extreme morphologies (pillars or holes of high aspect ratio) giving “folded cells”, for which it would be interesting to have a very little absorbing conductive channel (following the folding), and a flat metal or TCO connected to the tips.

Overall, lacquer shows promising applications in many configurations in a solar device due to its unique properties (preferential deposition inside the features, easy etching, glass-like optical properties, easy etching) compared to other materials involved in a solar cell stack. This novel element is thought to enable a better addressing of the many trade-offs limiting the efficiency of present solar devices.

# D Micromorph properties as a function of the substrate morphology

## D.1 Mapping of Micromorph properties

In this appendix, the original tables (Fig. D.1) used to draw the map presented in Chapter 5 are presented. The feature sizes were estimated from SEM images, and the typical inclination angles were estimated by using the values published in [Cuony 11].

The thicknesses of the first three layers are 0.5  $\mu\text{m}$ , 1  $\mu\text{m}$ , and 2  $\mu\text{m}$ . The doping of ZnO film was stronger for these first layers compared to the last four layers that were 2- $\mu\text{m}$ -, 3- $\mu\text{m}$ -, 4- $\mu\text{m}$ -, and 5- $\mu\text{m}$ -thick. Modifying the doping level changes the typical feature size, making the features at the surface of the second 2  $\mu\text{m}$  thick layers larger. Also, this doping change increases slightly the difference in  $J_{\text{sc, bottom}}$  between 300 nm and 400 nm of feature sizes, but the trend was the same with “comparable EQE” based on Equation 6.1, and correlates well with the Haze value measured at 550 nm for the electrodes, as illustrated in Fig. D.2. The  $J_{\text{sc, sum}}$  obtained from the sum of comparable EQE of both sub-cells is also indicated, to exclude any intermediate reflector artifact.

**Appendix D. Mapping of Micromorph properties**

		Typical features size (nm)						
		100	200	300	400	500	600	800
typical surface inclination (°)	$V_{OC}$	45	1.35	1.33	1.31	1.27	1.26	1.25
	30	1.37	1.39	1.37	1.37	1.35	1.34	
	15			1.38	1.38	1.38	1.38	1.40
								1.42

		Typical features size (nm)							
		100	200	300	400	500	600	800	
typical surface inclination (°)	$J_{SC, top}$	45	12.06	12.40	12.37	12.26	12.10	11.82	11.54
	30		11.90	12.05	11.94	11.58			
	15			11.59	11.33	11.19	11.18	11.02	
								10.19	

		Typical features size (nm)							
		100	200	300	400	500	600	800	
typical surface inclination (°)	$J_{SC, bottom}$	45	9.88	11.12	11.75	12.75	12.83	13.47	13.57
	30		10.98	11.75	12.58	12.91			
	15			11.53	12.39	12.51	13.28	12.33	
								9.44	

Figure D.1:  $V_{OC}$  (in V),  $J_{sc, top}$  and  $J_{sc, bottom}$  (in mA/cm<sup>2</sup>) of Micromorph cells as a function of the typical size and inclination of the features composing its surface.

## D.1. Mapping of Micromorph properties

Haze @ 550nm		Typical features size (nm)						
		100	200	300	400	500	600	800
typical surface inclination (°)	45			0.35	0.53	0.74	0.89	0.96
			0.14			0.70	0.81	
	30	0.03		0.31	0.47			
			0.11			0.67		
	15			0.24	0.43	0.53	0.68	0.76
								0.48

$J_{sc,bot,comp}$		Typical features size (nm)						
		100	200	300	400	500	600	800
typical surface inclination (°)	45			12.35	12.78	13.02	13.59	13.84
			11.50			13.11	13.70	
	30	10.11		12.39	12.69			
			11.26			13.21		
	15			12.06	12.65	12.74	13.34	12.72
								9.50

$J_{sc,sum,comp}$		Typical features size (nm)						
		100	200	300	400	500	600	800
typical surface inclination (°)	45			24.67	24.99	25.10	25.41	25.47
			23.81			24.81	25.22	
	30	22.07		24.42	24.56			
			23.08			24.83		
	15			23.76	24.30	23.98	24.53	23.89
								19.71

Figure D.2: Haze at 550 nm, comparable  $J_{sc,bottom}$  (in  $\text{mA}/\text{cm}^2$ ), and comparable  $J_{sc,sum}$  (in  $\text{mA}/\text{cm}^2$ ) of Micromorph cells as a function of the typical size and inclination of the features composing its surface.



# Abbreviations and symbols

ADF	angular distribution function
AFM	atomic force microscopy
ARS	angle resolved scattering
<i>a</i> -Si:H	hydrogenated amorphous silicon
EQE	external quantum efficiency
FCA	free-carrier absorption
IOH	hydrogenated indium oxide
IRL	intermediate reflecting layer
ITO	indium tin oxide
LPCVD	low-pressure chemical vapor deposition
n-i-d	non-intentionally-doped
PECVD	plasma-enhanced chemical vapor deposition
SEM	scanning electron microscopy
SiO <sub>x</sub>	Sub-stoichiometric silicon oxide
SOIR	silicon-oxide-based intermediate reflector
ZnO	zinc oxide
<i>μc</i> -Si:H	hydrogenated microcrystalline silicon
<i>A<sub>p</sub></i>	parasitic absorption
EQE <sub>c</sub>	corrected EQE, defined as $EQE_c = EQE / (EQE + R)$
<i>FF</i>	fill factor
<i>J<sub>sc</sub></i>	short-circuit current density
<i>J<sub>sc, top</sub></i>	top-cell short-circuit current density
<i>J<sub>sc, bottom</sub></i>	bottom-cell short-circuit current density
<i>J<sub>sc, sum</sub></i>	summed short-circuit current density
<i>n</i>	refractive index
<i>R</i>	reflectance
<i>R<sub>oc</sub></i>	open-circuit resistance
<i>R<sub>sq</sub></i>	sheet resistance
<i>V<sub>oc</sub></i>	open-circuit voltage
<i>α</i>	absorption coefficient





# Bibliography

- [Achour 12] Hamed Achour. Implementation of planarizing layers in tandem solar cells. Master's thesis, EPFL, 2012.
- [Aranovich 79] Julio Aranovich, Armando Ortiz & Richard H. Bube. *Optical and electrical properties of ZnO films prepared by spray pyrolysis for solar cell applications*. Journal of Vacuum Science and Technology, vol. 16, no. 4, pages 994–1003, jul 1979.
- [Bailat 06] J Bailat, D Dominé, R Schlüchter, J Steinhauser, S Faÿ, F Freitas, C Bücher, L Feitknecht, X Niquille, R Tschärner, A Shah & C Ballif. *High-Efficiency P-I-N Microcrystalline and Micromorph Thin Film Silicon Solar Cells Deposited on LPCVD ZnO Coated Glass Substrates*. In Proceedings of the Fourth WCPEC Conference, Hawaiï, 2006.
- [Bailat 10] Julien Bailat, Luc Fesquet, J.-B. Orhan, Y. Djeridane, B. Wolf, P. Madliger, J. Steinhauser, S. Benagli, D. Borrello, L. Castens, G. Monteduro, M. Marmelo, B. Dehbozorgi, E. Vallat-Sauvain, X. Multone, D. Romang, J.-F. Boucher, J. Meier, U. Kroll, M. Despeisse, G. Bugnon, C. Ballif, S. Marjanovic, G. Kohnke, N. Borrelli, K. Koch, J. Liu, R. Modavis, D. Thelen, S. Vallon, A. Zakharian & D. Weidman. *Recent Developments of High-Efficiency Micromorph(R) Tandem Solar Cells in KAI-M PECVD Reactors*. In 25th European Photovoltaic Solar Energy Conference and Exhibition / 5th World Conference on Photovoltaic Energy Conversion, 6-10 September 2010, Valencia, Spain, 2010.
- [Ballif 11] C. Ballif, L. Barraud, C. Battaglia, M. Benkhaira, A. Billet, R. Biron, M. Boccard, G. Bugnon, M. Charrière, P. Cuony, M. Despeisse, L. Ding, J.P. Escarré, F.-J. Haug, S. Hänni, L. Löfgren, F. Sculati-Meillaud, S. Nicolay, C. Pahud, G. Parascandolo, B. Perruche, S. De Wolf, K. Söderström & M. Stükelberger. *Novel Materials and Superstrates for High-Efficiency Micromorph Solar Cells*. In Proceedings of the 26th European Photovoltaic Solar Energy Conference and Exhibition, Hambourg, 2011.
- [Battaglia 10] Corsin Battaglia, Karin Soederstroem, Jordi Escarre, Franz-Josef Haug, Didier Domine, Peter Cuony, Mathieu Boccard, Gregory Bugnon, Celine Denizot, Matthieu Despeisse, Andrea Feltrin & Christophe Ballif. *Efficient light*

## Bibliography

---

- management scheme for thin film silicon solar cells via transparent random nanostructures fabricated by nanoimprinting.* Applied Physics Letters, vol. 96, no. 21, page 213504, May 2010.
- [Battaglia 11a] Corsin Battaglia, L. Barraud, A. Billet, M. Boccard, G. Bugnon, M. Charrere, P. Cuony, Matthieu Despeisse, S. De Wolf, L. Ding, L. Erni, J. Escarré, S. Hanni, Franz-Josef Haug, L. Lofgren, F. Meillaud, S. Nicolay, G. Parascandolo, K. Söderström, M. Stuckelberger & Christophe Ballif. *Advanced Nanostructured Materials for Pushing Light Trapping Towards the Yablonovitch Limit.* In Renewable Energy and the Environment, page PWC6. Optical Society of America, 2011.
- [Battaglia 11b] Corsin Battaglia, Lukas Erni, Mathieu Boccard, Loris Barraud, Jordi Escarre, Karin Soederstroem, Gregory Bugnon, Adrian Billet, Laura Ding, Matthieu Despeisse, Franz-Josef Haug, Stefaan De Wolf & Christophe Ballif. *Micro-morph thin-film silicon solar cells with transparent high-mobility hydrogenated indium oxide front electrodes.* Journal of Applied Physics, vol. 109, no. 11, page 114501, June 2011.
- [Battaglia 11c] Corsin Battaglia, Jordi Escarre, Karin Soederstroem, Lukas Erni, Laura Ding, Gregory Bugnon, Adrian Billet, Mathieu Boccard, Loris Barraud, Stefaan De Wolf, Franz-Josef Haug, Matthieu Despeisse & Christophe Ballif. *Nanoimprint Lithography for High-Efficiency Thin-Film Silicon Solar Cells.* Nano Letters, vol. 11, no. 2, pages 661–665, February 2011.
- [Battaglia 12a] Corsin Battaglia, Jordi Escarré, Karin Söderström, M. Boccard & C. Ballif. *Experimental Evaluation of the Light Trapping Potential of Optical Nanostructures for Thin-Film Silicon Solar Cells.* Energy Procedia, vol. 15, no. 0, pages 206 – 211, 2012. International Conference on Materials for Advanced Technologies 2011, Symposium O.
- [Battaglia 12b] Corsin Battaglia, Ching-Mei Hsu, Karin Söderström, Jordi Escarré, Franz-Josef Haug, Mathieu Charrere, Mathieu Boccard, Matthieu Despeisse, Duncan T. L. Alexander, Marco Cantoni, Yi Cui & Christophe Ballif. *Light Trapping in Solar Cells: Can Periodic Beat Random?* ACS Nano, vol. 6, no. 3, pages 2790–7, 2012.
- [Battaglia 13] Corsin Battaglia, Mathieu Boccard, Franz-Josef Haug & Christophe Ballif. *Light Trapping in Solar Cells: When does a Lambertian scatterer scatter Lambertianly?* Journal of Applied Physics, 2013. to be published.
- [Benagli 09] S. Benagli, D. Borrello, E. Vallat-Sauvain, J. Meier, U. Kroll, J. Hoetzel, J. Bailat, J. Steinhauser, M. Marmelo, G. Monteduro & L. Castens. *HIGH-EFFICIENCY AMORPHOUS SILICON DEVICES ON LPCVD-ZNO TCO PREPARED IN INDUSTRIAL KAI TM-M R&D REACTOR.* In 24th European Photovoltaic Solar

- Energy Conference and Exhibition, 21-25 September 2009, Hamburg, Germany, pages 2293–2298, 2009.
- [Berginski 07] Michael Berginski, Jürgen Hüpkes, Melanie Schulte, Gunnar Schöpe, Helmut Stiebig, Bernd Rech & Matthias Wuttig. *The effect of front ZnO:Al surface texture and optical transparency on efficient light trapping in silicon thin-film solar cells*. Journal of Applied Physics, vol. 101, no. 7, page 074903, 2007.
- [Berginski 08] Michael Berginski, Jürgen Hüpkes, Aad Gordijn, Wilfried Reetz, Timo Wätjen, Bernd Rech & Matthias Wuttig. *Experimental studies and limitations of the light trapping and optical losses in microcrystalline silicon solar cells*. Solar Energy Materials and Solar Cells, vol. 92, no. 9, pages 1037 – 1042, 2008.
- [Bittkau 12] K. Bittkau, W. Böttler, M. Ermes, V. Smirnov & F. Finger. *Light scattering at textured back contacts for n-i-p thin-film silicon solar cells*. Journal of Applied Physics, vol. 111, no. 8, page 083101, 2012.
- [Boccard 10a] M. Boccard, P. Cuony, T. Soderstrom, G. Bugnon, M. Despeisse, C. Battaglia, L. Ding, S. Nicolay & C. Ballif. *Transparent Conducting Oxide Electrodes Requirements for High Efficiency Micromorph Solar Cells*. In 25th European Photovoltaic Solar Energy Conference and Exhibition / 5th World Conference on Photovoltaic Energy Conversion, 6-10 September 2010, Valencia, Spain, pages 3108–3111, 2010.
- [Boccard 10b] Mathieu Boccard, Peter Cuony, Corsin Battaglia, Matthieu Despeisse & Christophe Ballif. *Unlinking absorption and haze in thin film silicon solar cells front electrodes*. Physica Status Solidi-rapid Research Letters, vol. 4, no. 11, pages 326–328, November 2010.
- [Boccard 11] M. Boccard, P. Cuony, M. Despeisse, D. Dominé, A. Feltrin, N. Wyrsh & C. Ballif. *Substrate dependent stability and interplay between optical and electrical properties in single junction solar cells*. Solar Energy Materials and Solar Cells, vol. 95, no. 1, pages 195 – 198, 2011. 19th International Photovoltaic Science and Engineering Conference and Exhibition (PVSEC-19) Jeju, Korea, 9-13 November 2009.
- [Boccard 12a] M. Boccard, P. Cuony, C. Battaglia, S. Hanni, S. Nicolay, L. Ding, M. Benkhaira, G. Bugnon, A. Billet, M. Charriere, K. Soderstrom, J. Escarre, F. Sculati-Meillaud, M. Despeisse & C. Ballif. *Nanometer- and Micrometer-Scale Texturing for High-Efficiency Micromorph Thin-Film Silicon Solar Cells*. Photovoltaics, IEEE Journal of, vol. 2, no. 2, pages 83 –87, april 2012.
- [Boccard 12b] M. Boccard, T. Soderstrom, P. Cuony, C. Battaglia, S. Hanni, S. Nicolay, L. Ding, M. Benkhaira, G. Bugnon, A. Billet, M. Charriere, F. Meillaud, M. Despeisse

## Bibliography

---

- & C. Ballif. *Optimization of ZnO Front Electrodes for High-Efficiency Micro-morph Thin-Film Si Solar Cells*. Photovoltaics, IEEE Journal of, vol. 2, no. 3, pages 229–235, July 2012.
- [Boccard 12c] Mathieu Boccard, Corsin Battaglia, Simon Hänni, Karin Söderström, Jordi Escarré, Sylvain Nicolay, Fanny Meillaud, Matthieu Despeisse & Christophe Ballif. *Multiscale Transparent Electrode Architecture for Efficient Light Management and Carrier Collection in Solar Cells*. Nano Letters, vol. 12, no. 3, pages 1344–1348, 2012.
- [Boccard 12d] Mathieu Boccard, Corsin Battaglia, Franz-Josef Haug, Matthieu Despeisse & Christophe Ballif. *Light trapping in solar cells: Analytical modeling*. Applied Physics Letters, vol. 101, no. 15, page 151105, 2012.
- [Boccard 12e] Mathieu Boccard, Matthieu Despeisse & Christophe Ballif. *Innovative Device Architecture for High Efficiency Thin Film Silicon Solar Cells*. MRS Proceedings, page 1426, April 2012.
- [Böttler 12] W. Böttler, V. Smirnov, J. Hüpkes & F. Finger. *Texture-etched ZnO as a versatile base for optical back reflectors with well-designed surface morphologies for application in thin film solar cells*. Physica Status Solidi (A) Applications and Materials Science, vol. 209, no. 6, pages 1144–1149, 2012.
- [Buehlmann 07] P. Buehlmann, J. Bailat, D. Domine, A. Billet, F. Meillaud, A. Feltrin & C. Ballif. *In situ silicon oxide based intermediate reflector for thin-film silicon micro-morph solar cells*. Applied Physics Letters, vol. 91, no. 14, OCT 1 2007.
- [Bugnon 11] G. Bugnon, G. Parascandolo, T. Soderstrom, R. Bartlome, S. Hänni, M. Boccard, J. Holovsky, M. Despeisse, F. Meillaud & C. Ballif. *High rate deposition of microcrystalline silicon with silicon oxide doped layers: highlighting the competing role of both intrinsic and extrinsic defects on the cells performances*. In Proceedings of the 37th IEEE PV Conference, Seattle, 2011.
- [Bugnon 12] Grégory Bugnon, Gaetano Parascandolo, Thomas Söderström, Peter Cuony, Matthieu Despeisse, Simon Hänni, Jakub Holovský, Fanny Meillaud & Christophe Ballif. *A New View of Microcrystalline Silicon: The Role of Plasma Processing in Achieving a Dense and Stable Absorber Material for Photovoltaic Applications*. Advanced Functional Materials, vol. 22, no. 17, pages 3665–3671, 2012.
- [Calnan 08] S. Calnan, J. Hüpkes, B. Rech, H. Siekmann & A.N. Tiwari. *High deposition rate aluminium-doped zinc oxide films with highly efficient light trapping for silicon thin film solar cells*. Thin Solid Films, vol. 516, no. 6, pages 1242–1248, 2008.

- [Chen 12] T. Chen, Y. Huang, A. Dasgupta, M. Luysberg, L. Houben, D. Yang, R. Carius & F. Finger. *Microcrystalline silicon carbide window layers in thin film silicon solar cells*. Solar Energy Materials and Solar Cells, vol. 98, pages 370–378, 2012.
- [Cuony 10] P. Cuony, M. Marending, D. T. L. Alexander, M. Boccard, G. Bugnon, M. Despeisse & C. Ballif. *Mixed-phase p-type silicon oxide containing silicon nanocrystals and its role in thin-film silicon solar cells*. Applied Physics Letters, vol. 97, no. 21, page 213502, November 2010.
- [Cuony 11] Peter Cuony. *Optical layers for thin-film silicon solar cells*. PhD thesis, EPFL, 2011.
- [Cuony 12] Peter Cuony, Duncan T. L. Alexander, Ivan Perez-Wurfl, Matthieu Despeisse, Gregory Bugnon, Mathieu Boccard, Thomas Soderstrom, Aicha Hessler-Wyser, Cecile Hebert & Christophe Ballif. *Silicon filaments in silicon oxide for next-generation photovoltaics*. Advanced materials, vol. 24, no. 9, pages 1182–6, March 2012.
- [Deckman 83a] H. W. Deckman, C. B. Roxlo & E. Yablonovitch. *Maximum statistical increase of optical absorption in textured semiconductor films*. Opt. Lett., vol. 8, no. 9, pages 491–493, Sep 1983.
- [Deckman 83b] H. W. Deckman, C. R. Wronski & H. Witzke. *Fabrication of optically enhanced thin film a-SiH[sub x] solar cells*. Journal of Vacuum Science & Technology A: Vacuum, Surfaces, and Films, vol. 1, no. 2, pages 578–582, 1983.
- [Deckman 83c] H W Deckman, C R Wronski, H Witzke & E Yablonovitch. *Optically enhanced amorphous silicon solar cells*. Applied Physics Letters, vol. 42, no. 11, pages 110968–110970, 1983.
- [Despeisse 10] M. Despeisse, M. Boccard, G. Bugnon, P. Cuony, T. Soderstrom, G. Parascandolo, M. Stuckelberger, M. Charriere, L. Lofgren, C. Battaglia, S. Hänni, A. Billet, L. Ding, S. Nicolay, F. Sculati-Meillaud, N. Wyrsh & C. Ballif. *Low-Conductivity Doped Layers for Improved Performance of Thin Film Silicon Solar Cells on Highly Textured Substrates*. In 25th European Photovoltaic Solar Energy Conference and Exhibition / 5th World Conference on Photovoltaic Energy Conversion, 6-10 September 2010, Valencia, Spain, pages 2793–2797, 2010.
- [Despeisse 11] Matthieu Despeisse, Corsin Battaglia, Mathieu Boccard, Gregory Bugnon, Mathieu Charriere, Peter Cuony, Simon Haenni, Linus Lofgren, Fanny Meillaud, Gaetano Parascandolo, Thomas Soederstroem & Christophe Ballif. *Optimization of thin film silicon solar cells on highly textured substrates*. Physica Status Solidi A-applications and Materials Science, vol. 208, no. 8, pages 1863–1868, August 2011.

## Bibliography

---

- [Ding 11] Kaining Ding, Thomas Kirchartz, Bart E. Pieters, Carolin Ulbrich, Alexander M. Hermes, Sandra Schicho, Andreas Lambertz, Reinhard Carius & Uwe Rau. *Characterization and simulation of a-Si:H/ $\mu$ c-Si:H tandem solar cells*. Solar Energy Materials and Solar Cells, vol. 95, no. 12, pages 3318 – 3327, 2011.
- [Ding 12] L. Ding, M. Boccard, G. Bugnon, M. Benkhaira, S. Nicolay, M. Despeisse, F. Meillaud & C. Ballif. *Highly transparent ZnO bilayers by LP-MOCVD as front electrodes for thin-film micromorph silicon solar cells*. Solar Energy Materials and Solar Cells, vol. 98, no. 0, pages 331 – 336, 2012.
- [Ding 13] Laura Ding, Sylvain Nicolay, Jérôme Steinhauser & Christophe Ballif. *in preparation*. 2013.
- [Dominé 06] D Dominé, J. Bailat, J. Steinhauser, A. Shah & C. Ballif. *Micromorph solar cell optimization using a ZnO layer as intermediate reflector*. Conference Record of the 2006 IEEE 4th World Conference 3, page 1465, 2006.
- [Domine 08] Didier Domine, Peter Buehlmann, Julien Bailat, Adrian Billet, Andrea Feltrin & Christophe Ballif. *Optical management in high-efficiency thin-film silicon micromorph solar cells with a silicon oxide based intermediate reflector*. Physica Status Solidi-rapid Research Letters, vol. 2, no. 4, pages 163–165, AUG 2008.
- [Dominé 09] Didier Dominé. *The role of front electrodes and intermediate reflectors in the optoelectronic properties of high-efficiency micromorph solar cells*. PhD thesis, University of Neuchatel, 2009.
- [Domine 10] Didier Domine, Franz-Josef Haug, Corsin Battaglia & Christophe Ballif. *Modelling of light scattering from micro- and nanotextured surfaces*. Journal of Applied Physics, vol. 107, no. 044504, 2010.
- [Eminian 11] C. Eminian, E.-J. Haug, O. Cubero, X. Niquille & C. Ballif. *Photocurrent enhancement in thin film amorphous silicon solar cells with silver nanoparticles*. Progress in Photovoltaics: Research and Applications, vol. 19, no. 3, pages 260–265, 2011.
- [Escarré 11] Jordi Escarré, Karin Söderström, Corsin Battaglia, Franz-Josef Haug & Christophe Ballif. *High fidelity transfer of nanometric random textures by UV embossing for thin film solar cells applications*. Solar Energy Materials and Solar Cells, vol. 95, no. 3, pages 881 – 886, 2011.
- [Fahr 11] Stephan Fahr, Thomas Kirchartz, Carsten Rockstuhl & Falk Lederer. *Approaching the Lambertian limit in randomly textured thin-film solar cells*. Opt. Express, vol. 19, no. S4, pages A865–A874, Jul 2011.

- [Faÿ 06] S. Faÿ, L. Feitknecht, R. Schlüchter, U. Kroll, E. Vallat-Sauvain & A. Shah. *Rough ZnO layers by LP-CVD process and their effect in improving performances of amorphous and microcrystalline silicon solar cells*. Solar Energy Materials and Solar Cells, vol. 90, no. 18-19, pages 2960–2967, November 2006.
- [Feltrin 09] A. Feltrin, R. Bartlome, C. Battaglia, M. Boccard, G. Bugnon, P. Buehlmann, O. Cubero, M. Despeisse, D. Domine, F. J. Haug, F. Meillaud, X. Niquille, G. Parascandolo, T. Soederstroem, B. Strahm, V. Terrazoni, N. Wyrsh & C. Ballif. *An Introduction To the Technology of Thin Film Silicon Photovoltaics*. Informacije Midem-journal of Microelectronics Electronic Components and Materials, vol. 39, no. 4, pages 231–236, December 2009.
- [Feltrin 12] Andrea Feltrin & et al. *Advanced super light trapping of high efficiency thin film silicon solar cells*. In 4th international workshop on thin-film silicon solar cells, March 2012, Neuchatel, Switzerland, 2012.
- [Finger 09] F. Finger, O. Astakhov, T. Bronger, R. Carius, T. Chen, A. Dasgupta, A. Gordijn, L. Houben, Y. Huang, S. Klein, M. Luysberg, H. Wang & L. Xiao. *Microcrystalline silicon carbide alloys prepared with HWCVD as highly transparent and conductive window layers for thin film solar cells*. Thin Solid Films, vol. 517, no. 12, pages 3507–3512, 2009.
- [Green 95] M. A. Green. *Silicon solar cells : advanced principles & practice*. Kensington, N.S.W., 1995.
- [Han 11] Kang-Soo Han, Ju-Hyeon Shin, Kang-In Kim & Heon Lee. *Nanosized Structural Anti-Reflection Layer for Thin Film Solar Cells*. Japanese Journal of Applied Physics, vol. 50, no. 2, page 020207, 2011.
- [Hanak 79] J.J. Hanak. *Monolithic solar cell panel of amorphous silicon*. Solar Energy, vol. 23, no. 2, pages 145 – 147, 1979.
- [Hänni 11] S. Hänni, C. Battaglia, M. Boccard, G. Bugnon, P. Cuony, M. Despeisse, L. Ding, S. Nicolay, F. Sculati-Meillaud & C. Ballif. *Towards Better Understanding of Long-Term Stability in Thin Film Microcrystalline Silicon Solar Cells*. In 26th European Photovoltaic Solar Energy Conference and Exhibition, 2011, Hamburg, Germany, pages 2699–2703, 2011.
- [Hänni 12] S. Hänni, D. T. L. Alexander, L. Ding, G. Bugnon, M. Boccard, C. Battaglia, P. Cuony, J. Escarré, G. Parascandolo, S. Nicolay, M. Cantoni, M. Despeisse, F. Meillaud & C. Ballif. *On the Interplay Between Microstructure and Interfaces in High-Efficiency Microcrystalline Silicon Solar Cells*. Photovoltaics, IEEE Journal of, vol. PP, no. 99, pages 1 –6, 2012.

## Bibliography

---

- [Harvey 99] James E. Harvey, Cynthia L. Vernold, Andrey Krywonos & Patrick L. Thompson. *Diffractioned Radiance: A Fundamental Quantity in Nonparaxial Scalar Diffraction Theory*. Appl. Opt., vol. 38, no. 31, pages 6469–6481, Nov 1999.
- [Haug 11] F. J. Haug, K. Soderstrom, A. Naqavi & C. Ballif. *Resonances and absorption enhancement in thin film silicon solar cells with periodic interface texture*. Journal of Applied Physics, vol. 109, no. 8, page 084516, April 2011.
- [Holovský 12] J. Holovský, M. Bonnet-Eymard, M. Boccard, M. Despeisse & C. Ballif. *Variable light biasing method to measure component I-V characteristics of multi-junction solar cells*. Solar Energy Materials and Solar Cells, vol. 103, no. 0, pages 128 – 133, 2012.
- [Hüpkes 12] Jürgen Hüpkes, Jorj I. Owen, Sascha E. Pust & Eerke Bunte. *Chemical Etching of Zinc Oxide for Thin-Film Silicon Solar Cells*. ChemPhysChem, vol. 13, no. 1, pages 66–73, 2012.
- [Isabella 09] O. Isabella, B. Lipovšek, J. Krč & M. Zeman. *Photonic crystal back reflector in thin-film silicon solar cells*. volume 1153, pages 41–46, 2009.
- [Isabella 10a] Olindo Isabella, Janez Krč & Miro Zeman. *Modulated surface textures for enhanced light trapping in thin-film silicon solar cells*. Applied Physics Letters, vol. 97, no. 10, page 101106, 2010.
- [Isabella 10b] Olindo Isabella, Folkert Moll, Janez Krč & Miro Zeman. *Modulated surface textures using zinc-oxide films for solar cells applications*. physica status solidi (a), vol. 207, no. 3, pages 642–646, 2010.
- [Jäger 09] Klaus Jäger & Miro Zeman. *A scattering model for surface-textured thin films*. Applied Physics Letters, vol. 95, no. 17, page 171108, 2009.
- [Kambe 07] M. Kambe, K. Masumo, N. Taneda, T. Oyama & K. Sato. Technical Digest of the 17th International Photovoltaic Science and Engineering Conference, pages 1161–1162, 2007.
- [Klein 11] Stefan Klein, Stephan Wieder, Susanne Buschbaum, Martin Rohde, Konrad Schwanitz, Tobias Stolley, Christian Stömmmer, Daniel Severin, Axel Straub, Ursula I. Schmidt & Khaled Ahmed. *Large area thin film silicon modules with 10% efficiency for production*. physica status solidi (c), vol. 8, no. 10, pages 2978–2981, 2011.
- [Koida 08] T. Koida, H. Fujiwara & M. Kondo. *Structural and electrical properties of hydrogen-doped films fabricated by solid-phase crystallization*. Journal of Non-Crystalline Solids, vol. 354, no. 19-25, pages 2805 – 2808, 2008. Proceedings of the 22nd International Conference on Amorphous and Nanocrystalline Semiconductors - Science and Technology.



- [Koida 09] T. Koida, H. Fujiwara & M. Kondo. *High-mobility hydrogen-doped  $In_2O_3$  transparent conductive oxide for a-Si:H/c-Si heterojunction solar cells*. Solar Energy Materials And Solar Cells, vol. 93, no. 6-7, pages 851–854, JUN 2009. 17th International Photovoltaic Science and Engineering Conference, Fukuoka, JAPAN, DEC 03-07, 2007.
- [Koida 10] Takashi Koida, Hitoshi Sai & Michio Kondo. *Application of hydrogen-doped  $In_2O_3$  transparent conductive oxide to thin-film microcrystalline Si solar cells*. Thin Solid Films, vol. 518, no. 11, pages 2930–2933, March 2010.
- [Kroll 11] U. Kroll, J. Meier, L. Fesquet, J. Steinhauser, J.B Orhan S. Benagli, B. Wolf, D. Borrello, L. Castens, Y. Djeridane, G. Choong X. Multone, D. Domine, J.-F. Boucher, P.-A. Madliger, G. Monteduro M. Marmelo, B. Dehbozorgi, D. Romang, E. Omnes, M. Chevalley, G. Charitat, A. Pomey, E. Vallat-Sauvain, S. Marjanovic, K. Koch G. Kohnke, J. Liu, R. Modavis, D. Thelen, S. Vallon & D. Weidman A. Zakharian. *Recent Developments of High-Efficiency Micromorph Tandem Solar Cells in KAI-M/ Plasmabox PECVD Reactors*. In Proceedings of the 26th European Photovoltaic Solar Energy Conference and Exhibition, 2011, Hamburg, Germany, pages 2340 – 2343, 2011.
- [Krč 03] Janez Krč, Franc Smole & Marko Topič. *Analysis of light scattering in amorphous Si:H solar cells by a one-dimensional semi-coherent optical model*. Progress in Photovoltaics: Research and Applications, vol. 11, no. 1, pages 15–26, 2003.
- [Krč 04] J. Krč, F. Smole & M. Topič. *Study of enhanced light scattering in microcrystalline silicon solar cells*. Journal of Non-Crystalline Solids, vol. 338-340, no. 0, pages 673–676, 2004.
- [Krč 09] J. Krč, M. Zeman, S.L. Luxembourg & M. Topič. *Modulated photonic-crystal structures as broadband back reflectors in thin-film solar cells*. Applied Physics Letters, vol. 94, no. 15, 2009.
- [Krč 10] J. Krč, B. Lipovsek, M. Bokalic, A. Campa, T. Oyama, M. Kambe, T. Matsui, H. Sai, M. Kondo & M. Topič. *Potential of thin-film silicon solar cells by using high haze TCO superstrates*. Thin Solid Films, vol. 518, no. 11, pages 3054–3058, March 2010.
- [Li 09] Hongbo B. T. Li, Ronald H. Franken, Jatindra K. Rath & Ruud E. I. Schropp. *Structural defects caused by a rough substrate and their influence on the performance of hydrogenated nano-crystalline silicon n-i-p solar cells*. Solar Energy Materials and Solar Cells, vol. 93, no. 3, pages 338–349, MAR 2009.
- [Matsui 12] Takuya Matsui, Hitoshi Sai & Michio Kondo. *High efficiency thin film silicon solar cells with improved light-soaking stability*. In Proc. of 27<sup>th</sup> EU-PVSEC, Frankfurt, Germany, 2012.

## Bibliography

---

- [Meier 94] J. Meier, S. Dubail, R. Flückiger, D. Fischer, H. Keppner & A. Shah. *Intrinsic microcrystalline silicon ( $\mu\text{c-Si:H}$ ) - a promising new thin film solar cell material*. In Proceedings of the First World Conference on Photovoltaic Energy Conversion; Dec. 5-9, 1994; Hawaii, 1994.
- [Meier 96] J. Meier, P. Torres, R. Platz, J.A. Anna Selvan S. Dubail. U. Kroll, N. Pellatonvaucher, C. Hof, D. Fischer, H. Keppner, A. Shah, K.-D. Ufert, P. Giannoulès & J. Köhler. *On the Way towards High-Efficiency Thin Film Silicon Solar Cells by the "Micromorph" Concept*. In Proceedings of the Material Research Society Symposium, Spring meeting (San Francisco), 1996.
- [Meillaud 06] F. Meillaud, A. Shah, C. Droz, E. Vallat-Sauvain & C. Miazza. *Efficiency limits for single-junction and tandem solar cells*. Solar Energy Materials and Solar Cells, vol. 90, no. 18-19, pages 2952 – 2959, 2006. 14th International Photovoltaic Science and Engineering Conference.
- [Meillaud 11] F. Meillaud, A. Feltrin, M. Despeisse, F.-J. Haug, D. Dominé, M. Python, T. Söderström, P. Cuony, M. Boccard, S. Nicolay & C. Ballif. *Realization of high efficiency micromorph tandem silicon solar cells on glass and plastic substrates: Issues and potential*. Solar Energy Materials and Solar Cells, vol. 95, no. 1, pages 127 – 130, 2011. 19th International Photovoltaic Science and Engineering Conference and Exhibition (PVSEC-19) Jeju, Korea, 9-13 November 2009.
- [Moulin 08] E. Moulin, J. Sukmanowski, M. Schulte, A. Gordijn, F.X. Royer & H. Stiebig. *Thin-film silicon solar cells with integrated silver nanoparticles*. Thin Solid Films, vol. 516, no. 20, pages 6813–6817, 2008.
- [Moulin 12] Etienne Moulin, U. W. Paetzold, K. Bittkau, M. Ermes, L. Ding, L. Fanni, S. Nicolay, J. Kirchhoff, A. Bauer, A. Lambertz, C. Ballif & R. Carius. *Thin-Film Silicon Solar Cells Applying Optically Decoupled Back Reflectors*. in preparation, vol. 0, no. 0, page null, 2012.
- [Nakajima 04] Akihiko Nakajima, Mitsuru Ichikawa, Toru Sawada, Masashi Yoshimi & Kenji Yamamoto. *Spectral Characteristics of Thin-Film Stacked-Tandem Solar Modules*. Japanese Journal of Applied Physics, vol. 43, no. 10, pages 7296–7302, 2004.
- [Naqavi 11] Ali Naqavi, Karin Söderström, Franz-Josef Haug, Vincent Paeder, Toralf Scharf, Hans Peter Herzig & Christophe Ballif. *Understanding of photocurrent enhancement in real thin film solar cells: towards optimal one-dimensional gratings*. Opt. Express, vol. 19, no. 1, pages 128–140, Jan 2011.
- [Nasuno 01] Y Nasuno, M Kondo & A Matsuda. *Effects of substrate surface morphology on microcrystalline silicon solar cells*. JAPANESE JOURNAL OF APPLIED PHYSICS PART 2-LETTERS, vol. 40, no. 4A, pages L303–L305, APR 1 2001.

- [Naughton 10] M. J. Naughton, K. Kempa, Z. F. Ren, Y. Gao, J. Rybczynski, N. Argenti, W. Gao, Y. Wang, Y. Peng, J. R. Naughton, G. McMahon, T. Paudel, Y. C. Lan, M. J. Burns, A. Shepard, M. Clary, C. Ballif, F. J. Haug, T. Soederstroem, O. Cubero & C. Eminian. *Efficient nanocoax-based solar cells*. Physica Status Solidi-Rapid Research Letters, vol. 4, no. 7, pages 181–183, JUL 2010.
- [Nicolay 09] S. Nicolay, S. Fay & C. Ballif. *Growth Model of MOCVD Polycrystalline ZnO*. Crystal Growth & Design, vol. 9, no. 11, pages 4957–4962, 2009.
- [Obermeyer 08] Philipp Obermeyer, Christian Haase & Helmut Stiebig. *Advanced light trapping management by diffractive interlayer for thin-film silicon solar cells*. Applied Physics Letters, vol. 92, no. 18, page 181102, 2008.
- [Owen 10] J.I. Owen, J. Hüpkes, E. Bunte, S.E. Pust & A. Gordijn. *Etching Modulated Surface Textures into Sputtered ZnO:Al Films*. In Proceedings of the 25th European Photovoltaic Solar Energy Conference and Exhibition / 5th World Conference on Photovoltaic Energy Conversion, 6-10 September 2010, Valencia, Spain, pages 2951 – 2955, 2010.
- [Poruba 00] A. Poruba, A. Fejfar, Z. Remeš, J. Špringer, M. Vaneček, J. Kočka, J. Meier, P. Torres & A. Shah. *Optical absorption and light scattering in microcrystalline silicon thin films and solar cells*. Journal of Applied Physics, vol. 88, no. 1, pages 148–160, 2000.
- [Python 08] Martin Python, Evelyne Vallat-Sauvain, Julien Bailat, Didier Dominé, Luc Fesquet, Arvind Shah & Christophe Ballif. *Relation between substrate surface morphology and microcrystalline silicon solar cell performance*. Journal of Non-Crystalline Solids, vol. 354, no. 19-25, pages 2258–2262, May 2008.
- [Python 09] M. Python, O. Madani, D. Dominé, F. Meillaud, E. Vallat-Sauvain & C. Ballif. *Influence of the substrate geometrical parameters on microcrystalline silicon growth for thin-film solar cells*. Solar Energy Materials and Solar Cells, vol. 93, no. 10, pages 1714 – 1720, 2009.
- [Python 10] M. Python, D. Dominé, T. Soderstrom, F. Meillaud & C. Ballif. *Microcrystalline silicon solar cells: effect of substrate temperature on cracks and their role in post-oxidation*. Progress in Photovoltaics: Research and Applications, vol. 18, no. 7, pages 491–499, 2010.
- [Riedel 10] Boris Riedel, Inga Kaiser, Julian Hauss, Uli Lemmer & Martina Gerken. *Improving the outcoupling efficiency of indium-tin-oxide-free organic light-emitting diodes via rough internal interfaces*. Opt. Express, vol. 18, no. S4, pages A631–A639, Nov 2010.
- [Rockstuhl 10] C. Rockstuhl, S. Fahr, K. Bittkau, T. Beckers, R. Carius, F.-J. Haug, T. Soderstrom, C. Ballif & F. Lederer. *Comparison and optimization of randomly*

## Bibliography

---

- textured surfaces in thin-film solar cells*. Optics Express, vol. 18, no. S3, page 129212, 2010.
- [Ruske 10] F. Ruske, M. Roczen, K. Lee, M. Wimmer, S. Gall, J. Hüpkes, D. Hrunski & B. Rech. *Improved electrical transport in Al-doped zinc oxide by thermal treatment*. Journal of Applied Physics, vol. 107, no. 1, page 013708, 2010.
- [Sai 10] Hitoshi Sai, Haijun Jia & Michio Kondo. *Impact of front and rear texture of thin-film microcrystalline silicon solar cells on their light trapping properties*. Journal of Applied Physics, vol. 108, no. 4, page 044505, 2010.
- [Sakai 90] Hiroshi Sakai, Takasi Yoshida, Toshio Hama & Yukimi Ichikawa. *Effects of Surface Morphology of Transparent Electrode on the Open-Circuit Voltage in a-Si:H Solar Cells*. Japanese Journal of Applied Physics, vol. 29, no. Part 1, No. 4, pages 630–635, 1990.
- [Schiff 11] E. A. Schiff. *Thermodynamic limit to photonic-plasmonic light-trapping in thin films on metals*. Journal of Applied Physics, vol. 110, no. 10, page 104501, 2011.
- [Schulte 11a] M. Schulte, K. Bittkau, K. Jäger, M. Ermes, M. Zeman & B. E. Pieters. *Angular resolved scattering by a nano-textured ZnO/silicon interface*. Applied Physics Letters, vol. 99, no. 11, page 111107, 2011.
- [Schulte 11b] Melanie Schulte, Karsten Bittkau, Bart Elger Pieters, Silvia Jorke, Helmut Stiebig, Jürgen Hüpkes & Uwe Rau. *Ray tracing for the optics at nano-textured ZnO-air and ZnO-silicon interfaces*. Progress in Photovoltaics: Research and Applications, vol. 19, no. 6, pages 724–732, 2011.
- [Shah 10] Arvind Shah. *Thin-film silicon solar cells*. EPFL Press, 2010.
- [Sichanugrist 93] P. Sichanugrist, T. Yoshida, Y. Ichikawa & H. Sakai. *Amorphous silicon oxide with microcrystalline Si phase*. Journal of Non-Crystalline Solids, vol. 164-166, Part 2, no. 0, pages 1081–1084, 1993. Proceedings of the Fifteenth International Conference on Amorphous Semiconductors-Science and Technology.
- [Smirnov 12] V. Smirnov, A. Lambertz, B. Grootoink, R. Carius & F. Finger. *Microcrystalline silicon oxide ( $\mu\text{c-SiOx:H}$ ) alloys: A versatile material for application in thin film silicon single and tandem junction solar cells*. Journal of Non-Crystalline Solids, vol. 358, no. 17, pages 1954–1957, 2012.
- [Söderström 09] T. Söderström, F.-J. Haug, X. Niquille, V. Terrazzoni & C. Ballif. *Asymmetric intermediate reflector for tandem micromorph thin film silicon solar cells*. Applied Physics Letters, vol. 94, no. 6, page 063501, 2009.
- [Söderström 10] T. Söderström, D. Dominé, A. Feltrin, M. Despeisse, F. Meillaud, G. Bugnon, M. Boccard, P. Cuony, F.-J. Haug, S. Fay, S. Nicolay & C. Ballif. *ZnO transparent*

- conductive oxide for thin film silicon solar cells*. volume 7603, page 76030B. SPIE, 2010.
- [Söderström 11] K. Söderström, J. Escarré, O. Cubero, F.-J. Haug, S. Perregaux & C. Ballif. *UV-nano-imprint lithography technique for the replication of back reflectors for n-i-p thin film silicon solar cells*. Progress in Photovoltaics: Research and Applications, vol. 19, no. 2, pages 202–210, 2011.
- [Springer 03] J. Springer, A. Poruba, L. Mullerova, M. Vanecek, W Reetz & J Muller. *3-dimensional optical model for thin film silicon solar cells*. In Proceedings of 3rd World Conference on Photovoltaic Energy Conversion, Osaka, Japan, 2003, page 1827, 2003.
- [Staebler 77] D. L. Staebler & C. R. Wronski. *Reversible conductivity changes in discharge-produced amorphous Si*. Applied Physics Letters, vol. 31, no. 4, pages 292–294, 1977.
- [Steinhauser 07] J. Steinhauser, S. Faÿ, N. Oliveira, E. Vallat-Sauvain & C. Ballif. *Transition between grain boundary and intragrain scattering transport mechanisms in boron-doped zinc oxide thin films*. Applied Physics Letters, vol. 90, no. 14, page 142107, 2007.
- [Steinhauser 08] Jérôme Steinhauser. *Low pressure chemical Vapor deposited zinc oxide for silicon thin-film solar cells. Optical and electrical properties*. PhD thesis, University of Neuchâtel, 2008.
- [Tan 12] Hairen Tan, Rudi Santbergen, Arno H. M. Smets & Miro Zeman. *Plasmonic Light Trapping in Thin-film Silicon Solar Cells with Improved Self-Assembled Silver Nanoparticles*. Nano Letters, vol. 12, no. 8, pages 4070–4076, 2012.
- [Tiedje 84] T. Tiedje, E. Yablonovitch, G.D. Cody & B.G. Brooks. *Limiting efficiency of silicon solar cells*. Electron Devices, IEEE Transactions on, vol. 31, no. 5, pages 711 – 716, may 1984.
- [Tvingstedt 08] Kristofer Tvingstedt, Simone Dal Zilio, Olle Inganäs & Massimo Tormen. *Trapping light with micro lenses in thin film organic photovoltaic cells*. Opt. Express, vol. 16, no. 26, pages 21608–21615, Dec 2008.
- [Ulbrich 08] Carolin Ulbrich, Stephan Fahr, Johannes Üpping, Marius Peters, Thomas Kirchartz, Carsten Rockstuhl, Ralf Wehrspohn, Andreas Gombert, Falk Lederer & Uwe Rau. *Directional selectivity and ultra-light-trapping in solar cells*. physica status solidi (a), vol. 205, no. 12, pages 2831–2843, 2008.
- [Ulbrich 11] Carolin Ulbrich. *Spectral and directional dependence of light-trapping in solar cells*. PhD thesis, Forschung Zentrum Jülich, 2011.

## Bibliography

---

- [Üpping 11] Johannes Üpping, Andreas Bielawny, Ralf B. Wehrspohn, Thomas Beckers, Reinhard Carius, Uwe Rau, Stefan Fahr, Carsten Rockstuhl, Falk Lederer, Matthias Kroll, Thomas Pertsch, Lorenz Steidl & Rudolf Zentel. *Three-Dimensional Photonic Crystal Intermediate Reflectors for Enhanced Light-Trapping in Tandem Solar Cells*. *Advanced Materials*, vol. 23, no. 34, pages 3896–3900, 2011.
- [van den Donker 07] M. N. van den Donker, S. Klein, B. Rech, F. Finger, W. M. M. Kessels & M. C. M. van de Sanden. *Microcrystalline silicon solar cells with an open-circuit voltage above 600 mV*. *Applied Physics Letters*, vol. 90, no. 18, page 183504, 2007.
- [Vanecek 11] Milan Vanecek, Oleg Babchenko, Adam Purkrt, Jakub Holovsky, Neda Neykova, Ales Poruba, Zdenek Remes, Johannes Meier & Ulrich Kroll. *Nanos-structured three-dimensional thin film silicon solar cells with very high efficiency potential*. *Applied Physics Letters*, vol. 98, no. 16, page 163503, 2011.
- [Vetterl 01] O. Vetterl, A. Lambertz, A. Dasgupta, F. Finger, B. Rech, O. Kluth & H. Wagner. *Thickness dependence of microcrystalline silicon solar cell properties*. *Solar Energy Materials and Solar Cells*, vol. 66, no. 1-4, pages 345–351, 2001.
- [Wiesendanger 11] Sämi Wiesendanger, Stephan Fahr, Thomas Kirchartz, Carsten Rockstuhl & Falk Lederer. *Achieving the Yablonovitch Limit in Thin-Film Solar Cells with Tailored Randomly Textured Interfaces*. In *Renewable Energy and the Environment*, page PThB4. Optical Society of America, 2011.
- [Würfel 00] Peter Würfel. *Physics of solar cells: From principles to new concepts*. Wiley-VCH Verlag GmbH, 200.
- [Yablonovitch 82a] E. Yablonovitch & G.D. Cody. *Intensity enhancement in textured optical sheets for solar cells*. *Electron Devices, IEEE Transactions on*, vol. 29, no. 2, pages 300 – 305, feb 1982.
- [Yablonovitch 82b] Eli Yablonovitch. *Statistical Ray Optics*. *Journal of the Optical Society of America*, vol. 72, no. 7, page 899, July 1982.
- [Yamamoto 03] K. Yamamoto, A. Nakajima, M. Yoshimi, T. Sawada, S. Fukuda, T. Suezaki, M. Ichikawa, Y. Koi, M. Goto, H. Takata, T. Sasaki & Y. Tawada. *Novel hybrid thin film silicon solar cell and module*. In *Photovoltaic Energy Conversion, 2003. Proceedings of 3rd World Conference on Photovoltaic Energy Conversion*, volume 3, pages 2789 –2792 Vol.3, may 2003.
- [Yamamoto 04] Kenji Yamamoto, Akihiko Nakajima, Masashi Yoshimi, Toru Sawada, Susumu Fukuda, Takashi Suezaki, Mitsuru Ichikawa, Yohei Koi, Masahiro Goto, Tomomi Meguro, Takahiro Matsuda, Masataka Kondo, Toshiaki Sasaki & Yuko Tawada. *A high efficiency thin film silicon solar cell and module*. *Solar Energy*, vol. 77, no. 6, pages 939 – 949, 2004. *Thin Film PV*.

- [Yamamoto 05] Kenji Yamamoto, Akihiko Nakajima, Masashi Yoshimi, Toru Sawada, Susumu Fukuda, Takashi Suezaki, Mitsuru Ichikawa, Yohei Koi, Masahiro Goto, Tomomi Meguro, Takahiro Matsuda, Masataka Kondo, Toshiaki Sasaki & Yuko Tawada. *A thin-film silicon solar cell and module*. Progress in Photovoltaics: Research and Applications, vol. 13, no. 6, pages 489–494, 2005.
- [Yan 12] Baojie Yan, Jeffrey Yang & Subhendu Guha. *Amorphous and nanocrystalline silicon thin film photovoltaic technology on flexible substrates*. Journal of Vacuum Science Technology A: Vacuum, Surfaces, and Films, vol. 30, no. 4, pages 04D108–04D108–10, jul 2012.
- [Yu 10] Zongfu Yu, Aaswath Raman & Shanhui Fan. *Fundamental limit of nanophotonic light trapping in solar cells*. Proceedings of the National Academy of Sciences, 2010.
- [Zeman 08] M. Zeman & J. Krč. *Optical and electrical modeling of thin-film silicon solar cells*. Journal of Material Research, vol. 23, no. 4, pages 889–898, APR 2008. Spring Meeting Symposium of the Materials-Research-Society, San Francisco, CA, APR 09-13, 2007.
- [Zhang 12] Deming Zhang, Shelby Vorndran, Juan M. Russo, Michael Gordon & Raymond K. Kostuk. *Ultra light-trapping filters with broadband reflection holograms*. Opt. Express, vol. 20, no. 13, pages 14260–14271, Jun 2012.
- [Zhu 10] Jia Zhu, Ching-Mei Hsu, Zongfu Yu, Shanhui Fan & Yi Cui. *Nanodome Solar Cells with Efficient Light Management and Self-Cleaning*. Nano Letters, vol. 10, no. 6, pages 1979–1984, 2010.





# Acknowledgements

I first acknowledge Christophe Ballif for giving me the opportunity to work in PV-lab. His never ending enthusiasm and faith in the usefulness of our every-day work has always been a great motivation. Funding by the Swiss Federal Office of Energy is also largely acknowledged.

Special thanks go then to my first thesis supervisor, Andrea Feltrin, who warmly welcomed me in his team and took a lot of time to introduce me the new technology, and to my second supervisor, Matthieu Despeisse, for his warm support in many occasion, his valuable advices during the many doubtful moments that arose during this work, and finally for his permanent good mood and communicative smile.

Warm thanks go then to Peter, who admirably welcomed me in the laboratory and helped me to find my place in this new environment with his continuous support and availability. Many thanks also to Fanny, our adoptive mother (in the sense we adopted her) for her pragmatism and guidance in delicate situations, and to Corsin, for the never-ending – but always interesting – discussions.

I warmly thank other members of the lab, notably (but not exclusively) the team of PhD students, for their contribution in making PV-lab a happy and lively place to work. A special thought goes to the “dépôt pirate” team and to the Friday-afternoon-teaching-in-EPFL team, who contributed to brighten up the end of the days or of the week quite some time.

I also warmly acknowledge the support of Brigitte Khan and Mary-Claude Gauteaub, for the guidance in the labyrinth of administrative procedures, and of all colleagues that helped me in one or the other way (notably the technical team, Mustapha for his impressive commitment in having ZnO deposition system working, Mathieu and Greg for all the cell depositions, and Sylvain, Luc and Simon for the nice atmosphere in the office).

I also could count on the very valuable help of Lara Sands in proof-reading this manuscript, which was of a huge help, especially considering the short notice. Many thanks for that!

Then, moltes gracies to Pere Roca i Cabarrocas for my last-minute conversion from nuclear to photovoltaics energy, a conversion which could not have been better sealed than by the six-month internship in his laboratory under the friendly supervision of Martin Labrune. Drastic changes in the direction of one's life come from apparently insignificant moments.

## **Acknowledgements**

---

The four-half-day class on photovoltaics he gave in 2008 was one of these moments for me.

Finally, warm thanks to my friends and family whose support contributed to make this work possible, and to Laura for her invaluable help in so many indescribable ways in bringing this work to a happy end.

*Neuchâtel, November 2012*

M. B.

**Mathieu BOCCARD**

*Master degree in Physics from University of Paris,  
 Engineer from École Polytechnique, Paris.*



Place Coquillon, 4  
 2000 Neuchâtel  
 Switzerland  
 Phone : +41 79 76 76 999

mathieu.boccard@epfl.ch  
 Nationality: French  
 Age: 27

---

**EXPERIENCE**


---

11/2008 – 11/2012	<b>IMT – PVlab, École Polytechnique Fédérale de Lausanne (EPFL)</b>	<b>PhD candidate in Material Science:</b> Novel Micromorph solar cell structures for efficient light trapping and high-quality absorber layers
04/2008 – 09/2008	<b>LPICM, École Polytechnique, Paris</b>	<b>Master thesis in Physics:</b> Optimization of silicon thin-films for Photovoltaic applications
05/2007 – 07/2007	<b>Facultad de Física, Univesitat de Barcelona</b>	<b>Bachelor internship:</b> Role of dipolar interaction in nanoparticles clusters
11/2004 – 04/2005	French Army (Annecy)	Officer Military Period
07/2001 & 08/2006	Miscellaneous	Summer jobs as gardener

---

**EDUCATION**


---

09/2007 – 04/2008	<b>ENSTA, Paris:</b> Engineer degree in Electricity and Nuclear Power. <b>University of Paris, Master in Physics:</b> New technologies for energy.
09/2004 – 04/2007	<b>École Polytechnique, Paris:</b> non-specialized Engineer degree.
09/2002 – 05/2004	Physics and Engineering classes, lycée la Martinière, Lyon, France
09/1999 – 06/2002	Scientific Baccalauréat, pass with 70–80%, Annemasse, France

Language skills: French (mother tongue), English (fluent), Spanish (intermediate level), German (basics). Computer skills: good knowledge of office suite, LaTeX, basic knowledge of various simulation, mathematics and graphics tools.

---

**SCIENTIFIC CONTRIBUTIONS**


---

I coauthored 28 scientific contributions, including six peer-reviewed papers as a first author. An updated list is available on: <http://infoscience.epfl.ch/search?ln=en&p=Boccard%2C+M&f=author>. I took part to four international conferences, for which I gave three oral presentations. I was awarded the best student presentation award during the 27<sup>th</sup> IEEE Photovoltaic Specialists Conference in 2011.

---

**MISCELLANEOUS**


---

During my military training, I obtained a diploma of mountain leadership for winter activities with small groups. In 2006, I participated to the “Shell eco-marathon,” for which I worked on the optimization of the transmission of the prototype representing École Polytechnique. During my PhD thesis at IMT-PVlab, I supervised one master thesis student. I like running, skiing, soccer and badminton. I like playing music, and have been singing for 3 years in the choir of Neuchâtel University.